Loading Conditions Due to Violent Wave Impacts on Coastal Structures with Cantilever Surfaces

Belasting ten gevolge van zware golfimpacten
op kustwaterbouwkundige constructies met een uitkragend gedeelte

Dogan Kisacik

Promotoren: prof. dr. ir. P. Troch, prof. dr. ir. P. Van Bogaert
Proefschrift ingediend tot het behalen van de graad van
Doctor in de Ingenieurswetenschappen: Bouwkunde

Vakgroep Civiele Techniek
Voorzitter: prof. dr. ir. J. De Rouck
Faculteit Ingenieurswetenschappen en Architectuur
Academiejaar 2011 - 2012

UNIVERSITEIT
GENT

ISBN 978-90-8578-501-9
NUR 956, 955
Wettelijk depot: D/2012/10.500/27

Universiteit Gent
Faculteit Ingenieurswetenschappen en
Architectuur
Vakgroep Civiele Techniek
Afdeling Weg-en Waterbouwkunde

Supervisors:

Prof. dr. ir. P. Troch
Prof. dr. ir. Ph. Van Bogaert

Research institute:

Ghent University
Faculty of Engineering and Architecture

Department of Civil Engineering
Coastal Engineering Division
Technologiepark 904
B-9052 Zwijnaarde, Belgium

Tel.: +32-9-264-54-89
Fax.:+32-9-264-58-37

Acknowledgments

As the journey of writing this dissertation has come to end, it is now my turn of saying thank you.

I would like to express my gratitude and special thanks to my supervisors Prof. dr. ir P. Troch and Prof. dr. ir Ph. Van Bogaert for their academic and financial supports. They both contributed to the arguments in this work by commenting on several versions. Without their help, it would not be possible to finish my PhD.

I want to thank Prof. dr. ir H. De Backer for his corrections, ideas, and contributions to my thesis in all steps. He had always five minutes to explain me every small question.

I would also like to thank Prof. dr. ir J. De Rouck for providing a friendly working environment, the possibilities to go abroad and his valuable advices.

I want to give special thanks to Prof. Dr. Ahmet Cevdet Yalciner for encouraging me in every level of my academic life and giving me hope and courage during my hardest times.

Many thanks go to all my colleagues: Anny, Bart, Mathias, Yvan, Dieter, David, Dennis, Giang, Tomas, Florent, Ellen, Vicky, Koen, Lander, Lien, Ludo, Pieter M., Li. It was great for me to share five pleasant years with my colleagues. Having an experience in an intercultural environment has contributed to my personal development. A special thanks should go to the technical staff at our department. Thank you Herman, Tom, Dave and Sam. Tom, I can not imagine how difficult this research would have been without your support. I would also like to express my special thankfulness to my office mates: Amelie, Corneel, Dries, Ken and Wim, Wouter.

I particularly thank my dear friends Nursen Avci, Aykut Avci and Setenay Ozturk for all the times we spent together and for their friendships. A special thanks goes out Deniz Eren Avci for being very sweet and deviled. I also thank my family in Germany Melek-Osman Kizilkan and Yasemin-Yavuz Kizilkan for their supports. They all stood with us in our hardest times and created a family environment for us when we missed Turkey.

Finally, the most special gratitude goes to my love Zelal Basak Kisacik for encouraging and supporting me, for being there all the time and making me know that she is taking care of me. I would like to thank her especially for sitting with me during the evenings when I was running tests in the cold laboratory. I would have never been successful with this thesis without her support.

TABLE OF CONTENTS

Samenvatting

De groei van de wereldhandel noodzaakt de uitbouw van een groot netwerk van havens en terminals voor het aanmeren van schepen en de overslag van cargo. Verticale golfbrekers en dijken zijn frequent gebruikte structuren om die havens te beschermen tegen de invloed van de zee, b.v. golfslag en hoge waterstanden. Het beperken van de golfoverslag over golfbrekers is dus een kritiek onderdeel van golfbrekerontwerp. Daarom wordt er door ingenieurs en ontwerpers vaak voor gekozen om een overkraging of zelfs een ingeklemde horizontale plaat te voorzien aan de bovenzijde van de golfbreker. De opwaartse impact van de golven op dit horizontale deel van de golfbreker kan echter zorgen voor een aanzienlijke belasting. Deze belasting is bovendien een impactbelasting zodat ze niet gelijkgesteld kan worden aan een statisch equivalente belasting. Daarom is het nodig dat de vorm van deze golfimpacten, zowel in ruimte als in tijd, exact beschreven kan worden.

Dit onderzoek gebruikt de Pier van Blankenberge aan de Belgische Kust als voorbeeld van een verticale structuur met een horizontaal uitkragend gedeelte. Deze structuur is bij hoog tij of stormen blootgesteld aan zware golfimpacten, b.v. golfoploop op de verticale delen tot de golven stukslaan op het horizontale dek. Ten gevolge van de uiterst specifieke geometrie is de Pier dus kwetsbaar onder golfimpact.

Het hoofddoel van dit doctoraal onderzoek is de golfbelasting op een verticale structuur met horizontaal uitstekend gedeelte te bestuderen, gebaseerd op de correlatie tussen de kinematica van brekende golven enerzijds en de hoogte, distributie, duur en karakteristieken van golfimpacten gebaseerd op traditionele modelproeven.

Daarom worden testen uitgevoerd op een tweedimensionaal verschaald model in een golfgoot van de vakgroep Civiele Techniek (Universiteit Gent) met als basisafmetingen 30 x 1 x 1.2 meter. Het proefmodel bevindt zich 22.5m van het golfschot op een helling met constante hellingshoek en een waterdiepte van een halve meter ter plaatse van het model. De schaalfactor bedraagt 1 op 20 en is zo gekozen dat alle golfbewegingen correct

gereproduceerd worden. Het proefmodel is geïnstrumenteerd met 10 drukopnemers, 9 golfhoogtemeters en een hogesnelheidscamera (HSC). Er wordt gewerkt met een uiterst hoge meetfrequentie, 20 kHz, zodat het impactprobleem in detail bestudeerd kan worden. Er worden parameters bestudeerd zoals de golfperiode (T), golfhoogte (H), en waterdiepte (h_s) en dit zowel voor regelmatige als onregelmatige golven. De golfhoogtes worden zo gekozen dat het schaalmodel blootgesteld wordt aan de complete impactbelasting gaande van zowel niet-gebroken tot gebroken golven.

De belangrijkste resultaten van het doctoraal onderzoek worden samengevat in volgende paragrafen.

Het golfklimaat, gedefinieerd door golfhoogte (H) en golfperiode(T), wordt geïdentificeerd rekening houdende met “shoaling”, golfreflectie en breking. “Shoaling” werd bestudeerd voor regelmatige golven doch zonder rekening te houden met de aanwezigheid van de uitgeoefende druk op het schaalmodel. Tegelijk werd de golfreflectie geanalyseerd, zowel bij regelmatige als onregelmatige golven. De gebruikte reflectiecoëfficiënt C_r wordt gemeten aan de teen van de golfbreker. Vervolgens worden de golfhoogtes van gebroken golven vergeleken met waarden uit de literatuur. Ten slotte wordt geconcludeerd dat de aanwezigheid van het schaalmodel er voor zorgt dat de start van het breken uitgesteld wordt.

De correlatie tussen golfkinematica en de bijhorende impactdrukken en krachten wordt vervolgens bestudeerd. Elke naderende golf resulteert in twee afzonderlijke impacten die achtereenvolgens inslaan op het schaalmodel. De eerste impact gebeurt op het verticale gedeelte waarna de tweede impact optreedt op het horizontale deel nabij de hoek met het verticale deel. Beide impactdrukken en –krachten zijn niet herhaalbaar onder identieke testomstandigheden. De brekende golven worden vervolgens ingedeeld in 4 verschillende groepen gebruik makend van de classificatie van Oumeraci et al., 1993. Deze 4 groepen zijn: beperkt brekende golven, brekende golven met een kleine hoeveelheid gevangen lucht, brekende golven met een grote hoeveelheid gevangen lucht en gebroken golven. De karakteristieken van de maximaal teruggevonden drukken en krachten voor elke groep brekende golven worden vervolgens in meer detail bestudeerd, net als het kinematisch gedrag tijdens het breken en de variatie van drukken en krachten in de tijd. De tweede impact op het horizontale gedeelte veroorzaakt een toename van de druk op het bovenste deel van het verticale gedeelte in vergelijking met de situatie zonder horizontaal gedeelte. De totale horizontale krachtswerking (F_h) neemt dus toe voor de gevallen SBW en BW. De

variatie van de snelheids- (V_h, V_v) en versnellingscomponenten (a_h, a_v) van de golf wordt vervolgens geanalyseerd tot de impact plaats vindt, voor de gevallen SBW, BWSAT en BWLAT. Voor het geval van SBW geldt, in tegenstelling tot wat teruggevonden wordt in literatuur, dat bij impact V_h iets hoger is dan V_v. Na impact neemt V_v drastisch toe wegens de hoge verticale versnelling (tot 20g). De hoogste verticale versnellingen, 53g, werden geregistreerd voor BWSAT.

In een volgend deel wordt de drukverdeling ten gevolge van de golfimpact op een verticale structuur bestudeerd. Zowel de ligging als de grootte van p_{max} op een horizontale structuur met uitkragend horizontaal gedeelte wordt bepaald. Het blijkt dat voor het verticale gedeelte, de dimensieloze term (z_{max}/h_s) die de locatie van p_{max} bepaalt, geleidelijk aan afneemt van een punt boven SWL naar een locatie onder SWL bij toenemende h_s. Op het horizontale gedeelte wordt p_{max} steeds teruggevonden aan de hoek met het verticale deel en neemt de grootte sterk af onder $10\,\rho g H$ tussen $x/h_s = 0.8 - 1$. Het verband tussen de gemeten waarden voor p_{max} op het verticale deel en de bijhorende t_r kan grafisch weergegeven worden en vergeleken met empirische literatuurwaarden. Voor de nieuwe meetdata worden functies voorgesteld die gelden als bovenmarge voor het verband tussen p_{max} en t_r en dit zowel voor het horizontale als het verticale deel van het schaalmodel. Vervolgens worden de grenzen van het interval van de genormaliseerde golfhoogte $\frac{H}{h_s}$ gedefinieerd waarbinnen een zware dynamische impact optreedt bij een variatie van de vrije hoogte $\frac{c}{a}$. Ten slotte wordt voor de verschillende drukprofielen de lokale maximale druk bij SWL en aan de boven en onderzijde van het verticale gedeelte beschouwd(p_{h1}, p_{h2} and p_{h3}). Voor elk geval worden de verhoudingen p_{h3}/p_{h1}, p_{h1}/p_{v1}, en p_{h2}/p_{v1} opgesteld.

In een laatste hoofdstuk wordt een nieuw voorspellingsmodel ontwikkeld voor de verticale gerichte krachten op het horizontaal uitkragende gedeelte van het schaalmodel. Als bijdragende factoren worden alle parameters die de krachtswerking op het verticale deel bepalen bestudeerd. Bovendien worden regelmatige en onregelmatige golven vergeleken. De golfhoogte (H_1), waterdiepte aan de voet van het schaalmodel (h_s), golfperiode (T), gemiddeld overslag-debiet (q) en verticale gemiddelde snelheid (V_{av}) blijken de belangrijkste invloedsfactoren te zijn voor de verticale krachten. Gebaseerd op het experimenteel onderzoek naar de golfkinematica en impulsbelastingen kunnen formules afgeleid worden voor de verticale belasting op de onderzijde van een horizontaal uitkragend gedeelte van een verticale structuur. Hierdoor kan een ontwerpconcept voor de belasting ten gevolge van brekende golven voorgesteld worden. Hierbij is het belangrijk te

vermelden dat de afgeleide formule gebaseerd is op de gemiddelde waarden van alle meetgegevens.

Oumeraci, H.; Klammer, P.; Partenscky, H.W., 1993, "Classification of breaking wave loads on vertical structures", Journal of Waterway, Port, Coastal and Ocean Eng. v 119, n 4, p 381-397

English summary

The growth of world trade requires the construction of a large number of ports and terminals for receiving ships and transferring cargos. Vertical breakwaters and sea walls are frequently used structures to protect ports from sea actions like waves and high water levels. In view of this, controlling overtopping of the waves at the top of the vertical breakwaters is a critical issue. This is why engineers/designers tend to provide the vertical breakwaters with a return crown wall or even a completely horizontal cantilever slab to reduce the overtopping. However, upward impact beneath the horizontal cantilever slab gives rise to a significant uplifting force. These forces are impact loads and they cannot be substituted by a static equivalent. Therefore, a detailed description of the space and time distribution of the wave impacts becomes imperative for design purposes.

In this particular research, the Pier of Blankenberge which is located along the Belgian coast is shown as an illustrative example of a vertical structure with an overhanging horizontal cantilever slab. Throughout high tides and storms, the structure is exposed to violent wave impacts, including waves running up against the vertical core and slamming on the horizontal deck. Therefore, the pier is vulnerable to the wave impact loads due to its special closed geometry.

The general aim of this PhD research is to analyze wave loading on a vertical structure with an overhanging horizontal cantilever slab, based on the correlation between the kinematics of breaking waves and the height, distribution, duration and characteristics of the wave impacts, by using traditional physical model tests.

For this purpose, two dimensional scaled model tests are carried out in the wave flume at the Department of Civil Engineering (Ghent University) with dimensions 30 m x 1 m x 1.2 m. The model is located 22.5 m away from the wave paddle on a uniform slope with 0.5 m depth at the location of the structure. A scale factor of 1:20 is selected to ensure correct reproduction of all wave processes. The scaled model is instrumented with 10 sets of

pressure sensors, 9 sets of wave gauges and a high speed camera (HSC). A very high sampling frequency of 20 kHz is used for the pressure recordings which allow a detailed look into the problem. The scaled model is tested for the variation of parameters like the wave period (T), incident wave height (H) and water depth (h_s). Tests are carried out for regular and irregular waves. Wave heights (H) are arranged somehow that the scaled model became exposed to full impacts from non-breaking to broken waves.

The main outcomes from this research are listed below.

Wave conditions given by wave height (H), wave period (T) are identified by taking account of wave shoaling, reflection, and breaking. Wave shoaling has been analyzed for regular waves with test results without taking into account the pressure of the scaled-model. In addition, the wave reflection is analyzed for regular and irregular waves. The reflection coefficients C_r, measured at the toe of the foreshore. Then, breaking wave heights from regular waves are compared with the literature findings. Finally, it is found that the presence of the model postpones the inception of wave breaking for some waves which would normally break without the presence of the scaled model.

The correlation between wave kinematics and related impact pressures and forces are analyzed. Each approaching wave results in two individual impacts occur sequentially on the scaled model. The first one appears on the vertical part while the second one develops at the attached corner of the horizontal part. Both impact pressures and forces exhibit large variability under nominally identical conditions. Then, the breaker types are classified into four groups based on the classifications of Oumeraci et al., 1993. These are (a) slightly breaking waves (SBW), (b) breaking with small air trap (BWSAT), (c) breaking with large air trap (BWLAT) and (a) broken waves BW). For each group, the kinematic behavior of wave breaking and the related time series of pressures and forces are analyzed. Moreover, characteristics of maximum pressures and forces and the evaluation of instantaneous pressure profiles are discussed in more detail. Due to the secondary impact below the horizontal part, a pressure increase is observed at the upper corner of the vertical part when compared to the case of simple vertical walls. Therefore, the total force in the horizontal direction (F_h) increases in the cases of SBW and BW. For breaker types SBW, BWSAT and BWLAT, the variation of velocity and acceleration components (V_h, V_v) and (a_h, a_v) are analyzed up to the impact time instant. In the case of SBW, V_h is slightly higher than V_v at the time of impact which does not agree with present literature. After the impact

time, V_v dramatically increases due to the high vertical acceleration to a value of 20g. The highest vertical acceleration of 53g is measured in the case of BWSAT.

The pressure distribution due to the violent water wave impacts on vertical structures with cantilever slab is analyzed. Both the location and the magnitude of p_{max} on a vertical structure with an overhanging horizontal cantilever slab are determined. On the vertical part, the non-dimensional term (z_{max}/h_s) for the location of p_{max} is gradually decreasing from a point above the SWL to a point below the SWL with the increase of h_s. On the horizontal part, p_{max} is located at the attached corner of the scaled model and its magnitude decreases sharply below $10\,\rho g H$ between $x/h_s = 0.8 - 1$. The relation between the measured value of p_{max} on the vertical part and related rise time t_r are plotted and compared with empirical values from literature. For the new data set, new upper envelope functions between p_{max} and t_r (both on vertical and horizontal part) are proposed. Then, the boundary expressions for the interval of normalized wave height, $\frac{H}{h_s}$, which creates a high dynamic impact on the vertical part with the variation of the clearance, $\frac{c}{a}$, are expressed. Finally, for the pressure profiles, local p_{max} at SWL and at the top and bottom of the vertical part (p_{h1}, p_{h2} and p_{h3}) and at the attached corner of the horizontal part (p_{v1}) are considered. For each case, the relation for p_{h3}/p_{h1}, p_{h1}/p_{v1}, and p_{h2}/p_{v1} are determined.

Finally, a new prediction model for the vertical forces acting on the cantilever slab is being proposed based on small scale model results. Within this effort, a parameter set responsible for the prediction of wave loading on a vertical wall with a cantilever slab is investigated. The results of regular and irregular waves are compared. Wave height (H_1), water depth at the model toe (h_s), wave period (T), overtopping discharge (q) and vertical averaged velocity (V_{av}) are found to be the main parameters influencing the vertical impact forces. Then, based on the experimental investigations on breaking wave kinematics and impulsive loadings, a prediction formula for vertical impact forces on the slab of a vertical wall with an overhanging horizontal cantilevering slab has been derived for 1/20 foreshore slope. The design concept for breaking wave loads is developed. It is worth to mention that the proposed formula represents the mean value of the measurement regular wave results.

Oumeraci, H.; Klammer, P.; Partenscky, H.W., 1993, "Classification of breaking wave loads on vertical structures", Journal of Waterway, Port, Coastal and Ocean Eng. v 119, n 4, p 381-397

1

INTRODUCTION

***

1.1 VERTICAL BREAKWATERS

The high growth of world trade requires the construction of a large number of ports and terminals for receiving ships and transferring cargos. Vertical breakwaters and sea walls are frequently used structures to protect ports from sea actions like waves and high water levels. In general, vertical structures are impermeable and solid structures with vertical faces. Figure 1.1 shows four different types of vertical breakwaters. The first one is a vertical caisson breakwater which is placed on a thin (rubble mound) foundation layer. The second one is a caisson breakwater which is placed on a thick rubble mound foundation (a vertical composite caisson breakwater) and the third one is a perforated breakwater which is placed on a thin foundation layer, while the fourth one is a caisson breakwater which is armoured by a protection.

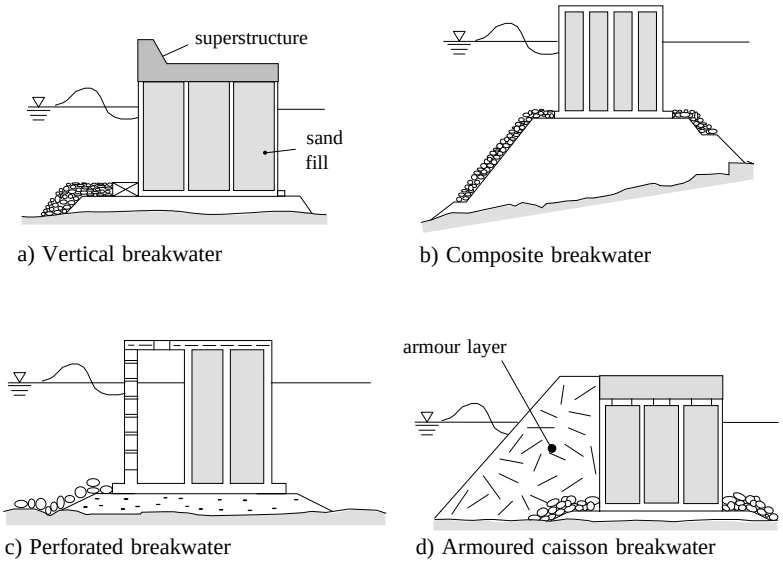

a) Vertical breakwater

b) Composite breakwater

c) Perforated breakwater

d) Armoured caisson breakwater

Figure 1.1 *Main types of vertical breakwaters addressed in PROVERBS (after Oumeraci, et al., 2001)*

Controlling overtopping of the waves at the top of vertical breakwaters is a critical issue. This is why engineers/designers tend to provide the vertical breakwaters with a return crown wall or even a completely horizontal cantilever slab to reduce overtopping. However, upwards impact beneath the horizontal cantilever slab gives rise to a significant uplifting force. These forces are impact loads and they cannot be substituted by a static equivalent. Therefore, a detailed description of the space and time distribution of the wave impacts becomes imperative.

Offshore oilrigs are typical examples in which the effect of the upward impact of a wave beneath a rigid horizontal deck needs to be assessed. Wood and Peregrine (1996) mention that a main platform of rigs should be build out of reach of green water because of the lack of good estimates of upward impacts.

In the past decades, the qualitative and quantitative determination of wave loads on vertical structures has already been examined intensively (e.g. Oumeraci et al., 2001). Uplift loads below horizontal decks have been investigated (e.g. McConnell et al., 2003) and recently prediction methods for wave loading have been developed in several research projects (e.g. Coumo et al., 2007). Adversely to the previous problem of a simple vertical wall or a horizontal deck, a combined structure consisting of both a vertical and a horizontal part has scarcely been considered. One of the rare examples of research with this combined type of structure is the work of Wood and Peregrine (1996), who consider an analytical approach, based on the pressure-impulse method for a flat deck close to the mean water level. In general, a consensus on the necessary approach for the research on this combined type of structure lacks completely (Okamura 1993). In addition, the structure prevents most of the overtopping due to its particular geometry involving closed angles, which does not allow incident waves to dissipate. Therefore the loading condition is more severe than in the preceding situations.

In this particular research, the Pier of Blankenberge (see Figure 1.2) which is located along the Belgian coast is shown as an illustrative example of a vertical structure with an overhanging horizontal cantilever slab. This majestic building, constructed on piles in the intertidal zone of the coast, has been renovated between 1999 and 2002. The renovation consisted partly of constructing a concrete core for the building from the sea bottom up to the first floor whereas formerly the complete building was entirely supported by piles.

During high tide, the sea flows freely under the building so that the vertical concrete core of the structure is prone to wave loads. The waves entering below the building are entrapped: they hit the concrete core and successively slam at high tide on the horizontal plates of the first floor (see cross-section in Figure 1.4a).

Figure 1.2 *The renovated Pier of Blankenberge, Belgium. Picture taken during high tide*

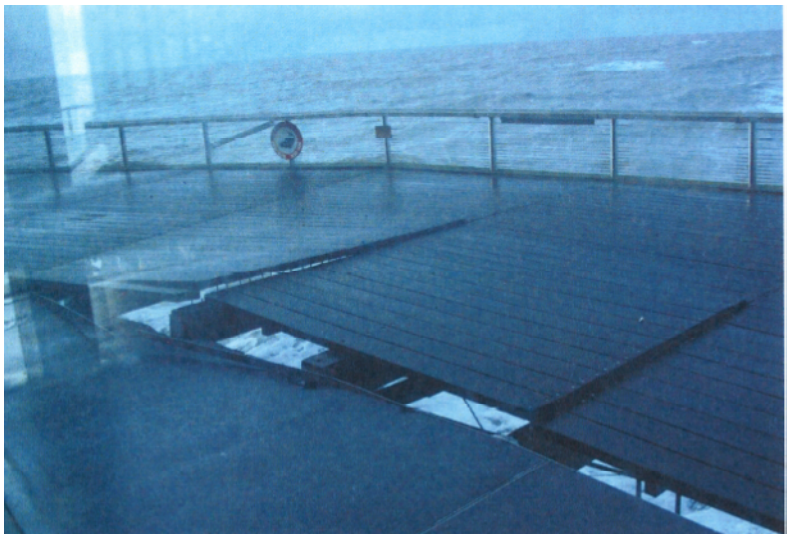

Figure 1.3 *Wave uplift damage to outer walkway, 9 November 2007 (after Alderson & Allsop, 2008)*

During the winter season of 2002-2003, the structure was damaged during storms, due to wave impacts. Figure 1.3 shows a photo taken just after a storm on 9 November 2007. To damp the wave impacts, a steel screen was constructed in front of the pier on the sea side.

In the past, wave loads on the pier have been investigated at prototype scale at Ghent University and in a scale model at HR-Wallingford. Verhaeghe et al. (2006) have described the field monitoring equipment installed on the pier for measuring wave loading. Alderson et al. (2008) have reported the 3-dimensional physical model tests to assist in the optimization of a protective wave screen to ensure the stability of the pier slab against wave up-lift.

As the previous researches on the pier have pointed out, the pier is vulnerable to the wave impact loads due to its special closed geometry. Therefore, detailed analysis for quantifying the wave loads and improvement of the design aspect are necessary.

1.2 OBJECTIVE AND APPROACH OF THE STUDY

The general aim of this PhD research is to analyze wave loading on a vertical structure with an overhanging horizontal cantilever slab, based on the correlation between the kinematics of breaking waves and the height, distribution, duration and characteristics of the wave impacts, by using traditional physical model tests. Within this research, the following individual objectives are covered.

1. Analysis of hydrodynamic conditions in front of vertical structures.

Wave loadings on vertical structures are strictly connected to the hydrodynamic conditions. Therefore, it is important to identify wave conditions given by wave height (H), wave period (T) and taking account of wave shoaling and reflection, and of depth limited breaking.

2. Analysis of the correlation between wave kinematics and impact pressures and forces.

Defining the breaker shape which produces the highest impact on a vertical structure with cantilever slab is of practical importance. Based on the differences in breaker shape, it is possible to group the measured pressure and force histories. Due to the complicated geometry, the structure is exposed to two individual impacts in sequence on the vertical part and below the cantilever surfaces. The characteristics of pressure and forces due to both impacts are rather different to each other and should be well understood.

3. Analysis of pressure distribution due to the violent water wave impacts on vertical structures with cantilever slab.

For design purposes, it is important to know the pressure distribution due to the wave loading. In this respect, the location of the maximum pressure is an important issue. It will be practical to define it by means of a parametrical function. In addition, the maximum impact pressures are inversely related to the rising time which is well accepted for vertical structures. A similar expression should also be developed for the second impact below the cantilever slab.

4. Applicability of existing prediction methods for the horizontal forces on the proposed geometry.

The cantilever slab blocks the wave overtopping which creates an additional stress on the vertical part. Therefore, the amount of additional stress due to the cantilever slab can be tested by comparing with the results of a simple vertical structure. In addition, measured horizontal forces on a simple vertical structure can also be used to check the efficiency of the existing prediction methods.

5. Possibility for a new prediction model for the vertical forces exerted on the cantilever slab.

Many prediction models exist to predict the horizontal forces on vertical structures. In the same manner, similar efforts are necessary to propose a new prediction method to predict vertical forces acting on the cantilever slab.

In this particular research, two dimensional small-scale model tests are carried out to achieve the aforementioned goals, by means of an instrumented scale model. The two dimensional scaled model is simplified from the cross-section which is shown in Figure 1.4b. The fundamental geometry of a simple vertical structure is also tested and serves as theoretical reference. Then, the structure with overhanging cantilever slab is tested, in different variations of parameters. The tests are carried out in the wave flume (30m x 1m x 1.2m) of Ghent University on a scale of ~1/20.

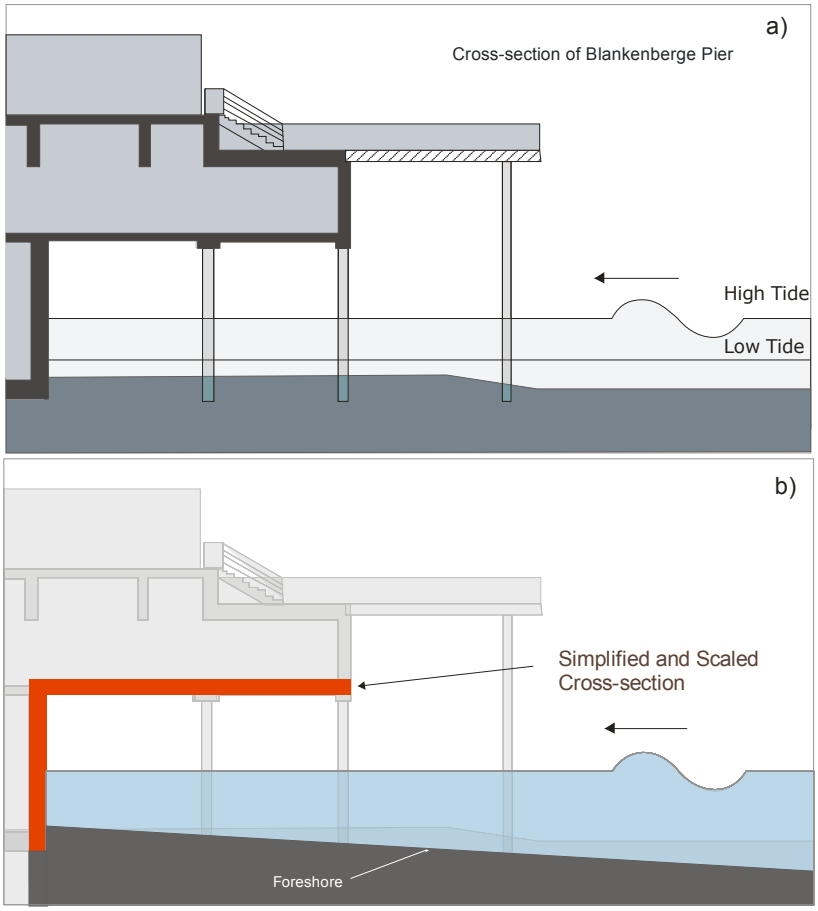

Figure 1.4 *a) Schematic view of Blankenberge Pier with vertical wall and horizontal deck subjected to incoming waves, b) Simplified and scaled cross-section from Blankenberge Pier with sloped foreshore*

1.3 THESIS OUTLINE

The various chapters of this PhD thesis cover the aforementioned aspects and are briefly summarized in the following.

Chapter 2 describes the theoretical background on wave forces on the vertical structures.

Chapter 3 deals with the preparation of a series of experiments carried out to investigate the loading conditions. A total of 192 regular wave tests and 80 irregular wave tests were performed.

Chapter 4 discusses the hydraulic performance of load tests such as wave shoaling, wave reflection, wave breaking and overtopping. This chapter gives a summary of the methods to predict wave shoaling and breaking in a wave flume with uniform bed slope and wave reflection from vertical structures with overhanging cantilevering surfaces. The measured results are compared with literature values.

Chapter 5 deals with the occurrence of shock pressures. Then, it is focused on the classification of waves according to the breaker types. For each breaker type, the relation between the horizontal velocity of the wave crest and the vertical velocity of the water level at the wall are defined. The variations of instantaneous pressure distributions are introduced.

Chapter 6 concentrates on the presentation of the location of the maximum pressures. A set of new relationships between maximum pressure and rise time are proposed. The boundary conditions for the existing region of dynamic pressures both on the vertical and horizontal part are drawn. The local pressure ratios are defined in each breaker type.

Chapter 7 discusses the effectiveness of existing prediction methods with the use of horizontal wave loads on a simple vertical structure. In addition, the results measured on a simple vertical structure are compared with results measured on a vertical structure with cantilever slab to observe the influence of cantilever slab on the force and pressure distribution of vertical structures.

Chapter 8 reports the results of the parametric analysis of the vertical forces on the cantilever slab. The results from the regular as well as the irregular waves are compared. Based on the effective parameters, a semi-empirical prediction model is proposed for the vertical forces.

Chapter 9 summarizes the conclusions and ends with recommendations for wave loadings on vertical structures with cantilever slabs.

Each chapter contains a list of references which points the reader to further and more detailed information on the respective subject.

REFERENCES

Alderson, J.; Cuomo, G.; Allsop, W., 2008, "*Why do suspended decks coastal structures keep failing*", In: 4th International Conference on Forensic Engineering 2008, 2 - 4th December 2008, London

Cuomo G.; Tirindelli M.; and William Allsop W., 2007, '*Wave-in-deck loads on exposed jetties*', Coastal Engineering Volume 54, Issues-9, 2007, pp: 657-679

McConnell, K.J; Allsop, N.W.H; Cuomo, G; and Cruickshank, I.C, 2003, "*New guidance for wave forces on jetties in exposed locations"*, Paper to Conf. COPEDEC VI, Colombo, Sri Lanka pp: 20

Okamura, M., 1993, "*Impulsive pressure due to wave impact on an inclined plane wall"*, Fluid Dynamics Research, volume 12, issue 4, pp. 215-228

Oumeraci, H; Kortenhaus, A; Allsop, W; de Groot, M; Crouch, R; Vrijling, H; Voortman, H, 2001, "*Probabilistic Design Tools for Vertical Breakwaters*", Balkema Publishers, New York.

Verhaeghe, H.; Cherlet, J.; Boone, C.; Troch, P.; De Rouck, J.; Awouters, M.; Ockier, M.; Devos, G., 2006, "*Prototype monitoring of wave loads on concrete structure in intertidal zone*", COASTLAB06. pp. 117-125

Wood, D.J.; Peregrine, D.H., 1996, "*Wave impact beneath a horizontal surface*", In: Proc. 25th Int. Conf. on Coastal Engineering. Orlando, USA, ASCE, pp. 2573–2583.

2

LITERATURE REVIEW

***

2.1 INTRODUCTION

In this Chapter, a theoretical background is given on wave forces on the vertical structures. This Chapter is particularly intended for the reader who is not familiar with these subjects. This chapter starts with the description of vertical breakwaters and possible failure modes. The purpose of the following section is to briefly describe and categorize the wave forces on the vertical structures, the well known methods used to predict quasi-static forces is discussed in the latter section. Then methods for impulsive forces are reviewed. Later, the scaling of the forces and 3-D effect of approaching waves are discussed. Finally, some important points related to the aeration are described and explained.

2.2 VERTICAL BREAKWATERS

Breakwaters are constructed to provide a calm basin for ships and to protect harbor facilities. They are also sometimes used to protect the port area from the intrusion of littoral drift (Takahashi, 1996).

There are two main types of breakwaters: rubble mound and composite breakwaters. Rubble mound breakwaters have a rubble mound and an armor layer that usually consists of shape-designed concrete blocks. Due to the development of these blocks, modern-day rubble mound breakwaters can strongly resist the destructive power of waves, even in deepwaters. Composite breakwaters consist of a rubble foundation and vertical wall, and are therefore classified as vertical breakwaters. By using caissons as the vertical wall, composite breakwaters provide an extremely stable structure even in rough, deep seas (Takahashi, 1996).

The original concept of the vertical breakwater was to reflect waves, while that for the rubble mound breakwater was to break them. Figure 2.1 shows four vertical type breakwaters having different mound heights. The basic vertical wall breakwater is shown in (a), while the others are composite breakwaters with a rubble mound foundation, namely, the low-mound (b) and high-mound composite breakwaters (d).

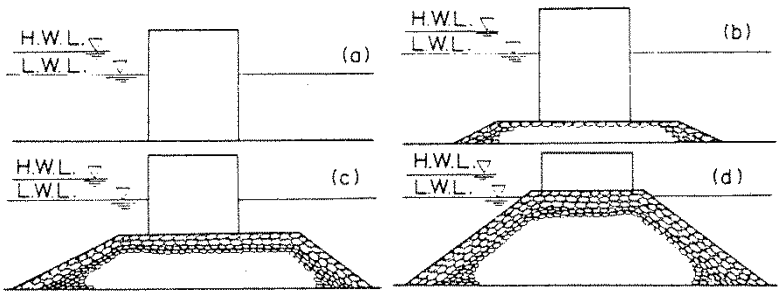

Figure 2.1 *Vertical type breakwaters (after Takahashi, 1996)*

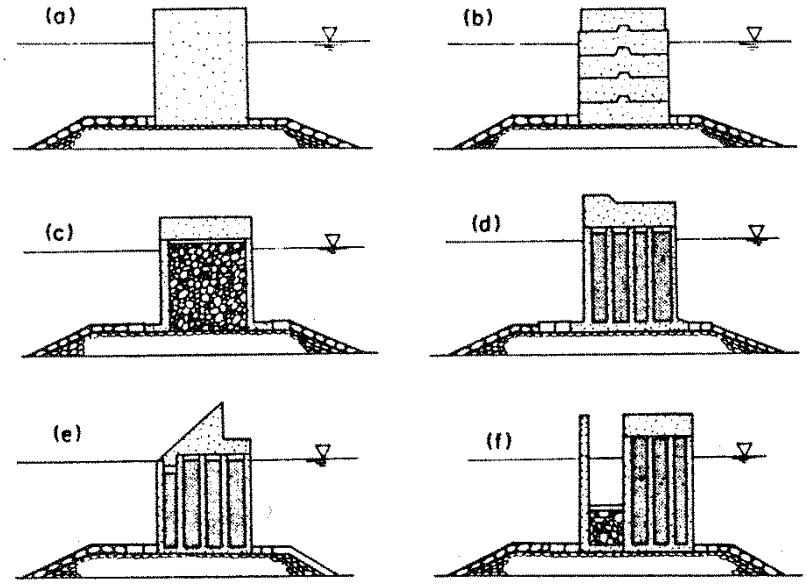

Figure 2.2 *Composite breakwaters (after Takahashi, 1996)*

In Figure 2.2, Takahashi (1996) shows several kinds of composite breakwaters having different upright sections. An upright wall with block masonry (b) was initially most popular, in which many different methods were applied to strengthen the interlocking between the blocks. Cellular blocks (c) have also been used to form the upright wall of vertical breakwaters. However, the invention of caissons (d) made these breakwaters more reliable, and many were subsequently constructed around the world. Caisson breakwaters have been improved using sloping top caissons (e) or perforated walls (f).

2.2.1 FAILURE OF VERTICAL BREAKWATERS

Several failure modes of vertical breakwaters can be distinguished. In order to examine the interaction between the possible modes of failure and their total effect on the failure of the breakwater, a fault tree has been proposed by Oumeraci (1994). The most important failure mechanisms of vertical breakwaters and the fault tree are summarized in Figure 2.3. Throughout the figure, he consider only one cross-section of the vertical breakwater.

The main modes of failure of vertical breakwaters can be divided into two categories: overall failure modes and local failure modes. He summarized the most important failure mechanisms of the vertical structure as:

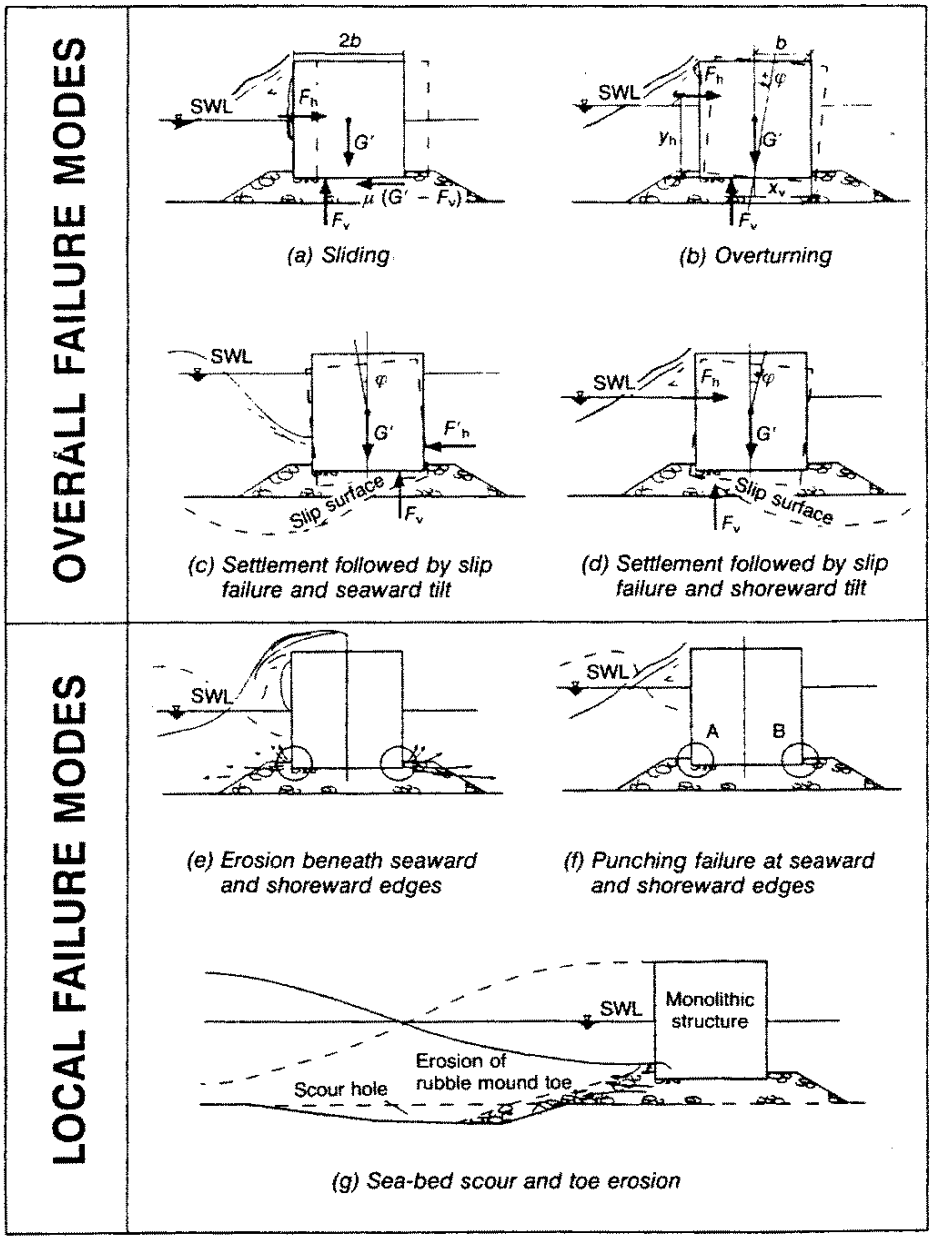

Figure 2.3 *An overview of the failure mechanisms (after Oumeraci,1994)*

- sliding of the caisson over the rubble foundation;
- Overturning of the caisson (not realistic; limited by:)
- foundation failure consisting of
- landward sliding of the subsoil;
- seaward sliding of the subsoil;
- changes to the geometry of the foundation at sea or land side by
- erosion of the toe of the mound;
- erosion of the subsoil at the sea floor;
- loss of material from the rubble foundation (filter failure);
- breach of the wall of the caisson (front side);
- breach of the floor of the caisson;
- cracking due to torsion (differential settlement)

The design of a vertical breakwater may be more complicated than the design of an ordinary rubble mound breakwater. There have been numerous vertical breakwater failures in the last century. Because of this fact, vertical breakwaters have almost been abandoned except in countries like Italy and Japan. However, a number of important (scientific) developments which might promote the revival of vertical breakwaters have taken place in the last decades and nowadays vertical breakwater are becoming more and more of interest due to the increasing draught of vessels and off-shore land reclamations in deep water (Oumeraci, 1994).

Impact loads due to wave breaking on a vertical breakwater are main reasons of the failure of vertical breakwaters. Wave impacts are dynamical hydraulic loads with a very short duration and a very high peak force.

Therefore, the breaker shape which can produce the highest impact becomes an important issue. In the following, the breaker shape which creates the highest impact is discussed in deep.

2.3 CLASSIFICATION OF WAVES

2.3.1 OCCURRENCE OF SHOCK PRESSURES

On vertical structures, the front shape of the breaking wave has a significant consequence on the wave impact pressure. In this manner, the shape which creates the largest pressure is becoming an important issue and is uncertain (Hull and Muller, 2002). In this context, some of the breaker shapes which create the largest

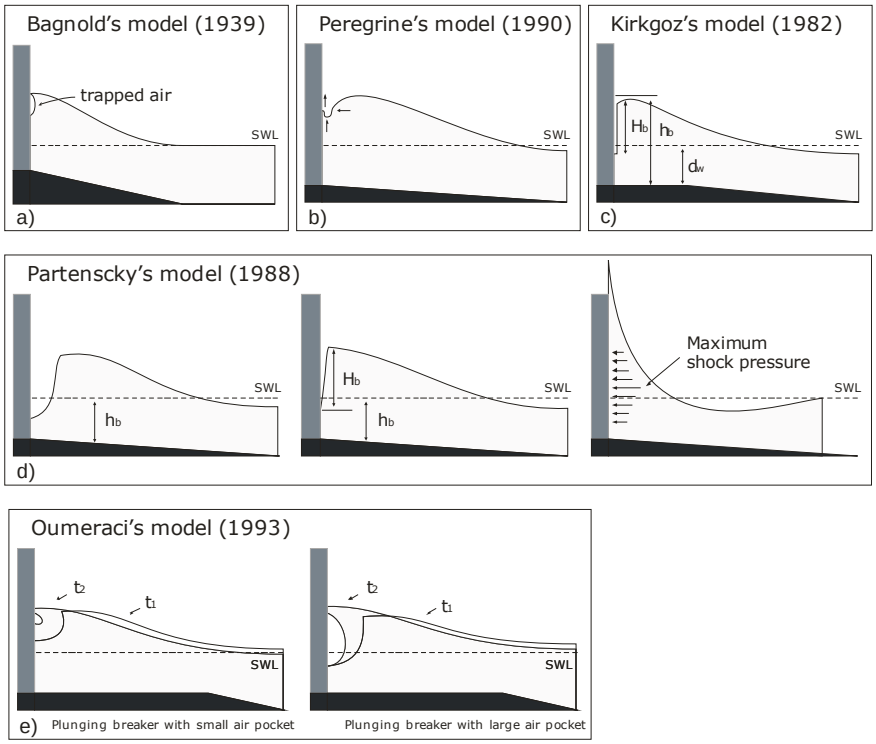

Figure 2.4 *Suggested breaker shapes for the occurrence of very high shock pressures*

shock pressures are discussed and suggested in literature. One of the first literature suggestions was made by Bagnold (1939). He described the breaker shape as a very flat vertical wave front, enclosing a thin cushion of air between itself and the wall (Figure 2.4a). Hence, the maximum pressure occurs, when the thickness of the air cushion is small, but not zero. The conclusion of Bagnold is partly inaccurate because very high pressures are measured in breaking waves without any air trap called 'flip through' (Walkden et al., 1996). The term of 'flip-through' was first introduced by Cooker and Peregrine (1990) on the basis of a nonlinear potential-flow model. This type of breaker is generated by the converging of the wavefront to a point without any trapping of air between the wall and the wavefront (Figure 2.4b) which is similar to the measurements by Chan and Melville (1988). After the impact, an uprising water jet occurs.

However, Kirkgoz (1982) found that a breaking wave having its front face parallel to the wall at the instant of impact produces the largest shock pressures (Figure 2.4c). His method is based on observation of small scale model tests. He developed a sliding wall mechanism which slides vertically at the moment of impact. In this way, the influence of reflection is avoided but it also avoids the influence of the wall on the breaking location and breaker shape. His approach has not been confirmed by Hull and Muller (2002).

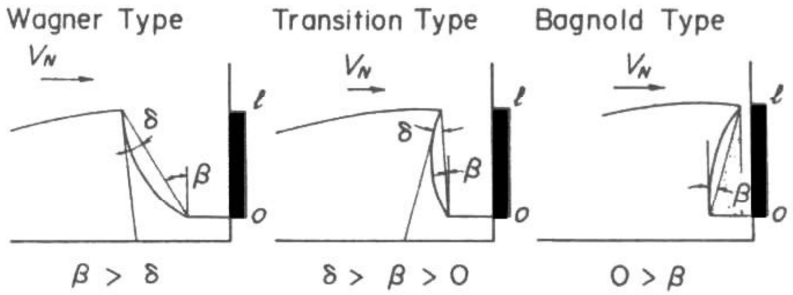

Figure 2.5 *Three types of impulsive pressures (after Takahashi, 1996)*

Furthermore, researchers like Bullock et al. (2007), Partenscky (1988) and Hattori et al. (1994) showed that the largest impact pressures occur when the breaking wave traps a very thin pocket of air. Figure 2.4d shows the example given by Partenscky (1988).

Oumeraci et al. (1995) found that a plunging breaker with a large air pocket causes the highest pressures (Figure 2.4e). In addition, Richert (1968),

Partenscky (1988), Hattori et al. (1994) and Hull and Muller (2002) observed the most severe impulsive pressures when a breaking wave with a vertical face strikes the wall with entrapped air either in the form of small air bubbles or a very thin lens shaped air pocket. Moreover, Oumeraci et al. (1993) show that the breaker type with a small cushion of air induces the impact force with the highest intensity while the breaker type with the large cushion of air results in the highest pressures (Oumeraci et al., 1995).

Takahashi (1996) categorize impacts into three groups as impacts occurring without air entrapment called “Wagner type pressure”, with air entrapment called “Bagnold type pressure” and transition region between these two types (see Figure 2.5).

When the attacking angle β of the wave front is larger than the curvature angle δ of the wave front, Wagner type pressure acts on the wall. When β is negative, Bagnold type pressure arises. When β is between these values, a transition type pressure acts generating an impulsive pressure similar to the Bagnold type. He found the maximum average wave pressure intensity in the transition region.

The Wagner type pressure is described as the hitting of a wedge on the water surface. The maximum impulsive force on the wedge is described as $\rho_0 c_w V_N$ for the case of zero attacking angle of the wedge head ($\beta = 0$). where ρ_0 is the specific density of water, c_w the speed of sound in water, and V_N the decent speed of the wedge. The time history of Wagner type pressure is characterized by a sudden rise and exponential decay in pressure. Takahashi (1996) mentioned that the “flip through” impact due to the occurrence of a pile-up effect of water at the intersection point is an example of the Wagner type pressure.

2.3.2 CLASSIFICATION OF WAVE LOADING

As mentioned above, the breaker shape of the waves has an important influence on the magnitudes of impact pressures and forces. The presented test results are categorized according to the breaker shapes, and therefore features of each group are summarized here. Figure 2.6 shows several suggested classifications for the breaker types. Some of the researchers like Chan and Melville (1988), Partenscky (1988), Oumeraci et al (1993) and Kirkgoz (1995) carried out experiments to determine the relationship between the breaker shape and wave impact on the vertical structures. Chan and Melville (1988) performed experiments in deep water on a surface-piercing vertical plate which is not penetrating to the bottom of the wave flume. They explain that the kinematics of the impact process is dependent on the breaking point with respect to the wall location which also determines the breaker shape. The variation of impact characteristics with wall location is summarized in Figure 2.6-I. Accordingly, they suggest three regions given by the following approximate boundaries: a) wave breaks on the wall ($3.56 < x/L_c < 3.76$) [Figure 2.6-I (b-c)], b) transition region where no significant impact pressures are obtained ($3.76 < x/L_c < 3.84$) [Figure 2.6-Id] and c) wave fronts have already plunged back into the fluid before impact on the wall ($3.84 < x/L_c < 4.03$) [Figure 2.6-I (e-f)], where, L_c is the characteristic wavelength and x is the location of wave breaking away from wave generator.

Partenscky (1988) categorizes breaking waves which create high impact pressures into two categories: breaking with enclosed air volume and without enclosed air (Figure 2.6-II). In the second case, the wave collides with a more vertical face which lets the wave transfer its full momentum into pressure.

Kırkgöz (1995) classifies the wave breaking according to the breaker shape on the vertical walls as: a) early breaking without air escaping, b) early breaking with air escaping, c) late breaking and d) perfect breaking when a breaker with vertical face strikes the vertical wall (Figure 2.6-III).

Based on model studies, Oumeraci et al. (1993) developed some criteria for classification of breaker types depending on both the ratio of breaking water depth to the still-water depth at the wall (d_s/d_w) and the ratio of the horizontal velocity of the breaker to the vertical upward velocity of the water surface directly at the wall (V_H/V_V). According to his results, four main breaker shapes/types are suggested. These are (a) upward deflected breaker, (b) plunging breaker with a small air cushion, (c) well-developed plunging breaker with a large air pocket and (a) turbulent bore (Figure 2.6-IV). In addition, based on detailed analysis combined with visual records, they suggest that the observed breaker shape can be identified by the recorded force and pressure histories.

Based on data from a series of small-scale model tests completed at HR Wallingford for vertical and composite breakwaters, Allsop et al. (1996) suggested a parameter response map for prediction of the type of wave loading on vertical and vertically composite breakwaters based on structure geometry and wave conditions.

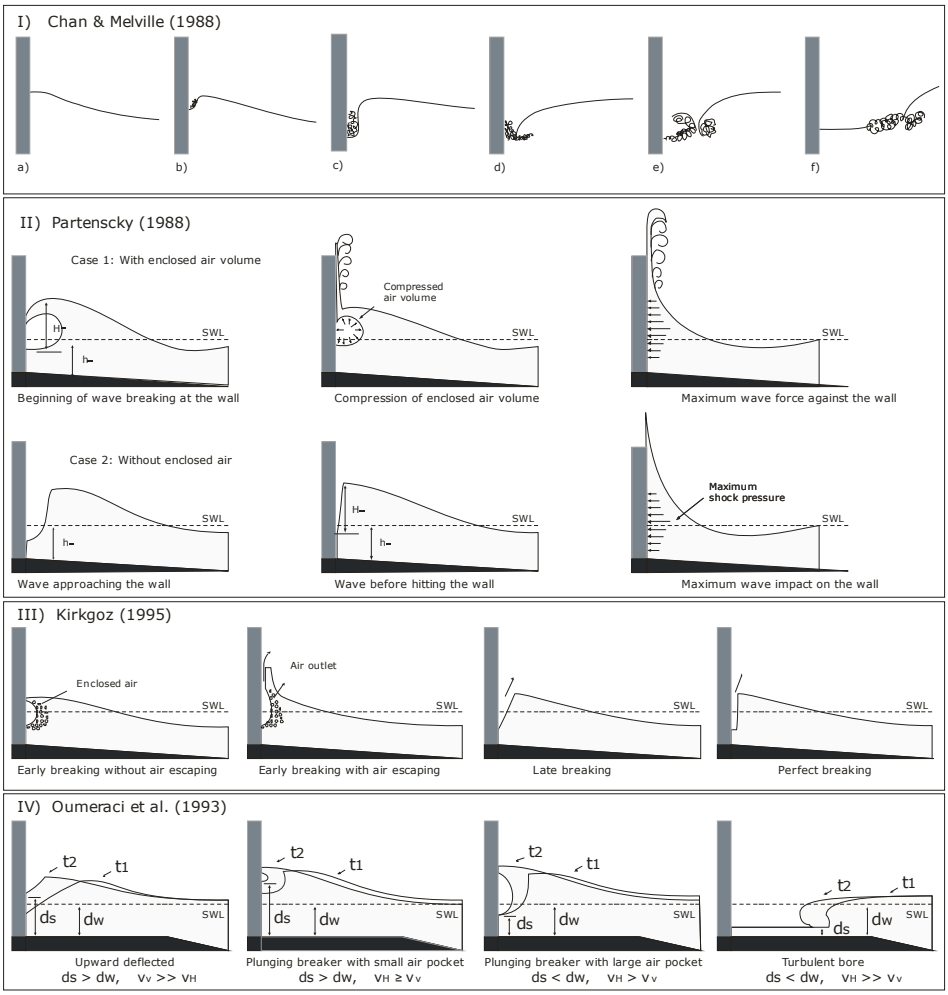

Figure 2.6 *Suggested classifications for wave breaker types from literature*

The parameter map suggested by Allsop et al. (1996) was further tested against a wide range of data within PROVERBS (Probabilistic Design tools for Vertical Breakwaters) project including large scale model tests. Then, a modified version of the parameter map was proposed by Kortenhaus and Oumeraci (1997) which is shown in Figure 2.7.

The map uses three relative parameters to determine wave loading conditions. These are the relative berm height (h_b/h_s), the relative wave height (H_{si}/d), and the relative berm width (B_{eq}/L_{pi}). The wave parameters H_{si} and L_{pi} are determined in the water depth h_s and geometric parameters h_b, h_s, B_{eq} and d are defined in Figure 2.15.

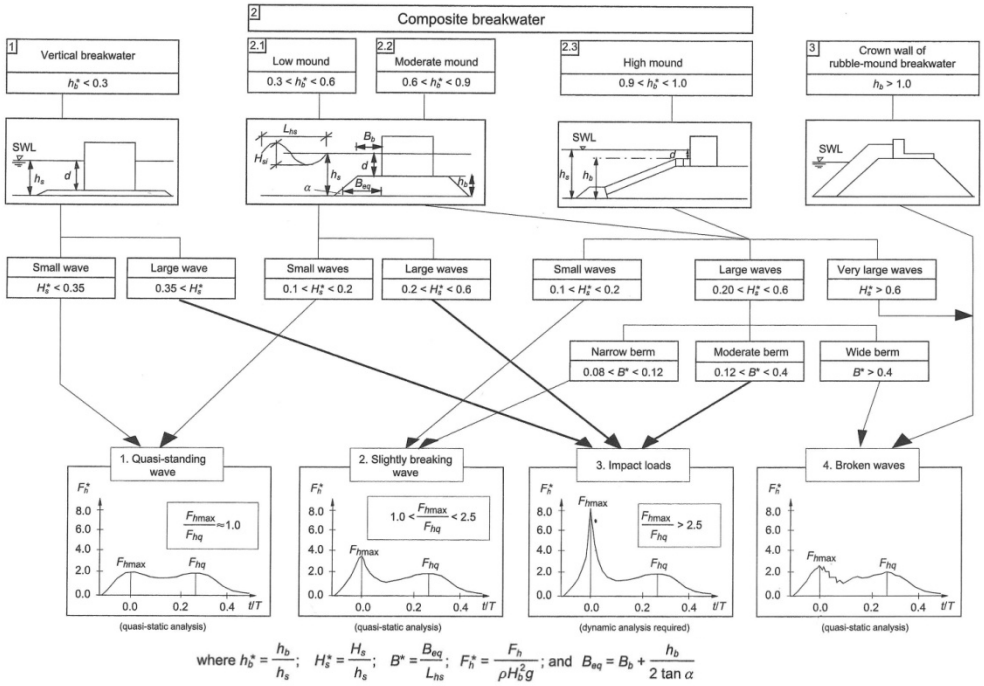

Figure 2.7 *Parameter map developed for PROVERBS (after Oumeraci et al., 2001)*

2.4 WAVE LOADS

2.4.1 QUASI-STATIC WAVE LOADS

Waves do not trap an air pocket against the wall. The pressure at the wall has a gentle variation in time and is almost in phase with the wave elevation. Wave loads of this type are called pulsating or quasi-static loads because the period is much larger than the natural period of oscillation of the structures. For conventional caisson breakwaters the period is approximately one order of magnitude larger. Consequently, the wave load can be treated like a static load in stability calculations. Special considerations are required if the caisson is placed on fine soils where pore pressure may build up, resulting in significant weakening of the soil (U.S. Army Corps of Engineers, 2002).

Following methods are used to calculate quasi static wave loads on the vertical structures.

2.4.1.1 LINEAR WAVE THEORY

The standing wave loads on a vertical wall can be derived from the linear wave theory and its pressure distribution is shown in Figure 2.8.

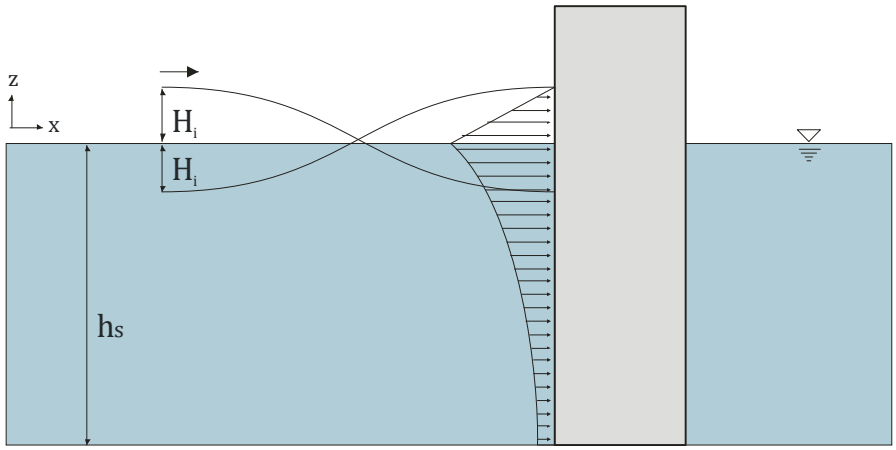

Figure 2.8 *Pressure distribution of standing waves according to linear wave theory*

If a wave is stopped by a wall a part is reflected. The result is a superposition of the incident (H_i) and reflected waves (H_r). The resulting wave height is approximately twice the incident wave height (H_i), if the incident wave is fully reflected.

When a monochromatic wave field is present with incident wave height H_i and length L, a standing wave occurs with nodes and antinodes. This phenomenon is also called "Clapotis".

According to the linear wave theory with full reflection of the incoming wave the pressure in z-direction is:

Equation 2.1 $$p(z) = \rho g H_i \frac{Coshk(h_s+z)}{Cosh(kh_s)} \qquad for\ -h_s<z<0$$

$$p(z) = \rho g H_i (1 - \frac{z}{H_i}) \qquad \text{for } 0 < z < H_i$$

where, the wave number is $k = 2\pi/L$, angular wave frequency is $\sigma = 2\pi/T$, h_s is the water depth at the structure. ρ is the water density and g is the acceleration due to the gravity.

The pressure takes following values:

$p = 0$ at $z = H_i$

$p = \rho g H_i$ at $z = 0$

$p = \rho g h_s + \frac{\rho g H_i}{Cosh(kh_s)}$ at $z = -h_s$

The resulting wave forces acting on the vertical wall can be calculated by assuming a hydrostatic pressure distribution above still water level (SWL).

Integration of the pressure distribution over the water depth results in the formulae for the wave forces on the vertical forces.

Equation 2.2 $F = \int_{-h_s}^{0} \rho g H_i \frac{Coshk(h_s+z)}{Cosh(kh_s)} dz + \int_{0}^{H_i} \rho g H_i (1 - \frac{z}{H_i}) dz$

$$F = \rho g H_i \frac{sinhkh_s}{kCosh(kh_s)} + \frac{H_i}{2}$$

This formula will usually be replaced by the method of Sainflou (see Section 2.4.1.2). This method applies a wave theory of a higher order.

2.4.1.2 SAINFLOU METHOD (1928)

Second order theory has been studied by Sainflou (1928). Sainflou uses a second order Stokes theory and full reflection ($H_i = H_r$) and expresses the pressure as a function of the incoming non-reflected wave H_i. The pressure distribution is sketched as in Figure 2.9. In this case the still water level (SWL) will increase with:

Equation 2.3 $\delta_0 = \frac{kH_i^2}{2} coth(kh_s)$

The pressure distribution is assumed to be linear between surface elevation and bottom level. Experiments by many researchers, particularly by Nagai, proved that Sainflou's method was an oversimplification. Experimental observations by Rundgren (1958) have indicated Sainflou's method overestimates the nonbreaking wave force for steep waves. The maximum pressures at the SWL and at the toe of the structure are shown as p_1 and p_2, while p_3 shows the maximum pressure under the trough (U.S. Army Corps of Engineers, 2002).

Equation 2.4 $p_1 = (p_2 + \rho g h_s) \frac{H_i + \delta_0}{h_s + H_i + \delta_0}$

$$p_2 = \frac{\rho g H_i}{\cosh(kh_s)}$$

$$p_3 = \rho g (H_i - \delta_0)$$

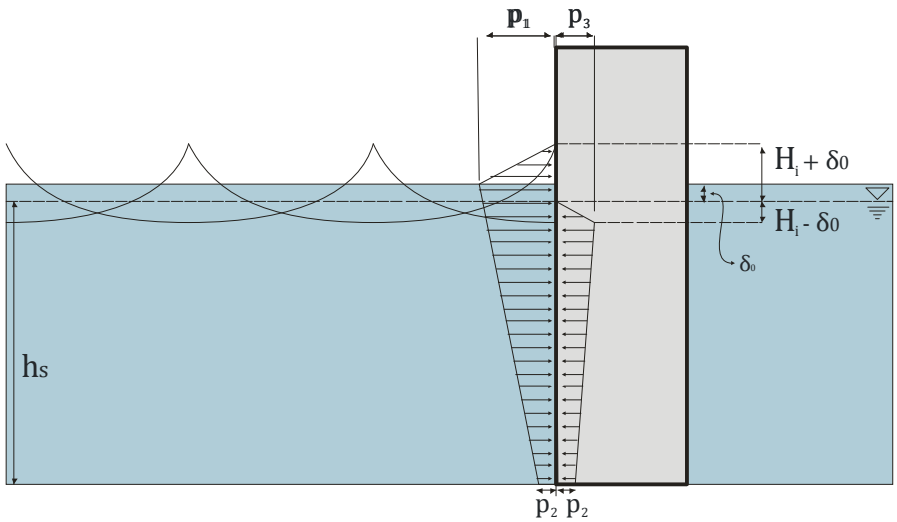

Figure 2.9 *Pressure distribution according to the Sainflou Method*

One should realize that when the Sainflou formula is employed in Japan the design wave H_i is $H_{1/3}$, while $H_{1/10}$ in some other countries. In any case, it is recommended that the maximum wave height be applied for the design wave. (Takahashi, 1996)

2.4.1.3 GODA METHOD (1974)

Study of fourth order theory for finite amplitude waves has been made by Goda (1967). The wave pressure formula proposed by Goda (1974) for the design of vertical breakwaters assumes the existence of a trapezoidal pressure distribution along a vertical wall. Goda takes H_{max} as the highest wave out of 250 waves. This has a probability of exceedance of 0.4%. Furthermore, the wave height is taken seaward of the surf zone. Within the surf zone the height is taken as the highest of the random breaking waves H_{max} at a distance of $5H_{1/3}$ seaward of the breakwater. The pressure distribution is sketched as in Figure 2.10.

The maximum pressures at different locations are shown as:

Equation 2.5 $$p_1 = 0.5(1 + cos\,\beta)(\lambda_1\alpha_1 + \lambda_2\alpha_* cos^2\,\beta)\rho g H_D$$

$$\eta^* = 0.75(1 + \cos\beta)\lambda_1 H_D$$

$$p_3 = \alpha_3 p_1$$

$$p_4 = \alpha_4 p_1$$

The α-factors are given by:

$$\alpha_1 = 0.6 + 0.5\left[\frac{4\pi h_s/L}{\sinh(4\pi h_s/L)}\right]^2$$

$$\alpha_* = \alpha_2 = min\left[\left(\frac{h_{br}-d}{3h_{br}}\right)\left(\frac{H_D}{d}\right)^2, \frac{2d}{H_D}\right]$$

$$\alpha_3 = 1 - \left(\frac{h_w - h_c}{h_s}\right)\left[1 - \frac{1}{\cosh(2\pi h_s/L)}\right]$$

$$\alpha_4 = \begin{bmatrix} 1 - \frac{h_c}{\eta^*} & \rightarrow \eta^* > h_c \\ 0 & \rightarrow \eta^* \leq h_c \end{bmatrix}$$

in which:

β: angle of incidence of the wave attack with respect to a line perpendicular to the structure;

H_D: Outside the surf zone: the highest wave in the design sea state is to be employed. Its height is taken as $H_{max} = 1.8H_{1/3}$ seaward of the surf zone. Within the surf zone: the height is taken as the heights of random breaking waves H_{br} at the location at a distance $5H_{1/3}$ seaward of the breakwater.

h_{br}: water depth at a distance of $5H_{1/3}$ seaward of the breakwater front wall.

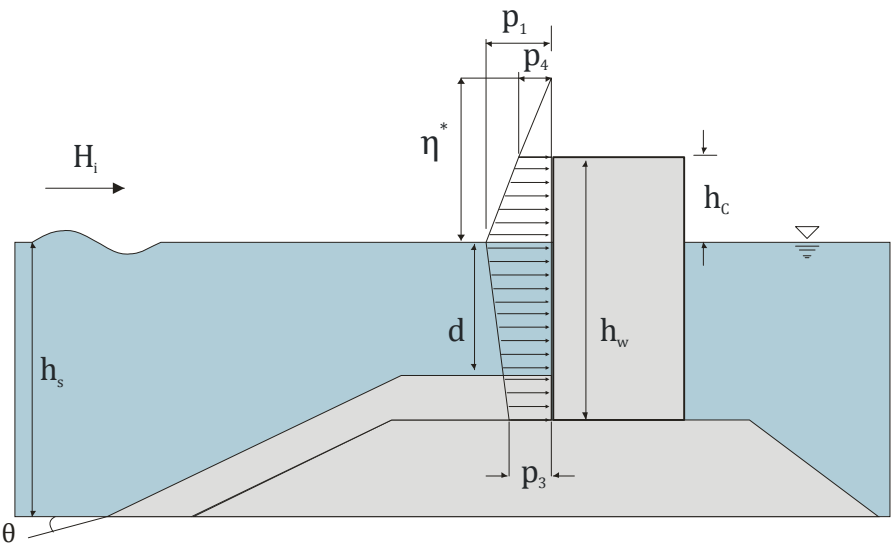

Figure 2.10 *Pressure distribution according to the Goda Method (after Goda,1974)*

For conventional vertical wall structures, $\lambda_1 = \lambda_2 = \lambda_3 = 1$. α_1 and α_2 have been determined empirically from the experimental data and were calibrated with case studies (Goda, 1974). α_1 represents the mean tendency of wave pressure in that it increases with the wave period. α_2 represents the effect of the rubble mound the wave passes over before it impacts the breakwater. As the shape of the rubble mound is constant, this term represents the increase of the wave height which increases parabolically.

Tested ranges:	Water depth (cm)	Wave height (cm)	Wave period (s)	Mound height (cm)
	35	7.1-31.2	2	0 &15
	45	6.7-41.6	1.7	0 &25
	45	7.6-32.8	1.3	0 &25
	45	9.2-22.9	1	0 &25

The formulae have been calibrated with the cases of 21 slidings and 13 nonslidings of the upright sections of the prototype breakwaters in Japan.

2.4.2 IMPULSIVE WAVE LOADS

Impulsive or impact loads are caused by breaking waves against the vertical structure. Impact loads are generally higher than quasi-static loads with a shorter duration. Following methods are developed to predict impact loads on the structures.

2.4.2.1 HIROI METHOD (1919)

Hiroi (1919) suggest a uniform pressure distribution (Figure 2.11) for the breaking waves which acts uniformly up to a height (η^*) above the SWL. This formula is based on field measurements and it was used for a long time in Japan before the developments of Goda Formula (see Section 2.4.1.3).

Equation 2.6 $$p = 1.5\rho g H_D$$

Equation 2.7 $$\eta^* = 1.25 H_D$$

where; H_D is the design wave height and it is usually considered as $H_D = H_{1/3}$ (because difference between H_{max} and $H_{1/3}$ is too small in the shallow waters).

Hiroi's formula is recommended to use for the application in the relatively shallow waters ($h_s < 2H_{1/3}$) and for $h_s > 2H_{1/3}$, Sainflou formula is suggested (Allsop et al., 1996c).

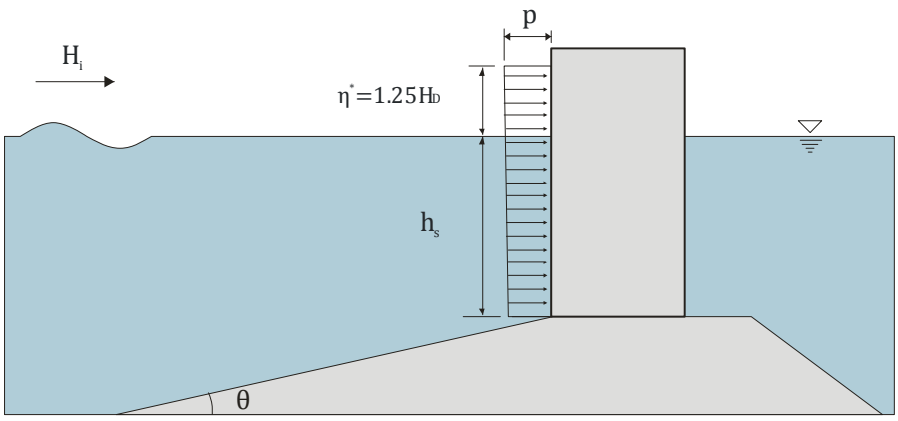

Figure 2.11 *Pressure distribution according to the Hiroi Method (after Takahashi, 1996)*

2.4.2.2 MINIKIN METHOD (1963)

Minikin (1963) suggests a parabolic pressure distribution for the breaking waves on the vertical walls. Dynamic pressure p_m (Equation 2.8) has a maximum value at the SWL and decreasing to zero at $0.5H_b$ below and above the SWL. The total horizontal force is represented by the area under the dynamic and hydrostatic pressure distribution which is shown in Figure 2.12.

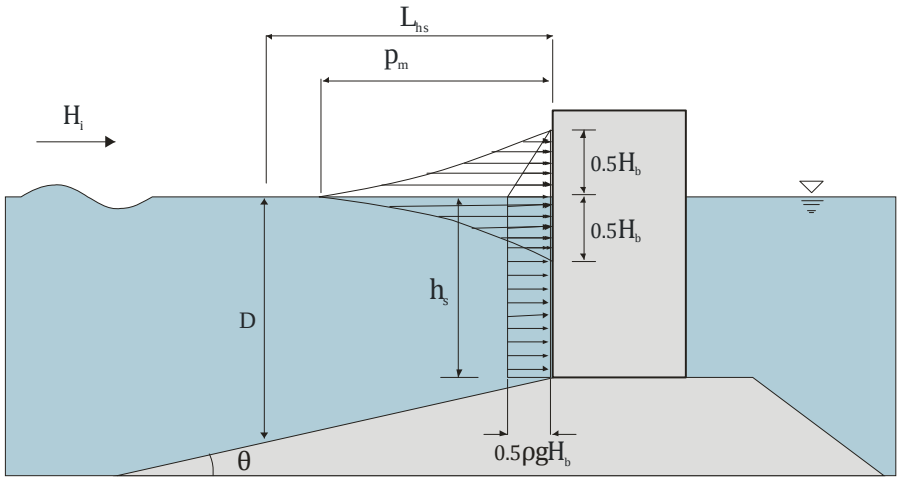

Figure 2.12 *Pressure distribution according to Minikin (SPM, 1984)*

The maximum dynamic pressure at SWL is:

Equation 2.8 $$p_m = 101\rho g \frac{H_b}{L_D}\frac{h_s}{D}(D + h_s)$$

and related total horizontal force is:

Equation 2.9 $$F_h = \frac{101}{3}\rho g \frac{H_b^2}{L_D}\frac{h_s}{D}(D + h_s) + 0.5\rho g H_b h_s \left(1 + \frac{H_b}{4}\right)$$

Where, $D = h_s + tan\theta \cdot L_{hs}$

In which:

H_b: is the breaking wave height

D: is the depth one wavelength in front of the wall;

L_D: is the wavelength in water depth D

L_{hs}: is the wavelength in water of depth h_s

Minikin formula is dimensionally inconsistent. Allsop et al. (1996c) consider the horizontal impact force (F_h) predicted by Minikin formula is incorrect due to the decrease with increasing L_D. There are some incompatibilities found between different version of Minikin formula which are mainly due to a unit mistake converting from British units to metric units. Therefore, Minikin formula is out of fashion in the recent years (Bullock, et al., 2004). However, Minikin used field measurements obtained by Rouville and Petry to calibrate his relationships and it is not known at what stage he made his mistake with units. Comparisons with the limited field data quoted by Minikin (1950) suggest that SPM (1984) may well reflect his true intentions.

2.4.2.3 BLACKMORE AND HEWSON METHOD (1984)

Blackmore & Hewson (1984) suggest a prediction formula based on full-scale field measurements (Equation 2.10). They consider the effect of entrained air which results in a reduction in the impact pressure of field tests compare to the laboratory tests.

Equation 2.10 $$p_1 = \lambda \rho C_b^2 T$$

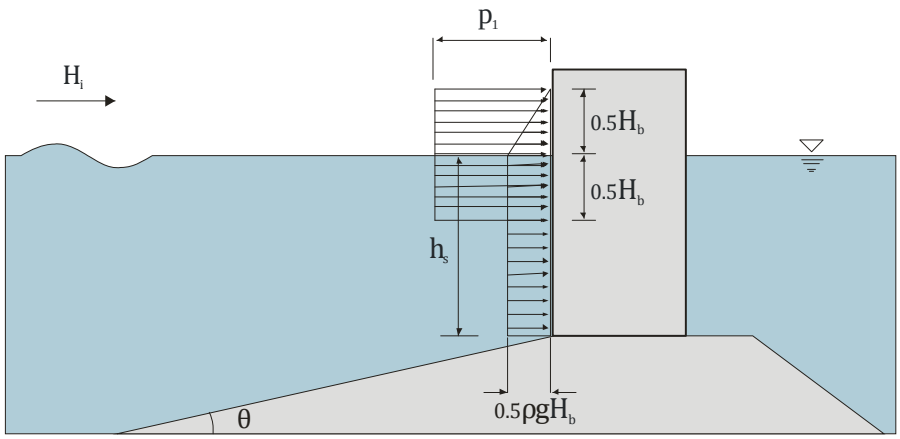

Figure 2.13 *Pressure distribution according to the Blackmore & Hewson Method (after Blackmore & Hewson, 1984)*

in which:

p_1: is the peak pressure at $z = 0.5H_b$;

H_b: is the breaking wave height;

T: is the wave period;

C_b: is the shallow water wave celerity, $C_b = \sqrt{gh_s}$;

λ: is the aeration factor with dimension [s^{-1}]; λ has a value between 0.1 s^{-1} and 0.5 s^{-1} at full scale and between 1 s^{-1} and 10 s^{-1} at model scale (Blackmore & Hewson, 1984). It is recommended to use value of 0.3 s^{-1} for rocky foreshore and 0.5 s^{-1} for regular beaches (BS 6349, 1994).

2.4.2.4 EXTENDED GODA FORMULA BY TAKAHASHI (1994)

The original Goda formula has many advantages like the ability to be employed both for standing and slightly breaking waves. To use this formula for impact waves, it was subsequently extended with the incident wave direction, modification factors applicable to other types of vertical walls and the impulsive pressure coefficient (Takahashi et al., 1994).

Goda formula is modified to include impulsive forces from breaking waves by modifying the coefficient α_* as:

Equation 2.11 $\alpha_* = max(\alpha_2, \alpha_I)$

where,

$$\alpha_I = \alpha_{I0} \cdot \alpha_{I1}$$

$$\alpha_{I0} = \begin{cases} H_{max}/d & \rightarrow H_D/d \leq 2 \\ 2 & \rightarrow H_D/d > 2 \end{cases}$$

$$\alpha_{I1} = \begin{cases} \frac{\cosh \delta_2}{\cosh \delta_1} & \rightarrow \delta_2 \leq 0 \\ \frac{1}{\cosh \delta_1 \cdot (\cosh \delta_2)^{\frac{1}{2}}} & \rightarrow \delta_2 > 0 \end{cases}$$

$$\delta_1 = \begin{cases} 20 \cdot \delta_{11} & \rightarrow \delta_{11} \leq 0 \\ 15 \cdot \delta_{11} & \rightarrow \delta_{11} > 0 \end{cases}$$

$$\delta_{11} = 0.93\left(\frac{B_m}{L} - 0.12\right) + 0.36\left(\frac{h_s - d}{h_s} - 0.6\right)$$

$$\delta_2 = \begin{cases} 4.9 \cdot \delta_{22} & \rightarrow \delta_{22} \leq 0 \\ 3 \cdot \delta_{22} & \rightarrow \delta_{22} > 0 \end{cases}$$

$$\delta_{22} = -0.36\left(\frac{B_m}{L} - 0.12\right) + 0.93\left(\frac{h_s - d}{h_s} - 0.6\right)$$

2.4.2.5 ALLSOP AND VICINANZA METHOD (1996)

According to the model tests at HR Wallingford within the PROVERBS project, Allsop and Vicinanza (1996) recommend a prediction formula for the horizontal wave impact force on the vertical walls (Equation 2.12). The adopted prediction line is shown on Figure 2.14. Data were produced on a slope of 1/50 at 1/250 level for the range of $0.3 < H_{si}/d \leq 2$. However, it is suggested to be applied between $0.35 < H_{si}/d \leq 0.6$ for simple vertical walls. The method is recommended in Oumeraci et al. (2001) for preliminary design.

Equation 2.12 $$F_h = 15\rho g d^2 (H_{si}/d)^{3.134}$$

where,

h_s; is the water depth at the model toe.

H_{si}; is the significant wave height at the model toe.

d; is the water depth above the berm.

Figure 2.10 shows the geometric parameters described above.

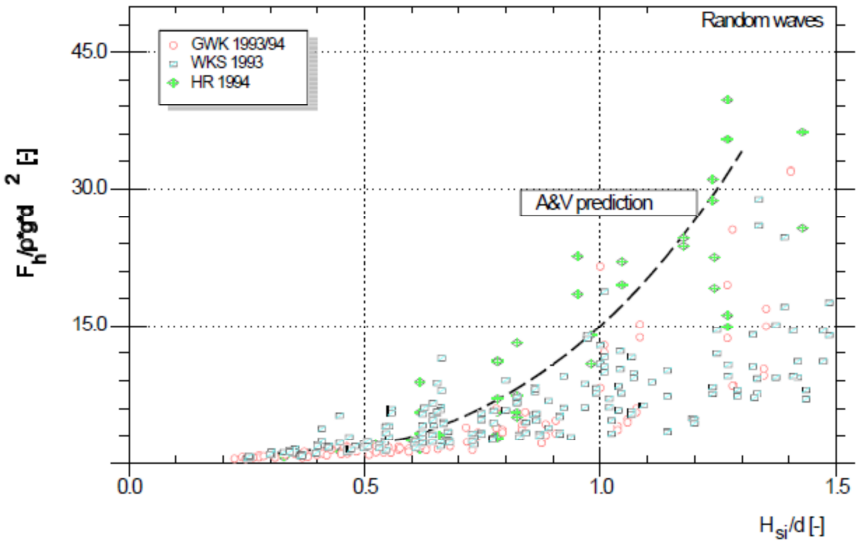

Figure 2.14 *Relative wave force $F_h/\rho g d^2$ plotted versus relative wave height H_{si}/d and comparison to calculation method given by Equation 2.12.*

2.4.2.6 PROVERBS METHOD (2001)

Probabilistic design tools for vertical breakwaters (PROVERBS) was a major European research project within the 4th framework program of the European Union. The overall objective of the project was to develop and implement a reliability based framework and associated probabilistic tools for the design of vertical breakwaters. Within the framework of the PROVERBS, Oumeraci et al. (2001) gave guidelines for assessment of wave forces on seawalls under breaking and non-breaking conditions.

The application of the PROVERBS methodology is nevertheless complex and may still lead to significant scatter in predictions of wave loads even under relatively similar design conditions with predicted design loads being often significantly different from estimates by the most generally accepted and established design methods (Cuomo et al., 2010).

Figure 2.15 shows the pressure distribution and main geometric features according to the PROVERBS method. In the following, the main geometric and wave parameters are described for the PROVERBS method described by Oumeraci et al., 2001.

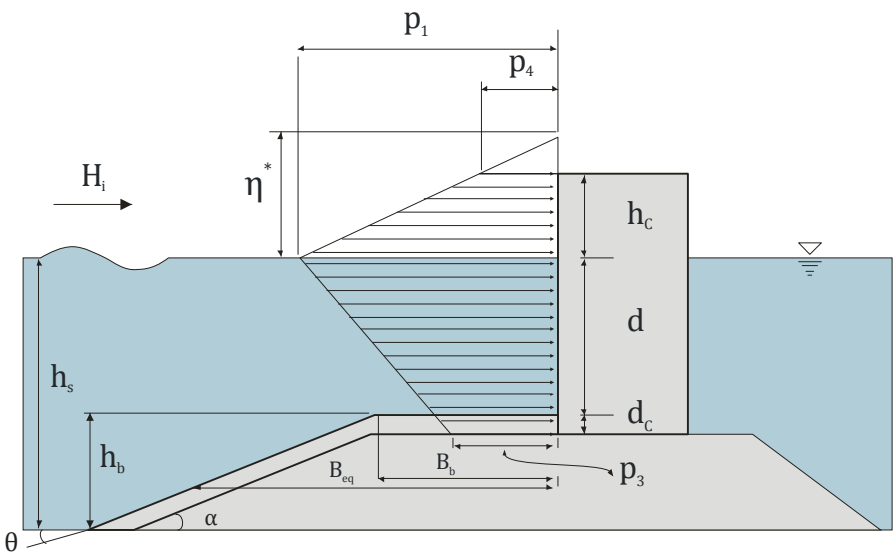

Figure 2.15 *Pressure distribution according to the PROVERBS Method (after Oumeraci et al., 2001)*

2.4.2.6.1 Determine breaker wave height H_b in front of reflective vertical walls

Equation 2.13 $$H_b = L_{pi}\left(0.1025 + 0.0217\left(\frac{1-K_r}{1+K_r}\right)\right)\left[tanh\left(\frac{2\pi k_b h_s}{L_{pi}}\right)\right]$$

L_{pi} is the local inshore wave length related to peak period T_p (at h_s) and determined by linear wave theory. K_r is the overall reflection coefficient from the vertical wall.

Equation 2.14 $$L_{pi} = \left(gT_p^2/2\pi\right)\left[tanh\left(2\pi h_s/L_{pi}\right)\right]$$

k_b is the empirical correction factor and determined from Equation 2.15.

Equation 2.15 $$k_b = 0.0076\left(B_{eq}/d\right)^2 - 0.1402\left(B_{eq}/d\right) + 1$$

where, B_{eq} is the equivalent berm width defined halfway up to berm

$$B_{eq} = B_b + \frac{h_b}{2\tan\alpha}$$

tanα is the steepness of the seaward berm slope and B_b, h_b are the berm width and height, respectively, d is the water depth at the caisson wall.

2.4.2.6.2 Determine the probability of impacts

The percentage of breaking and broken waves is determined according to the results of Equation 2.16. In Oumeraci et al. (2001), it is mentioned that P_b should be considered as an upper limit for the percentage of impact loading.

Equation 2.16 $$P_b(\%) = exp\left[-2\left(\frac{H_b}{H_{si}}\right)^2\right] \times 100$$

where H_{si} is considered as the incident significant wave height at water depth h_s.

The maximum wave height which describes the transition from impact to broken wave zone is defined from Equation 2.17.

Equation 2.17 $$H_{bs} = 0.1242\, L_{pi}\left[tanh\left(2\pi h_s / L_{pi}\right)\right]$$

Then the proportion of waves that may actually break directly on the structure causing impact, P_i calculated as follows.

Equation 2.18 $$P_i(\%) = \{exp[-2(H_b/H_{si})^2] - exp[-2(H_{bs}/H_{si})^2]\} \times 100$$

According to the results of Equation 2.18, following categorization is suggested:

$P_i(\%) < 2\%$	Little breaking, wave loads are primarily non-breaking
$2 < P_i(\%) < 10\%$	Breaking waves give impacts
$P_i(\%) > 10\%$	Heavy breaking may give impacts or broken loads

For very low value of f $P_i(\leq 1\%)$ the loading can be considered as pulsating and PROVERBS suggests to use Goda formula. For $P_i > 1\%$ or 2% F_h can be calculated using procedure explained below for impact loads.

2.4.2.6.3 Determine the maximum horizontal forces for impact loads

The total maximum horizontal force is shown in Equation 2.19.

Equation 2.19 $$F_h^* = \frac{F_h}{\rho g H_b^2}$$

F_h^* is the relative wave force in non-dimensional form. It is determined by assuming a generalised extreme value distribution (GEV):

Equation 2.20 $$F_h^* = \frac{\alpha}{\gamma}\{1 - [-lnP(F_h^*)]^\gamma\} + \beta$$

where, $P(F_h^*)$ is the probability of non exceedance of the impact force; generally taken as 90%. α, β, γ are the statistical parameters for GEV distribution; for $\theta = 1/20$, 3.745, 7.604 and -0.295 respectively.

2.4.2.6.4 Determine simplified impact force history

Figure 2.16 shows the actual and simplified force time histories. The area up to $t_{r,Fh}$ and $t_{d,Fh}$ are equal to force impulses $I_{r,Fh}$ and $I_{d,Fh}$ respectively. The actual and more complicated force history is reduced to an equivalent triangular force history having the same peak value F_h, the same force impulses $I_{r,Fh}$ and $I_{d,Fh}$, with different rise time (t_r) and total impact duration (t_d).

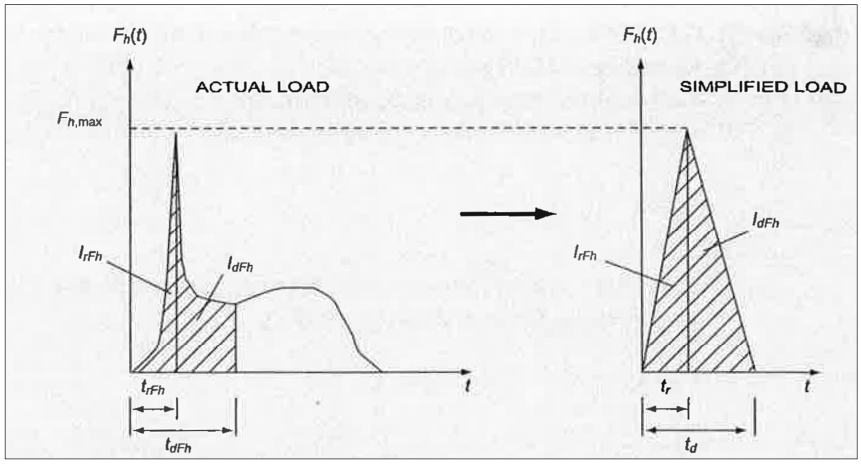

Figure 2.16 *Simplified force time history (after Oumeraci et al., 2001)*

$I_{r,Fh}$ is the momentum of water mass involved in the impact and $I_{d,Fh}$ is the momentum of the total mass in the breaking wave.

2.4.2.6.5 Determine equivalent rise time

The measured rise time is calculated from:

Equation 2.21 $$t_{r\,Fh} = 8.94k\frac{\sqrt{d_{eff}/g}}{F^*_{h,max}}$$

where, d_{eff} is the effective water depth in front of the structure:

Equation 2.22 $$d_{eff} = d + B_{rel}m_{rel}(h_s - d)$$

Where, B_{rel} is the part of the berm width which influences the effective water depth and m_{rel} is the part of the berm slope influencing the effective water depth.

Equation 2.23 $$B_{rel} = \begin{pmatrix} 1 & for \;\; B_b/L_{pi} \le 1 \\ 1 - \frac{0.5B_b}{L_{pi}} & for \;\; \frac{B_b}{L_{pi}} > 1 \end{pmatrix}$$

Equation 2.24 $$m_{rel} = \begin{pmatrix} 0 & without\ any\ berm \\ 1 & for \quad 0 < m < 1 \\ 1 & for \quad m \ge 1 \end{pmatrix}$$

k is the proportion of the water mass M_{imp} of the breaking wave mass M_{wave}, which is involved in the impact and causing the force impulse $I_{r,Fh}$. It depends on the breaker type, but can be estimated to be:

Equation 2.25 $$k = \frac{M_{imp}}{M_{wave}} = \frac{I_{r,Fh}}{I_{d,Fh}} = 0.16\ to\ 0.25$$

The equivalent rise time t_r for a deterministic approach is

Equation 2.26 $$t_r = (0.5\ to\ 1.0) \times t_{r\,Fh}$$

For a probabilistic approach, the uncertainties in k and in the relationship $t_r = f(t_{r\,Fh})$ are better considered together through the following relationship to calculate directly the equivalent rise time t_r:

Equation 2.27 $$t_r = k' \frac{\sqrt{d_{eff}/g}}{F^*_{h,max}}$$

Then, k' can be described by assuming a Log-normal distribution with a mean value of 0.086 and standard deviation of 0.084.

For a deterministic approach the upper bound of t_d/t_r is described by

Equation 2.28 $$t_d = t_r(2 + 8 \cdot exp[-18 \cdot t_r/T_p])$$

For a probabilistic approach t_d is calculated statistically by:

Equation 2.29 $$t_d = \frac{-c}{ln(t_r)}$$

where c is an empirical parameter, ($[-s \ln(s)]$) normally distributed with a mean value $\bar{c} = 2.17$ and a standard deviation of $\sigma_c = 1.08$ (derived from large scale model tests).

2.4.2.6.6 Determine simplified impact pressure distribution

Based on analysis of about 1000 impact pressure distributions recorded in large-scale-model tests the simplified distribution at the time of maximum impact F_h has been derived (Figure 2.15). Four parameters are required to describe this distribution:

The elevation of pressure distribution η^* and bottom pressure p_3 are:

Equation 2.30 $$\eta^* = 0.8H_b$$

Equation 2.31 $$p_3 = 0.45p_1$$

Then pressure p_1 at SWL and pressure at the high freeboard p_4 are determined based on the equivalent triangular shape of $F_h\ (t)$ for the cases of overtopping and non-overtopping.

Without overtopping $h_c > \eta^*$

Design water level: it is based on the equivalent triangular shape of $F_h\ (t)$. First, a high freeboard ($h_c > \eta^*$), so

$F_h\ (t)$ at any time of the equivalent triangular force history is described by the corresponding area of the pressure distribution:

Equation 2.32 $$F_h(t) = \frac{1}{2}p_1(t)\,\eta^* + (d + d_c)p_3 + \frac{1}{2}(d + d_c)\cdot(p_1(t) - p_3)$$

Equation 2.33 $$p_1(t) = \frac{F_h(t)}{0.4H_b + 0.725(d+d_c)}$$

Equation 2.34 $$p_4 = 0$$

With overtopping $h_c < \eta^*$

Force reduction due to overtopping is taken into account by cutting off the pressure distribution at the crest level:

Equation 2.35 $$F_{h.max,ov} = F_{h.max} - \frac{1}{2}(\eta^* - h_c)p_4$$

Equation 2.36 $$p_1(t) = \frac{F_h(t)}{0.725(d+d_c) + \frac{h_c}{2}\left(1 + \frac{\eta^* - h_c}{\eta^*}\right)}$$

Equation 2.37 $$p_4 = \frac{\eta^* - h_c}{\eta^*}p_1$$

2.4.2.7 CUOMO et al. METHOD (2010)

Recently, Cuomo et al. (2010) present prediction formulas for both quasi-static and impact forces on vertical face coastal structures (such as seawalls and caissons breakwaters) based on experimental work carried out in the CIEM/LIM large flume at Barcelona within the framework of the VOWS (Violent Overtopping by Waves at Seawalls) project.

The total impacting horizontal (force at 1/250 exceedance level) force in the seaward direction of a vertical structure is given by:

Equation 2.38 $$F_{h,imp,1/250} = C_r^{1.65}\rho g \cdot H_{mo} \cdot L_{hs} \cdot \left(1 - \frac{|h_b - d|}{d}\right)$$

where,

C_r: is the reflection coefficient

H_{mo}: is the significant (spectral) wave height

L_{hs}: is the wavelength at the toe of the structure,
for mean wave period $T = T_m$

d: is the water depth in front of the wall

h_s: represent water depth at the toe of the structure

The term $\left(1 - \frac{|h_b - \mathrm{d}|}{\mathrm{d}}\right)$ represents the severity of the breaking at the structure to a certain degree. In which h_b shows the water depth at breaking. Here h_b is evaluated by inverting Miche's breaking criteria assuming $H_b = H_{mo}$:

Equation 2.39 $$h_b = \frac{1}{k} arctanh\left(\frac{H_{mo}}{0.14 \cdot L_{hs}}\right)$$

where, k: $k = 2\pi / L_{hs}$

Based on past and new observations, they also proposed a prediction formula for quasi-static forces in Equation 2.40:

Equation 2.40 $$F_{h,qs,1/250} = 4.8\, \rho g H_{m0}^2$$

The above prediction formulae is valid $0.2\,m < H_{mo} < 0.7\,m$, $0.5\,m < h_s < 1.3\,m$ and $2\,s < T_m < 3.7\,s$.

All the methods discussed up to now consider plain vertical walls. In the case of perforated vertical walls, the reflection and turbulence will be lower. Despite their increased complexity and cost of construction as compared to plain caissons, perforated caissons are becoming more and more popular not only for anti-reflective quaywalls inside sheltered harbours, but also for external caisson breakwaters, in order to partly overcome the typical drawbacks of vertical structures: large reflections, forces, overtopping and toe scour. Perforated vertical breakwaters are intended to absorb part of the wave energy through various mechanisms, such as turbulence, resonance and viscous. The larger the water level difference at the two porous wall sides the larger the energy dissipation, which is therefore strongly dependent on the wave length L (Oumeraci et al., 2001).

2.5 SCALING

Hydraulic models are used to investigate the wave loading on vertical coastal structures subject to waves. However, most of these models are performed in small scale dimensions. For scaling of wave loading on hydraulic models, Froude or Cauchy models are often used.

Cuomo et al., (2010b) mentioned that the use of Froude similarity for scaling up wave impact pressures recorded during physical model tests may lead to over-estimation of impact maxima.

It has been suggested by Kortenhaus and Oumeraci (1999) that Cauchy law scaling could be used to correct for the presumed overestimation but this would reduce the magnitude of the impulse whereas small-scale physical-model tests (Bullock et al, 2001) indicate that the impulse should be conserved.

In the following, the Froude and Cauchy scaling laws are discussed in details.

2.5.1 Froude Law scaling

Measurements obtained from hydraulic models of sea wave action in which gravity is the dominant force are converted to full or prototype scale by application of the Froude law:

Equation 2.41 $$\frac{u_p}{\sqrt{g_p l_p}} = \frac{u_m}{\sqrt{g_m l_m}}$$

where u is the characteristic velocity and l is the characteristic length. The subscript p and m denotes quantities in prototype and model scale respectively.

Table 2.1 Scale relations for Froude and Cauchy

Parameter	Froude	Cauchy
Force ratio	Inertia/gravity	Inertia/Elastic
Equations	$\frac{u}{\sqrt{gL}} = const$	$\frac{\rho u^2}{K} = const$
Length	N_L	N_L
Time	$N_t = \sqrt{N_L}$	$N_t = \sqrt{\frac{N_\rho}{N_K}}\ N_L$
Pressure	$N_p = N_\rho\ N_L$	$N_p = N_K$
Force	$N_F = N_\rho N_L^3$	$N_F = N_K N_L^2$

This law is based on the concept that for dynamic similarity between two geometrically similar systems A and B, the ratio of the inertia force to the gravity force must be the same. The length, time, pressure and force in the two systems are related expressions shown in Table 2.1.

2.5.2 Cauchy Law scaling

It is related to the Cauchy number which is the ratio inertia forces and elastic forces:

Equation 2.42 $$Ca = \frac{\rho u^2}{K}$$

Where, u is the celerity, ρ is the density of the fluid and K is the bulk modulus of the fluid.

Scaling by Cauchy can then be implemented by:

Equation 2.43 $$\frac{\rho_p u_p^2}{K_p} = \frac{\rho_m u_m^2}{K_m}$$

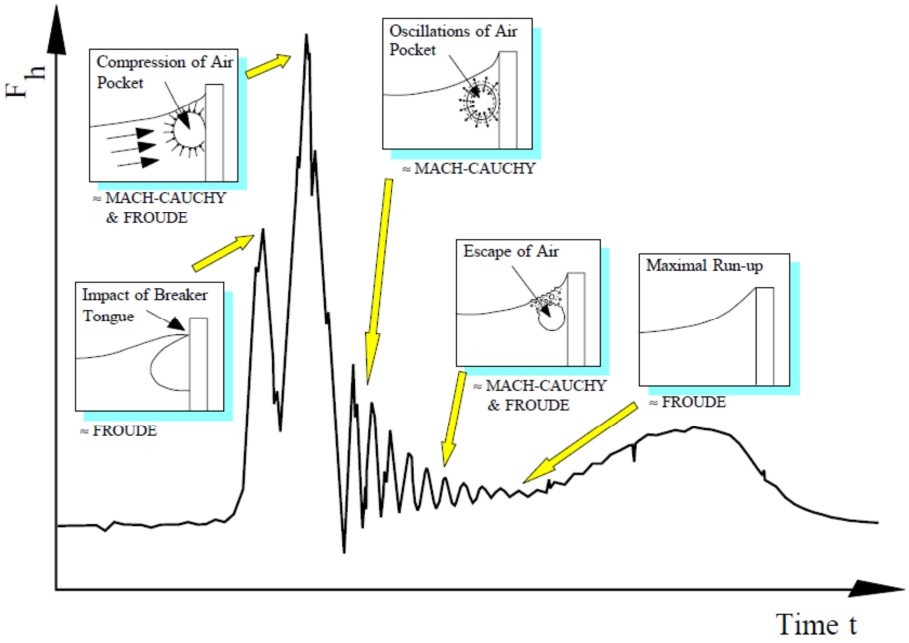

Figure 2.17 *Relevant scaling laws for the various processes of impact loading (after Oumeraci and Hewson, 1997)*

Cauchy's law is often suggested to scale pressure peaks as it considers air entrapments. Important scale relations are given in Table 2.1.

Within the PROVERBS project (Probabilistic Design Tools for Vertical Breakwaters) the scale effects of impact loading were investigated by performing field measurements, detailed laboratory testing and a better understanding of the physics of impact loading. Based on these measurements, a more complete approach has therefore suggested by Oumeraci & Hewson (1997) which is shown in Figure 2.17.

Depend on the level of aeration and the amount of entrapped air, they proposed to use whether FROUDE or MACH-CAUCHY similarity laws or a combination of both has to be applied for the scaling. Therefore, an improved scaling procedure based on the separation of the different components of the impact load history has been suggested (see Figure 2.17). For further details see Kortenhaus & Oumeraci (1999).

Recently, Cuomo et al. (2010b) suggested a practical method for adjusting impact pressures and rise time on the vertical structures to account for scale effect. Their model is based on the "compression model law" originally proposed by Mitsuyasu (1966) and successively extended by Lundgren (1969) and Takahashi et al. (1985).

The relative peak pressure which is called Bagnold number by Takahashi et al. (1985) is:

Equation 2.44 $$Bgn = \frac{\rho_w k_w u_0^2}{p_0 D}$$

where u_0 is the characteristic wave crest velocity, p_0 is the atmospheric pressure, k_w is the effective water mass and D is the thickness of the compressed air layer at impact. Parameters k_w, u_0 and D depend on the geometrical characteristics shown in Figure 2.18.

The characteristic wave crest velocity u_0 is:

Equation 2.45 $$u_0 = \sqrt{g(d + H_{mo})}$$

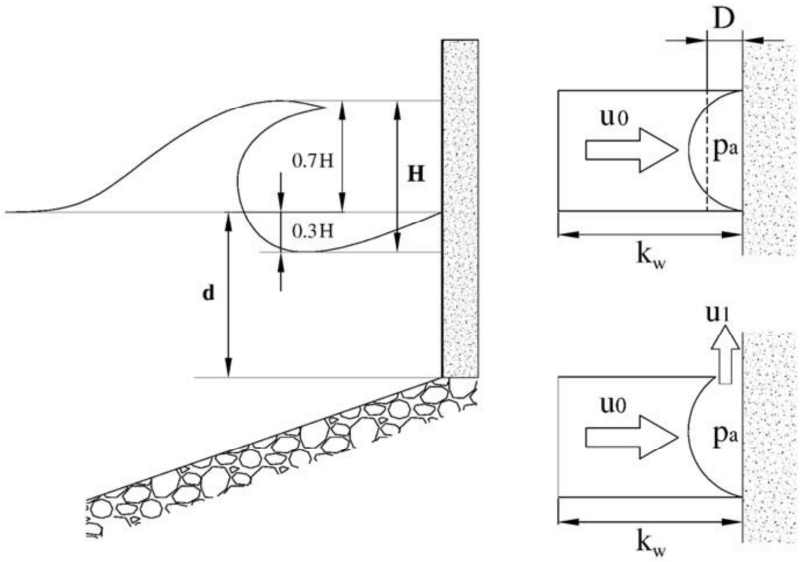

Figure 2.18 *Definition sketch for Cuomo's scaling Method (after Cuomo et al., 2010b)*

where, H_{mo} is the significant (spectral) wave height and d is the constant water depth.

The thickness of the compressed air layer at impact D is:

Equation 2.46 $$D = \pi/12\ H_{mo}$$

The effective water mass k_w is:

Equation 2.47 $$k_w = 0.2\ (1 - \pi/12)\ H_{mo}$$

Takahashi et al., (1985) expressed the following relation between Bgn and the relative (to atmospheric) maximum pressure $\frac{p_{max}}{p_0}$. They assumed adiabatic compression of air at impact for solving equation of motion.

Equation 2.48 $$Bgn = 5\left(\frac{p_{max}}{p_0}\right)^{2/7} + 2\left(\frac{p_{max}}{p_0}\right)^{-5/7} - 7$$

Both Equation 2.44 and Equation 2.48 has the quantity of $\frac{p_{max}}{p_0}$ and the atmospheric pressure p_0 cannot be scaled to the model dimension. Therefore, measurements at model scale need to be corrected by a factor λ_s given by:

Equation 2.49 $$\lambda_s = \frac{(p_{max,p} - p_0)/p_0}{(p_{max,m} - p_0)/p_0}$$

where $p_{max,p}$ and $p_{max,m}$ denotes the maximum peak pressures at prototype and model scale.

Cuomo et al. (2010b) suggest to following procedure to scale pressure $p_{max,m}$ at model scale to pressure $p_{max,p}$ at prototype scale:

1. evaluate (at both model and prototype scales) parameters u_0, D and k_w as functions of the geometrical characteristics of the problem;

2. evaluate Bagnold number at model (Bgn_m) and prototype (Bgn_p) scales using Equation 2.44;

3. solve Equation 2.48 for $p_{max,m}$ and $p_{max,p}$;

4. evaluate scaling factor λ_s using Equation 2.49.

It is also possible to read λ_s value from Figure 5 in Cuomo et al. (2010b) for Bgn_m and Bgn_p values from Equation 2.44.

2.6 3-D EFFECT

Wave forces for long-crested normal waves agree well with results from 3-D tests by Franco et al (1996) where there are no impacts, only pulsating loads. Comparisons with Goda predictions show relatively good agreement over the pulsating zone.

However, Bullock et al. (2003) have done some research to analyze the three-dimensional effect of the impulsive waves. Although the time of impact is not varying significantly horizontally, a considerable difference was noticed on the size of the pressure impact. Figure 2.19 shows the measured pressures in the horizontal (lateral) direction from pressure/aeration units (PAUs 3, 7 and 8) mounted alongside each other at an elevation of 6.2m CD over a horizontal distance of 3.1m. The respective values for PAUs 3, 7 and 8 were 337kPa, 132kPa and 116kPa. Furthermore, the pressures measured during the quasi-static section of the record obtained by PAU 3 were much lower than the quasi-static pressures measured by PAUs 7 and 8. This suggests that there was a fair amount of three-dimensionality in this particular event. Near the vertical walls of the flume, the pressure is dropping, probably due to friction. The quasi-hydrostatic part is also varying but this time the smallest values are to be found in the middle of the model.

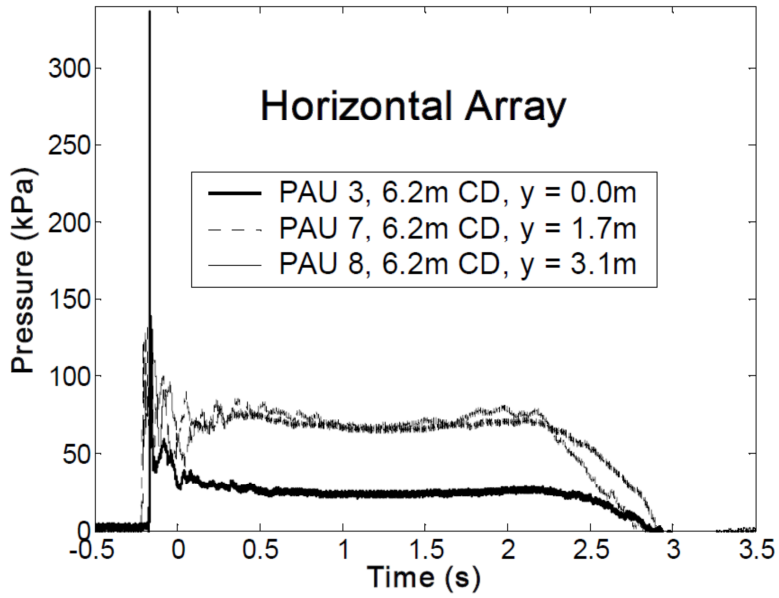

Figure 2.19 *Horizontal (lateral) variation in impact pressures when $H_{si} \approx 3.1m$ and $H_{sr} \approx 0.7m$*

In addition, Martinelli et al. (2007) proposed design diagrams to evaluate the reduction of the wave force induced by breaking and nonbreaking short-crested oblique waves with increasing horizontal length of the caisson units. They compare the theoretical reduction coefficient for different cases of spreading as a function of the integration length (the caisson length) scaled with incident peak wave length, separating pulsating and breaking waves. As expected, the reduction coefficient increases with decreasing spreading for breaking waves and it is modest for linear waves.

Furthermore they present the theoretical reduction coefficient for different wave obliquities. The reduction due to wave obliquity is small in breaking wave conditions, since the correlation is already small at long distances where the phase shift is pronounced.

2.7 CONCLUSION

Theoretical background on wave forces on the vertical structures is given. Different models for occurring shock pressures are discussed. According to the breaker shape, existing categorization of wave impacts are analyzed. The well known methods used to predict quasi-static and impact forces are reviewed in chronologic order. Then, the scaling of the forces and 3-dimensionality of the results are discussed.

REFERENCES

Allsop N.W.H.; Vicinanza D.; McKenna J.E., 1996, "*Wave forces on vertical and composite breakwaters*" Report SR443, HR Wallingford

Allsop, N. W. H.; Vicinanza, D., 1996, '*Wave impact loadings on vertical breakwaters: development of new prediction formulae*', 11th Int. Harbour Congress, Antwerp

Allsop, N.W.H.; Vicinanza, D.; Calabrese, M.; Centurioni, L., (1996c), "Breaking Wave Impact Loads on Vertical Faces", ISOPE International Offshore and Polar Engineering-Conference, pp-185, Los Angeles, California

Bagnold, R. A., 1939, "*Interim report on wave-pressure research"*, Proc. Inst, Civil Eng. 12, 201–226

Blackmore, P.A.; Hewson, P.J., (1984), "Experiments on full-scale wave impact pressures", Coastal Engineering Vol-08 Issues:4, pp:331-346

BS 6349, 1994, "Maritime structures, Code of practice for design of fendering and mooring systems", BSI, London, 1994

Bullock, G.N.; Crawford, A.R.; Hewson, P.J.; Walkden, M.J.A.; Bird, P.A.D., 2001, "*The influence of air and scale on wave impact pressures*", Coastal Engng, vol 42, pp 291-312

Bullock, G.N.; Obhrai, C.; Peregrine, D.H.; Bredmose, H., 2007, "*Violent breaking wave impacts, Part 1: Results from large-scale regular wave tests on vertical and sloping walls*" Coastal Engineering, v 54, n 8, p 602-617

Bullock, G; Obhrai, C.; Müller, G.; Wolters, G.; Peregrine, H.; Bredmose, H., (2004), "*Characteristics and design implications of breaking wave impacts*" -Coastal Engineering Conference, pp: 3966

Bullock, G; Obhrai, C; Müller, G; Wolters, G; Peregrine, H; and Bredmose, H, 2003, "*Field and Laboratory Measurement of Wave Impacts*" ASCE Conf. Proc. doi:10.1061/40733(147)29, Coastal Structures 2003, Proceedings of Coastal Structures 2003

Chan, E.S.; Melville, W.K., 1988, "*Deep-water plunging wave pressures on a vertical plane wall"*, Proc. Roy., Soc. London, A, 417(1852), 95-131

Cooker, M.J.; Peregrine, D.H., 1990, "*A model for breaking wave impact pressures*", Proc. 22nd Int. Conf. on Coastal Engineering Delft, ASCE, New York (1990), pp. 1473–1486

Cuomo, G.; Allsop, W.; Bruce, T.: Pearson, J., 2010, "*Breaking wave loads at vertical seawalls and breakwaters*", Coastal Engineering, Volume 57, Issue 4, 2010, Pages 424-439

Cuomo, G.; Allsop, W.; Takahashi, S., 2010b, "*Scaling wave impact pressures on vertical walls*", Coastal Engineering, Volume 57, Issue 6, June 2010, Pages 604-609

Franco, C.; Van der Meer, J.W.; Franco, L., 1996, "*Multidirectional wave loads on vertical breakwaters*", Proceedings International Conference Coastal Engineering (ICCE), ASCE, Orlando, Florida, USA, no. 25, Volume 2, Chapter 156, pp. 2008 2022

Goda, Y., 1967. The fourth order approximation to the pressure of standing waves. Coastal Engineering in Japan 10, 1–11.

Goda, Y., 1974. New wave pressure formulae for composite breakwaters, Proceedings of the 14th Conference of Coastal Engineering, ASCE, 1702–1720

Hattori, M.; Arami, A.; Yui, T., 1994, "*Wave impact pressure on vertical walls under breaking waves of various type"*' Coastal Engineering, v 22, n 1-2, p 79-114, Jan 1994

Hiroi, I., 1919, "*The force and power of waves*", The Engineer, August, 1919

Hull, P.; Müller, G., 2002, *'An investigation of breaker heights, shapes and pressures'* Ocean Engineering, v 29, n 1, p 59-79, September 21, 2002

Kirkgoz, M.S., 1982, "*Shock pressure of breaking waves on vertical walls"* Journal of the Waterway, Port, Coastal and Ocean Division, v 108, n WW1, p 81-95, Feb 1982

Kirkgoz, M.S., 1995, "*Breaking wave impact on vertical and sloping coastal structures"* Ocean Engineering, v 22, n 1, p 35-48, Jan 1995

Kortenhaus A.; Oumeraci H., 1997, "*Supplementary data for response map*" Proc. 1st Overall Workshop, MAST III PROVERBS, Las Palmas, Gran Canaria

Kortenhaus, A.; Oumeraci, H., 1999, "*Scale effects in modelling wave impact loading of coastal structures*", Proc. HYDROLAB-Workshop on Experimental Research and Synergy Effects with Mathematical Models Forschungszentrum Kuste, Hannover, pp. 285–294

Lundgren, H., 1969, "*Wave shock forces: an analysis of deformations and forces in the wave and in the foundation*", Proc. Symp. on Research in Wave Action. Delft Hydraulics Lab, Delft, The Netherlands, pp. 1–20.

Martinelli L.; Lamberti, A.; Frigaard P., "*Effect of short-crestedness and obliquity on non-breaking and breaking wave forces applied to vertical caisson breakwaters*", Coastal Engineering Journal, 49 (2), June 2007, 173-203.

Minikin, R.R., 1963, "*Wind, Waves and Maritime Structures*", (2nd Ed.), Charles Griffen, London (1963)

Mitsuyasu, H., 1966, "*Shock pressure of breaking waves*", Proc. of 10th Int. Conf. Coastal Eng., Tokyo, Japan, ASCE, New York, pp. 268–283.

Oumeraci, H., 1994, "*Multi-disciplinary research experience in Europe on vertical breakwaters*", Proceedings of the international workshop on Wave Barriers in Deep Waters, January 10-14, 1994, pp. 267-278, Port and Harbour Research Institute, Ministry of Transport, Nagase, Yokosuka, Japan

Oumeraci, H.; Bruce, T.; Klammer, P.; Easson, W.J., 1995, "*PIV measurement of breaking wave kinematics and impact loading of caisson breakwaters*" COPEDEC, no. 4, v 3, pp. 2394-2410

Oumeraci, H.; Hewson, P., 1997, "*Tentative recommendations for scaling wave impact loading*", Proceedings 2nd Task 1 Workshop, MAST III, PROVERBS-Project: Probabilistic Design Tools for Vertical Breakwaters, Edinburgh, U.K., Discussion note, Annex 1.1.6, 8 pp.

Oumeraci, H.; Klammer, P.; Partenscky, H.W., 1993, "*Classification of breaking wave loads on vertical structures"*, Journal of Waterway, Port, Coastal and Ocean Eng. v 119, n 4, p 381-397

Oumeraci, H; Kortenhaus, A; Allsop, W; de Groot, M; Crouch, R; Vrijling, H; Voortman, H, 2001, "*Probabilistic Design Tools for Vertical Breakwaters*", Balkema Publishers, New York.

Partenscky, H., 1988, "*Dynamic forces due to waves breaking at vertical coastal structures"* Twenty First Costal Eng Conf, p 2504-2518, 1988, Twenty First Costal Eng Conf

Richert, G., 1968, "*Experimental investigation of shock pressures against breakwaters"* In: Proc. Int. Conf. Coastal Engng, ASCE, London, pp. 954–973.

Rundgren, L., 1958, "Water Wave Forces," Bulletin No. 54, Royal Institute of Technology, Division of Hydraulics, Stockholm, Sweden, 1958,

Sainflou, G., 1928. Essai sur les digues maritimes verticales. Annual Ponts et Chaussees 98 (1), 5–48.

Shore Protection Manual. 1984. 4th ed., 2 Vol U.S. Army Engineer Waterways Experiment Station, U.S. Government Printing Office, Washington, DC

Takahashi S., 1996, "*Design of Vertical Breakwaters*, Reference Document No. 34, Port and Harbour Research Institute, 1996, Tokyo

Takahashi, S., Tanimoto, K., Miyanaga, S., 1985, "*Uplift wave forces due to compression of enclosed air layer and their similitude low*", Coast. Eng. Jpn. 28, 191–206.

Takahashi, S.; Tanimoto, K.; Shimosako, K., 1994, "*A proposal of impulsive pressure coefficient for design of composite breakwaters*," Proc. of International Conference on Hydro-technical Eng. for Port and Harbor Construction, Port and Harbour Res. Inst

U.S. Army Corps of Engineers, 2002, "Coastal Engineering Manual", Engineer Manual 1110-2-1100, U.S. Army Corps of Engineers, Washington, D.C. (in 6 volumes)

Vrijling, J.K., 2001, chapter 2: Fault tree analysis of a vertical breakwater, Proverb individual chapters,

Walkden, M.J.A.; Crawford, A.R.; Bullock, G.N.; Hewson, P.J.; Bird, P.A.D., 1996, "*Wave impact loading on vertical structures*", Advances in Coastal Structures and Breakwaters (1996), pp-273-287

3

EXPERIMENTAL SET-UP

***

3.1 INTRODUCTION

Within the framework of this research, an extensive series of experiment has carried out to investigate loading conditions due to violent wave impacts on coastal structures with cantilever surfaces. A total of 192 regular wave tests and 80 irregular wave tests were performed. The main focus lies on the kinematics of breaking waves and the height, distribution, duration and characteristics of the wave impacts.

To achieve these goals, two dimensional scaled model tests are carried out. The scaled model is tested under regular and irregular wave conditions. This chapter describes the experimental set-up, instrumentation and data acquisition, followed by the data analysis of the test results.

3.2 TESTS WITH REGULAR WAVES

The scaled model is tested using the test parameter matrix in Table 3.1. Tests are carried out for regular waves and each test is repeated twice. The objective of the regular wave tests is to provide a detailed understanding of the mechanics of a wave field through examination of waves of constant height and period. Also for pressure and force measurements, using regular waves is the most efficient way of investigating parameters under nominally constant conditions.

3.2.1 MODEL SET-UP

Physical model tests have been carried out in the wave flume (30 m x 1 m x 1.2 m) of Ghent University (Belgium). The flume is equipped with the testing technology including an advanced wave generator system for both regular and irregular waves, active wave absorption, data acquisition system and wave data analysis software. Waves are generated by a piston type wave paddle with a maximum stroke length of 1.50 m.

The model is located 22.5 m away from the wave paddle on a uniform slope with 0.5 m depth at the location of the structure. The model is 0.3 m high (h_m) and 0.6 m long (l_m). The selected foreshore slope is 1/20. Generally, the largest impact pressures are recorded with 1/10 foreshore slope. However, the range of breaking wave height which includes all different breaking types is narrow compared to the wave height range for 1/20 slope. Accordingly, the transitions between the different breaker types are too rapid and even sometimes unclear. Therefore, it is decided to consider 1/20 foreshore slope to analyze the characteristics of different breaker types.

Figure 3.1 shows the detailed model set-up and the instrumentations used in the tests.

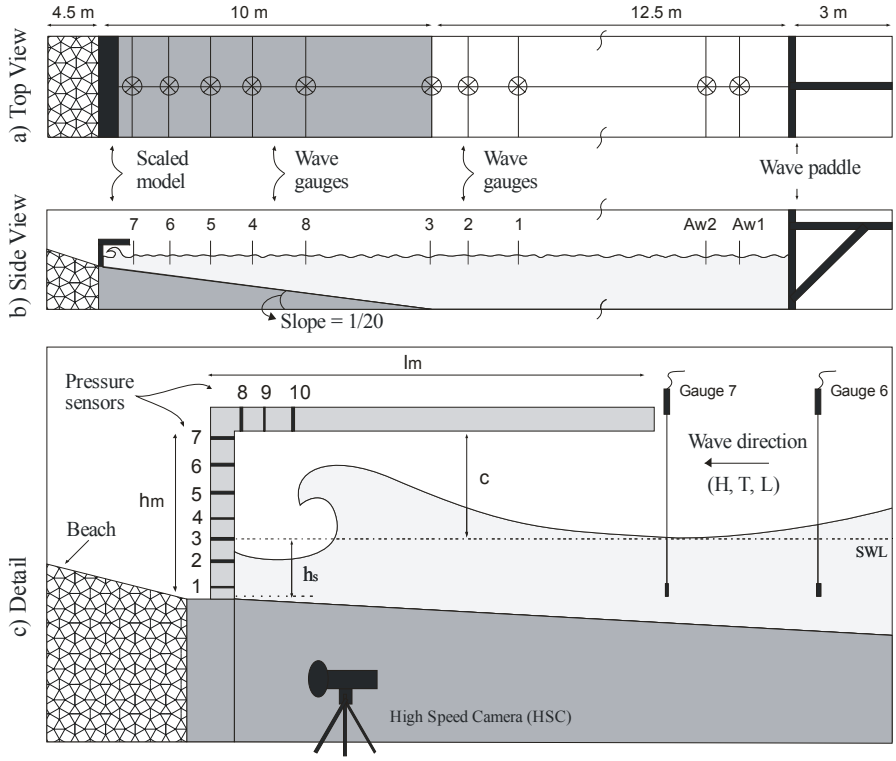

Figure 3.1. *Small-scale model set up for regular waves. a) is the top view, b) is the side view and c) is detailed view of model*

3.2.2 SCALED MODEL

3.2.2.1 SCALING MODEL FROM PROTOTYPE DIMENSION

The Pier of Blankenberge which is located along the Belgian coast is shown as an illustrative example of a vertical structure with an overhanging horizontal cantilever slab. This building (Figure 1.2), constructed on piles in the intertidal zone, has been renovated between 1999 and 2002. The renovation consisted partly of constructing a concrete core for the building from the sea bottom up to the first floor whereas formerly the complete building was entirely supported by piles (Verhaeghe et al., 2006). The model used in the physical tests is scaled with a scale factor of 1/20 to ensure correct reproduction of all wave processes from the cross-section of Blankenberge pier (Figure 3.2). This is more or less the largest possible scale that can be selected for the available test facility. Large model scale is selected because it is necessary for the accurate modelling of wave loading and structure responses due to its smaller/negligible scale effects. In addition, it is known that a correct representation of the conditions in nature cannot be guaranteed in a smaller scale.

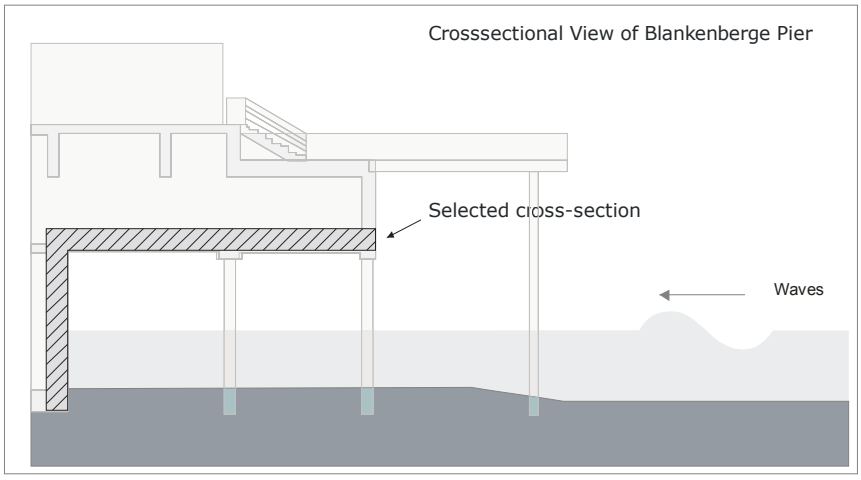

Figure 3.2. *Schematic view of Blankenberge Pier with vertical wall and horizontal deck subjected to incoming waves*

In general, Froude scaling law is applied in hydraulic applications to scale prototype dimensions to laboratory dimensions. Froude scaling relates the relative influence on inertial and gravity forces where Froude's number is equal both in model and prototype.

Rather than a purely geometrical scaling, it is also important to have the similar structural response under similar hydrodynamic conditions. Consequently, the Eigenfrequency of the model and prototype should be similar.

The eigenfrequency (f) can be expressed as (Vandepitte, 1979-1982).

Equation 3.1 $$f = \frac{\sqrt{EI}}{L^3\sqrt{\rho}}$$

where, f is the natural or eigenfrequency of the structure, E is the modulus of elasticity, I is the moment of inertia, L is the length and ρ is the density.

Equation 3.1 can be re arranged by considering $I \sim L^4$

Equation 3.2 $$f = \frac{\sqrt{E}}{L\sqrt{\rho}}$$

The full scaling similarity between eigenfrequencies can be calculated as:

Equation 3.3 $$\frac{f_p}{f_m} = \frac{\sqrt{E_p}}{L_p\sqrt{\rho_p}} \cdot \frac{L_m\sqrt{\rho_m}}{\sqrt{E_m}} = \frac{L_m}{L_p} \cdot \frac{\sqrt{\rho_m}}{\sqrt{\rho_p}} \cdot \frac{\sqrt{E_p}}{\sqrt{E_m}}$$

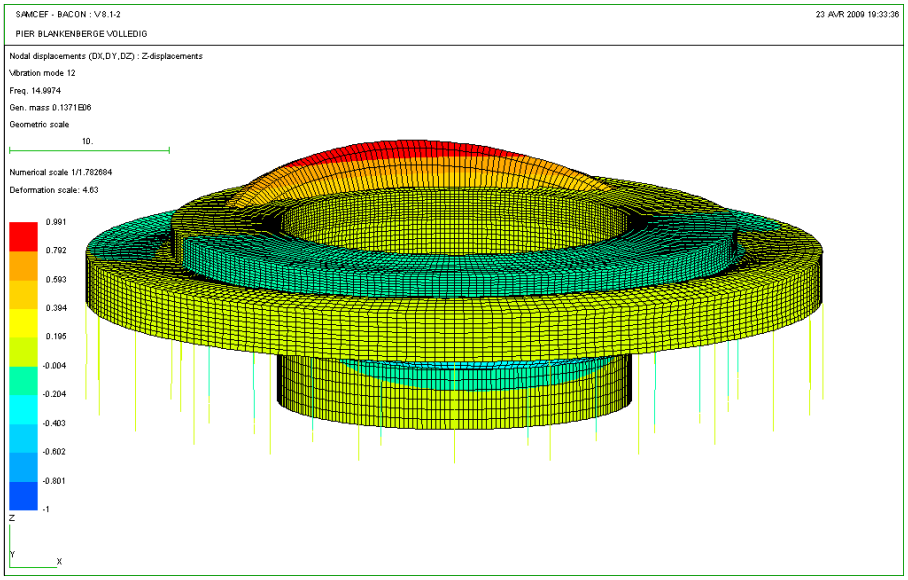

Figure 3.3. *Vibration mode of prototype for* $f_p = 14.997\ Hz$.

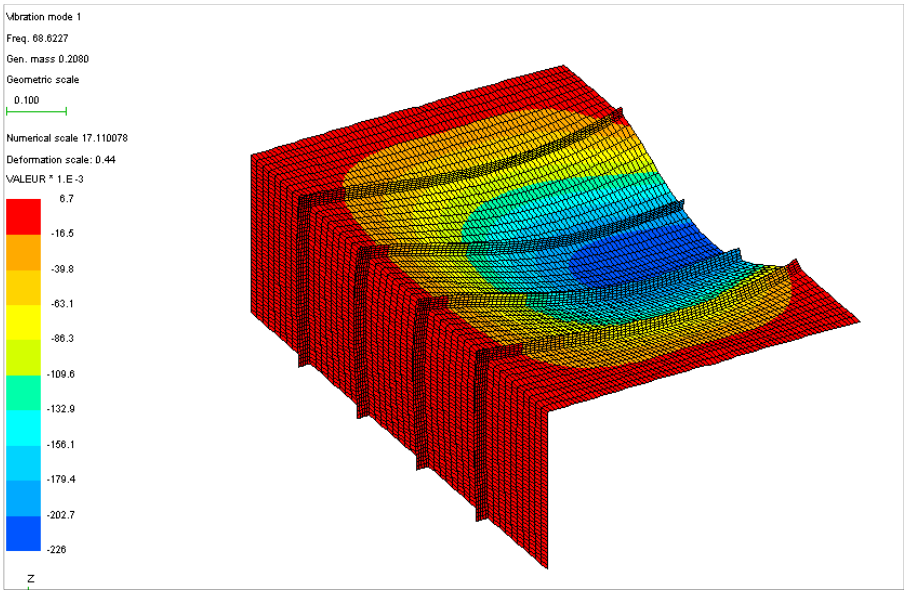

Figure 3.4. *Vibration mode of scaled model for* $f_m = 67.068\ Hz$

$\frac{f_p}{f_m} \cong \frac{1}{10}$ for $E_p = 25000\ N/mm^2$, $E_m = 2960\ N/mm^2$

$\rho_m = 1180\ kg/m^3$ and $\rho_p = 2500\ kg/m^3$

The subscript p and m denotes quantities in prototype and model scale respectively.

A second similarity can be written by considering unit of eigenfrequencies which is 1/time. The similarity for the time is expressed as;

Equation 3.4 $\frac{t_p}{t_m} = \sqrt{\frac{L_p}{L_m}}$

In the same manner, the similarity between eigenfrequencies will be written as;

Equation 3.5 $\frac{f_p}{f_m} = \sqrt{\frac{L_m}{L_p}}$

For 1/20 scaling factor, $\frac{f_p}{f_m} = \frac{1}{4.5}$

To calculate eigenfrequencies, we numerically modeled the Blankenberge pier in prototype dimensions. The lowest frequency corresponding to excitation of the concrete structure equals to 14.1157 Hz. However, this mode mainly excites the upper part of the structure. Vibration may occur in the cantilevering slab, but it is not likely to introduce large amplitudes.

The lowest frequency for vibration of the lower slab equals to 14.9974 Hz. Hence this is the fundamental mode for this slab and the model should correspond to this situation. Figure 3.3 shows the vibration mode for the lowest eigenfrequency (14.9974 Hz) exciting the horizontal part. The figure is created by Samcef code which is a finite element model. Shell elements with bending for slabs and walls and beam elements for piles and columns are considered.

According to the similarities found in Equation 3.3 and Equation 3.5, values of f_p are found as 149.97 and 67.068 Hz, respectively. However, for reaching $f_p = 149.97\ Hz$, the material should have an extremely high stiffness which is not possible with the material available. In addition, if such a high stiffness is supplied then the structure response will be limited compared to the reality. Figure 3.4 shows vibration mode of scaled model for $f_m = 67.068\ Hz$.

3.2.2.2 BUILDING SCALED MODEL

The scaled model is built from a transparent thermoplastic material [poly(methyl methacrylate) (PMMA)]. It is often used as a light or shatter-resistant alternative to glass. It is sometimes called acrylic glass. This material provides a good lightening of the model enabling better recording of the impact mechanism. Figure 3.5 shows the scaled model before and after installation. In addition to the scaled model described above, a simple vertical wall type model is also tested under the identical

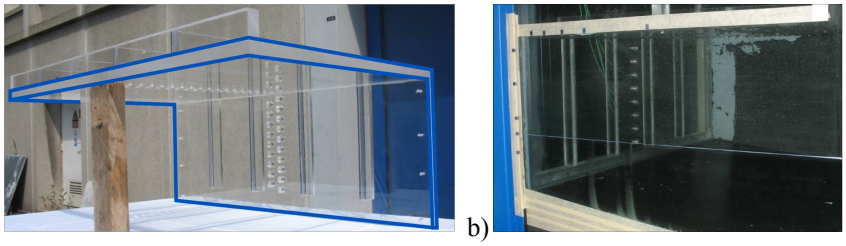

a) b)

Figure 3.5. *a) Scaled model before installation, b) Side view of scaled model in the wave flume*

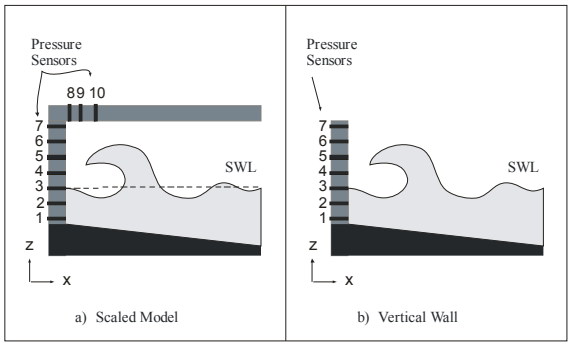

Figure 3.6. *a) scaled model, b) Simple vertical wall type model*

hydrodynamic conditions to identify the existing of the horizontal part on the pressure distribution of the vertical part. The simple vertical wall type model is also built from the same material with same sensor configuration used on the vertical part of the scaled model.

Figure 3.6 shows both the scaled and the simple vertical wall type models in operation. During the measurements, the top section of the vertical wall is extended by a wooden plate to block the overtopping. This way, both the scaled model and the simple vertical wall type model are tested for non-overtopping cases.

3.2.2.3 CONFIGURATION OF PRESSURE SENSOR HOLES

Figure 3.7 shows the configuration of the pressure sensor locations, both on the vertical and horizontal parts of the scaled model. The accuracy of the pressure profiles mainly depends on their spatial resolution, therefore two rows of pressure sensor holes are distributed along the centerline with a uniform interval of 3 cm. Due to the problem of material stability and installation difficulties, it is difficult to drill open holes closer than 3 cm. The second row is therefore shifted 1.5 cm along the centerline to achieve a uniform sensor interval. In addition, the lateral distance between the two centerlines is 3 cm. This configuration gives flexibility to define the sensors interval up to 1.5 cm.

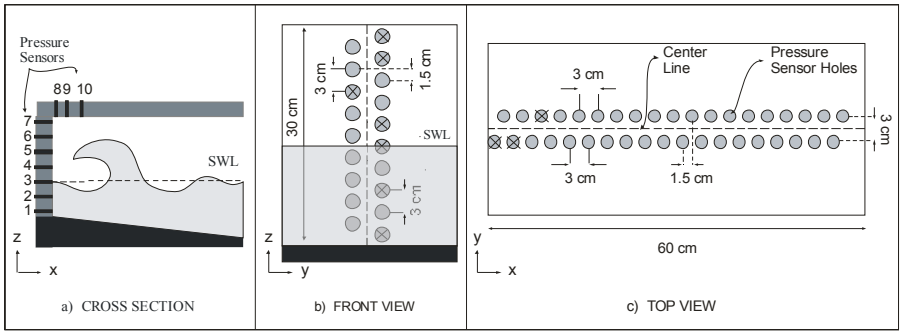

Figure 3.7. *Detail of scaled model and configuration of pressure sensor locations. Crosses show the selected sensor locations at* $h_s = 0.135\ m$

3.2.3 INSTRUMENTATIONS

The physical model is instrumented with 10 sets of pressure sensors and wave gauges and a high speed camera (HSC). Pressure sensors are used to register wave impact pressures and related forces. The high speed camera is used to capture images of the different stages of the wave impact. Wave gauges are installed for active wave absorption, wave reflection and wave height measurements. In the following, details about instrumentations are being discussed.

3.2.3.1 PRESSURE SENSORS

In total 10 Kistler pressure sensors are used to register wave impact pressures as a function of time (see Appendix II). These are quartz pressure sensors developed for measuring dynamic and quasi-static pressures with external amplifiers. The maximum measurement range for this device is up to 250 bar (25 MPa). For this particular research, sensors are calibrated for the range of 0 - 250 kPa with a linearity of ≤ ±0.16 % FSO (Full scale output). The value of 250 is defined based on the pre-measurement tests. A sampling frequency of 20 kHz is used for the pressure recording. The natural frequency of the sensor is 150 kHz. In addition, a small pressure cell diaphragm surface area is necessary since the pressure peaks require a high spectral resolution. The applied sensor has a small front diameter of 5.5 mm. The effective measuring membrane diameter of the sensor is roughly 4.2 mm. Consequently the sensors are very well suited for measuring impact phenomena. The sensors are flushmounted. Mounting adapters are used to fix the sensors on the model. These adapters are avoiding any possible external forces due to the bending of the structure or deformation of the installation holes. Particular attention needs to be taken when pressures are measured. Pressure sensors are very fragile. Figure 3.8 shows serial photos of used pressure sensor with adapter, amplifier, schematic representation of sensor installation and a photo during operation.

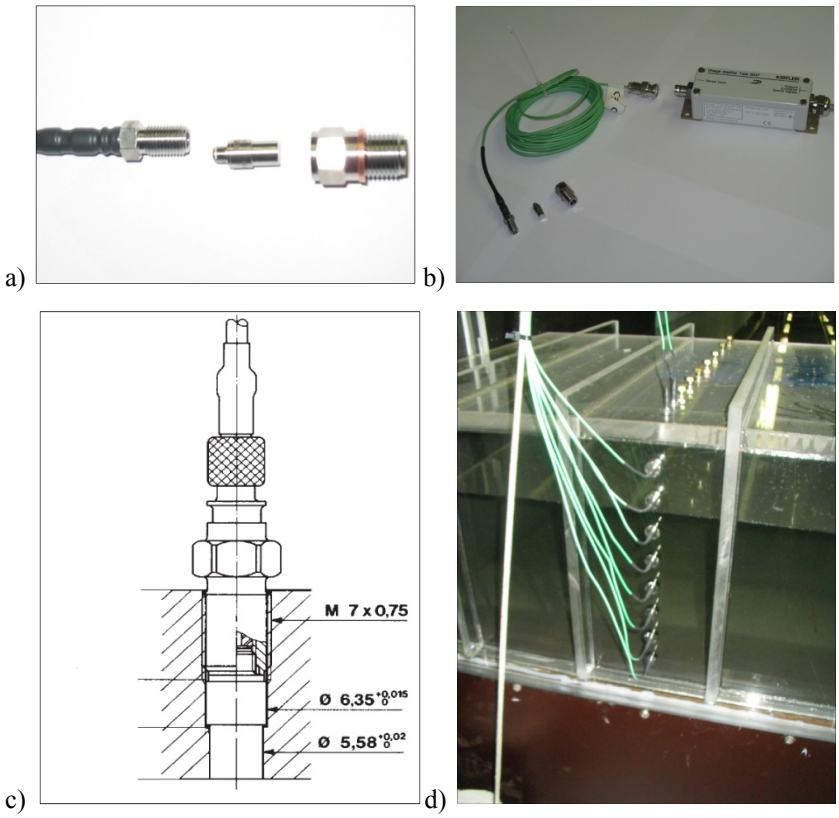

Figure 3.8. *a) Pressure sensor with adapter, b) Pressure sensor and signal conditioner, c) Schematic representation of sensor installation, d) A photo during operation*

3.2.3.1.1 SAMPLING FREQUENCY

The selection of a sufficiently high sampling rate for the measurement of impact pressures is important. The pressure peaks occur in a very small time interval (order of magnitude milliseconds). Therefore, such high sampling frequencies are required. Bullock et al. (2007) found that 10 kHz sampling frequency is adequate and Oumeraci et al. (1994) showed that beyond the 10 kHz sampling frequency 0 % reduction is obtained in the magnitude of peak pressure values.

Figure 3.9 shows the effect of sampling frequencies and down sampling on peak pressures (p_{max}). On this example, the measured signal at sampling frequency of $f_s = 20\ kHz$s is down-sampled and p_{max} values are re-calculated. Results are perfectly matching with Oumeraci's findings. Consequently, the selected 20 kHz sampling frequency is adequate for the measurements.

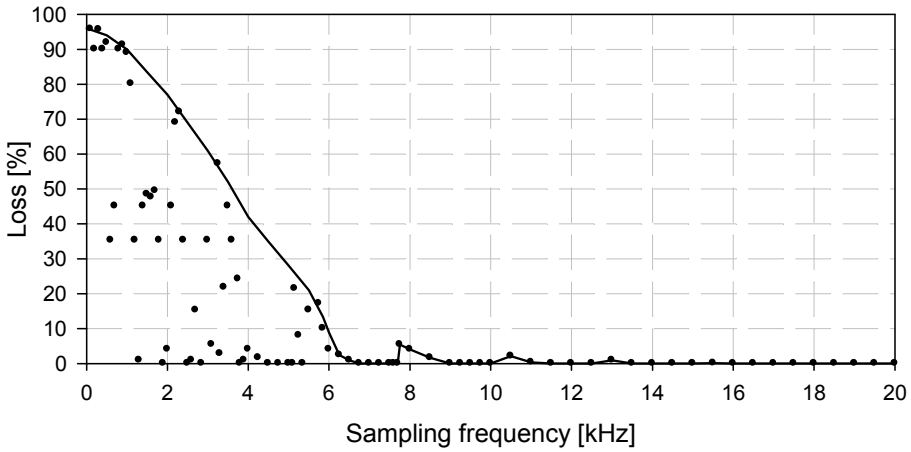

Figure 3.9. *Effect of sampling rate on peak pressures*

a)  b) 

Figure 3.10. *a) High speed camera (HSC), b) HSC during operation*

3.2.3.2 HIGH SPEED CAMERA

The high speed camera (HSC) is used to record the development of waves before breaking on the structure as a function of time (Figure 3.10a). The camera provides information on the breaking mechanism of waves and shape of impact which helps determining the types of breaking. For this purpose, an ultima APX-RS FASTCAM camera is used. It is able to deliver images up to 250 000 frames per second (fps) and has full mega pixel resolution at 3000 fps with a maximum storing capacity of 16 GB (see Appendix III). In this research, it is used at 250 fps, limited by the duration of the record. Because of the high frame rate, the camera shutter time is extremely short. In order to overcome low illumination, special flicker free lights have been used (see Figure 3.10b). During the tests, the background is painted black to have a good contrast on the shape of the recorded free surface. For calibration of measured distances on the HSC recording, a paper ruler is attached on the scaled model to make a known reference.

a) b)

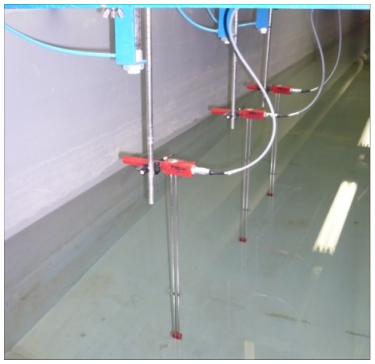

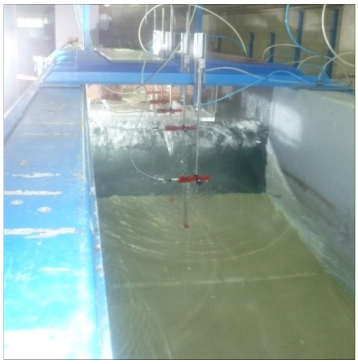

c)

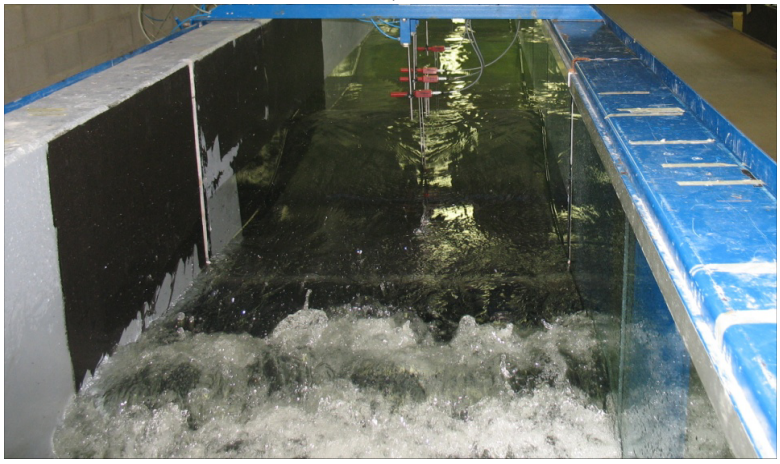

Figure 3.11. *a) Wave gauge, b) An instant during operation time, c) Another instant during operation time*

In addition, HSC recordings are used to visualize the development of wave breaking and identification of the breaking type, the amount of air entrapment, the exact impact location and the approaching velocity of breaking waves.

3.2.3.3 WAVE GAUGES

For the determination of wave heights and wave periods ten resistance type wave gauges are applied (Figure 3.11a). The locations of wave gauges are selected to allow the measuring of the hydrodynamic conditions in front of the wave generator, at and along the foreshore and at the model location. Two wave gauges (AW1 and AW2) in front of the wave paddle are used for the active wave absorption system (AWASYS) (see Figure 3.1). The AWASYS active wave absorption system enables the wavemaker to generate the desired incoming waves and to absorb reflected waves simultaneously. Three wave gauges which are located at the toe of the foreshore (gauge 1, 2 and 3) are used for measurement of incident and reflected

waves. We consider the three probes, two phase angle method of Mansard and Funke (1980) to resolve the 2D spectra into incident and reflected components. Figure 3.11b and c show gauges in operation.

3.2.4 SELECTION OF REPRESENTATIVE SEA STATES AND PLANNING OF TEST MATRIX

Wave characteristics from the actual project location are the basis for the selection of representative sea states for a model test program. Therefore, the test matrix is organized according to the wave properties ($H_s \approx 3.5$m and $T_p = 8.2$s) which create the highest impact (350 kPa) on the Blankenberge pier. The sea bottom slope around the pier is quite mild (1/150).

In Table 3.1, the test parameter matrix is presented. Tests are carried out for 18 regular waves and each test was repeated. In the model tests, the wave period (T), incident wave height (H) and water depth (h_s) at the toe of the scaled model are considered as variable input parameters. The variation of h_s is important, because the pier is located in the intertidal zone in relatively shallow water. Tests are conducted for four different values of h_s and five different values of T. For each combination of h_s and T, the wave height (H) has been increased in successive tests to achieve the range from non-breaking to broken waves. In addition, H and T are determined by the zero down-crossing method for each single wave at various locations, e.g. five wave heights ($5H$) before the structure.

In the tests, water depth h_s increments are considered up to a water level that still allows that most of the approaching wave crest fits into the space below the horizontal part. Results for wave crests first hitting the horizontal part are excluded from the analysis.

Table 3.1. Test parameter matrix for regular waves

Water depth at the structure h_s (m)	Target wave period T (s)	Target wave height H (cm)
0.075	2.2	3.5, 4.0, 4.5, 5.0, 5.5, 6.0, 6.5, 7.0, 7.5, 8.0
0.105	2.2	5.0, 5.5, 6.0, 6.5, 7.0, 7.5, 8.0, 8.5, 9.0, 9.5, 10.0, 10.5, 11.0, 11.5, 12.0, 12.5
0.135	2.0	9.5, 10.0, 10.5, 11.0, 11.5, 12.0, 12.5, 13.0, 13.5
	2.2	6.0, 6.5, 7.0, 7.5, 8.0, 8.5, 9.0, 9.5, 10.0, 10.5, 11.0, 11.5, 12.0, 12.5, 13.0, 13.5, 14.0, 14.5, 15.0, 15.5
	2.4	8.5, 9.0, 9.5, 10.0, 10.5, 11.0, 11.5, 12.0, 12.5, 13.0
	2.6	8.0, 8.5, 9.0, 9.5, 10.0, 10.5, 11.0, 11.5, 12.0, 12.5, 13.0, 13.5, 14.0
	2.8	7.0, 7.5, 8.0, 8.5, 9.0, 9.5, 10.0, 10.5, 11.0, 11.5, 12.0
0.165	2.2	9.0, 9.5, 10.0, 10.5, 11.0, 11.5, 12.0, 12.5, 13.0, 13.5, 14.0, 14.5, 15.0, 15.5, 16.0, 16.5, 17.0, 17.5, 18.0, 18.5

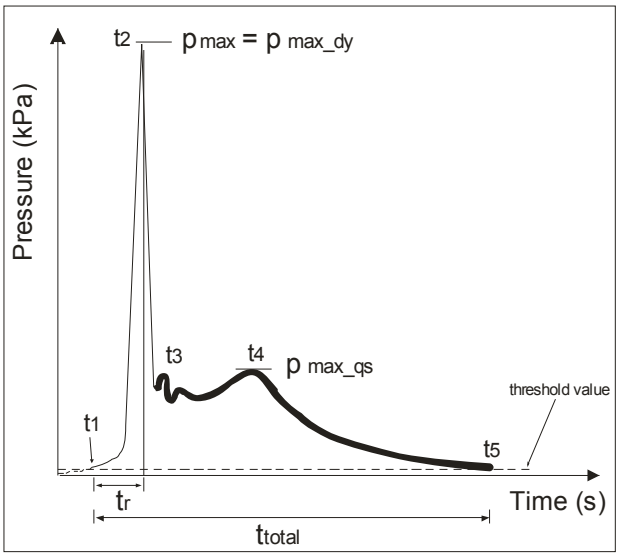

Figure 3.12. *Idealized time-history of an impact pressure associated on the vertical part.*

3.2.5 DATA ACQUISITION AND DATA PROCESSING FOR REGULAR WAVE TESTS

During the tests, various data acquisition and data processing systems are employed. Many of these have been developed in-house. Typical data acquisition rates of 40 Hz are employed for wave recording. Large data acquisition rates of 20 kHz are used for pressure measurements. HSC recordings have been done at 250 fps. The pressure signals are filtered during acquisition using low/high pass analog filters to filter out noise or to narrow the frequency range used in the analysis. Also, digital filters are employed during the analysis of pressure signals. For the synchronization of all instruments, a wave gauge mounted at the toe of the foreshore (gauge 3 in Figure 3.1b) serves as a trigger for the data acquisition system. When the initial wave heights exceed a threshold value at the location of gauge 3, the recordings of the pressure sensors, wave gauges and camera signal start automatically.

3.2.5.1 PRESSURE MEASUREMENTS

Breaking waves cause high impact pressures on the scaled model. Impact pressures are generally very high but last only a fraction of a second. The shape of the pressure signal at the wall per impact is defined with a nick name called “church roof”. Figure 3.12 shows a definition sketch, which is similar to Bullock et al. (2007), to determine the rising time (t_r) maximum dynamic and quasi-static pressures (p_{max_dy} and p_{max_qs}). In general, the maximum pressure (p_{max}) of the

breaking wave is equal to p_{max_dy}, whereas t_r is the time duration between points t_1 and t_2 which respectively show the instant of impact start and of maximum dynamic pressure. The t_1 is defined as the initial point where the wave-induced pressure raises above the noise level. Time from t_1 to t_3 shows the duration of dynamic pressure, while the time from t_3 to t_5 shows the duration of quasi-static pressure.

For defining t_1 in Figure 3.12, the threshold value for the noise level is always chosen as 1% of p_{max_dy}. The value of p_{max_qs} is measured after the dynamic portion is eliminated by a low pass filter (cutoff frequency 15 Hz). Data editing is carefully considered for the extreme values in the data clouds. In this study, p_{max_dy} and p_{max_qs} and t_r values are determined per impact.

3.2.5.1.1 DISTRIBUTION OF SENSORS IN THE DRILLED HOLES

It is important to measure wave impact pressures simultaneously on both the vertical and horizontal part of the scaled model. In this view, distributions of sensor locations are becoming quite important since only 10 pressure sensors are available. Due to the limited number of pressure sensors, one test is repeated several times while changing the sensor location to complete the high resolution pressure profile. From the measured complete pressure profile, critical sensor positions are selected. Figure 3.13a and b show an example case of a complete pressure profiles at $h_s = 0.135\,m$. From the results of these measurements, seven positions on the vertical part and three positions on the horizontal part are selected as the representative sensor positions for further tests. The resulting selected positions are indicated using red peak pressure symbols. Figure 3.13c shows overlapped sensor locations during the repeated tests by different colored symbols. The above procedure is repeated for the other water depths to define the critical sensor locations.

3.2.5.2 FORCE MEASUREMENTS

For applications described in this study, it is straightforward to measure pressures by using pressure sensors installed within the structure. However, force measurements are usually conducted by strain gauges or by averaging pressure sensor readings across the given area. For the first method it is often necessary to use suspended/independently anchored sensors or sensor arrays to produce reliable force estimates. The quality of the uplift force measurements however can be diminished due to the suspended model set-up. Additionally, force sensors are usually able to resolve only global or quasi-static forces. Peak loads arising from wave impacts are not measured with this system, as the force frame cannot respond quickly enough to peaks of very short durations.

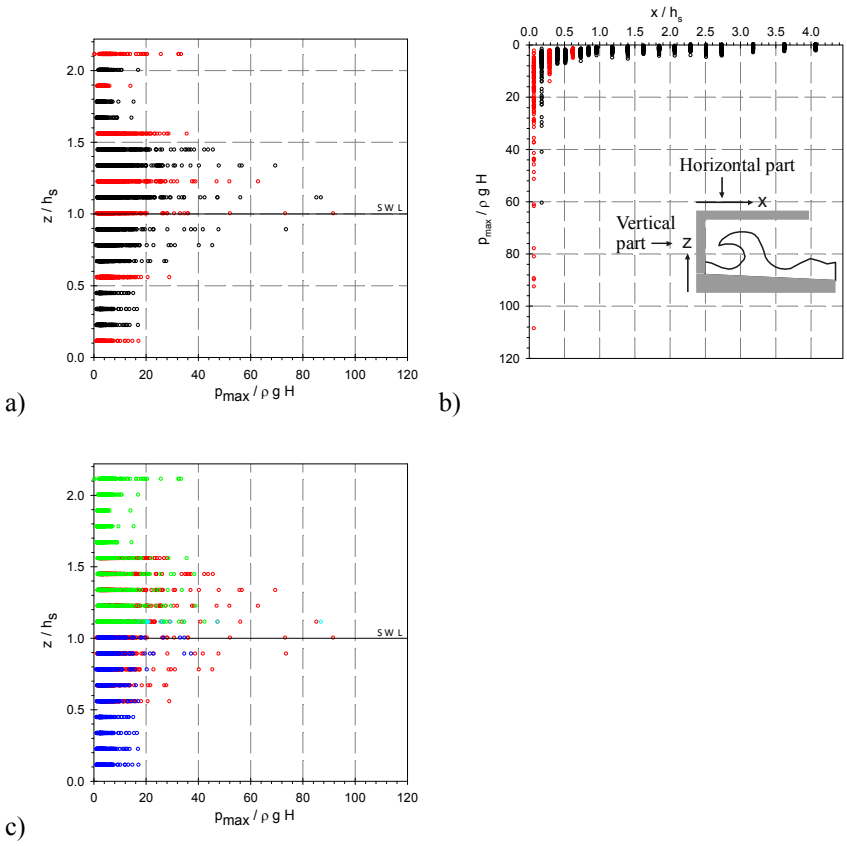

Figure 3.13. *a) Spatial distribution of maximum peak pressures (p_{max}) on the vertical part, b) Spatial distribution of p_max beneath the horizontal part and c) shows the regions of overlapped sensor locations, ($h_s = 0.135\ m$)*

Information on wave impact forces can generally be obtained only by detailed pressure measurements (second method). A disadvantage of this method is that pressures are measured only locally and then multiplied over the whole representative area to provide a force estimate. Therefore, increasing the number of sensors will improve the quality of the force results. Of course the budgets of the project and installation difficulties restrict the second method.

Figure 3.14 shows the comparison of measured horizontal forces with different sensor resolutions on the simple vertical wall type model. Measurements are done with 10 sensors installed on the simple vertical wall at $h_s = 0.135\ m$ and $T = 2.2\ s$. Then, horizontal forces with 10 sensors resolutions F_{10} are calculated by integration of all 10 sensors results. Later, horizontal forces with 7 sensors resolutions F_7 are calculated by omitting 3 sensors results from the same

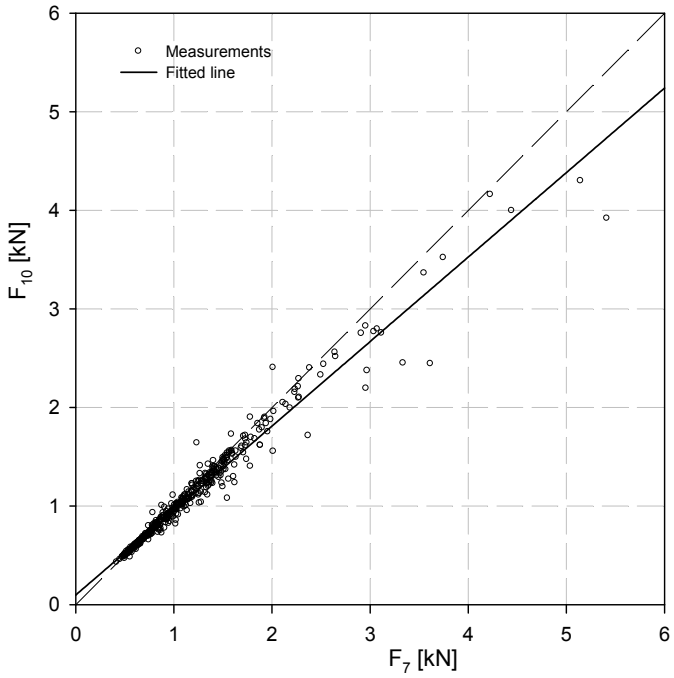

Figure 3.14. *Comparison of horizontal forces with 10 and 7 (F_{10} & F_7)sensors resolutions ($h_s = 0.135\ m$ and $T = 2.2\ s$)*

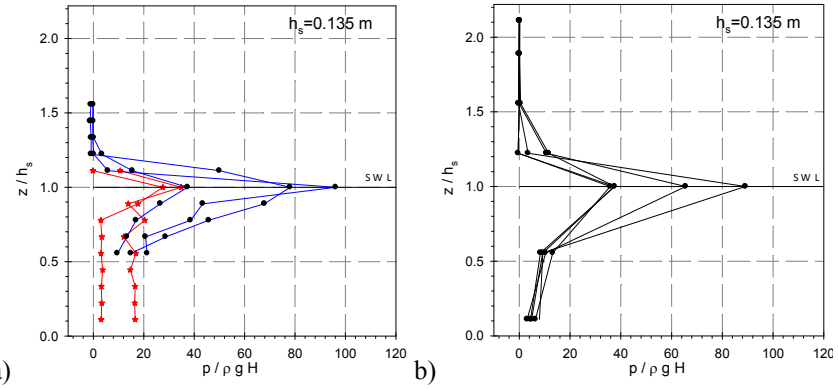

a) b)

Figure 3.15. *a) Instantaneous pressure profiles from full sensor resolution, b) Instantaneous pressure profiles from 7 sensors resolution*

measurements. The location of 7 sensors are the same locations defined for the vertical part of the scaled model at $h_s = 0.135\ m$. The extra three new sensors are located at $z = 0.045, 0.105$ and $0.225\ m$ to improve the vertical pressure profiles.

Especially for the large forces, the horizontal forces measured with 10 sensors F_{10} are lower than the horizontal forces measured with 7 sensors F_7.

Although the pressure averaging method looks better, the effect of sensor resolution on the measured force needs to be known. Figure 3.15 shows comparison of pressure profiles between full resolution (10 sensors) and resolution with 7 sensors. As it is explained before, 7 sensor positions are defined for the measurements on the vertical part. Figure 3.15a shows several pressure profiles with 10 sensors on the vertical part with two different orientations. In the first case, all 10 sensor filled holes starting from the bottom and instantaneous pressure profiles are taken at the instant of p_{max} around SWL. According to our experience, time of p_{max} and F_{h_max} are generally coinciding for the vertical walls. Even though it is not the best way to take instantaneous pressure at the time of p_{max}, it will give an idea about pressure distribution in the lower part. In the second case, all 10 sensors are distributed in the holes around SWL. Then, the results of these two dense pressure sensors are compared with the results of the case in which 7 pressure sensors are used (see Figure 3.15). The figures illustrate that the pressure profiles are quite similar even though small variations are present. Therefore, it is decided to use the pressure integration method to calculate the total force signals.

The total horizontal and vertical forces on the scaled model are calculated by integrating the pressure results (Equation 3.6 and Equation 3.7 respectively). Forces are calculated on a unit width of 1 m.

Equation 3.6 $$F_h(t) = 0.5 \sum_{k=1}^{n-1} [p_k(t) + p_{k+1}(t)] * \Delta z_k$$

Equation 3.7 $$F_v(t) = 0.5 \sum_{j=1}^{m-1} [p_j(t) + p_{j+1}(t)] * \Delta x_j$$

where $p_k(t)$ and $p_j(t)$ are the measured instantaneous pressures at the locations of the k-th and j-th sensors, Δz_k and Δx_j are the vertical distances between two sensors and n and m are the number of sensors on the vertical ($n = 7$) and horizontal part ($m = 3$), respectively. As it is described for pressure analysis, F_{max_dy} and F_{max_qs} and related t_r values are determined per impact.

3.2.5.3 WAVE HEIGHT MEASUREMENTS

When waves approach the scaled model on the foreshore, they are often subject to changes caused by the shallow water situation. Wave shoaling and wave breaking are two phenomena which can't be regarded. In the wave flume, wave gauges (see section 3.2.3.3) are used to measure the variation in the wave height, caused by a specific foreshore and scaled model. After each test an AWASYS-system (active wave absorption) is used to absorb the reflected waves by controlling the wave paddle. Before starting the next test, sufficient time is left to have a perfect smooth water surface. Besides active the use of a wave absorption system, wave numbers (18 waves) are kept limited not to have reflected waves from the paddle.

3.2.5.3.1 VERIFICATION OF INCIDENT WAVES

Most of the approaching waves to the scaled model are breaking or reflecting from it. Due to the turbulence left from breaking and reflected waves, it is hard to properly measure the incident waves. Therefore, tests are repeated under the identical hydrodynamic conditions for the case without scaled model. Figure 3.16 shows the model set-up for the case without the scaled model. By the results from this set-up, the incident wave results measured at the toe of the foreshore are validated. New gauge locations are selected at reference points for verification.

For the measurements without scaled model, besides the active wave absorption already performed by the wave paddle, a passive wave absorber is also placed at the end of the 2D wave channel. The gentle beach slope of 1/50 is built from the combination of crushed stone and shingle to minimize the reflection from the passive absorption beach.

3.2.5.3.2 REFLECTION DUE TO THE FORESHORE

Before starting the measurements with the scaled model, a preliminary test is also carried out to check the efficiency of the foreshore in terms of reflection. Reflected waves are unavoidable in wave models even in the case without the scaled model shown in Section 3.2.5.3.1. Here, the foreshore is built with a minimum of harmful reflection, but in any case it is necessary to document them.

Figure 3.17 shows reflection coefficients on the measured wave height values where the scaled model is not installed. Their values read less than 6% which is well within an acceptable range. This means that the built foreshore has a minimum wave reflection.

3.2.5.3.3 OCCURRENCE OF CROSS-WAVES

As mentioned before, the number of waves in one test is limited to 18 since lateral movement commences after about 20 to 25 waves. Reflection from the wall and the chaotic nature of wave breaking are the main sources of these lateral cross-waves. Therefore the wave number is limited to 18. Exceptionally, some cross-waves

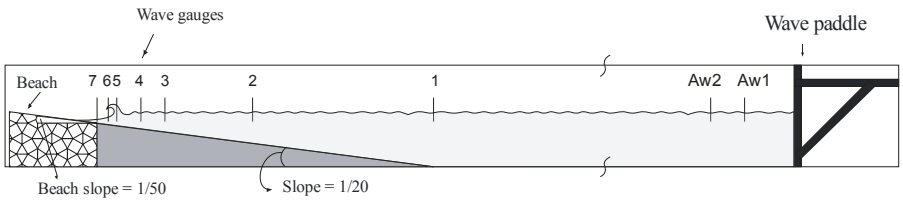

Figure 3.16. *Small-scale model set up and wave gauge orientation for the case without model*

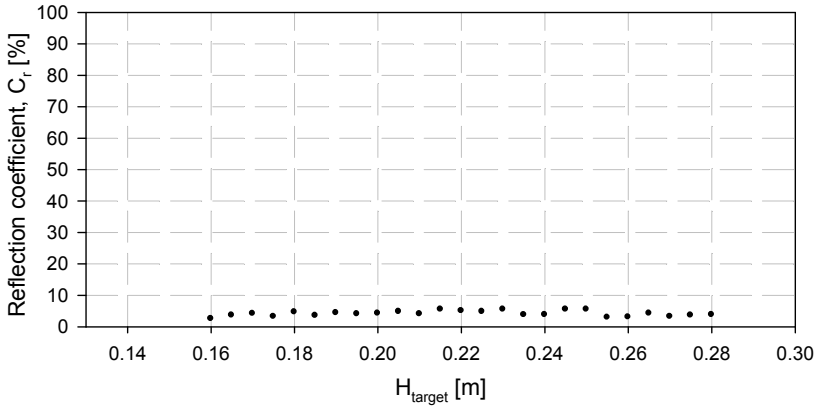

Figure 3.17. *Measured reflection coefficient at the toe of foreshore (T=2.2 s)*

may exist in the range of 18 waves and their results are eliminated during the analysis. It is also observed that narrowing the flume channel helps to avoid these cross-waves. In this way the two-dimensionality of the flume increases which eliminates or postpones the cross-waves. In addition, sufficient time is left between each repeating test to avoid possible unwanted long waves.

3.2.6 REGULAR WAVE TEST RESULTS

Figure 3.18 shows a comparison of wave heights measured for the cases with and without the scaled model. Both measurements are recorded at the locations of gauge 3 and 7 (see Figure 3.1). Results of the experiments without the scaled model, show only incident wave heights. However, results where the scaled model is present show the total wave heights. In the latter case, incident waves reflect from the model. Due to the distance between the location of the gauge and the scaled-model, a phase difference occurs between incident and reflected waves. This phase difference decreases when the gauges are closer to the model. The results without the scaled model case can also be used for verification of incident waves calculated from Wavelab. The considered band width for the calculation of the reflection coefficient in Wavelab is shown in Figure 3.18. This one single calculated reflection coefficient is used as the representative reflection coefficient for all 18 waves.

Figure 3.19 shows results obtained at gauge 3 with and without scaled model. Here reflection coefficients at the toe of the foreshore are determined by considering a part of the wave train that contains reflected waves. In addition, H and T are determined by the zero down-crossing method for each single wave gauge. Figure 3.19b shows wave train numbered from 1 to 18 in a single run. The first and last two wave results are removed from the analysis to have a uniform data set. So each test run shows the results of 14 uniformly developed waves. Figure 3.19c shows the selected waves with uniform wave height distributions.

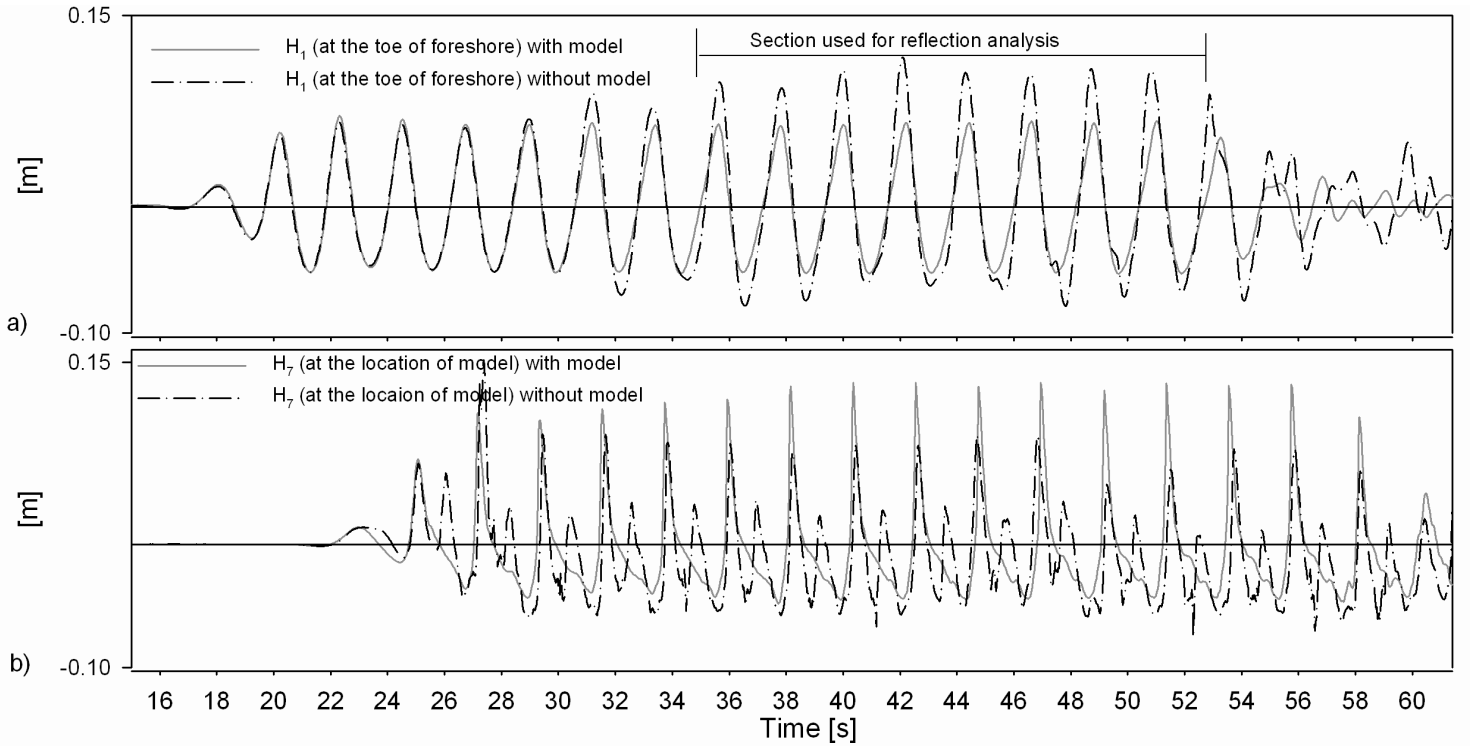

Figure 3.18. *a) Time-history of wave height (H_1) measured at the toe of the foreshore with and without model cases (at gauge 3), b) Time-history of wave height (H_7) measured at the location of the model with and without model cases (at gauge 7,) ($H_{target} = 0.115\ m$ and $h_s = 0.135\ m$)*

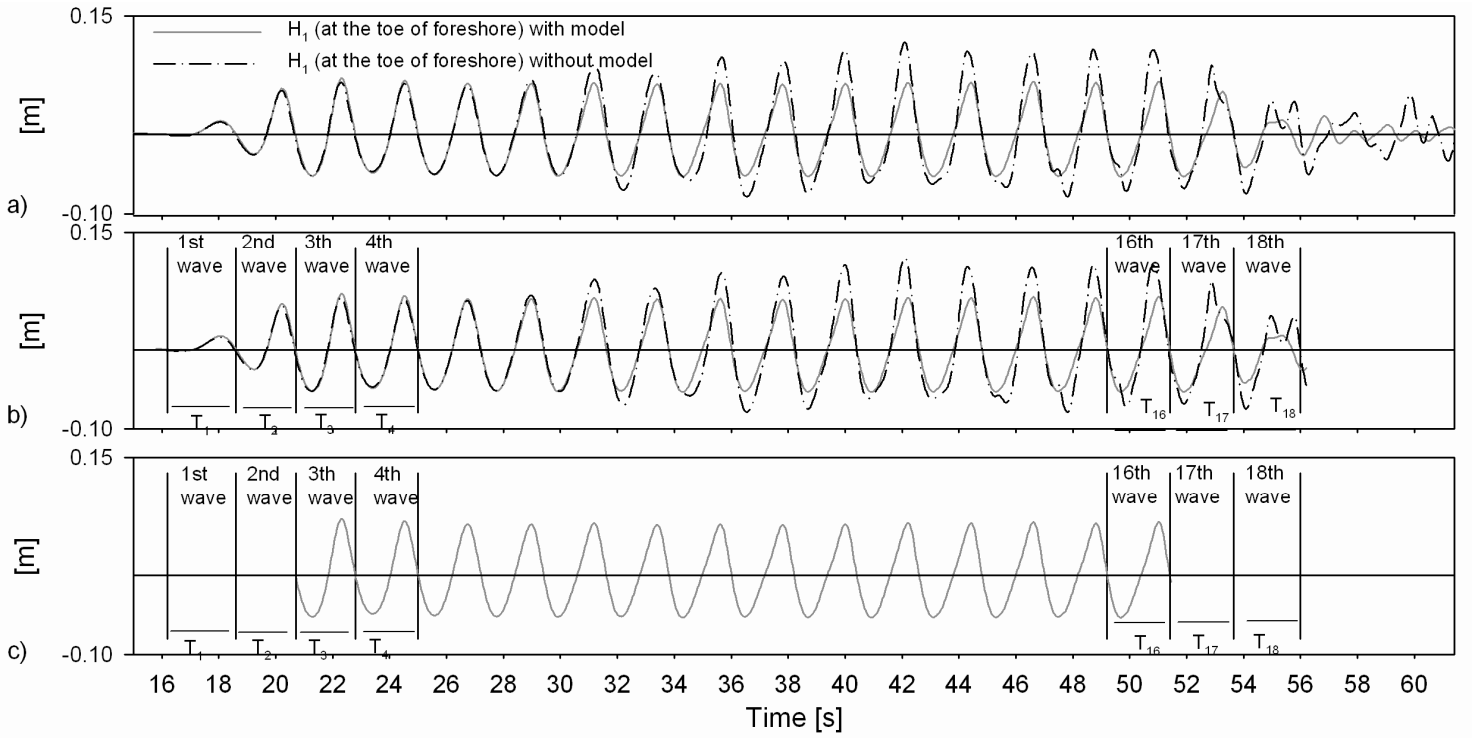

Figure 3.19. *a) Time-history of wave heights (H_1) measured at the toe of the foreshore with and without model cases (at gauge 3), b) Numbering wave train from 1 to 18, c) Reduced wave number to have a uniform wave height distribution in one run ($H_{target} = 0.115\ m$ and $h_s = 0.135\ m$)*

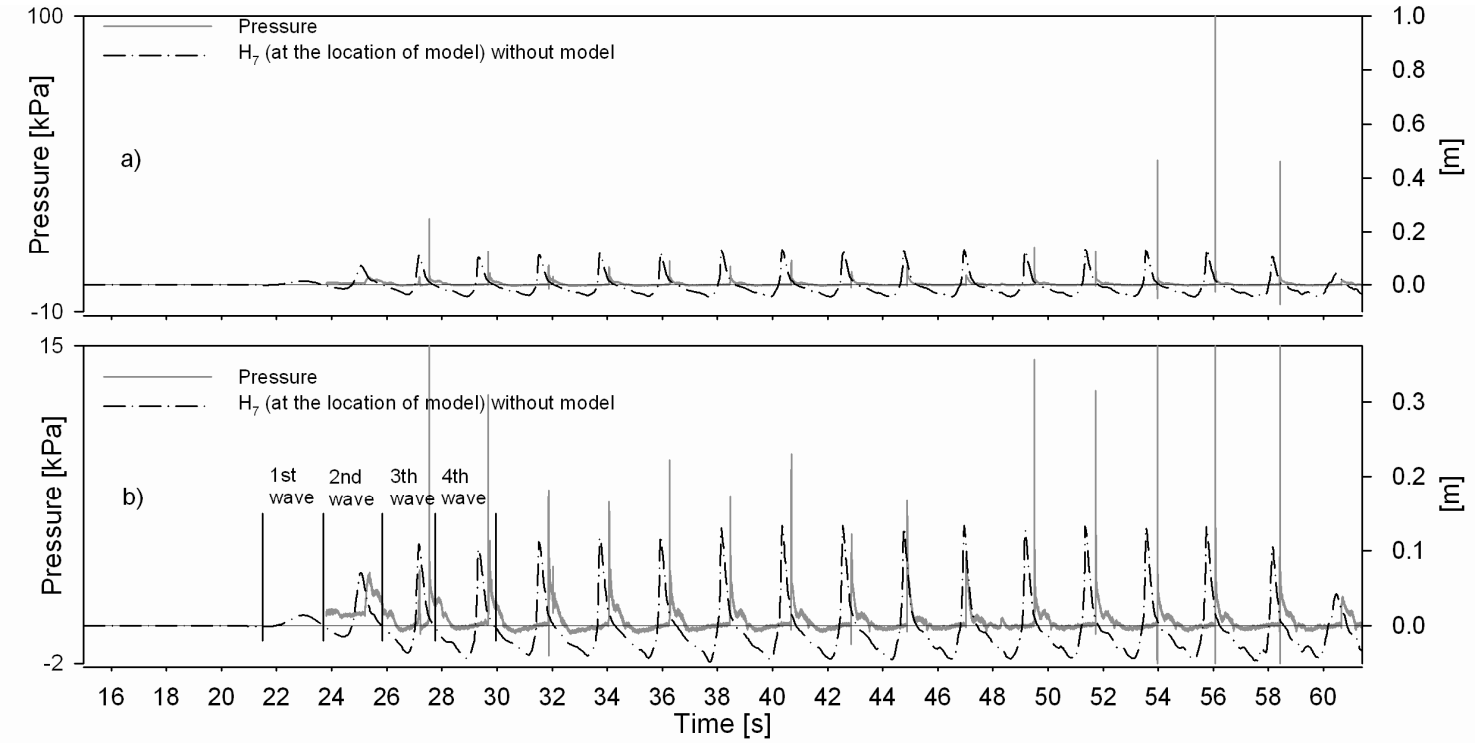

Figure 3.20. *Time-history of wave heights at gauge 7 and related impact pressures on the scaled model, b) a close look to a ($H_{target} = 0.115\,m$ and $h_s = 0.135\,m$)*

Figure 3.20 shows the comparison of the wave height measured at gauge 7 and the corresponding impact pressure on the scaled model (at SWL). Variations in impact pressure magnitude are more significant than the variation in wave height. The duration of the wave crest per impact is close to the duration of the total impact pressure (t_{total}).

From the results of regular waves the largest peak pressures are recorded at the SWL ($82 * \rho g h_s$) on the vertical part and at the fixed corner of the cantilever slab ($90 * \rho g h_s$).

3.3 TESTS WITH IRREGULAR WAVES

In fact, regular waves never occur in nature, although swell can come close. For an approximation of the phenomena of wave propagation, regular waves are used to solve the wave equations, and irregular wave models are based on these regular wave models. For irregular wave tests, a similar setup as used for the regular wave tests is considered. Each test is run for 500 irregular waves to a JONSWAP spectrum with γ=3.3. The JONSWAP spectrum is chosen since it is the most commonly employed wave spectra for confined young seas.

The difficulty with the irregular wave tests is that the duration of the irregular wave tests is too long. During such a long time, high reflection due to the vertical face of the model might provoke lateral movements in the flume. To avoid these lateral movements, the flume width is reduced to 35 cm using a vertical guide wall along the flume (12.5 m) (see Figure 3.21a). The open-end section of the flume ends with an absorption beach that has a slope of 1/50. The width of the scaled model is also reduced to 35 cm. All the other set-up and instrumentation are kept the same as in the regular wave tests.

Careful design of guide walls and passive absorbers are important for the minimization of wave reflection and lateral movements. Guide walls must be placed in such a way that a minimal amount of energy is diffracted outside the area of interest, but without impacting on the wave field in the area of interest. In addition, passive absorbers are designed to effectively reduce the wave energy at the open end of the flume. Zero reflection is assumed from the absorption beach and the undisturbed wave characteristics are measured simultaneously at the open end side.

Figure 3.22a shows the open end section of the flume where undisturbed incident wave heights are measured while Figure 3.22b illustrates the wave impact simultaneously at the closed end of the flume. The guide wall located along the flume is shown in Figure 3.22c.

3.3.1 DATA ACQUISITION FOR IRREGULAR WAVES

As mentioned before, the number of waves in one test is limited to 500 irregular waves. In the field of wave forces on the vertical structures, the Goda's works are considered as an important reference by many researchers to compare their results.

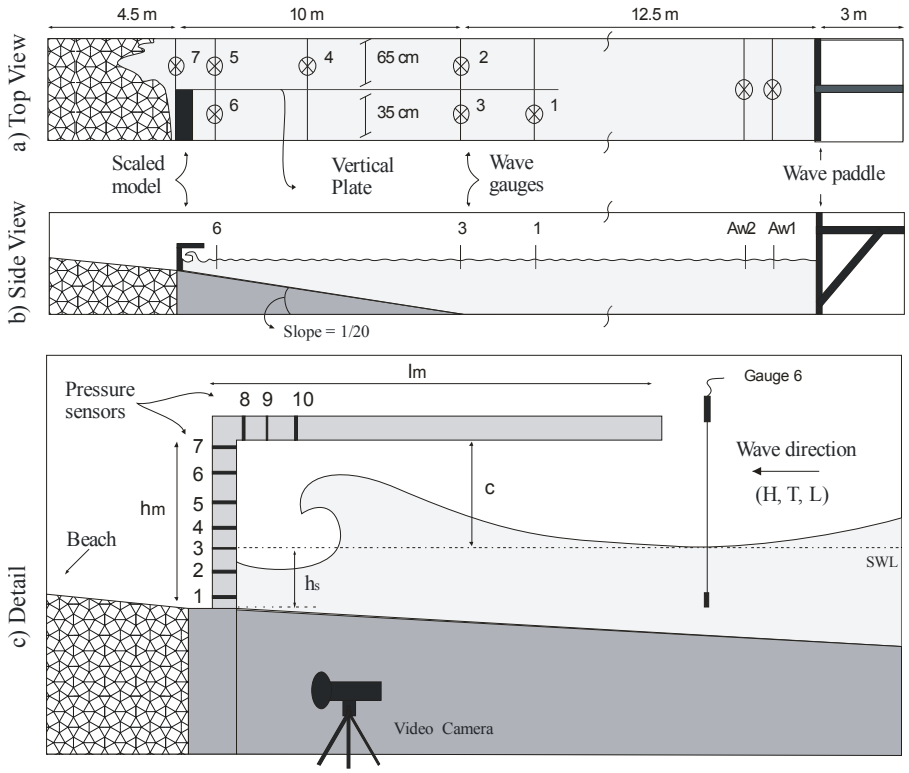

Figure 3.21. *Small-scale model set up for irregular waves. a) is the top view, b) is the side view and c) is detailed view of model*

He represented the average of the highest 1/250 waves based on a standard sample size of 500 waves which is also considered in this research for consistency. In each wave train, several wave results from the beginning and the end are removed to eliminate initiating and ending effects of the wave paddle. Each test is repeated under the same hydrodynamic conditions. Like the regular wave results, these repeated pressure sensor results show a high scatter. The test matrix of 35 different conditions (in terms of water depth, incident significant wave height and peak periods) is summarized in Table 3.2 for a total of 80 tests.

Incident significant wave heights (spectral) H_{m0} are derived from the measurements at wave gauge numbers 2, 4, 5 and 7 by assuming zero reflection from the absorption beach. H_{m0} is the significant wave height being estimated from the spectral information and T_p is the wave period corresponding to the frequency at the spectral peak.

a) b)

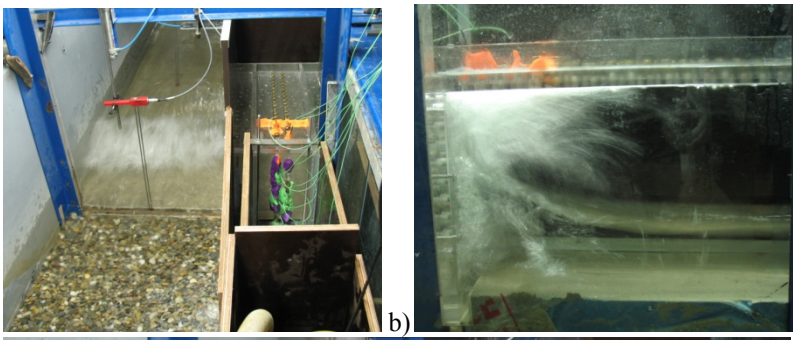

c)

Figure 3.22. *Top view of open end section, b) Side view closed end with scaled model c) Shows the guide wall along the flume*

The following extra information has been extracted from each test of 500 waves.

Horizontal force and maximum pressure at SWL: $F_{h\,(1/250)}$ and $p_{h\,(1/250)}$.

Vertical force and maximum pressure at the attached corner on the horizontal part: $F_{v\,(1/250)}$ and $p_{v\,(1/250)}$.

Here, where the subscript (1/250) indicates that the corresponding parameter has been evaluated as the average of the highest two events in a (nominally) 500-wave tests.

Table 3.2. Test parameter matrix for irregular waves

Water depth at the structure h_s (m)	Wave period T (s)	Wave height H_{m0} (m)
0.075	2.2	0.051, 0.057, 0.064
0.105	2.2	0.074, 0.082, 0.092
0.135	2.0	0.111, 0.116
	2.2	0.06, 0.065, 0.07, 0.072, 0.074, 0.083, 0.086, 0.09, 0.097, 0.105, 0.106, 0.113, 0.115, 0.116, 0.125, 0.128, 0.134, 0.135
	2.4	0.103, 0.107
	2.6	0.096, 0.099
	2.8	0.083, 0.084
0.165	2.2	0.115, 0.131, 0.144

3.4 CONCLUSIONS

The experimental set-up to investigate the loading conditions due to violent wave impacts on coastal structures with cantilever surfaces is discussed. The scaled model and used instrumentations are introduced. Data acquisition and data processing for both regular and irregular waves are explained. The test matrix for different conditions (in terms of water depth, incident significant wave height and peak periods) is summarized.

REFERENCES

Bullock, G.N.; Obhrai, C.; Peregrine, D.H.; Bredmose, H., 2007, "*Violent breaking wave impacts, Part 1: Results from large-scale regular wave tests on vertical and sloping walls*" Coastal Engineering, v 54, n 8, p 602-617

Mansard, EP, Sand, SE and Funke, ER., "*Reflection Analysis if Non-linear Regular Waves*", Hydraulics Lab Tech Rep TR-HY-01, Nat Res Council of Canada, Ottawa, 1985

Oumeraci, H.; Klammer, P.; and Kortenhaus, A., 1994, "*Impact loading and dynamic response of vertical breakwaters – Review of experimental results*", Proceedings of International workshop on Wave barriers in deepwaters, Japan, pp. 347-361.

Vandepitte, D., *Berekening van constructies – Bouwkunde en civiele techniek,* Wetenschappelijke uitgeverij E. Story-Scientia P.V.B.A., Gent, Antwerpen, Brussel, Leuven, 1979-1982.

Verhaeghe, H.; Cherlet, J.; Boone, C.; Troch, P.; De Rouck, J.; Awouters, M.; Ockier, M.; Devos, G., 2006, "*Prototype monitoring of wave loads on concrete structure in intertidal zone*", COASTLAB06. pp. 117-125

4

HYDRODYNAMIC CONDITIONS

***

4.1. INTRODUCTION

The main aspects of hydraulic performance of load tests on a vertical structure are wave shoaling, wave reflection, wave breaking and overtopping. This chapter gives a summary of methods to predict wave shoaling and breaking in a wave flume with uniform bed slope and wave reflection from vertical structures with overhanging cantilevering surfaces. The measured results are compared with literature values. The discussions here are primarily based on 2-D hydraulic model tests of regular and irregular waves as discussed in Chapter 3.

Waves are produced in a 2-D wave flume. A scaled model is installed at the top of a uniform foreshore with a slope of 1/20. Wave gauges are used to monitor the wave information along the flume and at the scaled model location. Figure 3.1 shows the test set-up with the scaled model.

The methods for the calculation of wave impacts on the scaled model, discussed in this research, are based on the incident waves at the location of the scaled model i.e. wave conditions as they will appear if the model is not there. Therefore, the tests conducted with the scaled model are repeated without the model present under similar hydraulic conditions to have the undisturbed wave conditions. After the location of the model, a passive absorption is installed using gravel beaches. The gravel beach slope is 1/50. The reflection from the foreshore and the gravel beach is less than 10% which is acceptable. The test set-up for the case without the scaled model is shown in Figure 3.15.

Reflection analysis has been performed for the tests with the scaled model using wave records of the first 3 wave gauges (gauge 1, 2 and 3) which were located about 10 m in front of the scaled model (see Fig. 3.1). The standard 3-gauge-procedure of Mansard & Funke, (1980) is used for the analysis of regular and irregular wave tests in the frequency domain. The partial standing wave field in front of the model has to be analyzed to determine: (i) the incident wave parameters as input parameters for the wave load of the structure and (ii) the wave reflection and thus the wave energy dissipation at the structure.

However, analyses for shoaling and wave breaking are conducted with the test results without scaled-model. As the wave propagates from offshore into shallow water, a number of different wave transformations will take place. When the water depth to wave length ratio becomes small, the sea bed influences the waves. Thus, the waves start to shoal, reducing the wave length, but increasing the wave height. Where water depths become even shallower, continuing shoaling of the waves, will lead some waves to approach the limiting value of steepness. Thereafter, any further increase will lead to wave breaking.

4.2. WAVE SHOALING

Most experimental studies on wave breaking have been on bed slopes shallower than 1:30, typically 1:50 or 1:100. On these slopes, wave shoaling is relatively mild,

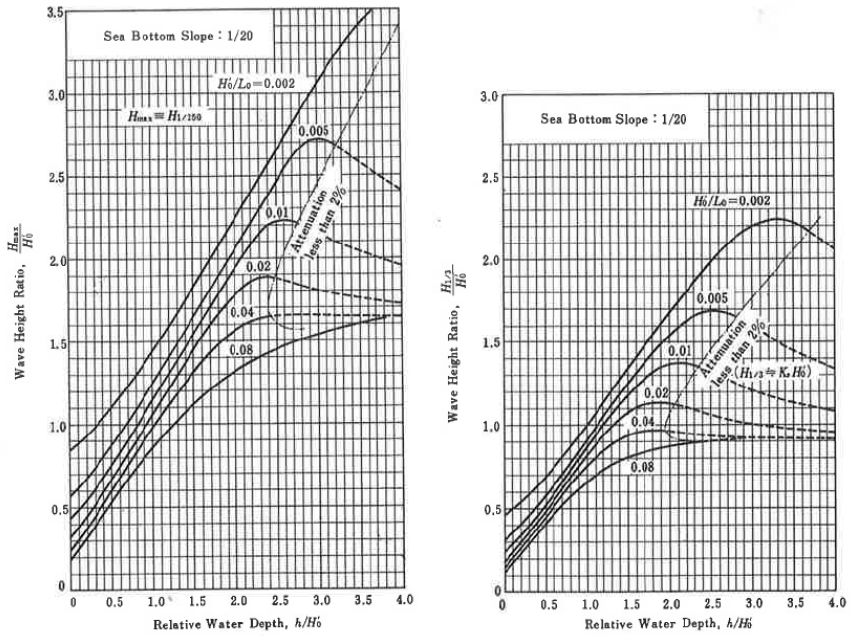

Figure 4.1 *Diagrams for the estimation of wave heights in the surf zone for sea bottom slope 1/20 (after Goda, 2000)*

and wave breaking reasonably well understood. However, there is evidence that steep bed slopes transform waves differently and give more severe hydraulic and structural responses. In the following, wave heights on a bed slope of 1/20 measured along the channel are compared with Goda's (2010) theoretical approach.

In Goda's approach, $H_{1/3}$ and H_{max} values are the significant and maximum wave heights, respectively. The following expressions show how to calculate $H_{1/3}$ and H_{max} and they are valid for $H_0'/L_0 \leq 0.04$. If $H_0'/L_0 > 0.04$, then Figure 4.1 (Goda 2010) must be used.

Equation 4.1 $$If\ h/L_0 \geq 0.2 \rightarrow H_{1/3} = K_s H_0'$$

Equation 4.2 $$If\ h/L_0 < 0.2 \rightarrow H_{1/3} = min\{(\beta_0 H_0' + \beta_1 h), \beta_{max} H_0', K_s H_0'\}$$

where, $$\beta_0 = 0.028(H_0'/L_0)^{-0.38} exp[20tan^{1.5}\theta]$$
$$\beta_1 = 0.52exp[4.2tan\theta]$$
$$\beta_{max} = max\{0.92, 0.32(H_0'/L_0)^{-0.29} \times exp[2.4tan\theta]\}$$

Equation 4.3 $$If\ h/L_0 \geq 0.2,\ H_{max} = H_{1/250} = 1.8 K_s H_0'$$

Equation 4.4 $If\ h/L_0 < 0.2\,, H_{max} = min\{(\beta_0^* H_0^{'} + \beta_1^* h), \beta_{max}^* H_0^{'}\,, 1.8 K_s H_0^{'}\}$

where, $\beta_0^* = 0.052(H_0'/L_0)^{-0.38} exp[20tan^{1.5}\theta]$

$\beta_1^* = 0.63exp[3.8tan\theta]$

$\beta_{max}^* = max\{1.65, 0.53(H_0'/L_0)^{-0.29} \times exp[2.4tan\theta]\}$

In the above equations, h is the water depth, H_0' is the equivalent offshore wave height, L_0 is the offshore wave length related to the $T_{1/3}$, $tan\theta$ is the foreshore slope and K_s denotes the shoaling coefficient. K_s can be calculated either from the below mathematical expressions or from graphs (Figure 3.26) in Goda (2010).

Equation 4.5 $If h_{30} \le h \quad \rightarrow K_s = K_{si}$,

(K_{si} is the linear shoaling coefficient)

$K_{si} = 1 / \sqrt{[(1 + (2kh)/sinh\,(2kh))tanh\,(kh)\,]}$

$L = \left(g\left(T_{1/3}\right)^2/2\pi\right)[\tanh(2\pi h/L)], \qquad k = 2\pi/L$

Equation 4.6 $If h_{50} \le h < h_{30} \qquad K_s = (K_{si})_{30}\left(\frac{h_{30}}{h}\right)^{\frac{2}{7}}$

$\left(\frac{h_{30}}{L_0}\right)^2 = \frac{2\pi}{30}\frac{H_0'}{L_0}(K_{si})_{30}$

$(K_{si})_{30} = 1 / \sqrt{[(1 + (2kh)/sinh\,(2kh))tanh\,(kh)\,]}$

$k = (k)_{30} = {}^{2\pi}/_{(L)_{30}}, \qquad (L)_{30} = \left(gT_{1/3}^2/2\pi\right)[\tanh(2\pi h_{30}/(L)_{30})]$

$\left(\frac{h_{50}}{L_0}\right)^2 = \frac{2\pi}{50}\frac{H_0'}{L_0}(K_s)_{50}$

h_{30} and h_{50} are the water depth satisfying Equation 4.6 and Equation 4.7 respectively.

Equation 4.7 $If h < h_{50} \qquad K_s\left(\sqrt{K_s} - B\right) - C = 0$

$B = \frac{2\sqrt{3}}{\sqrt{2\pi H_0'/L_0}}\frac{h}{L_0}, \quad C = \frac{C_{50}}{\sqrt{2\pi H_0'/L_0}}\left(\frac{L_0}{h}\right)^{\frac{3}{2}}$

$C_{50} = (K_s)_{50}\left(\frac{h_{50}}{L_0}\right)^{\frac{3}{2}}\left[\sqrt{2\pi\, H_0'/L_0 (K_s)_{50}} - 2\sqrt{3}\frac{h_{50}}{L_0}\right]$

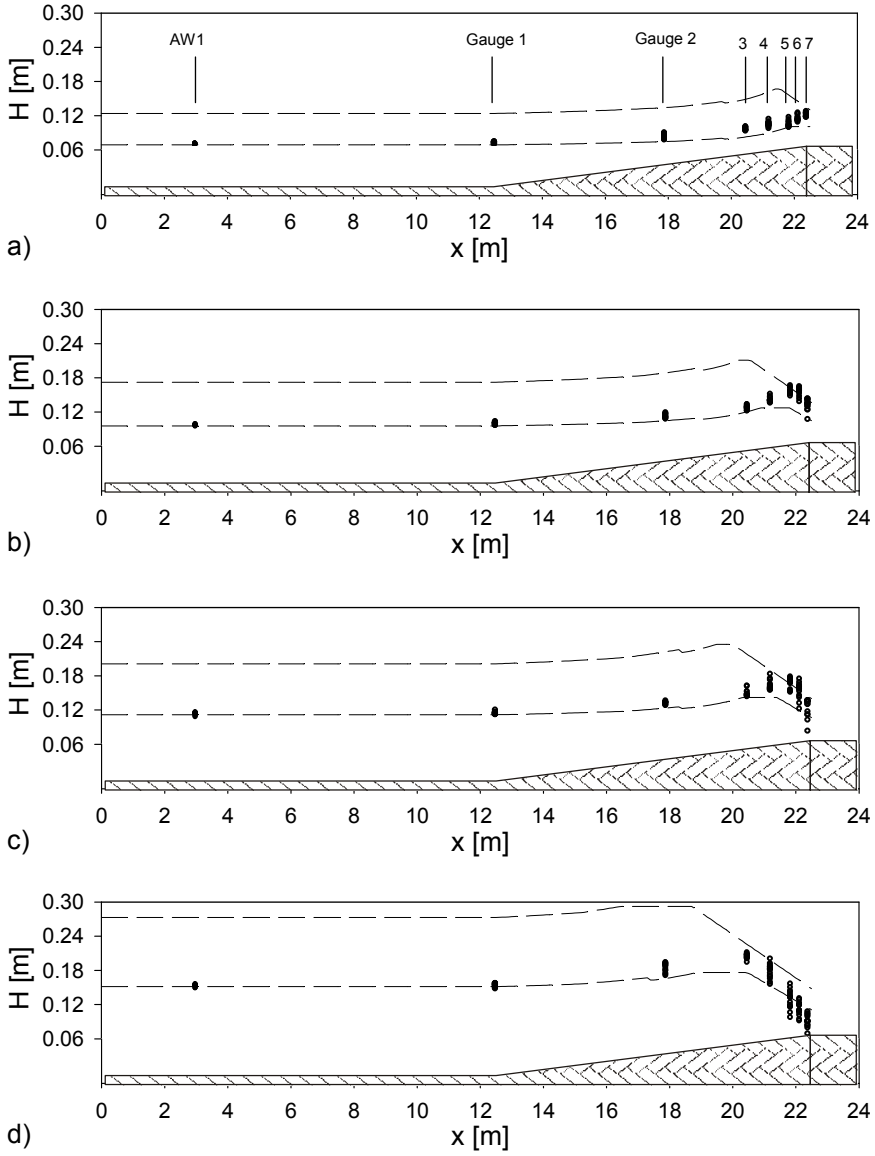

Figure 4.2 *Measured wave heights at eight locations along the flume cross-section. Results are compared with calculated Goda values of $H_{1/3}$ and H_{max}. a) $H_{Target} = 0.07\ m$, b) $H_{Target} = 0.095\ m$, c) $H_{Target} = 0.11\ m$ and d) $H_{Target} = 0.145\ m$.*

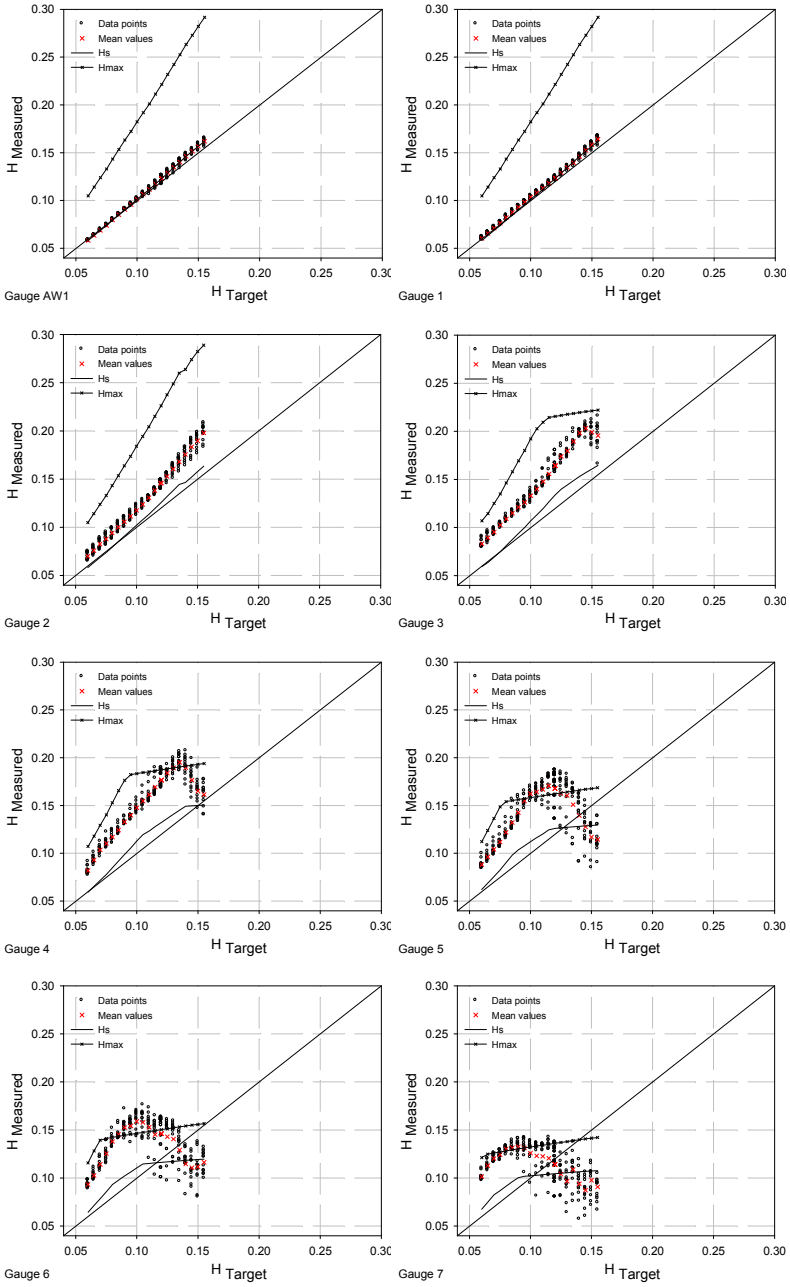

Figure 4.3 *Comparison of measured wave heights at the location of 8 gauges. Results are compared with calculated Goda values of $H_{1/3}$ and H_{max}. ($h_s = 0.135\ m$)*

Figure 4.2 shows the variation of the measured wave heights along the wave flume due to shoaling. Measurements are done at 8 different gauge locations ($h_s = 0.135\ m$). These are wave heights measured when the scaled model is not present in the flume. The gauge 7 is installed at the location of the scaled model. The lower and upper lines represent $H_{1/3}$ and H_{max}, are calculated according to Goda's theoretical approach. Figures from a to d show examples of wave shoaling selected in non-breaking, slightly breaking, breaking and broken waves. For each case, a single test is run and it shows the results of 14 uniformly developed waves. Along the horizontal bottom (out of the surf zone), all measured values are lying on the line of $H_{1/3}$. However in the surf zone (gauge 3, 4, 5, 6 and 7), scatter in the wave heights is increasing and measured values are closer to the H_{max} lines. The amount of scatter is more significant for the so called slightly breaking and breaking waves (Figure 4.2b and c). In these cases some values measured at gauges 5 and 6 are even higher than the H_{max} values. Figure 4.2d shows shoaling for the case of broken waves in which most of the waves break early and only turbulence reaches to gauge locations 5, 6 and 7. Therefore, measured wave heights in these locations are lower than the $H_{1/3}$ line.

Figure 4.3 shows wave height variations for all of the different wave gauge locations. Again measured values are compared with calculated values of $H_{1/3}$ and H_{max}. H_{Target} is the wave height introduced into the wave generator software. As opposed to Figure 4.2, these results show quite a wide range variation of the wave height considering that non-breaking, breaking and broken waves reach the model location. Red crosses are the mean values. It is assumed that the highest wave height is the height in which a wave breaks or waves with a higher wave height value will break. In this respect, it can be concluded that waves received by gauges 3, 4, 5, 6 and 7 have reached the breaking point.

4.3. WAVE PERIOD

Wave periods (T) are determined by the zero down-crossing method for each single wave gauge from the results of tests with the scaled model. Due to shoaling, reflection and breaking, T values measured near the model (in the surf zone) show scatter. However, T values measured at the toe of the foreshore are quite uniform and they are considered for the data analysis.

4.4. WAVE REFLECTION

Most of the structures placed in a wave field will reflect some proportion of the wave energy. The wave reflection depends on the wave length L, the water depth h and the wave height H at the toe of the breakwater as well as on a number of structural parameters like: steepness and roughness of the seaward slope, porosity of the structure, height and length of the berm. The reflection performance is also affected by the amount of wave overtopping.

For vertical structures, this reflected energy may cause problems within adjacent areas by increasing wave disturbance. The reflection from a vertical structure is described by the reflection coefficient (C_r). It is simply defined as the ratio of reflected and incident significant wave heights (H_{sr}, H_{si}).

Equation 4.8 $$C_r = \frac{H_{sr}}{H_{si}}$$

In literature, the reflection characteristics of vertical structures are generally related to the surf similarity number or the Iribarren number (ξ) (Battjes 1974).

Equation 4.9 $$\xi = \frac{tan\alpha}{(H_0/L_0)^{0.5}}$$

where, H_0 and L_0 are the wave height and wave length in deep water.

However, the surf parameter given in Equation 4.9 does not consider the effect of h_s. Therefore, an upgraded surf similarity number β, given by Yoo (1986), is considered in the following.

Equation 4.10 $$\beta = \frac{2*tan\alpha^2}{k^2 h_s H} = \frac{tan\alpha^2}{\pi k h_s (H/L)} = \frac{\xi^2}{\pi k h_s}$$

In which, k is the local wave number. For the simplicity, L, H and k values are calculated at h_s measured at the toe of the foreshore.

In Figure 4.4a, the wave reflection due to the scaled model at the toe of the foreshore is plotted against the surf similarity number (β) for both regular and irregular waves. The scatter in regular wave results is mainly due to defining only

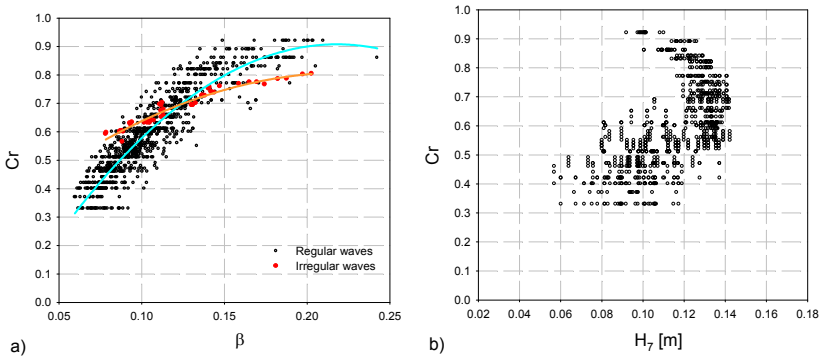

Figure 4.4 *Variation of reflection coefficient, C_r, with the variation of a) surf similarity number, β, and b) wave height at the toe of the scaled model, H. ($h_s = 0.135\ m$)*

one single Cr value for all 14 waves in one single test run. Therefore, a certain range of β is represented by a single Cr value. For irregular waves, H_{m0} and T_p values, measured at defined h_s, are considered for β calculations. H_{m0} is the significant wave height being estimated from the spectral information and T_p is the wave period corresponding to the frequency at the spectral peak. The irregular wave reflection analysis has been performed for a complete wave train of about 500 waves. Equation 4.11 and Equation 4.12 show the adopted line functions for regular and irregular waves.

Regular waves

Equation 4.11 $$C_r = -23.7\beta^2 + 10.3\beta - 0.2$$

Irregular waves

Equation 4.12 $$C_r = -11\beta^2 + 5\beta + 0.2$$

The regular wave reflection is increasing with increasing β. The maximum C_r is about 0.92 for the regular waves and about 0.80 for irregular waves. However, the minimum C_r is about 0.33 for regular waves and 0.56 for irregular waves. Normally, in a test run with uniformly distributed regular waves with small H values (non-breaking waves), most of the waves reflect from the scaled model with high C_r values. In the same manner, uniformly distributed regular waves with high H values break before reaching the model and C_r values will be low. However, in irregular wave terrain there are always some waves that break and some not. Therefore, the maximum C_r value is lower and minumum C_r value is higher for irregular waves compared to the C_r values for regular waves with equivalent wave heights.

Figure 4.4b shows the variation of Cr with the variation of the wave height (H_7) measured at the location of the scaled model. Because waves ranging from SBW to BW are considered, the first wave heights are increased up to a point where the waves might break. Then wave heights decrease because of the already broken waves arriving at the location. In this aspect, waves with Cr values lower than 0.65-0.70 can be considered as heavily breaking or broken waves.

Figure 4.5 shows the same data set shown in Figure 4.4. In this plot, C_r results are categorized based on breaker shapes as; slightly breaking waves (SBW), breaking with small air trap (BWSAT), breaking with large trap (BWLAT) and broken waves (BW). For vertical structures under non-breaking waves or SBW, the reflection is nearly total. Allsop (1999) summarized the wave reflection performance as:

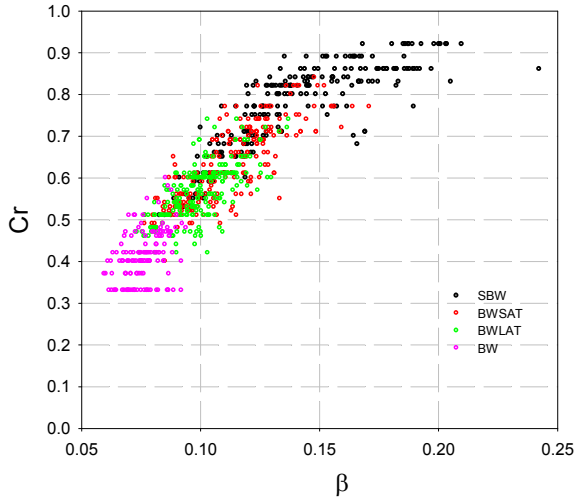

Figure 4.5 *Variation of reflection coefficient, C_r, with the variation of surf similarity number, β. Different colors show the different breaking types. ($h_s = 0.135\ m$)*

Equation 4.13 $C_r = 0.85 - 1.00$

In Figure 4.5 the range of C_r for SBW is close to the range recommended in Equation 4.13 and measured between $C_r = 0.80 - 0.92$. In addition, a few points are observed at $C_r < 0.80$. These points are probably errors occurring due to the measuring techniques which consider one C_r value for all 14 waves in one single test run.

Allsop (1999) suggested that the reflection coefficient for breaking waves might be assessed from:

Equation 4.14 $C_r = 0.70 - 0.90$ for little breaking
$C_r = 0.50 - 0.70$ for heavy breaking

The measurements in this particular research do not have a boundary as clear as mentioned by Allsop. The measured ranges of C_r are as follows:

Equation 4.15 $C_r = 0.55 - 0.80$ (BWSAT)
$C_r = 0.45 - 0.70$ (BWLAT)

On a simple vertical wall type structure, the degree of overtopping influences C_r

values. As the crest level of the wall is reduced, more energy is transmitted rather than reflected, and C_r is reduced. However, overtopping is not allowed during this particular research, due to the spatial shape of the scaled model. Since differences in overtopping condition will be a reason for the differences between measurements and literature values.

For the BW, most of the wave energy dissipated due to the breaking, thus potentially reducing reflections. Since, the range of measured C_r for BW is between 0.33-0.50.

4.5. WAVE BREAKING

In deep water, the breaker height is governed by the wavelength whereas in shallow water it is determined by water depth. Therefore, the two common breaker indices for shallow (γ_s) and deep water (γ_d) can be expressed as follows.

Equation 4.16 $$\gamma_s = \frac{H_b}{h_b}$$

Equation 4.17 $$\gamma_d = \frac{H_b}{L_b}$$

where, H_b is the breaker height, h_b is the water depth at the breaking point and L_b is the breaking wavelength.

It is possible to combine both expressions in single formula that is valid for all depths (Southgate et al., 1995).

Equation 4.18 $$\frac{H_b}{L_b} = \gamma_d \, tanh\left[tanh\left(\frac{h_b}{L_b}\right) * \frac{\gamma_s}{\gamma_d}\right]$$

For shallow water, $(\tanh x \approx x)$ Equation 4.18 simplifies to Equation 4.16. For deep water, $(\tanh x \approx 1)$ Equation 4.18 simplifies to Equation 4.17.

McCowan (1894) is the first researcher who derived $H_b/h_b = 0.78$. His assumption is based on the fact that a solitary wave breaks as its crest angle approaches a limiting value. At the limiting value the fluid velocity at the crest surpasses the celerity of the profile. However, Goda (2010) mentions that a value of 0.8261 is more accurate which is proposed by Yamada et al. (1968). From the field observations, it is found to be between $\gamma_s = 0.78 - 0.86$.

For deep water conditions, Michell (1893) found the limiting steepness as $\gamma_d = 0.142$. However, Goda (2010) underlined the misunderstanding of the definition of L in γ_d which is the length of finite amplitude waves. If the small amplitude wavelength is employed instead of the finite amplitude wavelength, the new γ_d is expressed as $\gamma_d = 0.1684$.

The method of linking shallow and deep water breaking criteria was first suggested

by Miche (1944) who adopted Michell's (1893) condition periodic waves over arbitrary water depth.

Equation 4.19 $$\frac{H_b}{L_b} = 0.142\ tanh\frac{2\pi h_b}{L_b}$$

In the last century, tremendous numbers of formulas have been proposed to describe the incipient condition of wave breaking. Detailed reviews of the existing researches have been made by Galvin (1972), Sawaragi (1973), Rattanapitikon et al. (2003), Camenen and Larson (2007), and Goda (2010).

Liu et al. (2011) categorized the breaking wave formulas into four groups based on their formation types.

They describe the first type as the form of Equation 4.16 which is known as the McCowan (1894) type.

Equation 4.20 $$\frac{H_b}{h_b} = \gamma(\theta, \lambda_0)$$

where $\lambda_0 = H_0/L_0$ is the deep water wave steepness with H_0 being the incident wave height.

The second type is known as the Miche (1944) type formula which is shown in Equation 4.21.

Equation 4.21 $$\frac{H_b}{L_b} = \alpha(s, \lambda_0) tanh\left[\xi(s, \lambda_0)\frac{2\pi h_b}{L_b}\right]$$

The third type is known as the Goda (1975) type formula (Equation 4.22). It is a form of Equation 4.21 by considering L_0 instead of L_b. It is also assumed that $tanhx$ can be approximated as $1 - \exp(-1.5x)$.

Equation 4.22 $$\frac{H_b}{L_0} = \alpha'(s, \lambda_0)\left\{1 - exp\left[-1.5\xi'(s, \lambda_0)\frac{2\pi h_b}{L_0}\right]\right\}$$

The fourth one is known as the Munk (1949) type formula (Equation 4.23). It is developed based on the relation between the shoaling coefficient that results from the conservation of the energy flux and the local value of the relative water depth.

Equation 4.23 $$\frac{H_b}{H_0} = \beta(s)\left(\frac{H_0}{L_0}\right)^m$$

The functional forms of $\gamma(\theta, \lambda_0)$ (in the first type), $\alpha(s, \lambda_0)$ and $\xi(s, \lambda_0)$ (in the second type, $\alpha'(s, \lambda_0)$ and $\xi'(s, \lambda_0)$ (in the third type) and $\beta(s)$ and m (in the fourth type) obtained by the previous authors are respectively summarized in Appendix I.

For engineering applications, Goda's (1970, 1975 and 2010) formula seems to have gained the best reputation. For regular waves, he considered $\alpha'(s,\lambda_0)$ as 0.17 and $\xi'(s,\lambda_0)$ as $1+11\theta^{4/3}$. Then Equation 4.22 simplifies to Equation 4.24.

Equation 4.24 $$\frac{H_b}{L_0} = A\left\{1 - exp\left[-1.5\frac{\pi h_b}{L_0}\left(1+11s^{4/3}\right)\right]\right\}$$

Figure 4.6 shows the comparison of measured breaking wave heights with the calculated breaking wave heights using the Goda (2010) method. Wave height values are measured from laboratory tests without scaled model. So, the results are not influenced by the existence of the model. The x-axis represents the horizontal distance along the flume from the paddle of the wave generator. The top bar of the x–axis shows the location of the gauges. The bottom figure displays the bed profile. Measurements are taken from 8 different locations of wave gauges (see Figure 4.2). At each gauge location, the highest measured wave height is considered as the measured value for the gauge. Wave gauge results are combined using solid lines, whereas calculated values are combined using dashed lines. For each water depth, the wave height increments are chosen as to have waves varying from non-breaking to broken at the location of the model. Therefore, only the highest wave heights measured at gauges 5, 6 and 7 (located close to the model) are reaching the height of breaking wave heights. Consequently, measured wave heights at gauges 1 to 4 are lower than the calculated braking wave heights. Even so, calculated values by the Goda method are underestimating the values at the location of gauge 7. Thus, the Goda method is calibrated by considering a new value $A = 0.21$, instead of 0.17. The difference between Goda and the measurements will be the difference in observation criteria that considered the highest wave height as the H_b.

Figure 4.7 and Figure 4.8 show the inception of wave breaking points for four different values of h_s. The top figure displays the variation of the wave height (H_7) measured at the model location with the variation of the wave height (H_1) measured at the toe of the foreshore. As described before, tests are conducted under the same test matrix with and without installation of the model. H_7 and H_1 are the results of waves recorded under identical conditions, but without the model. Therefore, wave heights are not influenced by the model existence. As seen previously, wave heights are slowly increasing up to the breaking wave height which is considered the highest wave height at the location of the gauge. Then, already broken waves are approaching the gauge location. Due to the chaotic nature of the breaking, some high wave heights can also be recorded after the breaking point. Therefore, a polynomial line of regression analysis is adapted to the scatter data. The crest point of adopted line is considered as the breaking wave height. The second figure shows the variation of the maximum pressure at the vertical wall with the variation of H_1. Pressure results are categorized as non-breaking and breaking waves. The appearance of breaking waves shows the inception point of wave breaking. Mainly, breaking wave results are high dynamic pressures whereas non-breaking wave

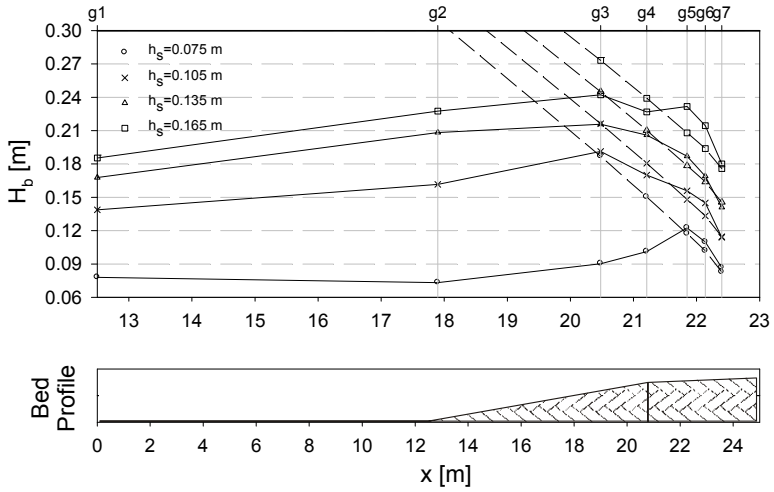

Figure 4.6 *Comparison of measured breaking wave heights H_b (solid lines) with the calculated breaking wave height from Goda (2010) formula (dashed lines).*

results are low quasi-static pressures. The third figure is a detailed version of the second one which shows the scattering of non-breaking wave results in the breaking wave zone in detail. This scatter is caused by the appearance of the wall on the inception of wave breaking. The last figure shows the p_{max} values of the third wave results. The third wave is already well developed but less affected by disturbances originating from the two preceding waves. The transition from non-breaking waves to breaking waves is clear and the influence of the wall on the inception of wave breaking is zero or limited.

From Figure 4.7 and Figure 4.8, it can be seen that both the transition points from non-breaking to breaking waves on the results of the third waves (d) and the inception points of breaking waves (a), the location of the highest H_8, are coinciding on the same H_1 values. These show that the third waves are less affected by the preceding waves and the criteria applied for distinguishing non-breaking and breaking waves work properly. However, the scatter of p_{max} values on (b) and (c) shows that the existence of the model postpones the inception of wave breaking for some waves which would normally break without the presence of the model. This postponing is the result of reflection or/and turbulence left from preceding waves. In addition, the influence of the wall on the inception point of breaking is increasing with rising water depth. This is in parallel with the increase of reflection amount in the higher water depths.

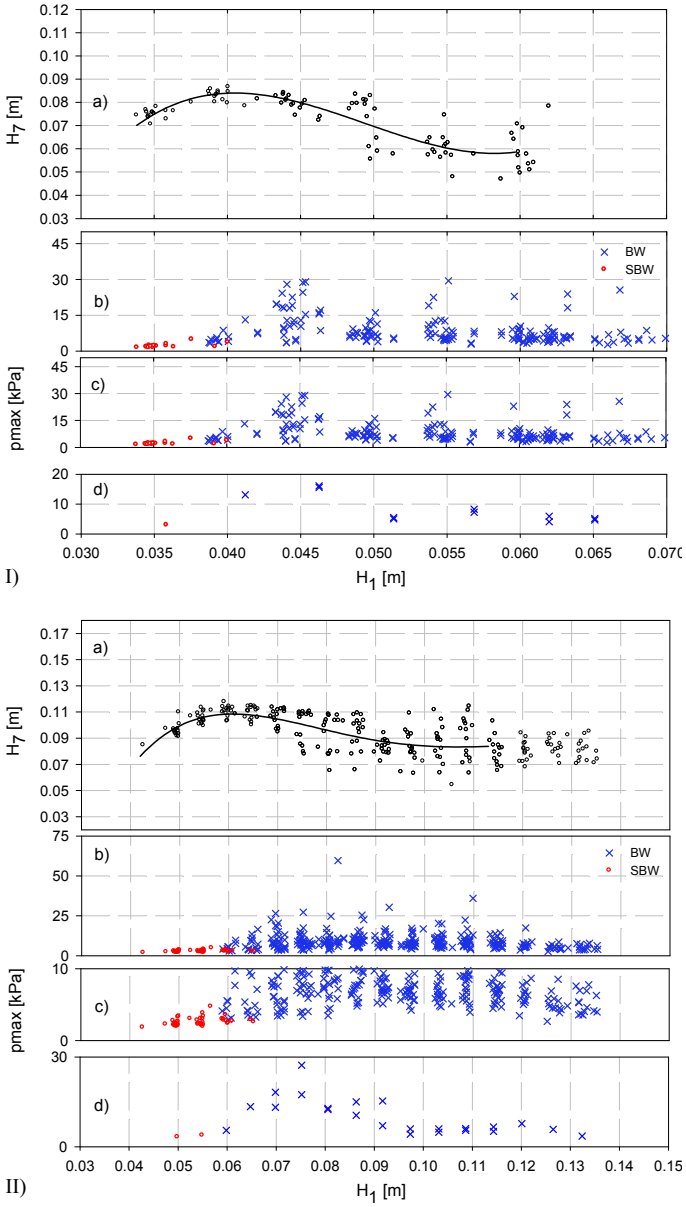

Figure 4.7 *Inception of wave breaking points a) Variation of wave height (H_7) measured at the model location with the variation of wave height (H_1) measured at the toe of the foreshore. b) Variation of maximum pressure on the vertical part c) Variation of maximum pressure measured from the impact of 3th wave which is unaffected by the preceding waves (I is at $h_s = 0.075\,m$ and II is at $h_s = 0.105\,m$)*

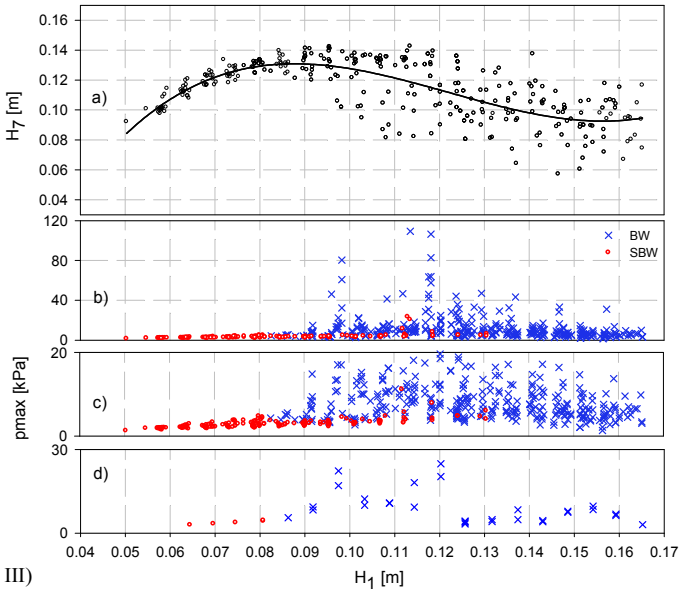

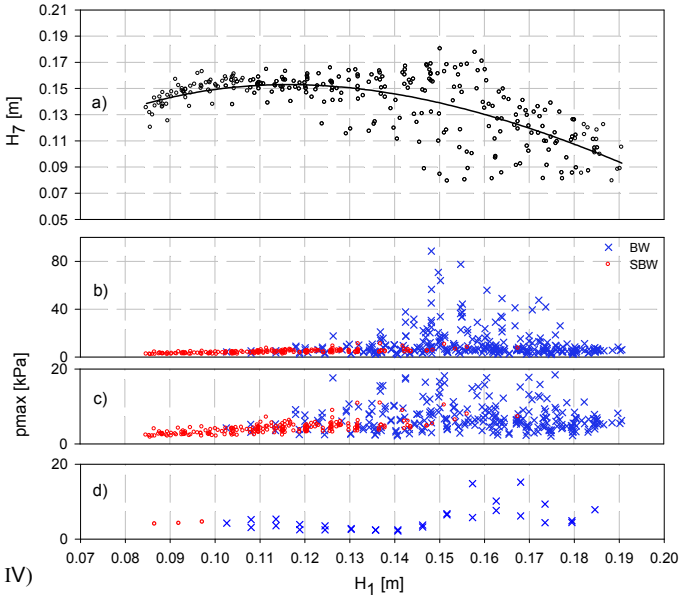

Figure 4.8 *Variation of wave height (H_7) measured at the model location with the variation of wave height (H_1) measured at the toe of the foreshore. b) Variation of maximum pressure on the vertical part c) Variation of maximum pressure measured from the impact of 3th wave which is unaffected by the preceding waves (III is at $h_s = 0.135\ m$ and IV is at $h_s = 0.165\ m$)*

4.6. WAVE OVERTOPPING

Wave overtopping is prevented due to the spatial shape of the scaled model. In addition, overtopping in tests with a simple vertical wall type model is also prevented by increasing the wall height with an external wooden plate.

4.7. CONCLUSIONS

Wave shoaling, reflection, breaking and overtopping are the main hydraulic aspects considered for the performance of the scaled model test of a vertical structure with overhanging cantilevering surface. Tests are conducted in a 2-D wave flume with a uniform foreshore slope of 1/20. Wave gauges are used to monitor the wave information along the flume and at the scaled model location.

Wave shoaling has been analyzed for regular waves with test results without the pressure of the scaled-model. In this aspect, wave height variations along the flume are compared with calculated values of $H_{1/3}$ and H_{max} based on Goda's theoretical approach for shoaling. Along the horizontal bottom (out of the surf zone), all measured values are on the line of $H_{1/3}$. However in the surf zone, the wave heights are increasing due to shoaling and the measured values are closer to the H_{max} lines.

In addition, the wave reflection is analyzed for regular and irregular waves. The reflection coefficients C_r, measured at the toe of the foreshore, are categorized based on the breaker shapes as: slightly breaking waves (SBW), breaking with small air trap (BWSAT), breaking with large trap (BWLAT) and broken waves (BW). These results are compared with findings of Allsop (1999). According to the results, C_r values between $0.80 - 0.92$, $0.55 - 0.80$, $0.45 - 0.70$ and $0.33 - 0.50$ are found for SBW, BWSAT, BWLAT and BW respectively.

The breaking process has finally been analyzed for regular waves. Breaking wave heights, measured from laboratory tests without the scaled model, are compared with the calculated breaking wave heights using the Goda (2010) method. The Goda method is underestimating the values at the location of scaled model. Thus, the Goda method is calibrated by considering a new value $A = 0.21$, instead of 0.17.

Pressures on the scaled model are categorized as non-breaking and breaking waves. The margin between non-braking and breaking waves is considered as the inception point of breaking. This point is compared with the breaking point for the measurements without the scaled model to determine the influence of the scaled model on the inception point of the wave breaking. It is seen that the existence of the model postpones the inception of wave breaking for some waves which would normally break without the presence of the scaled model. This postponing is the result of the reflection or/and turbulence left from preceding waves. In addition, the influence of the wall on the inception point of breaking is increasing with rising water depth.

REFERENCES

Allsop, W., 1999, "*Reflection coefficients*", Probabilistic design tool for the vertical walls, volume IIa – Hydraulic aspects, pp 13

Battjes, J. A., 1974, "*A Computation of Set-Up, Longshore Currents, Run-Up and Overtopping Due to Wind-Generated Waves*," Ph.D. diss., Delft University of Technology, The Netherlands

Goda, Y., 1970. A synthesis of breaker indices. Transactions of Japan Society of Civil Engineers 2, 39–49.

Goda, Y., 1975. Irregular wave deformation in the surf zone. Coastal Engineering in Japan 18, 13–26.

Goda, Y., 2010. "*Reanalysis of regular and random breaking wave statistics*". Coastal Engineering Journal 52 (1), 71–106.

McCowan, J. [1894] "*On the highest waves in water*," Phil. Mag. Ser. 5, 36: 351-358.

Miche, R. (1944). Mouvements ondulatoires de la mer en profondeur constante ou decroissante, Annales des Ponts et Chaussees, Vol. 114, 25–78, 131–164, 270–292, 369–406 (in French).

Michell, J.H., 1893. On the highest waves in water. Philosophical Magazine 36, 430–435 Ser. 5.

Munk, W.H., 1949. "*The solitary wave theory and its applications to surf problems*". Annals of the New York Academy of Sciences 51, 376–462.

Southgate, H.N., 1995. "*Prediction of wave breaking processes at the coastline"*. In: Rahman, M., Editor, , 1995. Advances in Fluid Mechanics vol. 6, Computational Mechanics Publications, Southampton, UK.

Yamada, H., Kimura, G. and Okabe, J. [1968] "*Precise determination of the solitary waves of extreme height on water of a uniform depth*," Rep. Res. Inst. Applied Mech., Kyushu Univ. XVI (52): 15-32.

Yu Liu, Xiaojing Niu, Xiping Yu, 2011 "*A new predictive formula for inception of regular wave breaking*", Coastal Engineering, Volume 58, Issue 9, September 2011, Pages 877-889

5

CLASSIFICATION OF BREAKER TYPES

***

5.1 INTRODUCTION

On vertical structures, the breaker type has a significant consequence on the wave impact pressure. In this manner, the type which creates the largest pressure is becoming an important issue and is uncertain (Hull & Muller, 2002). Bagnold (1939) described the shape of the breaker as a very flat vertical wave front, enclosing a thin cushion of air between itself and the wall. Hence, the maximum pressure occurs when the thickness of the air cushion is small, but not zero. Kirkgoz (1982) found that a breaking wave having its front face parallel to the wall at the instant of impact produces the largest shock pressures. His approach has not been confirmed by Hull and Muller (2002). Furthermore, researchers like Bullock et al. (2007), Partenscky (1988) and Hattori et al. (1994) showed that the largest impact pressures occur when the breaking wave traps a very thin pocket of air. Oumeraci et al. (1995) found that a plunging breaker with a large air pocket causes the highest pressures. In addition, Richert (1968), Partenscky (1988), Hattori et al. (1994) and Hull & Muller (2002) observed the most severe impulsive pressures when a breaking wave with a vertical face strikes the wall with entrapped air either in the form of small air bubbles or a very thin lens shaped air pocket.

As mentioned above, the breaker type has an important influence on the magnitudes of impact pressures and forces. Therefore, the wave impact results are classified according to the breaker types. Researchers like Chan & Melville (1988), Partenscky (1988), Oumeraci et al (1993) and Kirkgoz (1995) carried out experiments to determine the relationship between the breaker type and wave impact on the vertical structures. Based on model studies, Oumeraci et al. (1993) developed some criteria for classification of breaker types depending on both the ratio of breaking water depth to the still-water depth at the wall (d_s/d_w) and the ratio of the horizontal velocity of the breaker to the vertical upward velocity of the water surface directly at the wall (V_H/V_V). According to his results, four main breaker types are suggested. These are (a) upward deflected breaker, (b) plunging breaker with a small air cushion, (c) well-developed plunging breaker with a large air pocket and (a) turbulent bore. In addition, based on detailed analysis combined with visual records, they suggest that the observed breaker type can be identified by the recorded force and pressure histories.

Adversely to the previous problem of a simple vertical wall or a horizontal deck, a combined structure consisting of both a vertical and a horizontal part has scarcely been considered. One of the rare examples of research with this combined type of structure is the work of Wood and Peregrine (1996), who consider an analytical approach, based on the pressure-impulse method for a flat deck close to the mean water level. In general, a consensus on the necessary approach for the research on this combined type of structure lacks completely (Okamura 1993). In addition, the structure prevents most of the overtopping due to its particular geometry involving closed angles, which do not allow incident waves to dissipate. Therefore the loading condition is more severe than in the preceding situations.

For the vertical structures, the answers to the questions like which breaker type creates the highest impact shock, which criteria can be defined to categorize waves

and what are the characteristics of related pressures and forces, are considerably well understood. However, what will be the answer of similar questions on a vertical structure with an overhanging horizontal cantilever slab is of practical importance in this chapter.

This chapter gives a summary of literature. Non-repeatability of test results and occurring of shock pressures are discussed. This is followed by a section on the classification of breaker types. Detailed analyses of four breaking cases are discussed in Sections 5.5, 5.6, 5.7 and 5.8. For each breaker type, the relation between horizontal velocity of wave crest and vertical velocity of water level at the wall are defined in Section 5.9. Location of shock pressures and instantaneous pressure distributions are introduced in Section 5.10. Based on the discussion of the test results, detailed conclusions are formulated in Section 5.11.

5.2 NON-REPEATABILITY OF TESTS RESULTS

Although the generated waves in one test are nominally identical, their impact behavior varies significantly and it is possible to see various impact types in one run. Variations of results are more significant for the peak pressures than for the peak forces which are calculated from the integration of pressure over the vertical face. Figure 5.1a and Figure 5.1b show an example of force histories recorded on the horizontal and vertical parts of the scaled model, respectively. The non-repeatability of the breaking wave impact pressures and forces on the vertical structures is a well known phenomenon and has been reported by many researchers (Bagnold, 1939; Chan & Melville, 1988; Chan, 1994; Hattori et al., 1994; Kirkgoz, 1995; Walkden et al., 1996; Walkden and Bruce, 1999; Peregrine, 2003; Bullock et al., 2007). From literature, the main reasons for the non-repeatability are: the turbulence left behind by a preceding breaking wave, the strong interaction with the reflection of the preceding wave and the influence of trapped air.

These parameters have a strong influence on the breaking wave kinematics and on the shape of the waves which in turn have a strong relation to the value of peak pressures. In addition, the resolution of sensor locations and the sampling frequency of the sensors influence the results (Bullock et al., 2007), since the largest impact pressures tend to be highly localized both in space and in time. In this study, effects of sensor resolution and sampling frequency are kept to a minimum by producing first a complete pressure profile to select the representative locations for the sensors and using a very high sampling frequency (20 kHz). Furthermore, discrepancies are due to non-uniformity of the wave front across the wave flume introducing some three dimensional effect (Bredmose et al., 2010).

When looking at the ratio between measured horizontal and vertical forces (F_{h_max}/F_{v_max}), it shows a secondary scatter (Figure 5.1c). In addition to the above parameters affecting non-repeatability of results on the vertical part (this is the first impact), the following parameters are the reasons for these secondary scatters:

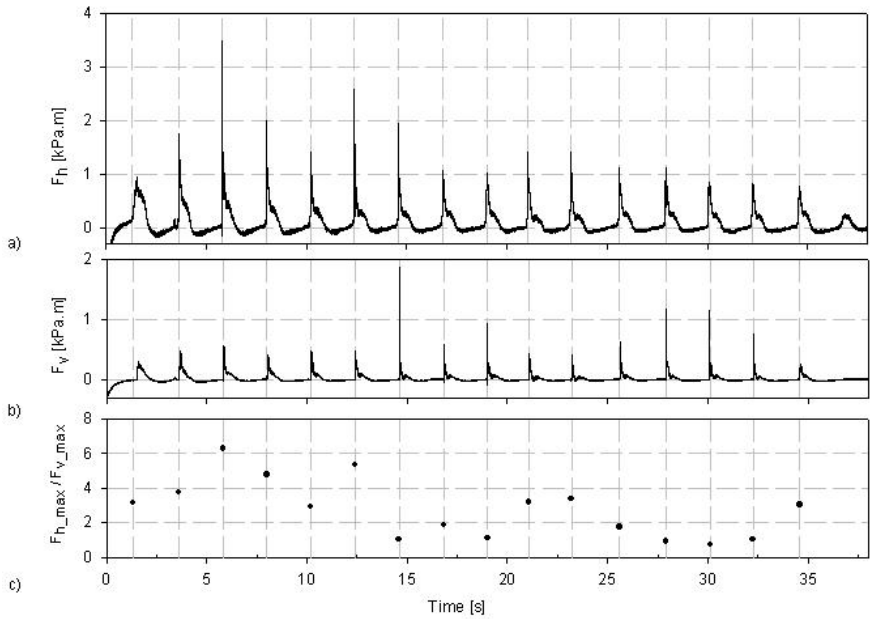

Figure 5.1 *a) Force histories for 18 regular identical waves, a) horizontal force (F_h), b) vertical force (F_v), c) ratio of F_{h_max} / F_{v_max} ($h_s = 0.135\ m$, $T = 2.2\ s$, $H_{target} = 0.105\ m$)*

- the form of the rising water on the vertical part (either in the form of rising water jet or water spray)
- the amount of air in the rising water and the additional air trapped at the corner of the scaled model

Both impacts on the vertical and horizontal parts are non-repeatable under nominally identical conditions and their scatter trends are also different.

5.3 OCCURRENCE OF SHOCK PRESSURES

The scaled model, consisting of a vertical and a horizontal part, is exposed to two distinct wave impacts during one complete wave cycle. The first impact occurs on the vertical part while the second occurs beneath the horizontal part. The latter results from the rising water on the vertical part. The results of waves which first hit on the horizontal part are excluded from the analysis to have a uniform data set. These impacts on the horizontal part from the direct hit of an approaching wave crest and impacts beneath the horizontal part from rising water diverted from a prior impact on the vertical part have different occurring mechanisms that should be separately investigated.

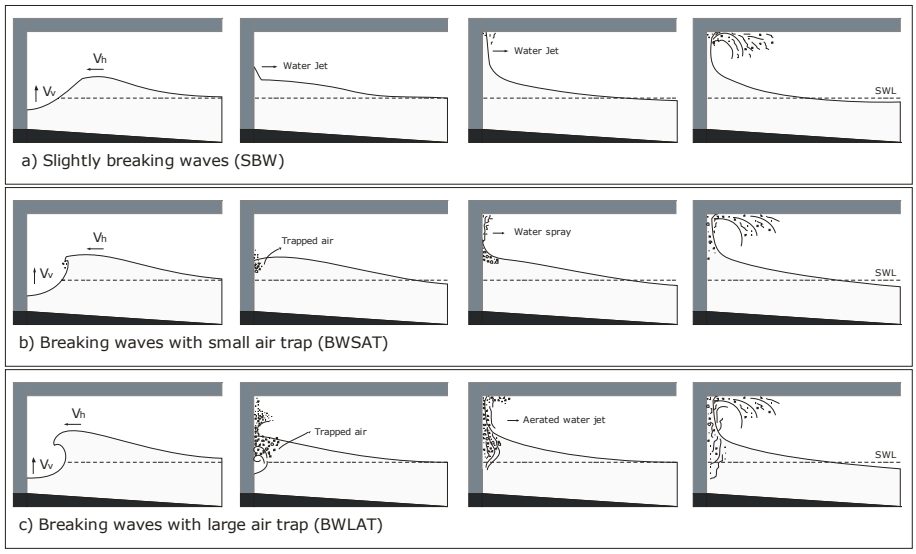

Figure 5.2 *Definition of breaker types which create shock pressures on vertical and horizontal parts*

Figure 5.2 displays three different cases in which shock impact pressures may occur on the scaled model. Kisacik et al. (2010) mentioned that wave heights which create high shock pressures on the vertical part range between $0.71 \leq H/h_s \leq 1.19$ while wave heights creating high shock pressures on the horizontal part range between $0.56 \leq H/h_s \leq 1.19$. This shows that on the horizontal part shock pressures may occur even in the slightly breaking and broken wave zones.

In the first case (slightly breaking waves), the waves tend to break but the water level at the wall accelerates fast and takes place before the wave crest reaches the wall (Figure 5.2a). Therefore, most of the energy reflects from the wall and the structure is subjected to pulsating loads. However, the accelerated vertical component collides beneath the horizontal part as an uprising water jet. This water jet results in a very high impact pressure at the upper corner of the scaled model. Therefore, this combined style structure is more vulnerable in design aspect even when it is designed for pulsating wave loads in moderate wave conditions.

In the second case (breaking waves with small air trap), the wave collides on the vertical part with a more or less parallel face and only a little amount of air is enclosed (Figure 5.2b). Due to impact effects, enclosed air compresses, the wave crest quickly breaks up into droplets and creates an upward water spray. The upward spray and the following aerated water jet hits beneath the horizontal part. In this case, high shock pressures occur both on the vertical and horizontal part.

In the third case (breaking waves with large air trap), the wave starts to break early and the tongue of the plunging wave hits on the vertical part (Figure 5.2c). In this case, a large amount of air is enclosed and it breaks up into bigger bubbles.

Splashes due to the first impact and the followed aerated water jet rise on the vertical part and collide on the corner of horizontal part. As in the second case, shock pressures occur both on the vertical and horizontal parts.

Rarely, it is also possible to measure high shock pressures on the horizontal part for the broken waves. In general however, the overall highest shock pressures, both on vertical and horizontal part, are measured for the second case of breaking waves with small air trap.

5.4 CLASSIFICATION OF BREAKER TYPES

On vertical structures, the breaker type is defined as an important parameter which has considerable influence on the wave impact pressures. In this study, the answer to the question what will be the pressure distribution on the scaled model (as described before) under the different breaker types is of practical importance. In order to reproduce all breaker types, a smooth shift between breaker types is provided by gradually increasing wave heights. Because waves first hit on the vertical part, the categorization method by Oumeraci et al. (1993), developed for vertical structures, is followed. They suggest the following breaker types with a gradual transition between them: slightly breaking waves, breaking waves with small air trap, breaking waves with large air trap and broken waves. There is another case, called flip through, which is situated between the types of slightly breaking waves and breaking waves with small air trap. The flip through impact type is a special breaker type, which occurs by the converging of wave components towards a point. It is very localized in space and occurring within a very narrow band of the wave height range (Bredmose et al., 2010). Therefore, special care is necessary to properly simulate the flip-through case. In the tests, wave heights are gradually increased between tests by an increment of 0.5 cm and this is too coarse to catch the 'flip through' type properly. Therefore, detailed analysis of this type is not included in this study.

In the following sections, detailed examples of measurements classified as slightly-breaking waves, breaking waves with small air trap, breaking waves with large air trap and broken waves from the model tests are presented. For photo visualizations, the 3rd wave in a test run with 18 regular waves is considered. The third wave is already well developed but less affected by disturbances coming from the first two, gently reflected, small waves.

It is always possible to see various wave types in each test run. The type of each single wave is analyzed and classified by looking at the HSC videos and the related pressure records.

5.5 CASE-I: SLIGHTLY BREAKING WAVES (SBW)

In the case of slightly breaking waves (SBW), the wave tends to break but the water level at the wall accelerates fast and results in an incomplete breaking due to the

presence of the wall. This loading case is defined as a transition zone between standing waves and breaking waves with small air trap.

5.5.1 Evaluation of water surface profile

Figure 5.3 shows eight photos (at instants from t_1 to t_8) in sequence showing the developments of the wave shape which depicts the case of SBW. The particular example is selected with $h_s = 0.105\,m,\ H = 0.057\,m\ and\ T = 2.2\,s$. These photographs are obtained from HSC recording which is synchronized by a trigger system with the results of the pressure sensors and wave gauges. The horizontal white line in the middle and black spots on the sides of the photos represent the level of still water level (SWL) and the sensor positions on the scaled model respectively. On the photos, the free water surface at each instant is marked with a white color.

Figure 5.3a shows the free surface profile of an approaching wave when the wave is tending to break. On the wall, the water level starts below the SWL and it rises to the level at instant t_2 (Figure 5.3b). Accelerated water which is rising on the vertical wall reaches the impact point before arrival of the wave crest (Figure 5.3c). Oumeraci et al. (1993) defined this rise as the reason for the delay of the development of breaking and mentioned that onset of breaking occurs at or just behind the wall boundary. Accelerated vertical water creates a thin water jet above the impact point of the wave crest (Figure 5.3d). This water jet hits the horizontal part and breaks up into droplets (Figure 5.3e). The water sprays out due to the impact and the horizontal force value reaches its maximum value (Figure 5.3f). Figure 5.3g shows a photo at the time of maximum vertical force with a phase shift of 0.0272 T from the maximum horizontal force. Lastly, Figure 5.3h represents the time of maximum downward acceleration which creates the second hump on the horizontal force signal. The area of impact is clearly located above the SWL and the contact point is exactly between the location of sensor 4 and 5. This shows the importance of the sensor resolution to measure the real peak pressures.

5.5.2 Time series of pressures and forces

Figure 5.4 shows the recording of the impact pressures associated with SBW. In the figure, the pressures are normalized by ρgH while the time scales are normalized by T (ρ is the water density and H is the wave height at the toe of the foreshore). Through the normalization, the pressures are correlated to the incident wave characteristics while the time scales are correlated to the local wave period. Sensors 1 to 7 are located on the vertical part and sensors 8 to 10 are located on the horizontal part (see Figure 3.7). Sections t_1 to t_8 represent the measured pressure time series at the same moments of the eight photos which are shown in Figure 5.3. The impact pressure quickly shifts downwards from the initial impact point through the water body. Downward propagating velocities of the wave impact, measured from the time differences between the pressure peaks at sensors 1, 2, and 3, are

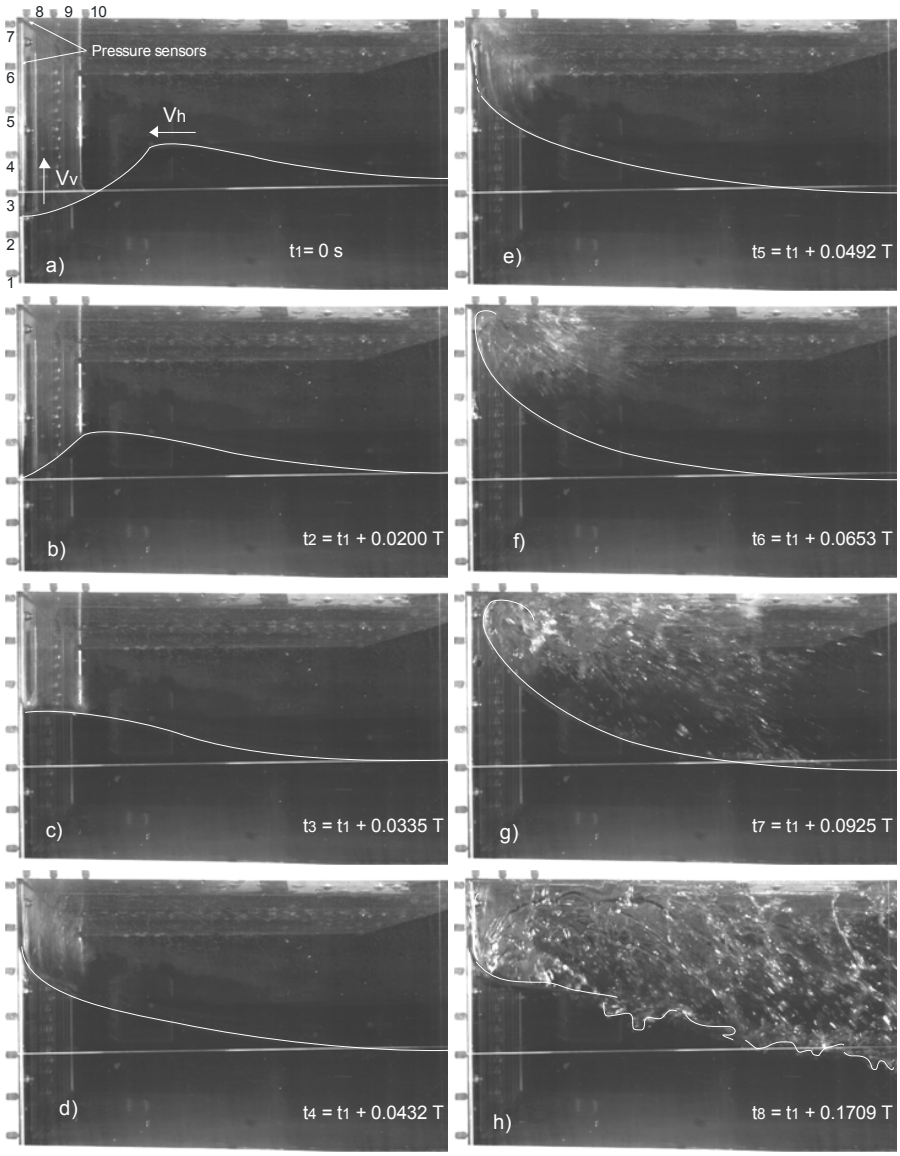

Figure 5.3 *Sequential photos from HSC records for the wave shape developments of SBW. HSC results are synchronized with pressure and force records ($h_s = 0.105\,m$, $H = 0.057\,m$ and $T = 2.2\,s$)*

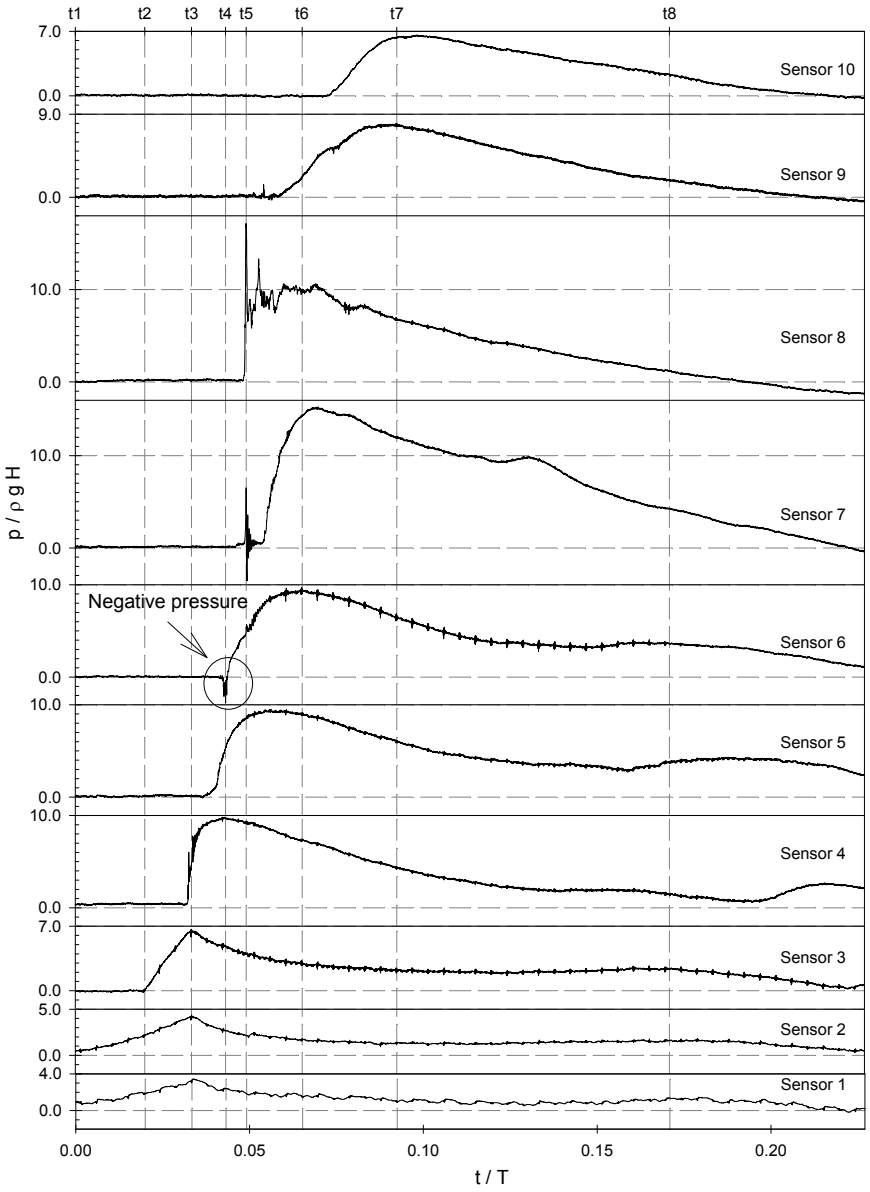

Figure 5.4 *Simultaneous pressure records from the 10 pressure sensors for the case of SBW. Time from t_1 to t_8 represents pressure profiles at the time instant of photos in Figure 5.3*

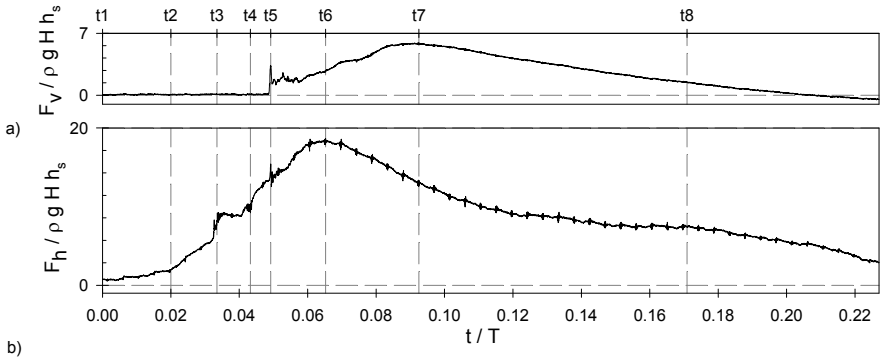

Figure 5.5 *Simultaneous horizontal and vertical force records (F_h and F_v) of SBW. Time from t_1 to t_8 represents force profiles at the instant of photos in Figure 5.3*

evaluated respectively at 900 m/s (p3–p2), and 90 m/s (p2–p1). The acceleration of the water level at the wall is reaching its highest level when the wave crest reaches the vertical wall which is above the SWL. This high acceleration results in relatively high pressures above the SWL (sensors 4, 5 and 6). There is a single negative pressure spike observed on sensor 6 just before the impact. This special phenomenon of the negative pressure is described by Hattori et al. (1994) as a result of an extremely high velocity jet shooting up the wall face. Due to the high velocities of the vertical shoot, a low pressure area exists around the sensor 6. Then, the rising jet shoots towards the upper corner of the scaled model which results in a dynamic impact pressure followed by a distinctly separated quasi-static pressure (sensor 7). However, this quasi-static component attaches to the dynamic component on the results of sensor 8. The dynamic pressure on sensor 7 shows an oscillation which is the result of trapped air at the corner. This blocked air is also the reason why there is a clear separation between dynamic and quasi static pressures. The frequency of this oscillation is 1047 Hz. After the impact, water converts from the corner and travels along the horizontal part which creates quasi-static pressures on sensors 9 and 10.

Figure 5.5 represents the measured horizontal and vertical forces (F_h and F_v) which are calculated from the integration of pressures in Figure 5.4. Forces are normalized by ($\rho g H h_s$) and time is normalized by T. Kisacik et al. (2011a) show that measured force values in both directions are very sensitive to the variation of h_s and increasing h_s results in a high impact force both on the horizontal and vertical part of the scaled model. The transition between SBW and BWSAT is indicated by the occurrence of two asymmetric humps on the F_h history (Oumeraci et al., 1993). Peregrine (2003) explains generation of sequential humps as follows: the first hump is the result of upward acceleration of a thin, narrow wave crest. This is followed by a pressure drop at the maximum upward excursion of the water and the second hump is developed by the downward acceleration of the upraised water. In this

Table 5.1 Ratio of dynamic and quasi-static components and variation of rising times (t_r) for SBW

	h_s 0.075 m	0.105 m	0.135 m	0.165 m
F_{h_dy} / F_{h_qs} :	1.00-1.12	1.00-1.30	1.00-2.28	1.00-2.48
F_{v_dy} / F_{v_qs} :	1.00-1.11	1.00-3.00	1.00-10.7	1.00-7.67
p_{max_dy} / p_{max_qs} on vertical part :	1.00-1.55	1.00-1.46	1.00-2.45	1.00-2.49
p_{max_dy} / p_{max_qs} on horizontal part :	1.00-1.34	1.00-8.00	1.00-26.57	1.00-21.76
t_r (F_h) :	70-120 ms	60-200 ms	60-203 ms	51-200 ms
t_r (F_v) :	74-129 ms	0.4-120 ms	0.2-90 ms	0.15-47 ms
t_r (p_{max}) on the vertical part :	13-44 ms	14-90 ms	3-100 ms	2-120 ms
t_r (p_{max}) on the horizontal part :	0.8-140 ms	0.2-89 ms	0.2-17 ms	0.2-16 ms

study, the first hump (t_6) is more developed because of the additional quasi static pressures which are coming from the upper part of the vertical wall and this makes the recognition of the second hump difficult (t_8) (Figure 5.5b). This additional pressure is the effect of the horizontal part of the scaled model. The irregularities at time t_3 and t_5 are due to the pressures measured at SWL and the upper corner of the vertical part. These times also represent the time of the first and the second impact instants. These are the positions where possible high dynamic pressures will occur. In addition, the signal shape of F_v is composed of a dynamic part (first peak) and a quasi static part (second hump) (Figure 5.5a). According to the velocity of the upper jet, either the dynamic or quasi static portion will be higher. Depending on the trapped air at the corner, these dynamic components may follow an oscillating behavior. The total duration of F_h and F_v are about 0.217T and 0.137T respectively.

5.5.3 Characteristics of maximum pressures and forces

Figure 5.6 shows the typical signal shape examples of F_h and F_v for the occurrence of high dynamic components. The first impact peak is due to the relatively high pressure at the SWL and the second impact peak is the result of the secondary impact at the corner of the scaled model (Figure 5.6a). Table 5.1 shows the ratio of maximum dynamic (dy) and quasi-static (qs) components for the force and pressure values ($F_{\max\_dy}$ / $F_{\max\_qs}$ and p_{max_dy} / p_{max_qs}) and the related rising times (t_r). t_r is the time duration between times of impact start and maximum

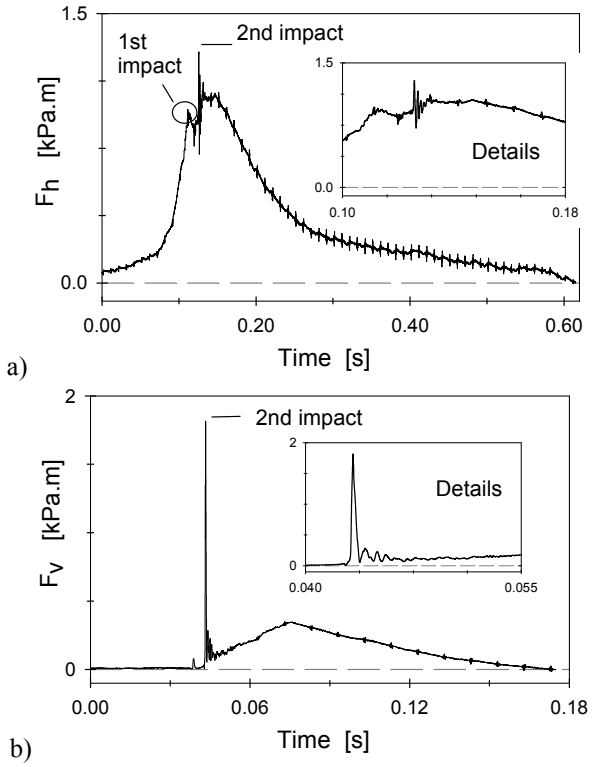

Figure 5.6 *Typical signal shapes for a) maximum F_h and b) maximum F_v in the case of SBW*

pressure. Obviously $F_{\max\_dy} / F_{\max\_qs}$ and p_{max_dy} / p_{max_qs} on the vertical part are increasing with the increase of the h_s up to a threshold value of 2.5, which is also mentioned by Kortenhaus and Oumeraci (1998). However, on the horizontal part $F_{\max\_dy} / F_{\max\_qs}$ and p_{max_dy} / p_{max_qs} are significantly higher and range up to 10.7 and 26.57 respectively. For the horizontal peak pressures and forces, t_r values are approximately between 2-120 and 51-203 ms, respectively. On the horizontal part dynamic forces (Figure 5.6b), which are short in rise-time and large in magnitude are remarkable. Therefore, related t_r for pressures and forces range between 0.2-140 and 0.2-129 ms, respectively.

5.5.4 Evaluation of instantaneous pressure profiles

Figure 5.7 illustrates the instantaneous pressure distributions both on the vertical and horizontal parts for the example shown in Figure 5.3. Each profile represents time instants from t_1 to t_8. On the vertical part, x and y axis show the normalized

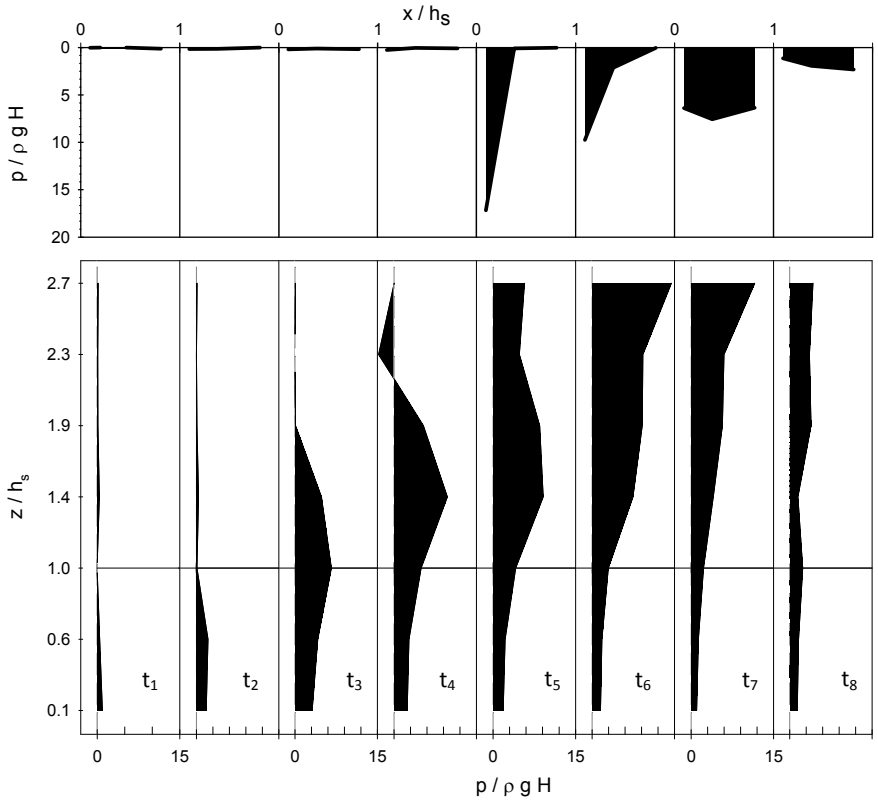

Figure 5.7 *Instantaneous pressure profiles both on vertical (lower graphs) and horizontal parts (upper graphs) for time instants t_1 to t_8 in Figure 5.3 (SBW)*

instantaneous pressure, p, and vertical distance from the model toe, z, respectively. For the horizontal part, an inverse orientation of the axis is considered. From left to right, the figures show the evolution of the pressure distribution in time. The sixth and seventh profiles represent the instantaneous pressure distribution at the time of the maximum horizontal and vertical forces respectively. Although there is a phase difference between them, the pressures which are effective during both instants will be a critical issue for overturning moment calculations. Also, it should be considered that the moment lever for F_h is larger compared to the moment levering arm on a simple vertical wall. Due to the high pressures at the upper corner, the centroid of the pressure profile shifts upwards which increases the moment levering arm. At the instant t_4, the negative pressure area is clearly noticeable which will be an important issue for removing any single element in a blockwork type coastal structure. The location of maximum pressure at the time of impact (t_4) is above the SWL with an elevation z around 1.4 h_s. However, overall the maximum pressures are measured at the upper corner of the scaled model at sensor 8.

5.6 CASE-II: BREAKING WAVES WITH SMALL AIR TRAP (BWSAT)

If the approaching wave height increases, impact shapes gradually shift from the case of SBW to breaking waves with small air trap (BWSAT). It should be considered that the transition between boundaries of cases always depends on subjective observations related to the amount of trapped air. In this case, the wave collides on the vertical part with a more parallel or slightly curved face. Little air is enclosed in the relatively small curve of the wave face.

5.6.1 Evaluation of water surface profile

Figure 5.8 shows some example photos (at instants t_1 to t_8) describing a sequential change of BWSAT ($h_s = 0.105\,m,\ H = 0.067\,m\ and\ T = 2.2\,s$). The onset of breaking occurs at a distance before the wall location (Figure 5.8a). White spikes are the evidence that waves already start to lose some energy through breaking of the wave tongue. The occurrence of parallel faces is not observed during impact which is similar to the findings of Hull and Muller (2002) (Figure 5.8b and Figure 5.8c). The accelerated wave crest arrives at the wall, before the water level rises at the wall and it fills the space between wall and wave crest. Therefore, it traps an air pocket (Figure 5.8d). Wave crest and trapped air break up into pieces very soon. Thus, the entire horizontal momentum of the breaker front is destroyed in a very short duration (Kirkgoz, 1995). Bullock et al. (2007) describe this explosive hit with a crack sound which makes the channel vibrate and sends sprays up to 20 m. The spray rises parallel to the vertical part and hits at the upper corner of the scaled model (Figure 5.8e). Aerated water follows the spray and creates the maximum quasi static pressure (Figure 5.8f). The projected upward water reaches its maximum level and then starts a nearly free fall (Figure 5.8g). Finally, Figure 5.8h represents the time of maximum downward acceleration. On the vertical part of the scaled model, the impact occurs on the location of sensor 4 which shows a little downward shift, compared to the location in the case of SBW.

5.6.2 Time series of pressures and forces

The corresponding pressure records at various levels on the scaled model are shown in Figure 5.9. Sections from t_1 to t_8 display the measured pressures at the instants of photos which are shown in Figure 5.8. In the case of BWSAT, the wave impact results in an impulsive pressure with very high magnitude and short duration. In this particular example, the maximum peak pressure occurs at the location of sensor 4 with a single-peaked pressure profile (42 ρgH or 27.6 kPa). On the vertical part, the highest impact pressure of 89.6 ρgH (or 109 kPa) is also measured in this case at SWL ($h_s = 0.135\,m$). This confirms the observation by Bagnold (1939) who states that the smaller the amount of trapped air is the larger the impact pressure

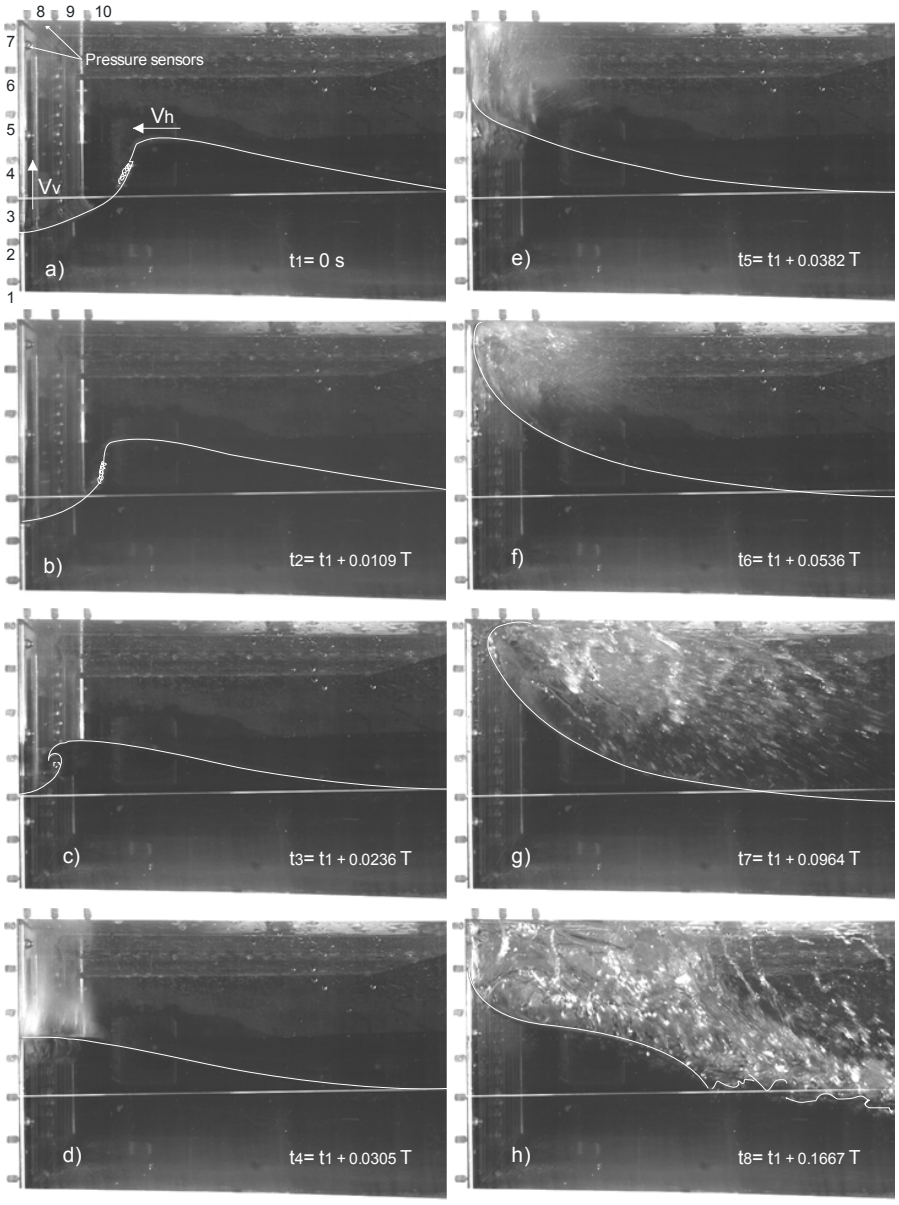

Figure 5.8 *Sequential photos from HSC records for the wave shape developments of BWSAT. HSC results are synchronized with pressure and force records ($h_s = 0.105\ m,\ H = 0.067\ m$ and $T = 2.2\ s$)*

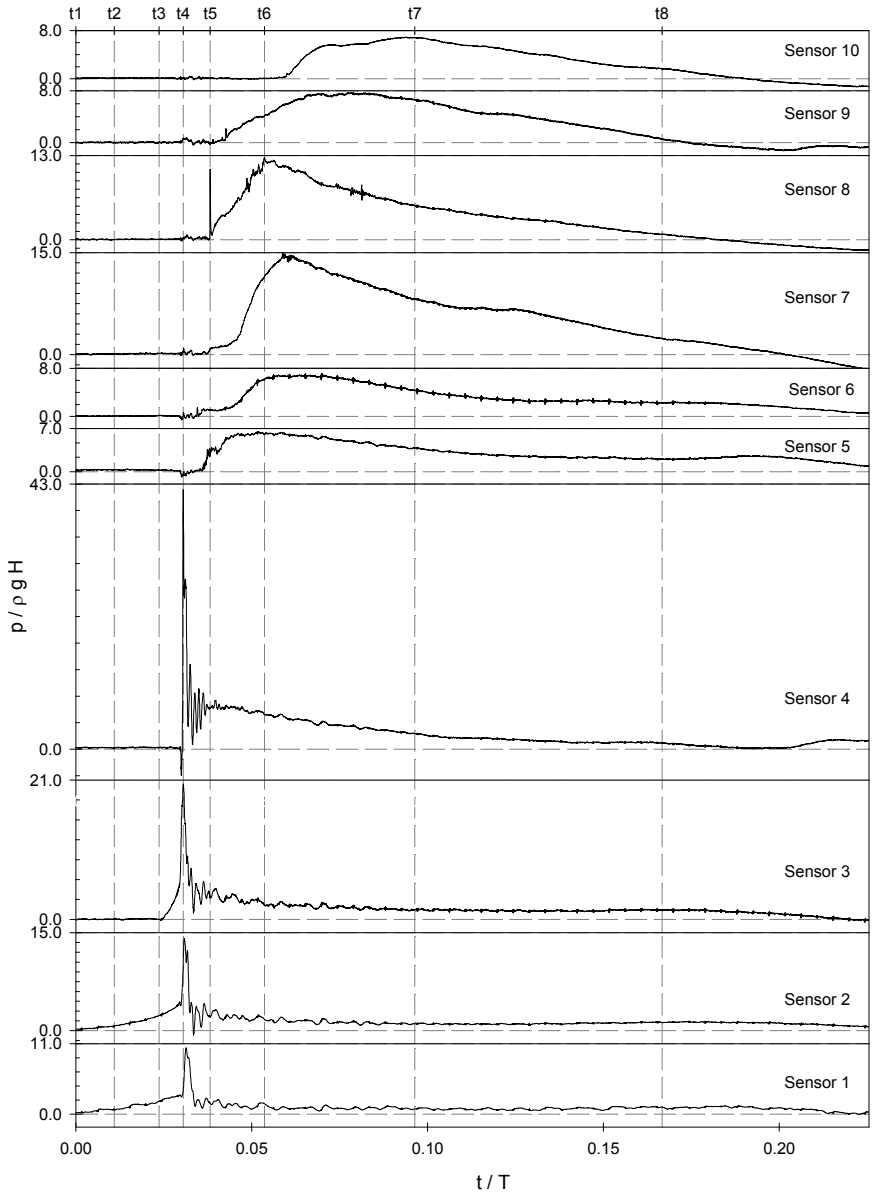

Figure 5.9 *Simultaneous pressure records from the 10 pressure sensors for the case of BWSAT. Time from t_1 to t_8 represents pressure profiles at the time instant of photos in Figure 5.8*

becomes. However, Peregrine (2003) mentioned that the air pocket is not essential for the high pressures. In addition, small irregularities which follow the peak pressure are due to the entrapped air bubbles (sensor 4). The peak pressure is quickly directed to downwards from the impact point through the water body. The downward propagation velocities between sensors are quite similar to case of SBW and are measured at 900 m/s (p4–p3), 90 m/s (p3–p2), and 36 m/s (p2-p1).

Furthermore, the upward spray results in small irregularities on the signal of the sensors above the impact point (sensor 5, 6 and 7) and it creates a sharp single spike at sensor 8. The overall highest impact pressure of $123\ kPa$ is also measured at this location in the case of BWSAT ($h_s = 0.135\ m,\ H = 0.114\ m$ and $T = 2.2\ s$).

Figure 5.10 represents measured F_h and F_v which are calculated from the integration of pressures in Figure 5.9. Oumeraci et al. (1993) described the force history as a sharp single peak followed by a quasi-static force and explained the superimposed irregularities as the result of high frequency and small amplitude oscillations. On the time series of F_h (Figure 5.10b), the magnitude of the quasi-static force is more significant than the quasi-static force on a simple vertical wall which is due to the effect of the horizontal part. However, no effect of the horizontal part on the dynamic component of F_h can be noticed. The small spike on F_v (around t_5) is due to the impact of water spray. For this particular example, this spike is smaller than the quasi static component which is not always true. The total duration of F_h and F_v are about 0.204 T and 0.129 T respectively. The duration of F_v in this case is slightly shorter compared to the duration of F_v in the case of SBW. This is due to the differences between upward velocities of water jets.

5.6.3 Characteristics of maximum pressures and forces

Figure 5.11 shows two examples of very high F_h and F_v measured at $h_s = 0.135\ m$. The signal shape of F_h (Figure 5.11a) is a single sharp peak which is in line with literature. In the signal shape of F_v (Figure 5.11b), several sharp peaks occur in sequence. These are the result of impacts due to the high velocity water sprays and following aerated jets which occur sequentially. The resulting shape is a summation which appears in an extremely short time interval (see detailed view in Figure 5.11b).

Figure 5.12 displays an example of pressure oscillation, extending in the negative span, at sensor 7 which is located at the upper corner on the vertical part. The main reason for the oscillation is the trapped air at the corner. Schmidt et al. (1992) describe oscillations with negative values by the fact that the trapped air is compressed so much that in re-expanding it throws the water mass back with such a velocity that the pressure drops below the atmospheric pressure value. The frequency of this oscillation is 646 Hz with a negative value of $p_{min}/\rho gH = -25$. This is corresponding to 53% of the positive peak pressure which is remarkably higher than the measurements (38%) of Hattori et al. (1994).

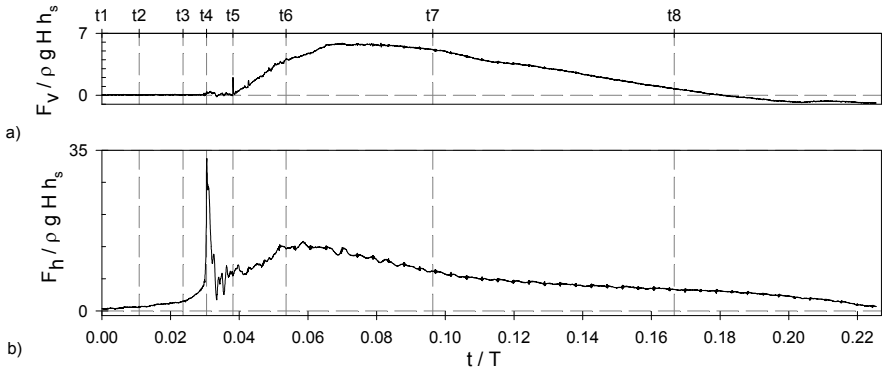

Figure 5.10 *Simultaneous horizontal and vertical force records (F_h and F_v) of BWSAT. Time from t_1 to t_8 represents force profiles at the instant of photos in Figure 5.8*

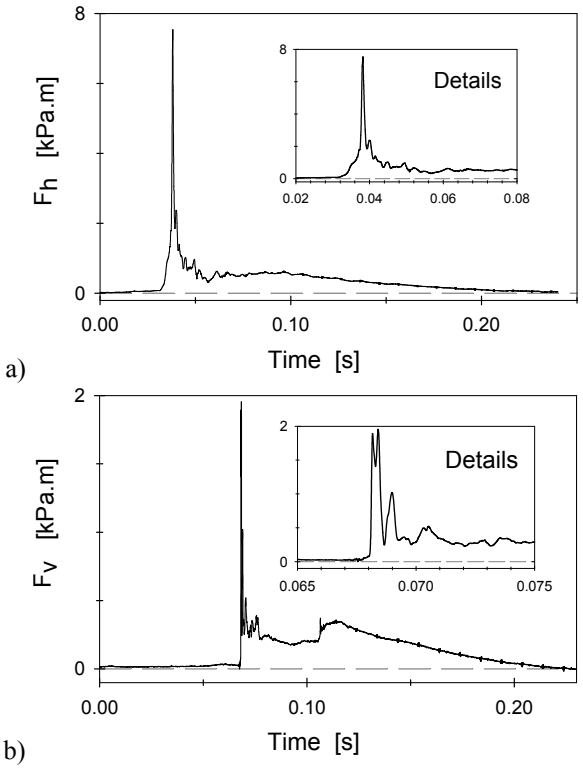

Figure 5.11 *Typical signal shapes for a) maximum F_h and b) maximum F_v in the case of BWSAT*

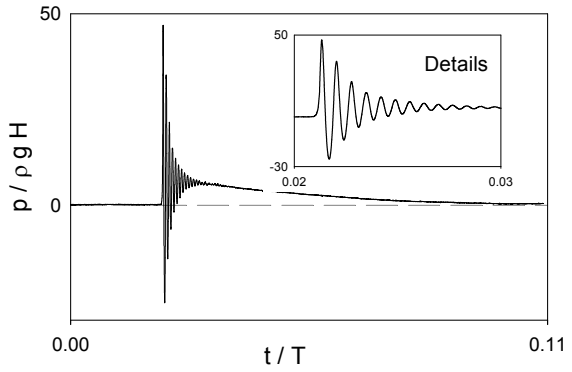

Figure 5.12 *Oscillation of pressure signal at sensor 7, for* $h_s = 0.135\,m$, $H = 0.105\,m$ *and* $T = 2.2\,s$

Table 5.2 shows the variation of $F_{\max\_dy} / F_{\max\_qs}$ and p_{max_dy} / p_{max_qs} and related t_r for the case of BWSAT. For different h_s, the ratio of horizontal forces and pressures are in the range of 1-6.21 and 1-16.40 respectively. Corresponding t_r values are between 3.5-149 and 0.35-42 ms. Bullock et al. (2007) state that the rising time for the peak pressures on the vertical walls are in the range of 80 to 200 ms, which is significantly higher than the measurements in this research. They made large scale tests and measured pressures with different sampling frequency (10 kHz) which will be the possible reasons for the differences. The ratio of vertical forces and pressures are increasing with larger h_s and reach a maximum value of 10 and 16.10 respectively. In addition, t_r for vertical forces and pressures are in the range of 0.15-144 and 0.15-110 ms respectively. In contrast to the magnitude of vertical pressures and forces, their rising times decrease with increasing water depth with a minimum value of 0.15 ms.

5.6.4 Evaluation of instantaneous pressure profiles

Figure 5.13 illustrates two examples of the instantaneous pressure distribution at the times of very high F_h and F_v for the case of BWSAT. From left to right, figures show the time evolution of the pressure distribution. The third and fourth profiles at time t_3 and t_4 (Figure 5.13a and Figure 5.13b) show the instantaneous pressure at the time of maximum F_h and F_v which shows that there is no effect of the horizontal part at the time of maximum F_h. However, it is clear that there is a pressure increase due to the horizontal part at the corner of the scaled model at times t_5 and t_6. These instants show the time of maximum horizontal and vertical quasi static forces. The location of the maximum pressure is found at the elevation $z = 1.4h_s$ which is above the SWL. As it is seen in the case of SBW, some negative pressures which are rather small compared to the maximum positive values are also observed above the SWL.

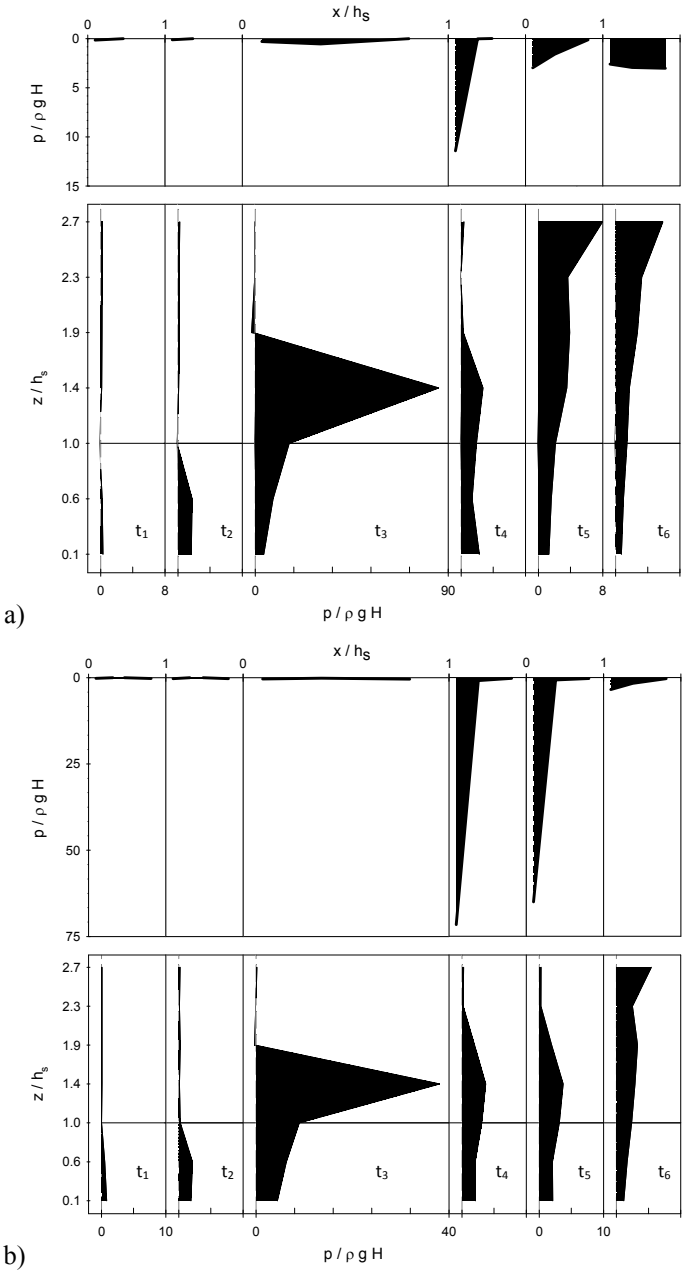

Figure 5.13 *Instantaneous pressure profiles both on vertical (lower graphs) and horizontal parts (upper graphs) for time instants t_1 to t_6 (BWSAT). a) for maximum F_h, b) for maximum F_v*

Table 5.2 Ratio of dynamic and quasi-static components and variation of rising times (t_r) for BWSAT

h_s 0.075 m	0.105 m	0.135 m	0.165 m
F_{h_dy} / F_{h_qs} :1.00-5.30	1.00-5.20	1.00-6.21	1.00-4.15
F_{v_dy} / F_{v_qs} :1.00-3.26	1.00-6.46	1.00-10.00	1.00-6.71
p_{max_dy} / p_{max_qs} on vertical part :1.00-8.70	1.00-5.12	1.00-16.40	1.00-10.87
p_{max_dy} / p_{max_qs} on horizontal part :1.00-2.40	1.00-11.29	1.00-15.20	1.00-16.10
t_r (F_h) :3.5-100 ms	13-149 ms	5-140 ms	13-140 ms
t_r (F_v) :0.2-156 ms	0.15-130 ms	0.15-144 ms	0.15-57 ms
t_r (p_{max}) on the vertical part :0.75-15 ms	0.45-40 ms	0.35-42 ms	0.4-23 ms
t_r (p_{max}) on the horizontal part :0.75-110 ms	0.2-47 ms	0.15- 45 ms	0.15-25 ms

5.7 CASE-III: BREAKING WAVES WITH LARGE AIR TRAP (BWLAT)

After further increasing the wave height, the wave starts to break early on the sloping foreshore. The wave profile curves more before hitting the wall and encloses a large amount of air. The boundary between the case of BWSAT and BWLAT is less clear than the boundary between the other cases and in some cases, it is easy to confuse these two types.

5.7.1 Evaluation of water surface profile

Figure 5.14 shows eight photographs in sequence of the development of a wave breaking in the case of BWLAT ($h_s = 0.105\,m,\ H = 0.078\,m\ and\ T = 2.2\,s$). Compared to the previous cases, the influence of the wall on the breaking onset is negligible. The first photograph shows the jet of the breaking wave curling over the wave front (Figure 5.14a). The water level at the wall is quite stable until the wave crest reaches the wall (Figure 5.14b). The crest impact occurs at the SWL which is lower compared to the corresponding points in the previous cases. The photo in Figure 5.14c shows the instant at the time of highest pressure and force on the vertical part. The shape of the trapped air looks like a semi-circle with a diameter equaling the breaking wave height (Figure 5.14c). Enclosed air in the semi-circle is compressed by the horizontal momentum of flow. Lugni et al. (2010a) describe this stage by an isotropic compression/expansion of the trapped air in the semicircle. Then a subsequent anisotropic compression/expansion process is followed. Air is compressed up to a certain pressure level and after a threshold value is reached, it bursts through an outlet between wall and wave crest. This reduces the enclosed air volume and thickness of the semi-circle (Figure 5.14d). Due to the compression, the trapped air breaks up into large and small air bubbles (Figure 5.14e). Larger air bubbles leave the water quickly while the smaller bubbles stay longer (Figure 5.14g and Figure 5.14h). An aerated water jet rises on the vertical part and hits the corner of the scaled model which results in the high pressure and force on the horizontal part (Figure 5.14f).

5.7.2 Time series of pressures and forces

Figure 5.15 shows pressure signals for the example presented in Figure 5.14. For this particular example, the maximum pressure ($14\,\rho gH$ or 10.8 kPa) on the vertical part is recorded at sensor 4. The overall highest pressure in this case is measured at SWL with a value of $95\,kPa$ (at $h_s = 0.135\,m$). Sensors 1 to 4, which are below the water, show an in-phase oscillation with a low frequency of 82 Hz. Hull and Muller (2002) mentioned that oscillations are in phase only at the positions covered by the air pocket. However, it is seen that sensor 1 is not covered by the air pocket (Figure 5.14d) and shows the same oscillation character. In

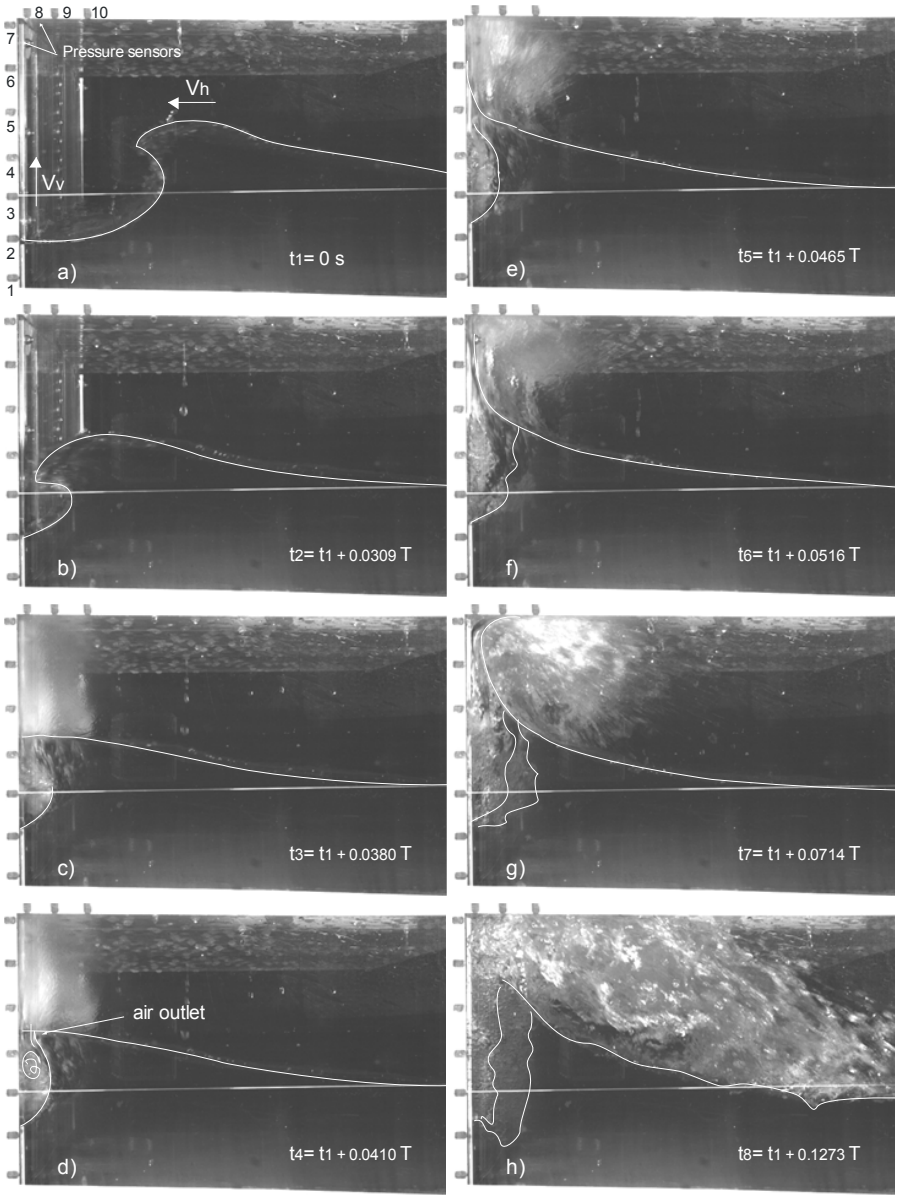

Figure 5.14 *Sequential photos from HSC results for the wave shape developments of BWLAT. HSC results are synchronized with pressure and force records* ($h_s = 0.105\,m,\ H = 0.078\,m$ *and* $T = 2.2\,s$ *)*

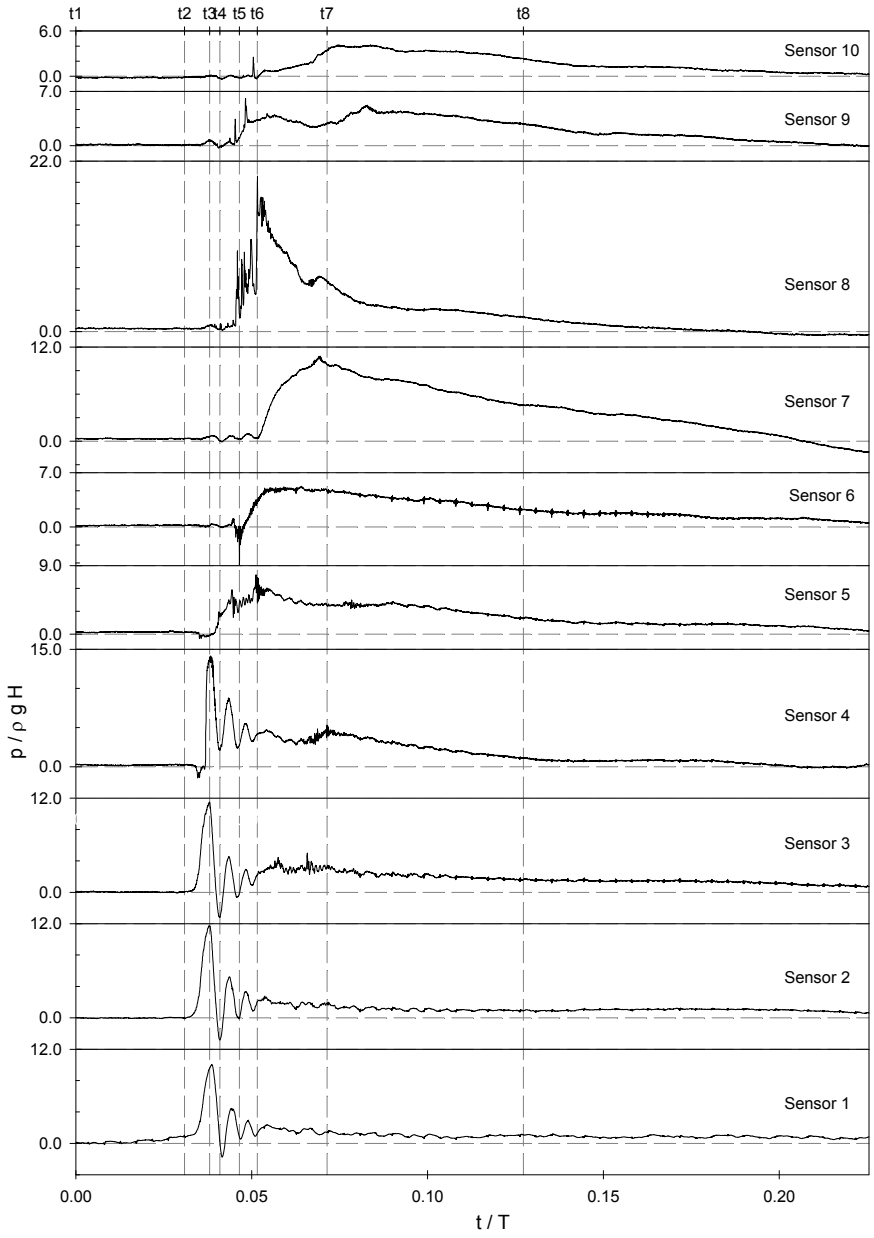

Figure 5.15 *Simultaneous pressure records from the 10 pressure sensors for the case of BWLAT. Time from t_1 to t_8 represents pressure profiles at the time instant of photos in Figure 5.14*

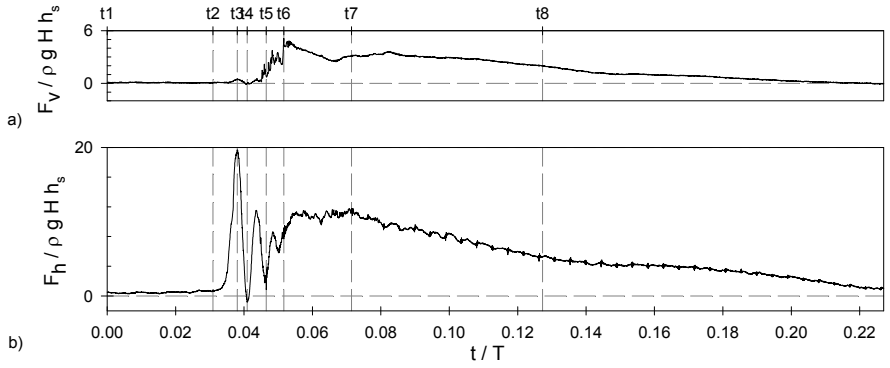

Figure 5.16 *Simultaneous horizontal and vertical force records of (F_h and F_v) BWLAT. Time from t_1 to t_8 represents force profiles at the instant of photos in Figure 5.14*

addition, results from sensor 1 to 3 show negative values with a maximum value of $-3.3\ \rho gH$ at sensor 3. Negative pressures by the end of the first oscillation are common features in the case of BWLAT and similar behavior has been measured by Bullock et al. (2007); Oumeraci et al. (1993); Hattori et al. (1994) and Walkden et al. (1996). Apart from Schmidt et al. (1992) approach, another idea which says that the cyclic pressure oscillation can also be explained by the sequential process of compression and volume reduction, may be developed based on observations between the correlation of the HSC and pressure recordings. This is the volume of trapped air pocket and reduction will occur either by air leakage or fragmentation of the air pocket. Very recently, Lugni et al. (2010b) describe the pressure oscillation in two stages. The first stage is the isotropic compression/expansion stage which is mainly governed by the local liquid acceleration and by air leaking out of the air pocket. This stage has been observed until the second peak occurs. The second stage is the anisotropic compression/ expansion stage where the fluid dynamics are mainly influenced by the air-cavity oscillations superposed on some remaining effects due to the air leaking. This occurs during the remaining cycles.

Pressure transfers downwards through the air water mixture with a propagation velocity of 149 and 39 m/s between sensors (p3–p2) and (p2–p1), respectively. The propagation velocity between p3-p2 is significantly lower compared to the velocity (900 m/s) in the previous cases. But it quickly decreases to a constant value of about 36 m/s in all cases. On the pressure signal of the horizontal part (sensor 8, 9 and 10), initial small spikes are the results of the water spray impact comes from the crest hitting on the vertical part while the following high pressures occur when aerated water jet hit on the horizontal part.

Figure 5.16 shows F_h and F_v of the example in Figure 5.15. Similar to the pressure results in Figure 5.15, F_h shows an oscillation with the same frequency. Schmidt et al. (1992) and Oumeraci et al. (1993) describe the characteristics of F_h with two adjacent force peaks in which the first one describes the force due to hammering of

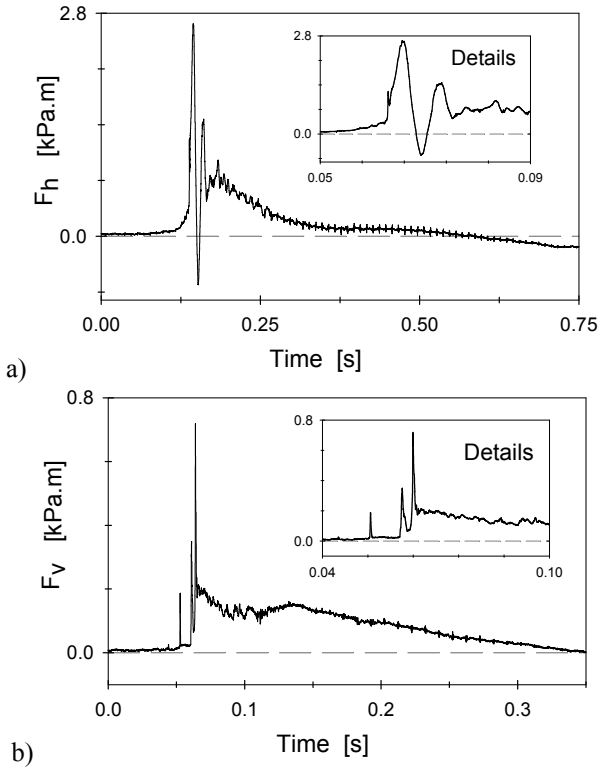

Figure 5.17 *Typical signal shapes for a) maximum F_h and b) maximum F_v in the case of BWLAT*

the crest and the second one is due to compression. In this example, the first peak does not visualize but it can be seen on the small detail visualization in Figure 5.17a. In addition, a relatively low vertical force (F_v) is measured. It shows some small spikes due to the spray and a maximum force at the time of the aerated jet impact (t_6).

5.7.3 Characteristics of maximum pressures and forces

Figure 5.17 gives some examples of F_h and F_v with very high magnitudes ($h_s = 0.105\ m,\ H = 0.117\ m\ and\ T = 2.2\ s$). The negative value on F_h is about 22.8% of the maximum peak value (Figure 5.17a). The water spray due to the wave crest impact is the cause for the first two individual sharp peaks occurring on F_v (Figure 5.17b). The consecutive highest peak is the result of an aerated water jet occurring behind the crest impact. However, in the case of BWSAT, the results of individual peaks are merging because of the very small phase difference between them.

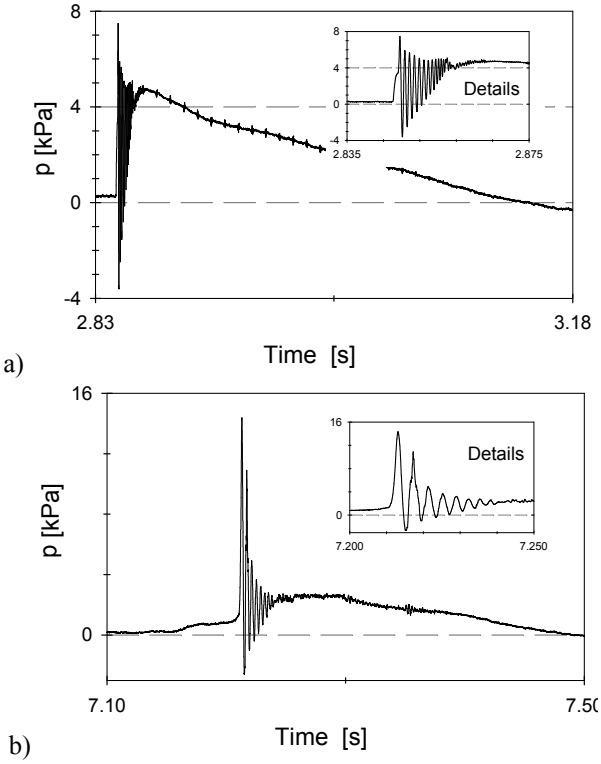

Figure 5.18 *Oscillation of pressure signal at sensor 8 ($h_s = 0.135\ m$ and $T = 2.2\ s$). a) $H = 0.099\ m$ and b) $H = 0.103\ m$*

In addition, Figure 5.18 displays two examples of pressure oscillation which occurred at sensor 8. Trapped air at the corner of the scaled model is the cause of this oscillation. The frequencies of these oscillations are 972 and 285 Hz respectively.

Table 5.3 shows the variation of forces, pressures and related value of t_r for the case of BWLAT. The ratio of F_{h_dy} / F_{h_qs} and F_{v_dy} / F_{v_qs} stays between 1-4.90 and 1-7.30 and the related t_r are measured between the ranges of 1.2-121 ms and 0.15-149 ms respectively. In addition, ratios of p_{max_dy} / p_{max_qs} on vertical and horizontal parts are in the range of 1.00-16.42 and 1.00-1.98 respectively. As it is measured in the case of BWSAT, t_r for horizontal and vertical pressure are in the range of 0.3-50 ms and 0.15-113 ms respectively.

5.7.4 Evaluation of instantaneous pressure profiles

Figure 5.19a shows seven instantaneous pressure profiles of wave impact which is shown in Figure 5.17a. The profile at t_2 shows the time of the maximum F_h. Profile t_3 represents the pressure distribution at the time of maximum negative force. The magnitude of negative pressure is high and almost uniformly distributed. The vertical distribution of negative pressure is not limited by the dimensions of the trapped air. Structures should be designed for the seaward forces as well.

Figure 5.19b shows another example of the instantaneous pressure profiles of BWLAT with a very high impact force. The third and fourth profiles at t_3 and t_4 show the instantaneous pressure at the time of maximum F_h and F_v. The location of F_h is at the SWL which is lower compared to the location in case of BWSAT. Therefore, for overturning failure modes, the moment levering arm is shorter compared to the moment levering arm in case of BWSAT. There is no effect of the horizontal part at the time of maximum F_h (t_3). However, on the vertical part, a quasi-static pressure distribution exists at the time of maximum F_v (t_4). Although the high pressures which exist at the upper corner of the vertical part (t_5 and t_6) are not critical at the time of maximum forces, they should be considered if any cracks / damage exist or for masonry structures which suffer from removal of blocks. On the vertical part, compared to the previous case the location of the maximum pressure shifts downwards and is located around a point at SWL.

Table 5.3 Ratio of dynamic and quasi-static components and variation of rising times (t_r) for BWLAT

h_s	$0.075\ m$	$0.105\ m$	$0.135\ m$	$0.165\ m$
F_{h_dy} / F_{h_qs}:	1.00-3.93	1.00-4.68	1.00-4.90	1.00-3.88
F_{v_dy} / F_{v_qs}:	1.00-5.87	1.00-7.30	1.00-7.00	1.00-4.89
p_{max_dy} / p_{max_qs} on vertical part:	1.00-10.50	1.00-16.42	1.00-6.07	1.00-10.30
p_{max_dy} / p_{max_qs} on horizontal part:	1.00-6.50	1.00-9.55	1.00-11.38	1.00-11.98
t_r (F_h):	1.2-119 ms	5-121 ms	12-73 ms	7.9-80 ms
t_r (F_v):	0.15-149 ms	0.25-116 ms	0.25-88 ms	1.1-80 ms
t_r (p_{max}) on the vertical part:	0.3-30 ms	0.6-50 ms	1.15-34	0.5-31 ms
t_r (p_{max}) on the horizontal part:	0.15-113 ms	0.3-75 ms	0.25-38 ms	0.2-39 ms

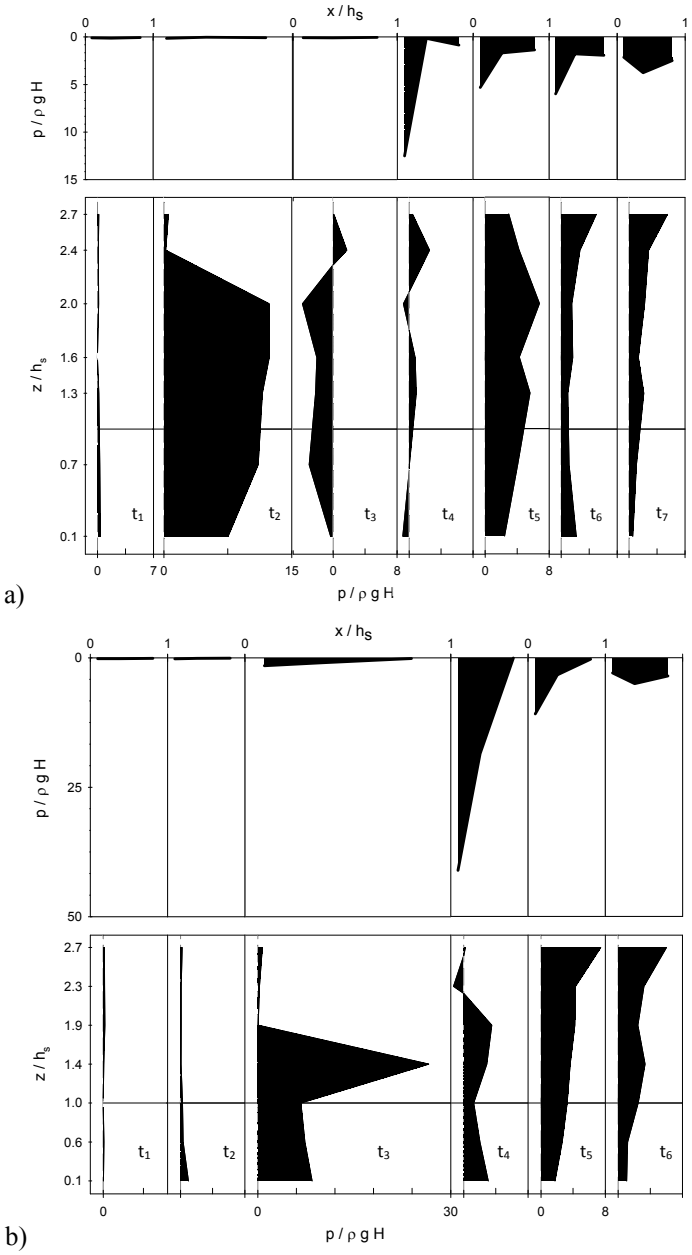

Figure 5.19 *Instantaneous pressure profiles both on vertical (lower graphs) and horizontal parts (upper graphs) for time instants t_1 to t_6 (BWLAT). a) occurrence of high negative F_h, b) occurrence of high positive F_h*

5.8 CASE-IV: BROKEN WAVES (BW)

If the wave height continues to increase, the wave breaks far away from the wall and, as a result, the curling wave tongue strikes the water before hitting the vertical wall. The strike point on the water extends just in front of the wall to the point where no significant effect of broken waves (BW) observed. Depending on the location, the impact of rolling or deflected wave crests from the water surface results in high pressures and forces. The impact characteristics will be a transition between the characteristics of BWLAT and fully broken turbulent bores. In this particular research, results for a fully broken turbulent bore will be discussed and the transition case will be skipped.

5.8.1 Evaluation of water surface profile

Photos from Figure 5.20a-h show BW at eight single instants from t_1 to t_8 ($h_s = 0.105\ m,\ H = 0.111\ m\ and\ T = 2.2\ s$). The onset of breaking occurs early and a lot of air remains in the water. The air-water mixture travels with its turbulent front (Figure 5.20a). The water level at the wall is smaller than the SWL and it is unaware of the approaching bore. Figure 5.20b illustrates the time instant of the first hit which is clearly located between $0.8 - 1\ h_s$. The bore front covered with foam is compressed (Figure 5.20c). Aerated water deflects upwards and creates the second impact at the upper corner (Figure 5.20d). Newly trapped air in both impacts (on the vertical and horizontal part) and water falling down contribute to the amount of entrained air in front of the structure.

5.8.2 Time series of pressures and forces

Recorded pressures from the BW impact shown in Figure 5.20 are displayed in Figure 5.21. For this particular example, the largest maximum pressures appear at sensors 7 ($11.4\ \rho gH\ or\ 12.4\ kPa$) and 8 ($10.1\ \rho gH\ or\ 11\ kPa$). In addition, the overall largest pressures ($36\ kPa\ and\ 58\ kPa$) are recorded for the same locations at the highest water level ($h_s = 0.165\ m$). Due to the damping effect of entrained air, low quasi-static pressures are measured on the vertical part. However, the second impact at the corner produced by the deflected water creates relatively high dynamic pressures even when it holds entrained air. This might be explained by a reduction in the amount of entrained air or more importantly by the differences between the impact velocity of the first and second impacts occurring on the vertical and horizontal parts (2.7 and 1.5 m/s).

Figure 5.22 shows F_h and F_v which are obtained by integrating the pressures in Figure 5.21. Shapes of the force signals are quite similar to the shape of signals in the case of SBW. In this case, the magnitudes of force are relatively small. This confirms findings of Oumeraci et al. (1993) who measured the smallest impact pressures and lowest impact forces. In addition, the total duration of forces F_h ,F_v, is about 0.215 T and 0.140 T and the durations are similar with the findings in SBW.

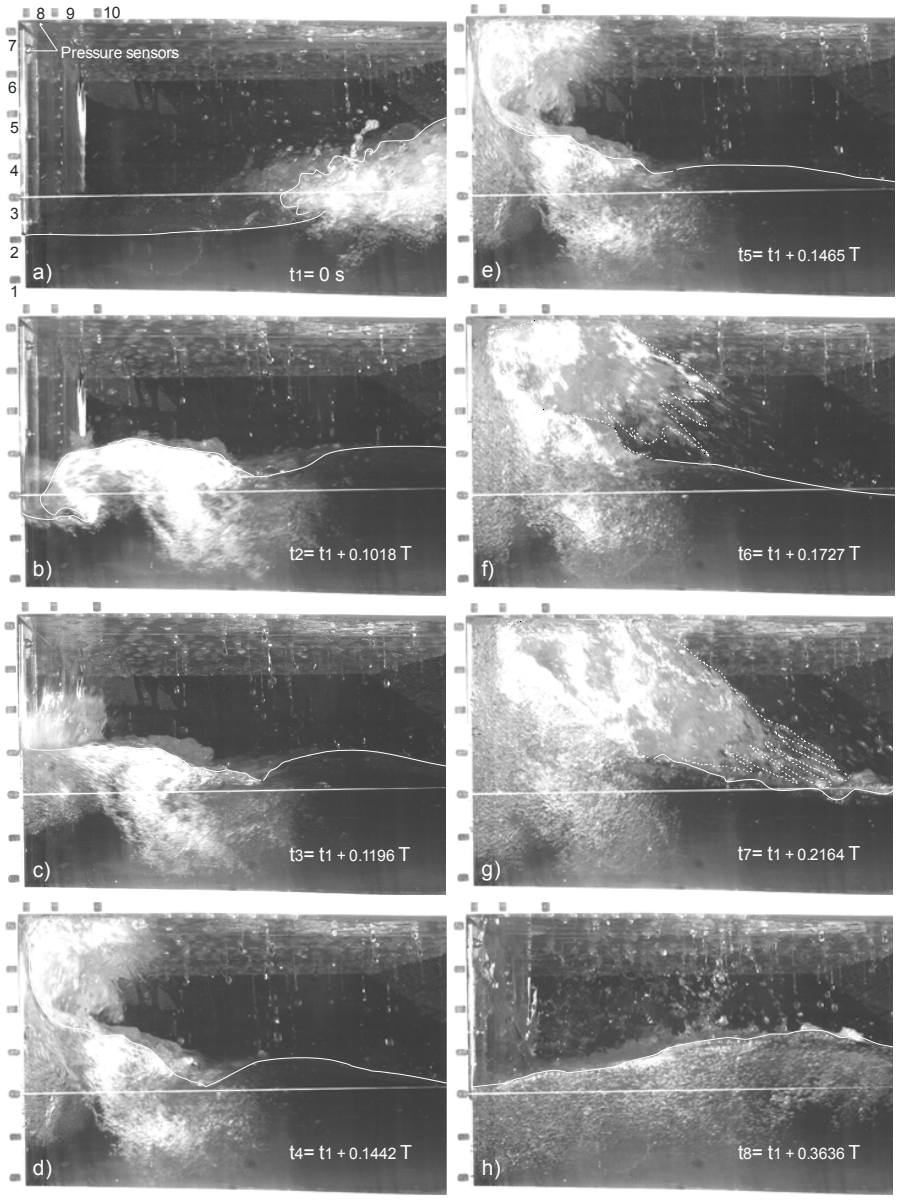

Figure 5.20 *Sequential photos from HSC results for the wave shape developments of BW. HSC results are synchronized with pressure and force records ($h_s = 0.105\ m$, $H = 0.111\ m$ and $T = 2.2\ s$)*

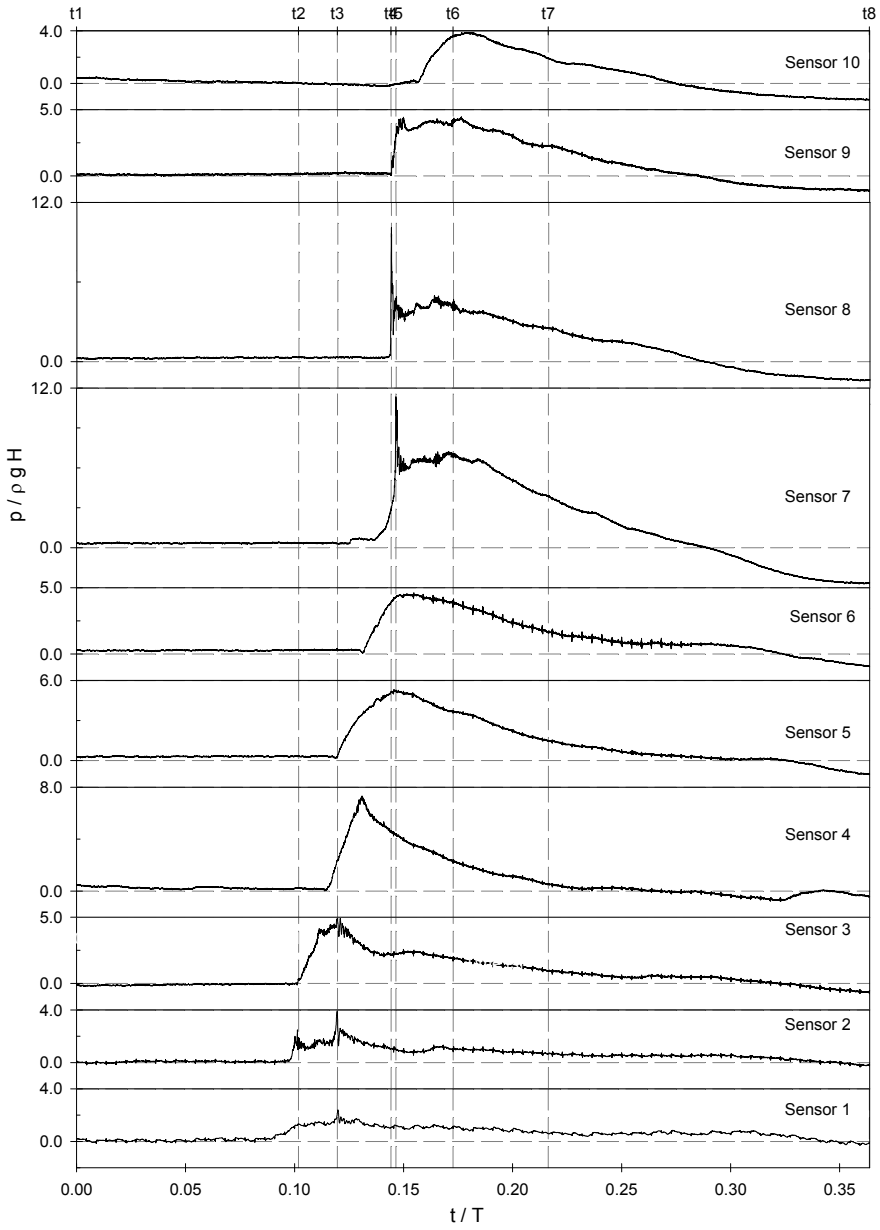

Figure 5.21 *Simultaneous pressure records from the 10 pressure sensors for the case of BW. Time from t_1 to t_8 represents pressure profiles at the time instant of photos in Figure 5.20*

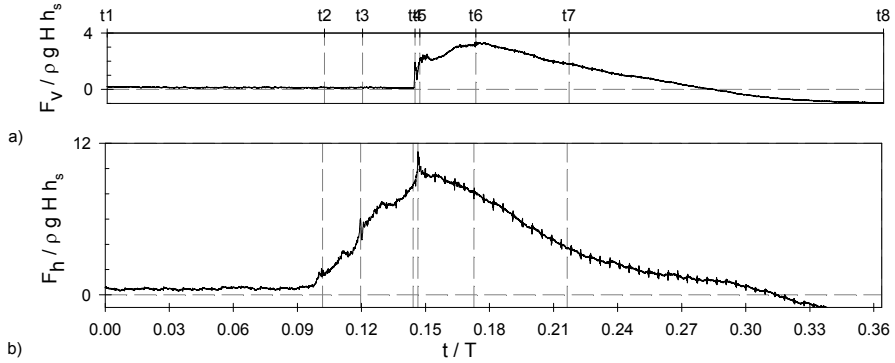

Figure 5.22 *Simultaneous horizontal and vertical force records (F_h and F_v) of BW. Time from t_1 to t_8 represents force profiles at the instant of photos in Figure 5.20*

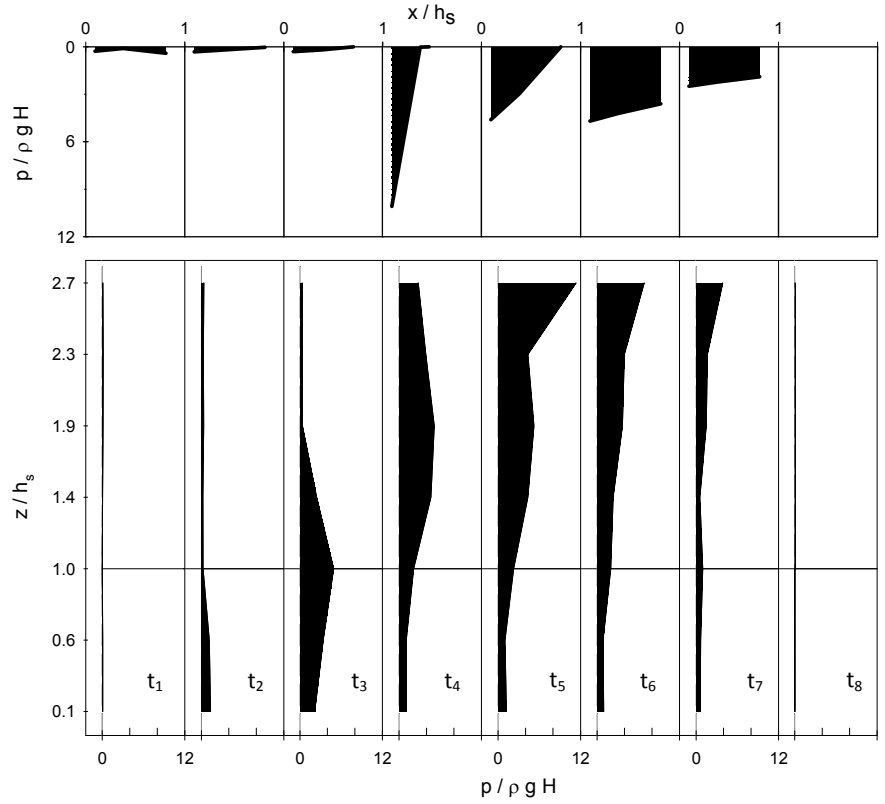

Figure 5.23 *Instantaneous pressure profiles both on vertical (lower graphs) and horizontal parts (upper graphs) for time instants t_1 to t_8 in Figure 5.20 (BW)*

Table 5.4 Ratio of dynamic and quasi-static components and variation of rising times (t_r) for BW

h_s	$0.075\ m$	$0.105\ m$	$0.135\ m$	$0.165\ m$
F_{h_dy} / F_{h_qs}:	1.00-1.40	1.00-1.36	1.00-1.40	1.00-1.34
F_{v_dy} / F_{v_qs}:	1.00-2.00	1.00-3.10	1.00-5.00	1.00-3.20
p_{max_dy} / p_{max_qs} on vertical part:	1.00-3.50	1.00-2.30	1.00-4.80	1.00-2.20
p_{max_dy} / p_{max_qs} on horizontal part:	1.00-1.60	1.00-5.00	1.00-10.00	1.00-10.00
t_r (F_h):	70-165 ms	61-249 ms	34-171	66-195
t_r (F_v):	2.2-171 ms	1-149 ms	0.5-118	1-108
t_r (p_{max}) on the vertical part:	3-115 ms	2.5-130	2-122	2-95
t_r (p_{max}) on the horizontal part:	1.7-259 ms	0.5-96	0.5-79	0.9-71

5.8.3 Characteristics of maximum pressures and forces

Table 5.4 shows the ratio of forces, pressures and related t_r for the case of BW. The ratio of F_{h_dy} / F_{h_qs} and p_{max_dy} / p_{max_qs} on the vertical part are in the range of 1.00-1.40 and 1.00-4.80 respectively. As it is observed in all cases, the ratio of vertical forces and pressures increases with an increase of h_s and reaches a maximum value of 5 and 10 respectively. Although the impact pressures and forces on the vertical part tend to be lower than in the previous cases, rising times are longer and starts from 2 and 34 ms respectively. In addition, both pressure and forces on the horizontal part have smaller rising times starting around 1 ms.

5.8.4 Evaluation of instantaneous pressure profiles

Figure 5.23 illustrates the instantaneous pressure profiles (from t_1 to t_8) for the example which is displayed in Figure 5.20. As it s mentioned above, the impact occurs at or below the SWL. Profiles at t_3 and t_5 represent the pressure distributions at the time of maximum horizontal pressure and force. Generally, on a simple vertical wall, the time of maximum pressure coincides with the time of maximum horizontal force which is not the case here. Pressures at the upper corner increase due to the effect of the horizontal part and this shifts the time of the maximum F_h from time t_3 to t_5. In the new situation, the moment levering arm for

the F_h is longer and some additional forces are appearing on the horizontal part. Therefore, forces on a simple vertical wall are less critical for the design because of the smaller moment levering arm. These should be considered in the design.

5.9 VARIATION OF VELOCITIES AND ACCELERATIONS COMPONENTS

The wave crest approaches the wall with a horizontal velocity (V_h) while the water at the wall rises with a vertical velocity (V_v) (Figure 5.3a, Figure 5.8a, Figure 5.14a and Figure 5.20a). The related accelerations of both components are a_h and a_v. The ratio of V_h/V_v is an important parameter to define the breaker type. As mentioned before, Oumeraci et al. (1993) categorized waves based on the ratio of (d_s/d_w) and V_h/V_v. They assumed $V_h/V_v \ll 1$ for SBW, $V_h/V_v \geq 1$ for BWSAT, $V_h/V_v > 1$ for BWLAT and $V_h/V_v \gg 1$ for BW.

Figure 5.24 and Figure 5.25 show the development of V_h, V_v and a_h, a_v in time for SBW, BWSAT and BWLAT. All velocities are measured based on the spatial displacements of the wave components between two adjacent frames of the HSC records. Velocity and acceleration values are normalized by the wave velocity in the shallow water ($\sqrt{gh_s}$) and the gravitational acceleration (g) respectively. Measured velocities are compared with the theoretical velocity calculated from Cnoidal wave theory, given in Equation 3. Time t_1, t_2 and t_3 show the velocities at instants in Figure 5.3, 5.14 and 5.18 in which t_3 is the time of impact.

Equation 5.1 is using Stokes' second definition of wave velocity, which is the velocity of the propagation of the wave form when the horizontal momentum of liquid has been reduced to zero by the addition of a uniform motion (Wiegel 1959).

Equation 5.1 $$\frac{C}{\sqrt{gh_s}} = \sqrt{1 + \frac{H}{h_s}}$$

In SBW (Figure 5.24), the horizontal velocity is almost constant ($\sim 1.3\sqrt{gh_s}$) up to the last stage of merging, where it is slightly higher than the results calculated from Cnoidal wave theory. In the surfzone, Svendsen (1986) measured the phase velocity in the range of $(1.1 - 1.4)\sqrt{gh_s}$. However the vertical velocity is increasing with higher acceleration around the contracting region and at the time of impact both velocities are reaching an almost identical value of $2.4\sqrt{gh_s}$. For SBW, Oumeraci et al. (1993) mentioned that the vertical velocity is quite higher than the horizontal one ($V_h/V_v \ll 1$) which is not the case here. Instead, a more general description can be formulated by stating that the vertical displacement of the water level occurs before the horizontal one. After infillment of the gap, a vertical jet emerges and reaches a velocity of $4\sqrt{gh_s}$ with an acceleration of 20g. This high acceleration is the cause for the very high pressures at sensors 7 and 8.

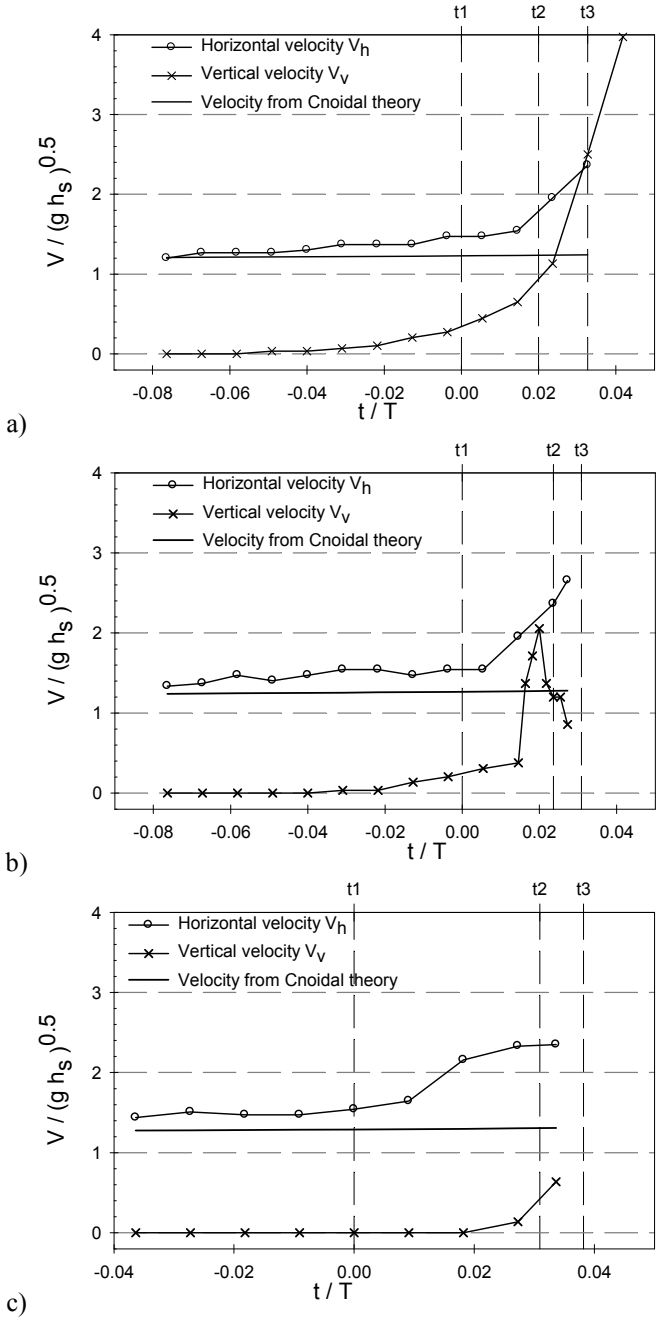

Figure 5.24 *Variation of velocities (V_h, V_v) a) SBW, b) BWSAT and c) BWLAT*

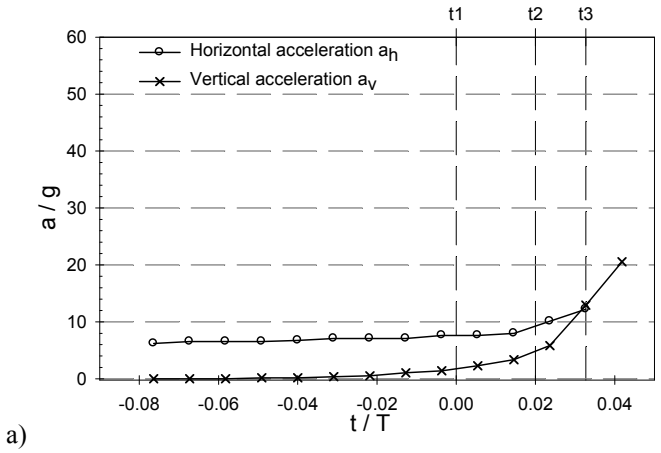

a)

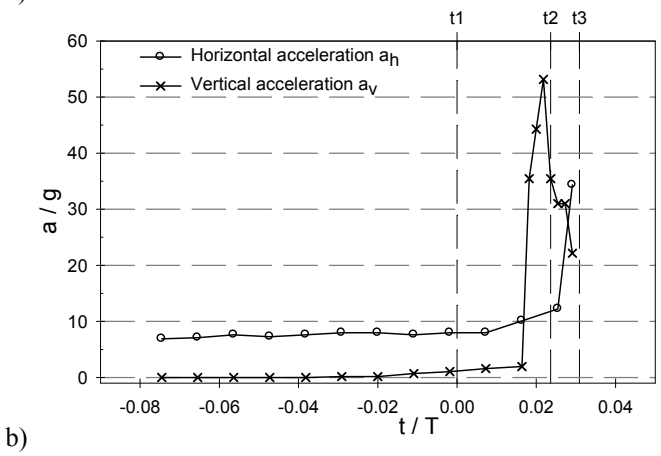

b)

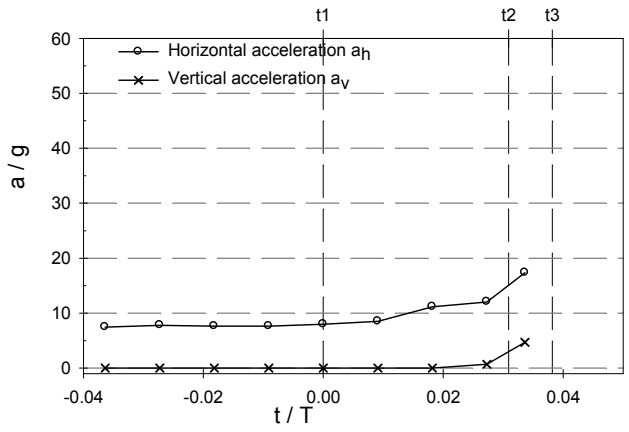

c)

Figure 5.25 *Variation of accelerations (a_h, a_v). a) SBW, b) BWSAT and c) BWLAT*

Figure 5.25 shows the results for BWSAT, $V_h/V_v \geq 1$, which is compatible with Oumeraci's findings. After a certain point, the wave crest curves enough preventing no further accelerate. The highest acceleration is observed in this case, being 52g. The lowest vertical acceleration is measured at BWLAT (Figure 5.25c). The water level at the wall is quite stable just before the wave crest hits the wall and $V_h/V_v \gg 1$.

5.10 DISTRIBUTION OF LOCAL AND INSTANTANEOUS PRESSURE PROFILES

Figure 5.26 and Figure 5.27 show normalized local peaks and instantaneous pressure profiles for ten wave impacts. On the local peak profiles, lines pass through the maximum values of all individual sensors. However, instantaneous pressure profiles on the vertical and horizontal parts represent profiles which occur at the instant of maximum F_h and F_v respectively. In general, localized peak pressures may not be important for the whole structure integrity, but it may be important in the case of any damage or crack exists. The location around SWL and the upper corner of the scaled model are the two most sensitive locations for receiving very high impact pressures.

For SBW (Figure 5.26a and Figure 5.27a), both pressure profiles above the SWL are showing a relatively high variation, which is due to the vertical acceleration above the impact point. On the vertical part, local and instantaneous pressure profiles are similar because of the long duration of the quasi-static force. In addition, the effect of the horizontal part is clearly seen at the upper corner of the scaled model on the both local and instantaneous pressure profiles.

Figure 5.26b and Figure 5.27b show the pressure profiles for BWSAT. The overall largest pressures are measured clearly above SWL at $z/h_s = 1.4$ and at the attached corner of the horizontal part. On the vertical part, both pressure profiles are different from each other due to the existing of high dynamic pressures. These pressures are high in magnitude and short in duration in which phase differences exist between local peak pressures of different sensors. On the vertical part, the zone of the instantaneous pressures diminishes around $1.85\ z/h_s$. This shows that no effect of the horizontal part is observed on the vertical instantaneous pressure profiles at the time of maximum F_h.

Furthermore, Figure 5.26c and Figure 5.27c display pressure profiles for BWLAT. Compared to the BWSAT, pressures are relatively smaller and the location of the maximum pressure shifts downward ($z/h_s = 1{\sim}1.4$). In some cases, it is even under the SWL (Figure 5.26c). In general, it is seen that the location of p_{max} shifts from a position above SWL for SBW, to below SWL for BWLAT. On the horizontal part, only the locations at the corner ($0.4\ x/h_s$) are exposed to the high pressures and further away, pressures diminish drastically to the quasi-static pressures.

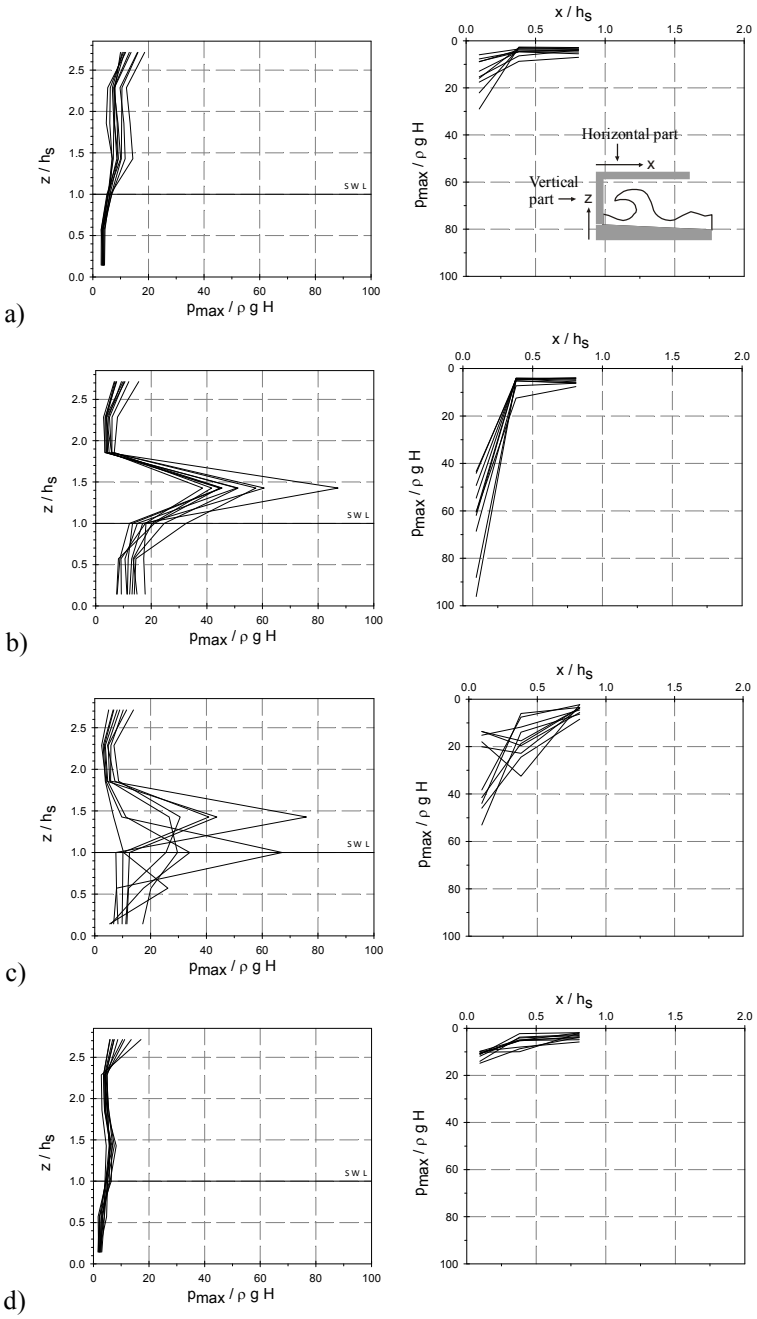

Figure 5.26 *Local peak pressure profiles at the time of maximum horizontal and vertical forces. Lines are passing from the peak pressures of each sensor. a) SBW, b) BWSAT, c) BWLAT and d) BW*

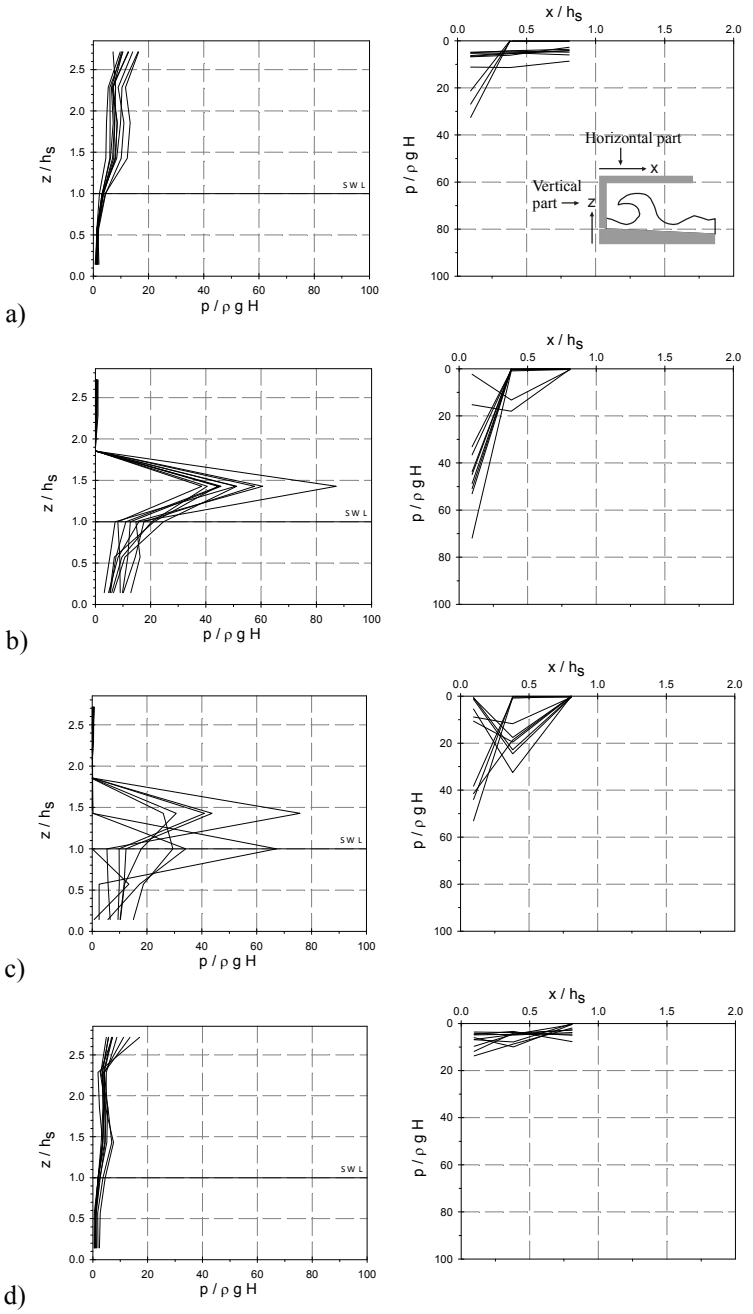

Figure 5.27 *Instantaneous pressure profiles at the time of maximum horizontal and vertical forces. a) SBW, b) BWSAT, c) BWLAT and d) BW*

Lastly, Figure 5.26d and Figure 5.27d show pressures for BW. Except in the upper corner, the scaled model is exposed to quasi-static pressures. Therefore, local and instantaneous pressure profiles are similar in shape. In general, if the structure is exposed to dynamic pressures, then the local and instantaneous pressures are different. Otherwise they are quite similar.

5.11 CONCLUSION

A vertical structure with an overhanging horizontal cantilevering slab is tested on a foreshore with a slope of 1/20 under loading conditions of violent wave impacts. The tests are carried out in a small scale test set-up with a scale factor of 1:20 which is a simplified version of the cross-section of the Blankenberge Pier. Tests are conducted under regular waves for four different values of water depth and five different values of wave period. All the test events have been recorded by a high speed camera at 250 frames per second. Pressures on the models have been measured by 10 pressure sensors using sampling frequency 20 kHz. A parametric analysis of the measured forces and pressures, both on the vertical and horizontal part of the scaled model, is conducted.

For one single approaching wave, two individual impacts occur sequentially on the scaled model. The first one appears on the vertical part while the second one develops at the attached corner of the horizontal part which is the result of the water jet rising on the vertical part. Both impact pressures and forces are non-repeatable under nominally identical conditions and their scatter trends are also different.

On the vertical part, the occurrence of shock pressures is limited to the case of breaking waves (BWSAT and BWLAT). However, on the horizontal part, this critical situation will extend to SBW and BW zones by the occurrence of very accelerated water jets, impacting beneath the horizontal part which makes the structure more vulnerable from a design view of point. As a result of this, the acceleration, the ratio of maximum dynamic and quasi-static components for F_v ($F_{\max\_dy} / F_{\max\_qs}$) ranges between 1-10.47 and 1-5 in the case of SBW and BW respectively, while it is measured between 1-2.5 for F_h.

Because the waves are allowed to break on the vertical part first, breaker types are classified into four groups based on method of Oumeraci et al. (1993) which is developed for vertical structures. For each group, the kinematic behavior of wave breaking and the related time series of pressures and forces are analyzed. Moreover, characteristics of maximum pressures and forces and the evaluation of instantaneous pressure profiles are discussed in more detail. The overall largest impact pressures are measured in the case of BWSAT: $109\ kPa$ at the SWL on the vertical part and $123\ kPa$ at the attached corner of the horizontal part. On the vertical part, the impact location of the waves shifts downwards between the points of $1.4\ h_s$ and $0.8\ h_s$ along cases gradually changing from SBW to BW.

Due to the second impact beneath the horizontal part, there is a pressure increase observed at the upper corner of the vertical part when compared to the case of

simple vertical walls. Even there, a phase difference exists between the two sequential impacts: the total force in the horizontal direction (F_h) increases in the cases of SBW and BW where long lasting quasi-static pressures exist. Therefore, the moment levering arm is also increased on top of the F_h increment which should be considered in the design. However, in the cases of BWSAT and BWLAT, impact loads which are high in magnitude and short in duration are effective. Therefore, the pressure increase at the upper corner is not active at the time of maximum F_h. Moreover, the highest pressure on the horizontal part is measured at the attached corner and it decreases along the slab.

For breaker types SBW, BWSAT and BWLAT, the variation of velocity and acceleration components (V_h, V_v) and (a_h, a_v) are analyzed up to the impact time instant. Velocity results are compared with the shallow water velocity ($\sqrt{gh_s}$). In the case of SBW, V_h is slightly higher than V_v at the time of impact which is different compared to literature. After the impact time, V_v dramatically increases due to the high vertical acceleration to a value of 20g. The highest vertical acceleration of 53g is measured in the case of BWSAT.

REFERENCES

Bagnold, R. A., 1939, "*Interim report on wave-pressure research*", Proc. Inst, Civil Eng. 12, 201–226.

Bredmose, H.; Hunt-Raby, A.; Jayaratne, R.; Bullock, G. N., 2010, "*The ideal flip-through impact: experimental and numerical investigation*", In: Journal of Engineering Mathematics, vol: 67(1-2), p. 115-136 (2010). Springer Netherlands

Bullock, G.N.; Obhrai, C.; Peregrine, D.H.; Bredmose, H., 2007, "*Violent breaking wave impacts, Part 1: Results from large-scale regular wave tests on vertical and sloping walls*" Coastal Engineering, v 54, n 8, p 602-617

Chan, E., 1994, "*Mechanics of deep water plunging-wave impacts on vertical structures*" Coastal Engineering, v 22, n 1-2, p 115-133, Jan 1994

Chan, E.S.; Melville, W.K., 1988, "*Deep-water plunging wave pressures on a vertical plane wall*", Proc Roy, Soc. London, A, 417(1852), 95-131

Cuomo G.; Tirindelli M.; and William Allsop W., 2007, '*Wave-in-deck loads on exposed jetties*', Coastal Engineering Volume 54, Issues-9, 2007, pp: 657-679

Hattori, M.; Arami, A.; Yui, T., 1994, "*Wave impact pressure on vertical walls under breaking waves of various type*"' Coastal Engineering, v 22, n 1-2, p 79-114, Jan 1994

Hull, P.; Müller, G., 2002, '*An investigation of breaker heights, shapes and pressures*' Ocean Engineering, v 29, n 1, p 59-79, September 21, 2002

Kirkgoz, M.S., 1982, "*Shock pressure of breaking waves on vertical walls*" Journal of the Waterway, Port, Coastal and Ocean Division, v 108, n WW1, p 81-95, Feb 1982

Kirkgoz, M.S., 1995, "*Breaking wave impact on vertical and sloping coastal structures*" Ocean Engineering, v 22, n 1, p 35-48, Jan 1995

Kisacik, D., 2011b, "*Loading conditions and structural response due to violent wave impacts on coastal structures with cantilever surfaces*", PhD Thesis (draft version), Ghent University

Kisacik, D.; Troch, P.; Van Bogaert, P., 2010, "*Experimental results of breaking wave impact on a vertical wall with an overhanging horizontal cantilever slab*", 32nd International Conference on Coastal Engineering (ICCE), 30 June – 5 July 2010, Shanghai – China

Kisacik, D.; Troch, P.; Van Bogaert, P., 2011a, "*Breaking Wave Impact on a Vertical Wall with an Overhanging Horizontal Cantilever Slab: Irregular Waves*" Conference proceedings, 3rd International Conference on the Application of Physical Modelling to Port and Coastal Protection (CoastLab10), 28 September-1 October, Barcelona –Spain

Kortenhaus, A.; Oumeraci, H., 1998, "*Classification of wave loading on monolithic coastal structures*", Proceedings International Conference Coastal Engineering (ICCE), ASCE, Copenhagen, Denmark, no. 26, 14 pp

Lugni, C.; Brocchini, M.; and Faltinsen, O. M., 2010b, "*Evolution of the air cavity during a depressurized wave impac*t, II, The dynamic field", Physics of Fluids 22, 056102 (2010)

Lugni, C.; Miozzi, M.; Brocchini, M.; and Faltinsen, O. M., 2010a, "*Evolution of the air cavity during a depressurized wave impact, I., The kinematic flow field*", Physics of Fluids 22, 056101 (2010)

McConnell, K.J; Allsop, N.W.H; Cuomo, G; and Cruickshank, I.C, 2003, *'New guidance for wave forces on jetties in exposed locations'*, Paper to Conf. COPEDEC VI, Colombo, Sri Lanka pp: 20

Okamura, M., 1993, '*Impulsive pressure due to wave impact on an inclined plane wall*', Fluid Dynamics Research, volume 12, issue 4, pp. 215-228

Oumeraci, H.; Bruce, T.; Klammer, P.; Easson, W.J., 1995, "*PIV measurement of breaking wave kinematics and impact loading of caisson breakwaters*" COPEDEC, no. 4, v 3, pp. 2394-2410

Oumeraci, H.; Klammer, P.; and Kortenhaus, A., 1994, "*Impact loading and dynamic response of vertical breakwaters – Review of experimental results*", Proceedings of International workshop on Wave barriers in deepwaters, Japan, pp. 347-361.

Oumeraci, H.; Klammer, P.; Partenscky, H.W., 1993, "*Classification of breaking wave loads on vertical structures*", Journal of Waterway, Port, Coastal and Ocean Eng. v 119, n 4, p 381-397

Oumeraci, H; Kortenhaus, A; Allsop, W; de Groot, M; Crouch, R; Vrijling, H; Voortman, H, 2001, "*Probabilistic Design Tools for Vertical Breakwaters*", Balkema Publishers, New York.

Partenscky, H., 1988, "*Dynamic forces due to waves breaking at vertical coastal structures*" Twenty First Costal Eng Conf, p 2504-2518, 1988, Twenty First Costal Eng Conf

Peregrine, D.H., 2003, "*Water-wave impact on walls*", Annual Review of Fluid Mechanics, volume 35, p: 23-43

Richert, G., 1968, "*Experimental investigation of shock pressures against breakwaters*" In: Proc. Int. Conf. Coastal Engng, ASCE, London, pp. 954–973.

Schmidt R.; Oumeraci H.; Partenscky H.W., 1992, "*Impact loads induced by plunging breakers on vertical structures*", Proc. 23rd Int. Conf. Coastal Eng., 1992, 1545-1558

Svendsen, I.A.; Hansen, J.B., 1986, "*The interaction of waves and currents over a longshore bar*", ASCE Proc. 20th Int. Conf. Coastal Engineering, Taipei, pp. 1580– 1594

Walkden, M.J.A.; Bruce, T.B., 1999, "Scatter in wave impulse maxima: a review", Proc. of Coastal Structures '99 Vol. I (1999), pp. 439–446

Walkden, M.J.A.; Crawford, A.R.; Bullock, G.N.; Hewson, P.J.; Bird, P.A.D., 1996, "*Wave impact loading on vertical structures*", Advances in Coastal Structures and Breakwaters (1996), pp-273-287

Wiegel, R. L., 1960, "*A presentation of cnoidal wave theory for practical application*", Journal of Fluid Mechanics, volume-7-2, pp-273-286

Wood, D.J.; Peregrine, D.H., 1996, "*Wave impact beneath a horizontal surface*", In: Proc. 25th Int. Conf. on Coastal Engineering. Orlando, USA, ASCE, pp. 2573–2583

6

PRESSURE DISTRIBUTION

***

6.1 INTRODUCTION

The objective of the present chapter is to understand the pressure distribution due to the violent water wave impacts on a vertical wall, including an overhanging horizontal cantilever slab, based on the breaking wave results. The model tests with a scale of 1/20 are carried out to fulfill the above goals. This chapter starts with a short summary of literature. The definition of the location of the maximum pressure is being discussed in section 6.2. Subsequently, the relationship between maximum pressure and rise time is being discussed (Section 6.3). Detailed analyses of boundary conditions for the region of dynamic pressures are presented in section 6.4.1. In each breaker type the local pressure ratios are defined in sections 6.4.2 through 6.4.4. Later, the scaling issue of the measured pressures is discussed in section 6.5. Based on the discussion of the test results, detailed conclusions are formulated in Section 6.6.

Wave attacks on vertical structures are usually classified as non-breaking, breaking and broken waves. Non-breaking or broken waves create quasi-static (pulsating) loads. For this type of wave loading, the method suggested by Goda (1974), based on his own theoretical and laboratory works, is well accepted. He assumed a trapezoidal pressure distribution on vertical walls with a maximum pressure at still water level (SWL) (see Figure 2.11). Nevertheless, his method predicts a static equivalent load instead of a short impulsive load for breaking waves. Therefore, Takahashi (1996) extended Goda's method for impulsive loads by adding the berm dimensions effect to the pressure at SWL (p_1) (for more details see section 2.4.1.4). In his method, the pressure profile is defined by using p_1 (pressure at SWL), p_3 (pressure at the toe of the wall) and p_4 (pressure at the wall crest).

Breaking waves create short impulsive (impact) loads on vertical structures which introduce local effects on the structure. However, coastal structures are bulk structures and most research did not consider these short-duration loads in design formulas. Oumeraci (1994) emphasized the importance of impulsive loads in the design of vertical structures. Several formulas [Minikin (1963); Goda (2000); Blackmore & Hewson (1984); Allsop et al. (1996); Oumeraci et al. (2001); Cuomo et al. (2011)] from design codes allow calculating impulsive loads on vertical structures. The method suggested by Oumeraci et al. (2001) allows predicting the pressure distribution due to breaking waves. The pressure profile on the vertical wall according to PROVERBS is shown in Figure 2.15. Section 2.4.2.5.6 describes the method for determining the value of the pressure at the SWL (p_1) and the pressure at the toe of the wall (p_3).

For describing the pressure profile, defining the location of the maximum pressure p_{max} is one of the critical points to consider. In literature, the location of p_{max}, denoted by z_{max}, is found to vary between slightly below and above SWL. Richert (1968) found the location below the SWL. However, Partenscky (1988) defined the location $0.7H_b$ above the mean water level and Chan & Melville (1988) considered a range from $z/L = 0.05$ to 0.07, covering the region just below the maximum crest elevation observed in the absence of the wall (L is the wave length). Hull and Muller (2002) and Oumeraci et al. (1995) defined SWL as the location of p_{max}.

Other researchers like Hattori et al. (1994) and Bullock et al. (2007) suggested a range of locations between SWL and the hitting point of the wave crest.

Kirkgoz (1982) recommended the following formula for the location of p_{max} depending upon the particular wave and beach conditions:

Equation 6.1 $$z_{max}/d_b = 0.58 + 0.16cot\theta - 0.008cot^2\theta$$

$$z_{max}/d_b = 1.4 \quad \text{for slope } 1/10$$

where d_b is the water depth at breaking and θ is the bed slope angle.

In addition to the definition of the position of p_{max}, the magnitude of this quantity has to be determined. Bagnold (1939) mentioned that, although the magnitude of p_{max} varies considerably from impact to impact, the area enclosed by the pressure-time curves never exceeds a definite value. Based on the Bagnold approach, if p_{max} is large, then its rise time (t_r) tends to be small and vice versa. Rise time t_r is the time duration from zero pressure to maximum pressure p_{max}. The general form of the relation between p_{max} and t_r, suggested by Weggel and Maxwell (1970), is given in Equation 6.2, which is based on observations during wave flume tests and considerations on the conservation of wave momentum. They derived the equation as an upper envelope of 12 regular wave results with a bottom slope of 1/20.

Equation 6.2 $$p_{max} = a[t_r]^b$$

wherein a and b are non-dimensional empirical coefficients.

In the same manner, various values of a and b in Equation 6.2 have been derived from test results (see Table 6.1). Kirkgoz (1990) suggested the best fit line based on 70 laboratory measurements of artificially derived single waves with a bottom slope of 1/10. Witte (1990) proposed an upper limit function based on 100 laboratory measurements with a bottom slope of 1/6. Hattori et al. (1994) also suggested an upper limit function developed using large sets of regular wave tests.

Table 6.1 Coefficients a and b in Equation 6.2 from previous experiments at small and large

Researchers	Wall condition	Bottom slope	Scale	p_{max} a	b
Weggel and Maxwell (1970)	Discontinuous	1/20	Small	232	−1.00
Kirkgöz (1990)	Continuous	1/10	Small	250	−0.90
Witte (1990)	Continuous	1/6	Small	261	−0.65
Hattori et al. (1994)	Continuous	1/20	Small	400	−0.75
Blackmore & Hewson (1984)	-		Full	3100	−1.00
Bullock et al. (2001)	-		Full	31000	−1.00

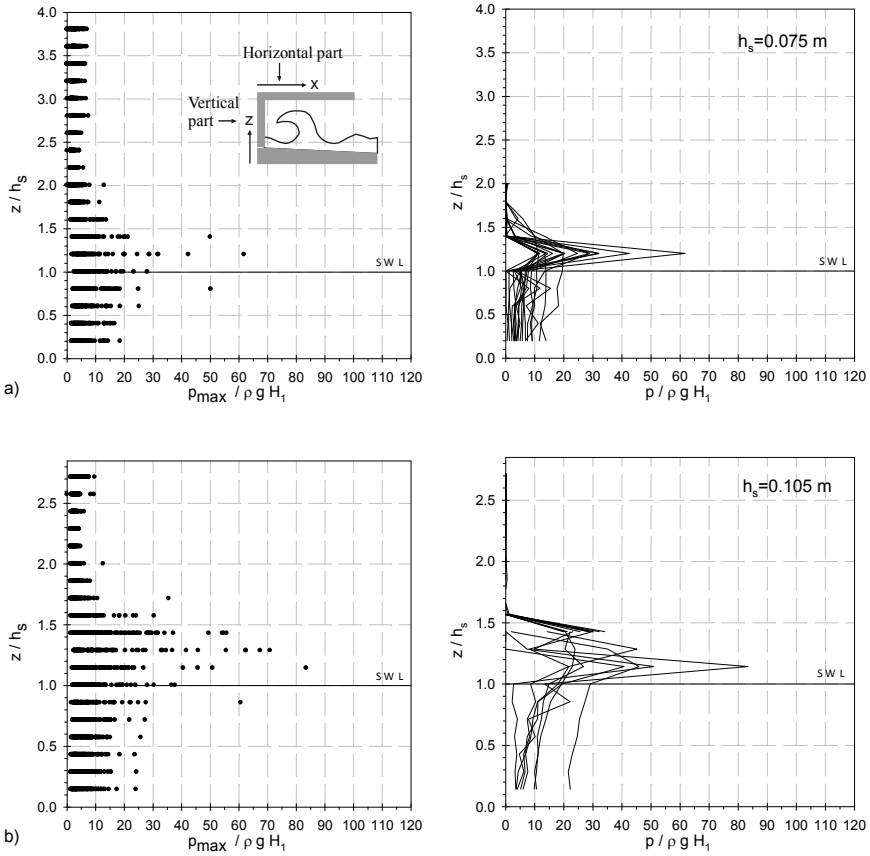

Figure 6.1 *Local peak pressures (p_{max}) distribution (first column) and instantaneous pressures distribution (second column) at the time of maximum horizontal force on vertical part for a) $h_s = 0.075\,m$ and b) $h_s = 0.105\,m$ (It continuous in Figure 6.2)*

In addition, Blackmore & Hewson (1984) proposed an upper limit for the full-scale data sets of field measurements on a sea wall. Very recently, Bullock et al. (2001) upgraded the full-scale relation of Blackmore & Hewson with a factor of 10 based on Alderney field data.

For vertical structures, the answer to questions like where is the location of p_{max}, what will be the magnitude of p_{max} and which pressure profile can be expected, are considerably well understood. However, what will be the answer of similar questions on a vertical structure with an overhanging horizontal cantilever slab is also of practical importance.

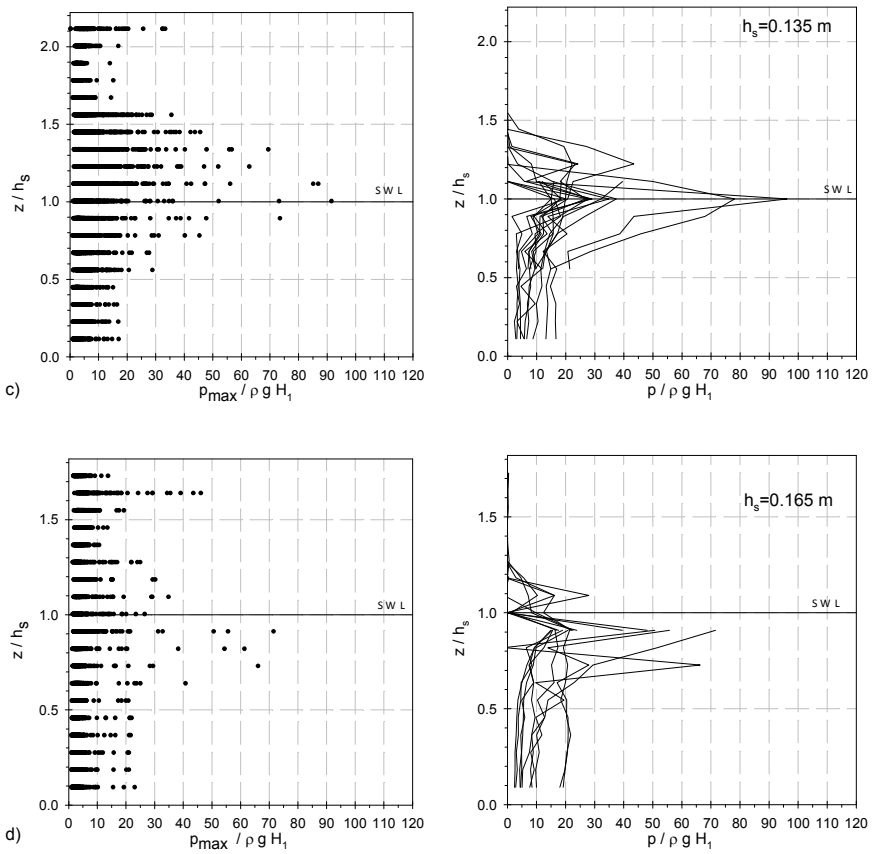

Figure 6.2 *Figure 6.3 is continued. Local peak pressures (p_{max}) distribution (first column) and instantaneous pressures distribution (second column) at the time of maximum horizontal force on vertical part for c) $h_s = 0.135\ m$ and d) $h_s = 0.165\ m$*

6.2 LOCATION OF p_{max}

On the vertical structures, defining the value of p_{max} and its location (z_{max}) are quite important parameters for structural designers. In general, SWL is suggested as a good choice of p_{max} in design. Most research locates p_{max} in the vicinity of the SWL, depending on parameters like beach conditions, water depth [Kirkgoz (1982) and Hattori et al. (1994)] and breaker type [Partenscky (1988) and Hull & Müller (2002)]. Kisacik et al. (2011) showed that p_{max} shifts from a position above SWL for SBW, to slightly below SWL for BWLAT. Similar findings are observed by Hull & Müller (2002).

In the present work, the variation of z_{max} with h_s is studied. For each value of h_s, a large data set which covers all breaker types from SBW to BW is considered and the highest pressures are mainly observed in the case of BWSAT. Figure 6.1 and Figure 6.2 (first column) show the measured peak pressures of 150 impacts presented in dimensionless terms from all 19 sensor locations on the vertical part. The second column shows the instantaneous pressure profiles at the instants of maximum horizontal forces. The black horizontal line at the centre marks the position of SWL. The locations of p_{max} are coinciding both on local and instantaneous pressure profiles since the peak pressures at z_{max} is dominant for determining the maximum horizontal forces. In the figure, the non-dimensional term of z_{max} (z_{max}/h_s) is gradually decreasing from a point above the SWL to a point below the SWL with the increase of h_s. In shallower water, the influence of the sea bottom forces the waves to hit higher locations.

Figure 6.3 shows the variation of z_{max}/h_s with the wave steepness (H_1/L_0), where L_0 is the deep water wave length. The H_1 value is the wave height (measured at the toe of the foreshore) which results in the highest impact pressure (p_{max}) on the vertical part. The resulting expression is given in Equation 6.3.

Equation 6.3 $$z_{max}/h_s = -23.2\ H_1/L_0 + 1.4$$

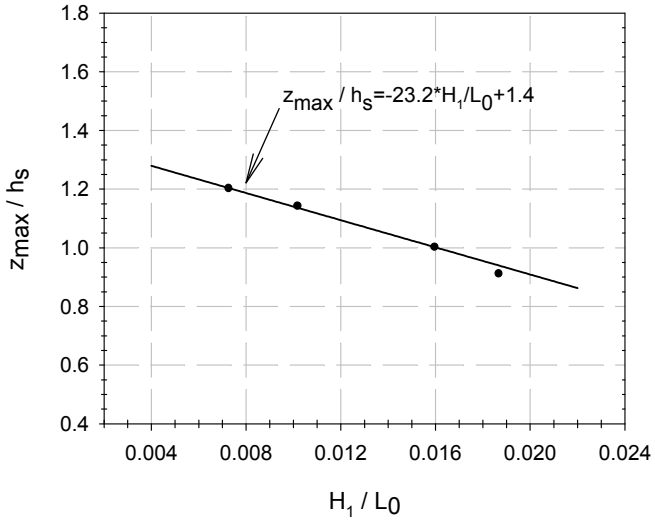

Figure 6.3 *Variation of non-dimensional p_{max} location (z_{max}/h_s) with the variation of H_1/L_0.*

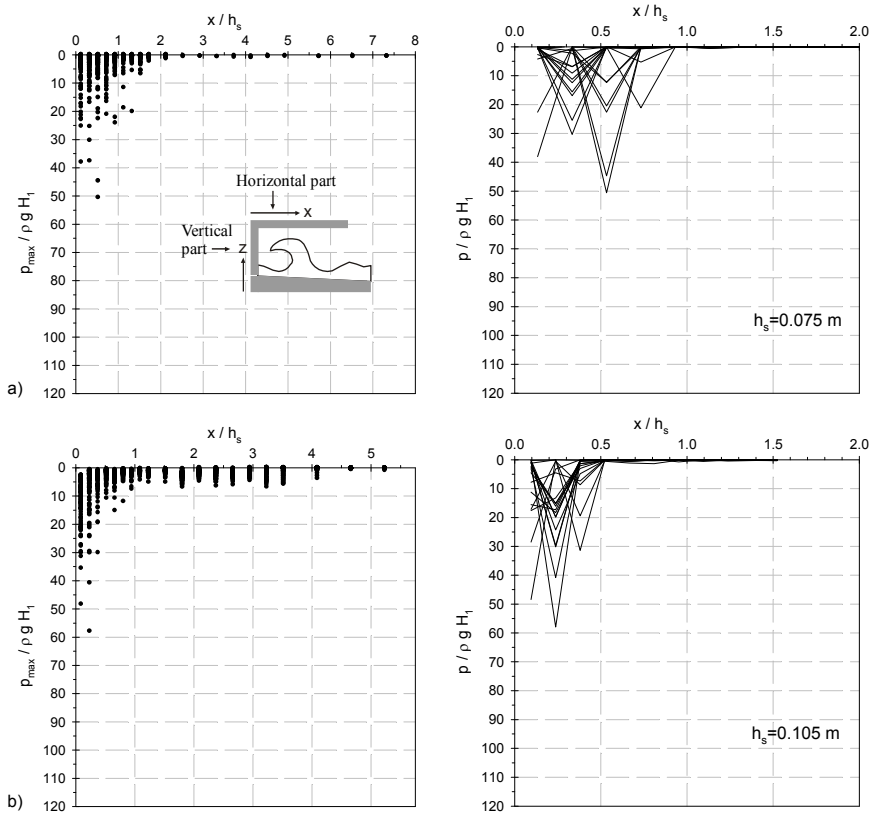

Figure 6.4 *Local peak pressures (p_{max}) distribution (first column) and instantaneous pressures distribution (second column) at the time of maximum horizontal force on vertical part for a) $h_s = 0.075\,m$ and b) $h_s = 0.075\,m$ (It continuous in Figure 6.5)*

The value of $H_1/L_0 = 0.0187$ which is measured at the highest water depth ($h_s = 0.165$ m), is slightly lower than the proposed line. For each water depth, normally the wave height H_1 has been increased in successive tests to achieve the highest p_{max}. However for the high water depths, high incident wave crests are rebounded by the horizontal slab due to the small clearance (c) between SWL and the horizontal part. Therefore, an early impact of the wave crest occurs at the head of the horizontal part, and the approaching wave loses its energy. The remaining wave travels below the horizontal part and results in low pressures at a high wave height H which normally creates high p_{max}. Therefore, the highest values of p_{max} are measured at relatively low values of H_1/L_0.

The magnitude of p_{max} also depends on h_s and increases with an increase of h_s. However, the overall highest p_{max} on the vertical wall is measured

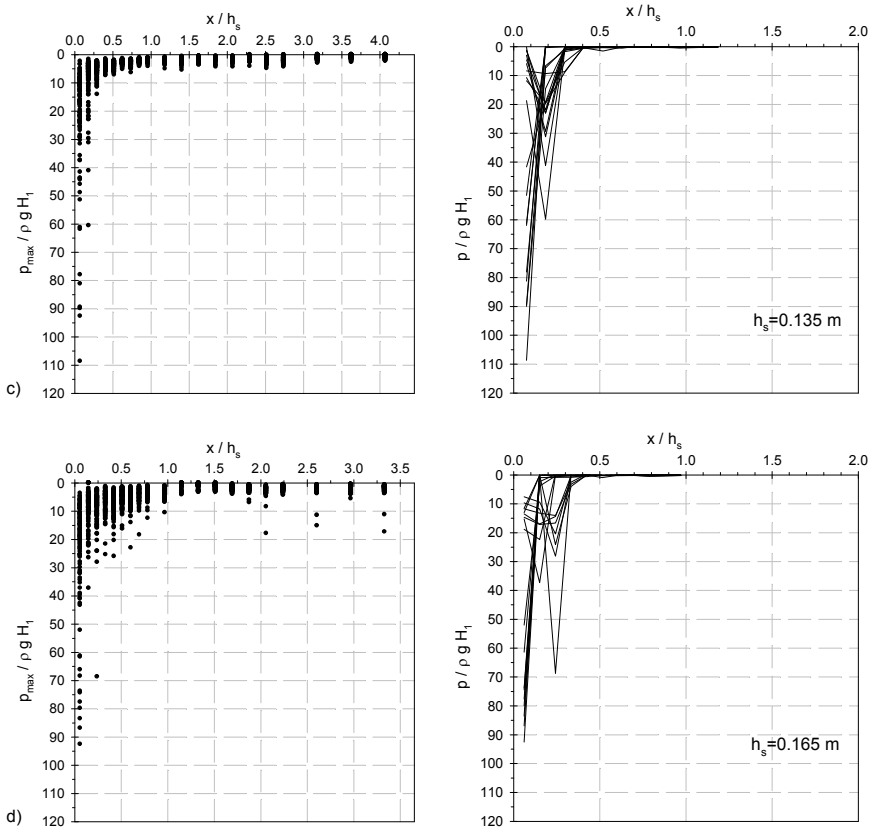

Figure 6.5 *Figure 6.5 is continued. Local peak pressures (p_{max}) distribution (first column) and instantaneous pressures distribution (second column) at the time of maximum horizontal force on vertical part for c) $h_s = 0.135\ m$ and d) $h_s = 0.165\ m$*

at $h_s = 0.135\ m$ (where $p_{max} = 92\ \rho g H_1$) which is not the highest water depth (Figure 6.2c). The reason for lower p_{max} values at the highest h_s is the same reason explained above for the rebounding effect of the horizontal part.

In addition, some other relatively high local impact pressures are measured at the upper corner of the vertical part. These pressures are also showing the same trend as the variation of p_{max} with h_s. These are due to the secondary impact, occurring at the upper corner of the scaled model, resulting from rising jets, produced on the vertical part. The region of these relatively high local impacts is rather small and its magnitude sharply decreases in downward direction. These localized high peak pressures at the corner show a phase difference compared to p_{max} at location z_{max} which may be less important for coastal structures sliding or overturning. However, they may threaten the structural integrity in the case of cracks or weak points [Peregrine (2003)].

Pressure profiles at the instant of maximum horizontal forces (second column of Figure 6.1 and Figure 6.2) extended over a relatively limited area above the SWL. The upper boundary ranges of the pressures are in between $z/h_s = 1.4 - 1.8, 1.3 - 1.65, 1.2 - 1.5$ and $1 - 1.3$ for h_s=0.075, 0.105, 0.135 and 0.165 m respectively and it is decreasing with increasing of h_s. The results are compatible with Kirkgoz's finding ($z/h_s = 1.4$) in Equation 6.1 for slope 1/10.

Figure 6.4 and Figure 6.5 (first column) show the non-dimensional measured local peak pressures on the horizontal part of the scaled model for the four different values of h_s. On the horizontal part, p_{max} ($108\,\rho g H_1$) is measured at the attached corner (Figure 6.5c) which is the highest pressure on the overall scaled model. The magnitude of p_{max} decreases sharply in power form below $10\,\rho g H_1$ between $x/h_s = 0.8 - 1$ (Figure 6.4a-d) (x is the horizontal distance from model toe). The region of high local impact is bounded by the impact area of the rising jet face. In the case of highest water level ($h_s = 0.165\,m$), some high local impacts are measured at a distance more than $x/h_s = 2$ which are due to the crest impact of approaching waves before hitting on the vertical part of the model. Figure 6.4 and Figure 6.5 (second column) show the instantaneous pressures at the time of appearance of maximum vertical forces on the horizontal part. Maximum pressures on the instantaneous pressure profiles are seen at a location very close to the wall or adjacent to it. The extension region is relatively small compared to the region of local peak pressures ($x/h_s = 0.3 - 0.5$).

6.3 RELATIONS BETWEEN MAXIMUM PRESSURE, p_{max}, AND RISE TIME, t_r

6.3.1 p_{max} and t_r relation on the vertical part

As explained by Bagnold, the variation in the area enclosed by the pressure-time curves is rather limited and this is observed by measuring that the highest wave impacts have a shorter t_r. Figure 6.6a shows the value of p_{max} and t_r relation measured on the vertical part for four water depths. Results on the vertical part are compared with empirical relationships between p_{max} and t_r derived by Weggel and Maxwell (1970), Kirkgoz (1990), Witte (1990) and Hattori et al, (1994). It is observed that formulas from literature underestimate the measurements especially for the values with high t_r. The form of Equation 6.2 is dimensionally inconsistent. Based on the suggestion of McConnell and Kortenhaus (1996), the following dimensionally consistent form of p_{max} and t_r is proposed in Equation 6.4 at 99.6% of non-exceedance level, with $a = 0.24$ and $b = -0.613$. For determining the proposed equation, all data points along the axis of t_r/T is divided in different intervals. Then statistical values are calculated for each interval and a power form function is passed through the calculated points.

Equation 6.4 $$\left(\frac{p_{max}}{p_{max\_qs}}\right)_{99.6\%} = 0.24\left[\frac{t_r}{T}\right]^{-0.613}$$

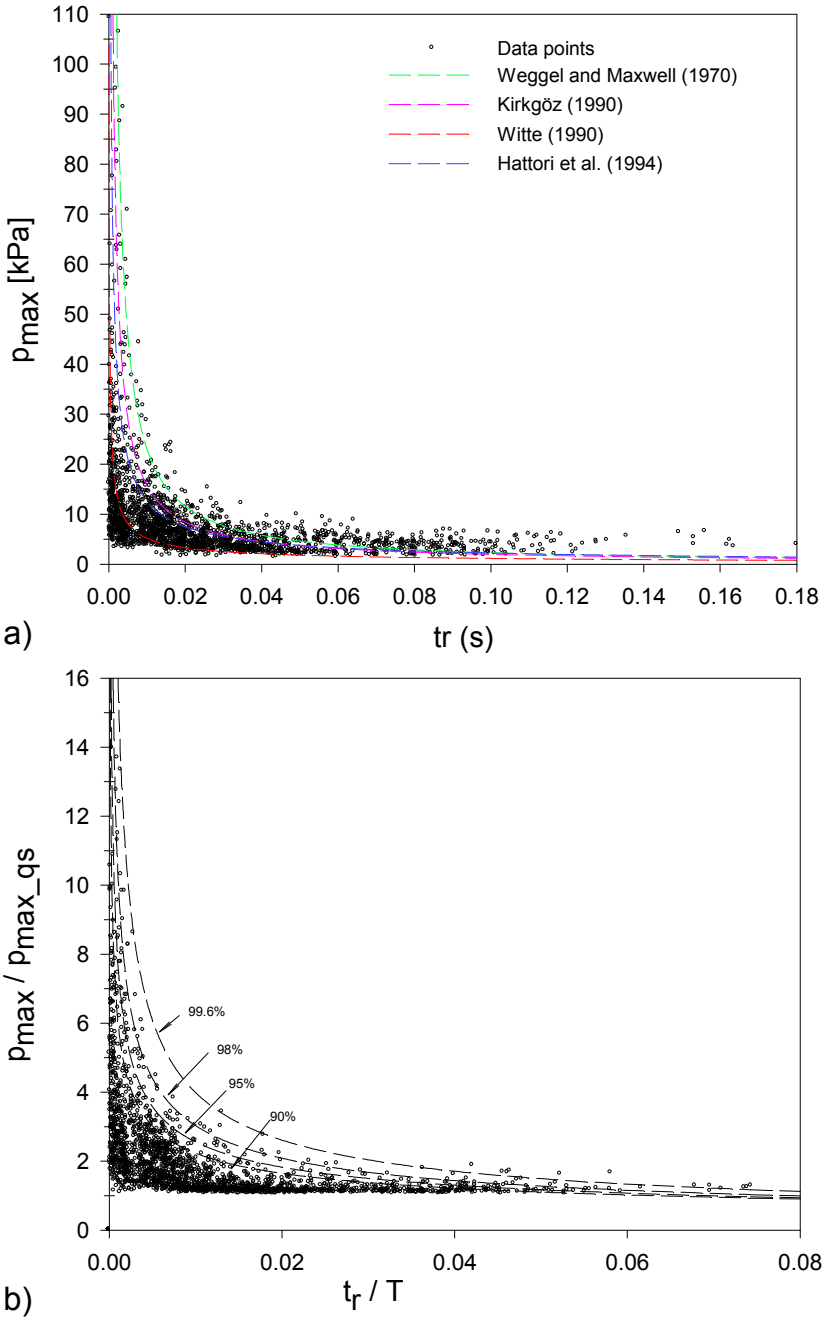

Figure 6.6 *Maximum impact pressures and rise times recorded on the vertical part. a) Model results are compared with suggested lines in literature. b) Visualization of non-dimensional form of impact pressures and rise times and fitted lines.*

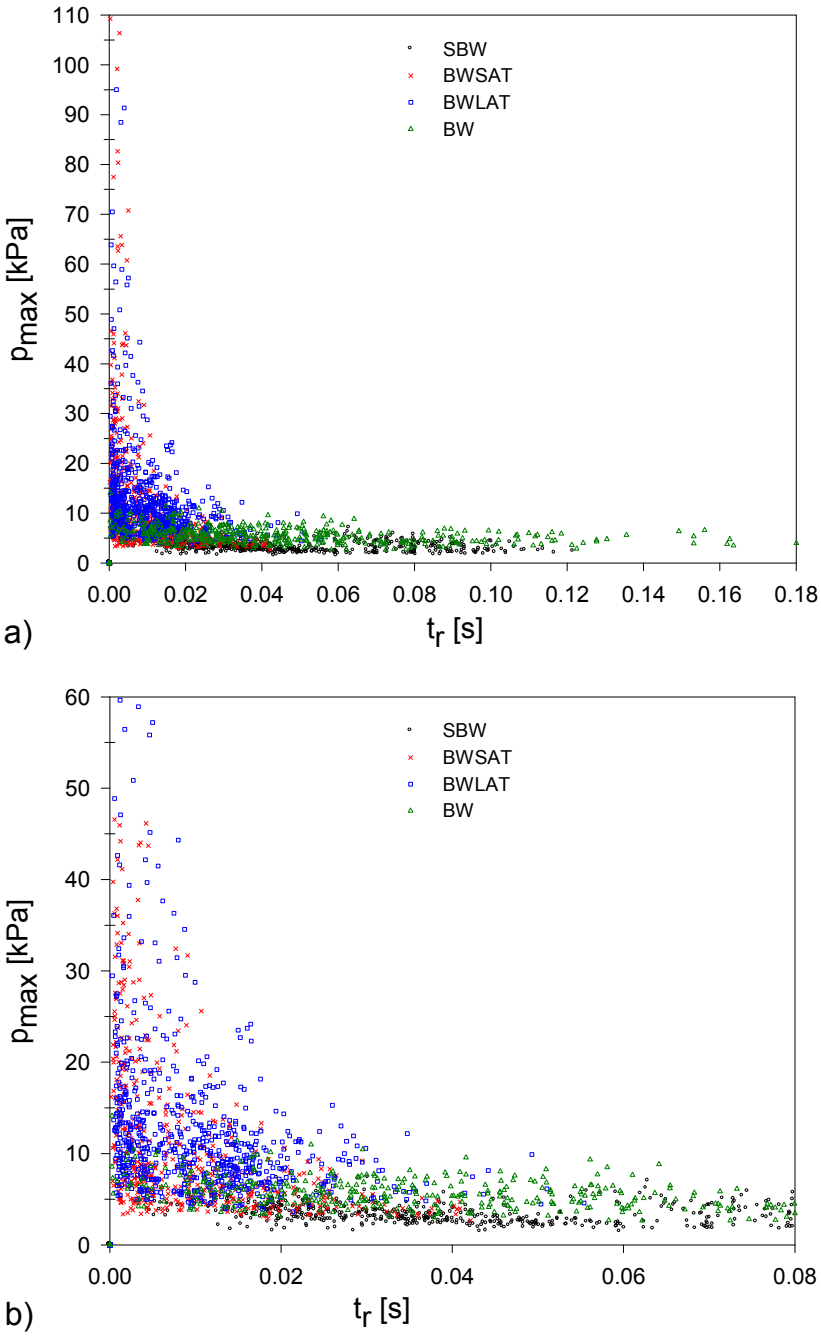

Figure 6.7 *Maximum impact pressures and rise times recorded on the vertical part. a) Model results are categorized according to the breaker types. b) close look at "a".*

In the new form, p_{max} and t_r are normalized by a maximum quasi-static pressure, p_{max_qs}, and wave period, T, respectively. The results are plotted in Figure 6.6b.

During the physical model tests, it is observed that the largest impacts recorded on the vertical part have rise times of $t_r \leq 0.3\ ms$. However, most of the significant impacts are observed between $0.3 \leq t_r \leq 8\ ms$. Walkden et al. (1996) show that the difficulties of recording consistent impact pressures between tests are the probable reasons for the discrepancy in coefficients between various researchers.

Figure 6.7a shows the categorized version of the same data sets based on breaker types as SBW, BWSAT, BWLAT and BW. Figure 6.7b represents in more detail the results for SBW, BWSAT and BWLAT in the region of high pressures. Results of SBW and BW are showing low values of p_{max} over a quite extensive t_r range. The average value of p_{max} for BW is larger than the value for SBW which means BW produce more significant impulses than do SBW. The results of BWSAT and BWLAT show a high scatter and overlap. Despite this overlap, there is segregation in the data cloud close to the envelope line region. Bullock et al. (2007) stated that this segregation between cases of BWSAT and BWLAT is mainly due to the longer rise times associated with high-aeration impacts. However, the detected degree of segregation is remarkably lower than the measurements done by Bullock et al. (2007). This difference is mainly due to the variation in defining the breaker type, which is based on more subjective observations.

6.3.2 $\boldsymbol{p_{max}}$ and $\boldsymbol{t_r}$ relation on the horizontal part

Kisacik et al. (2011) described that the model is exposed to two distinct wave impacts. The first impact occurs on the vertical part while the second occurs on the horizontal part. Figure 6.8 and Figure 6.9 show the results of the second impact occurring on the horizontal part of the scaled model. For the visualization, maximum pressures on the horizontal part, p_{max}, which are measured at the upper corner of the scaled model at sensor 8 (see Figure 3.1), are considered. Figure 6.8a shows the relation between p_{max} and t_r while Figure 6.8b shows the normalized relation between p_{max} and t_r. Equation 6.5 represents the adopted functions at 99.6% of non-exceedance level with $a = 0.24$ and $b = -0.618$. Both equations (Equation 6.4 and Equation 6.5) for the vertical and horizontal parts have almost identical coefficients.

Equation 6.5 $$\left(\frac{p_{max}}{p_{max\_qs}}\right)_{99.6\%} = 0.24\left[\frac{t_r}{T}\right]^{-0.618}$$

The largest measured pressures feature a rise time $t_r \leq 0.15\ ms$. The magnitude of the pressures of the second impact is higher than the magnitude of the first impact. The inverse relation between p_{max} and t_r is also valid for the horizontal part with smaller t_r from the results of second impacts. Figure 6.9a and Figure 6.9b show the results which are categorized again based on the breaker types. In contrast to the

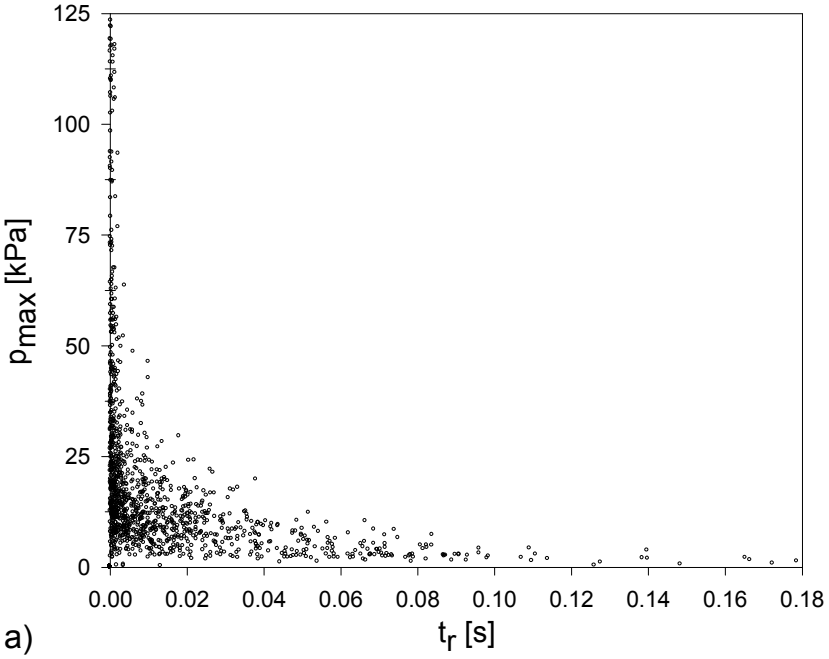

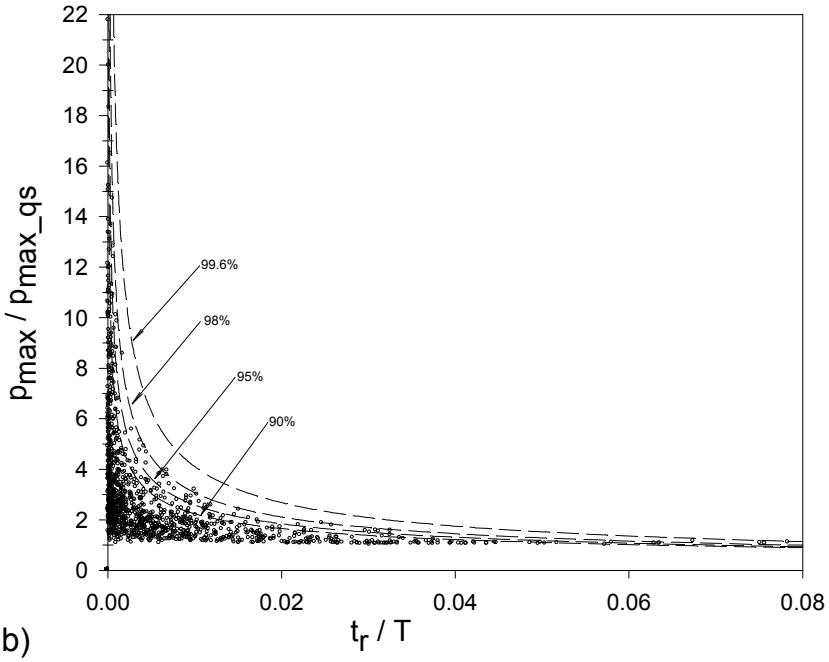

Figure 6.8 *a) Maximum impact pressures and rise times recorded on the horizontal part, b) Visualization of non-dimensional form of impact pressures and rise times and fitted lines.*

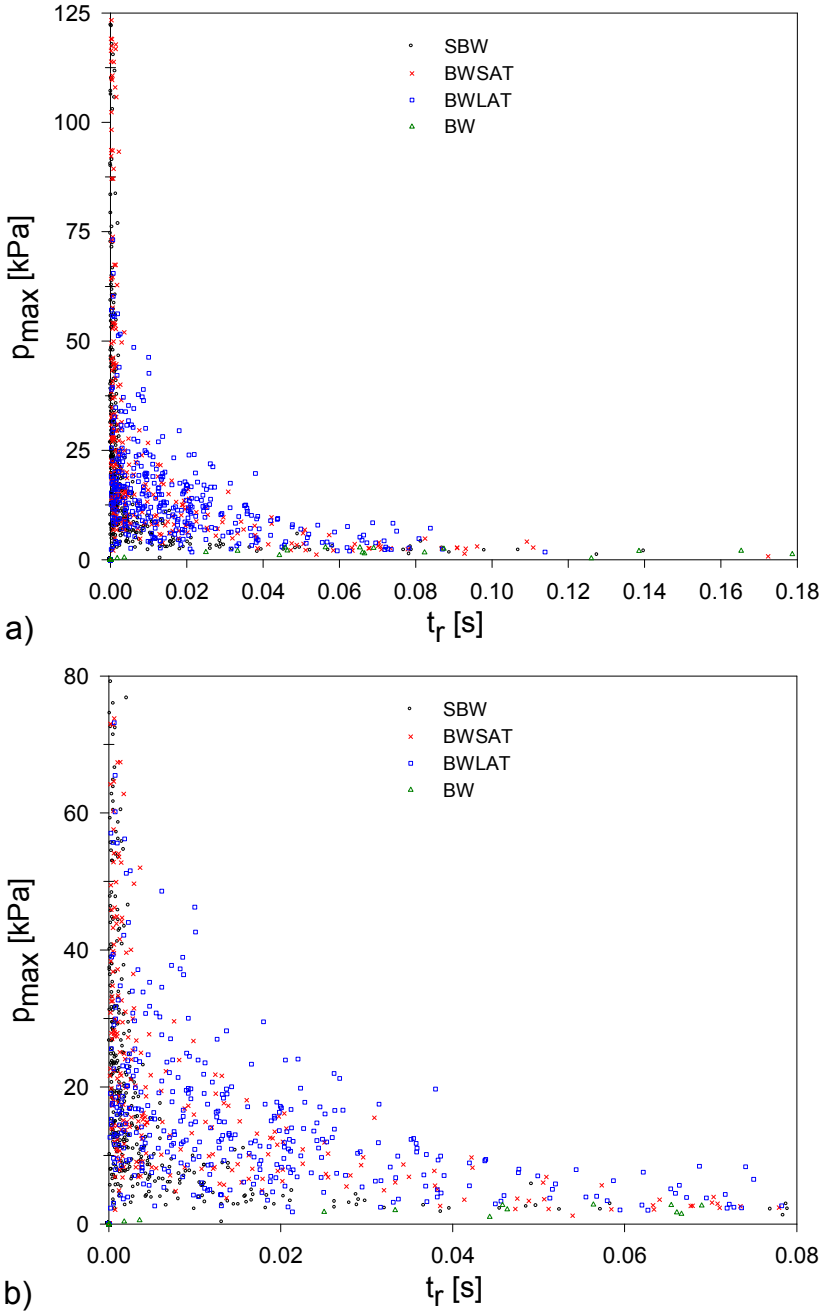

Figure 6.9 *Maximum impact pressures and rise times recorded on the horizontal part a) Model results are categorized according to the breaker types b) close look at "a".*

pressures on the vertical part, results with high p_{max} values are also observed on the horizontal part from the cases of SBW and BW. Between these two cases, the results from SBW are more intense compare to the results from BW. Thus, BW seems less likely to produce significant impulses than SBW.

6.4 PRESSURE DISTRIBUTIONS

Figure 6.10 shows an example of the spatial distribution of p_{max} both on the vertical and horizontal part for cases SBW, BWSAT, BWLAT and BW. The value of p_{h1}, p_{h2} and p_{h3} are the local peak pressure at the SWL and top and bottom of the vertical part respectively. Whereas, p_{v1} shows the local peak pressure on the horizontal part. This is the location of sensor 8 which is very close to the attached corner (see Figure 3.1). A combination of the maximum local peak pressures of all 10 sensors constitutes the pressure profile on the scaled model. One should keep in mind that a phase differences exist between these local peaks. For example, Kisacik et al. (2011) measured phase differences around 0.0272 T and 0.0150 T between p_{h1} and p_{v1} for cases of SBW and breaking waves (include both BWSAT and BWLAT) respectively. Therefore, pressure profile at the instant of maximum horizontal or vertical force or maximum overturning moment will be different and lower than the values calculated from these profiles. However, the total forces calculated from these profiles will be a good assessment for structural equilibrium.

6.4.1 Boundary conditions for occurring dynamic pressures

As seen from Figure 6.10, the pressure profiles of all four cases are quite different. Regarding design conditions, the region of occurrence of dynamic pressures is important in developing a generally feasible design method. Figure 6.11 shows the interval of wave height H_1 (measured at the toe of foreshore) which creates a high dynamic impact on the vertical part as a function of the clearance (c) between SWL and the horizontal part. In the figure, H_1 is normalized by the water depth h_s at the structure while c is normalized by the model height (h_m) (see Figure 3.1). Through the normalization, the breaking wave impact region is correlated to h_s while c is correlated to the model geometry. The bottom x-axis shows the ratio of the maximum dynamic and quasi-static peak pressures (p_{max_dy} / p_{max_qs}). For each $\frac{c}{h_m}$ value, the upper and lower boundaries of $\frac{H_1}{h_s}$ are defined at a threshold value corresponding to $p_{max\_dy}/p_{max\_qs} \geq 2.5$. This criterion for defining a dynamic pressure region is suggested by Kortenhaus and Oumeraci (1998). The continuous lines represent the measured lower and upper boundary regions. The dashed line shows the adopted upper boundary margins. Equation 6.6 and Equation 6.7 express the functions of upper and lower boundaries.

The boundary region of the dynamic pressures exists on the vertical part where $p_{max\_dy}/p_{max\_qs} \geq 2.5$:

Equation 6.6 and Equation 6.7 express the upper and lower boundaries, respectively.

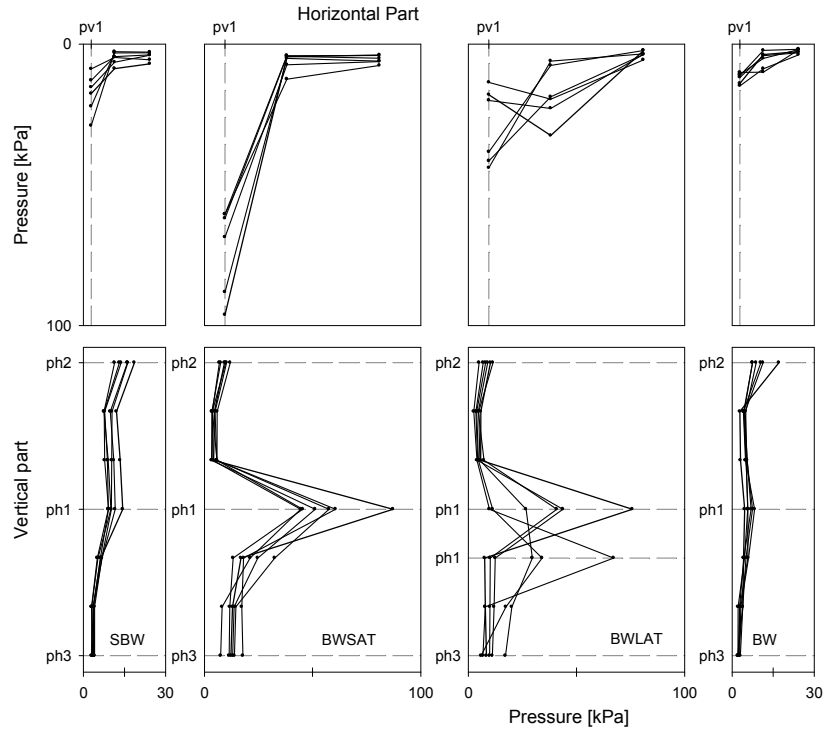

Figure 6.10 *Spatial distribution of maximum local peak pressures (p_{max}) both on the vertical and horizontal part for cases SBW, BWSAT, BWLAT and BW ($h_s = 0.105\ m$). p_{h1}, p_{h2} and p_{h3} are the local p_{max} at various location on vertical part and p_{v1} is the local p_{max} on the horizontal part.*

Equation 6.6 *a) for* $0.60 \leq \frac{c}{h_m} \leq 0.75$ $\quad \frac{H_1}{h_s} = -1.5\frac{c}{h_m} + 2.14$

b) for $0.45 \leq \frac{c}{h_m} < 0.60$ $\quad \frac{H_1}{h_s} = 0.82\frac{c}{h_m} + 0.73$

Equation 6.7 *for* $0.45 \leq \frac{c}{h_m} \leq 0.75$ $\quad \frac{H_1}{h_s} = -0.71\frac{c}{h_m} + 1.05$

The lower and upper boundaries for $\frac{H_1}{h_s}$ linearly decrease with the increase of $\frac{c}{h_m}$ in the zone of $0.60 \leq \frac{c}{h_m} \leq 0.75$. In this zone, both Equation 6.6a and Equation 6.7 are more or less parallel or little expanding. Consequently, the occurring region of dynamic pressure is around $0.5\frac{H_1}{h_s}$. However, the upper boundary shows lower

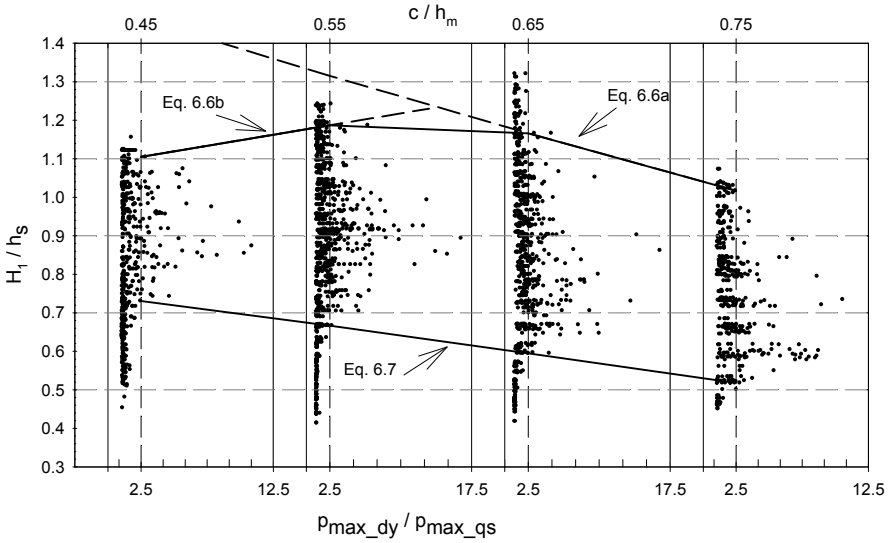

Figure 6.11 *Variation of wave height range ($\frac{H_1}{h_s}$) which creates high dynamic pressures on the vertical part with the change of $\frac{c}{h_m}$. Continuous lines are measured upper and lower boundaries while dashed lines represent adopted upper boundaries. Upper and lower boundaries are determined between the points where $p_{max\_dy}/p_{max\_qs} \geq 2.5$.*

values in the zone of $\frac{c}{h_m} < 0.65$. This is the area where H_1 ranges are incomplete because of the rebounding effect of the horizontal part. This issue is described already in Section 6.2. The reduction in the upper boundary reaches 24% at $\frac{c}{h_m} = 0.45$. Therefore, the upper boundary is modified in the zone of $\frac{c}{h_m} < 0.65$ (Equation 6.6b).

Figure 6.12 shows the interval of $\frac{H_1}{h_s}$, which creates a high dynamic impact on the horizontal part. Equation 6.8 and Equation 6.9 express the upper and lower boundaries for $\frac{H_1}{h_s}$, respectively. Both equations express that the area of dynamic pressures is getting larger with the decrease of clearance. As in the case of the vertical part, measured upper boundary shows lower values in the zone of $\frac{c}{h_m} \leq 0.64$. However, the reduction in this case is more significant than the reduction for the case of the vertical part. This can be explained by the fact that H_1 range, creating high dynamic pressures on the horizontal part, is larger than the range creating high

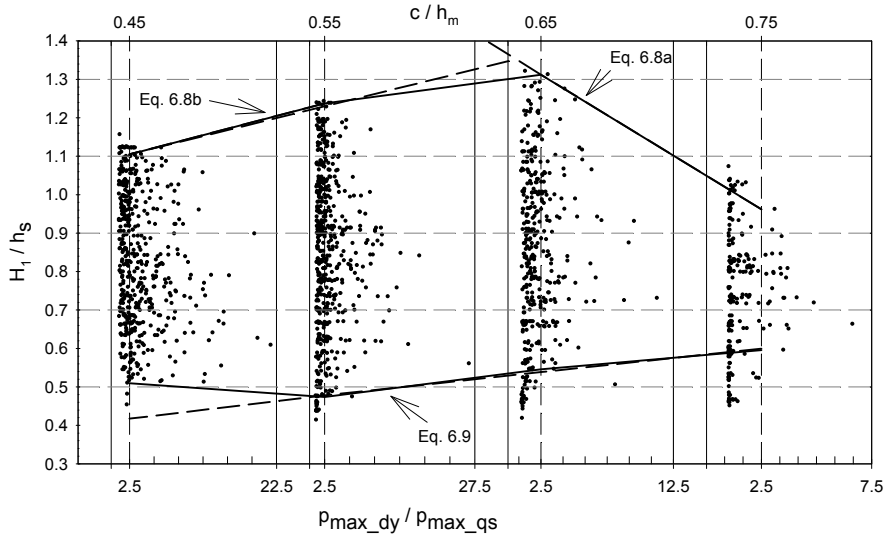

Figure 6.12 *Variation of wave height range ($\frac{H}{h_s}$) which creates high dynamic pressures on the horizontal part with the change of $\frac{c}{h_m}$. Continuous lines are measured upper and lower boundaries while dashed lines represent adopted boundaries. Upper and lower boundaries are determined between the points where* $p_{max\_dy}/p_{max\_qs} \geq 2.5$.

dynamic pressures on the vertical part. Equation 6.8b expresses the modified upper boundary in the zone of $\frac{c}{h_m} < 0.64$.

The boundary region of the dynamic pressures exists on the horizontal part where $p_{max\_dy}/p_{max\_qs} \geq 2.5$. Equation 6.8 and Equation 6.9 express the upper and lower boundaries, respectively.

Equation 6.8 *a) for* $0.64 \leq \frac{c}{h_m} \leq 0.75$ $\quad \frac{H_1}{h_s} = -3.5 * \frac{c}{h_m} + 3.59$

b) for $0.45 \leq \frac{c}{h_m} < 0.64$ $\quad \frac{H_1}{h_s} = 1.33 * \frac{c}{h_m} + 0.51$

Equation 6.9 *for* $0.45 \leq \frac{c}{h_m} \leq 0.75$ $\quad \frac{H_1}{h_s} = 0.61 * \frac{c}{h_m} + 0.14$

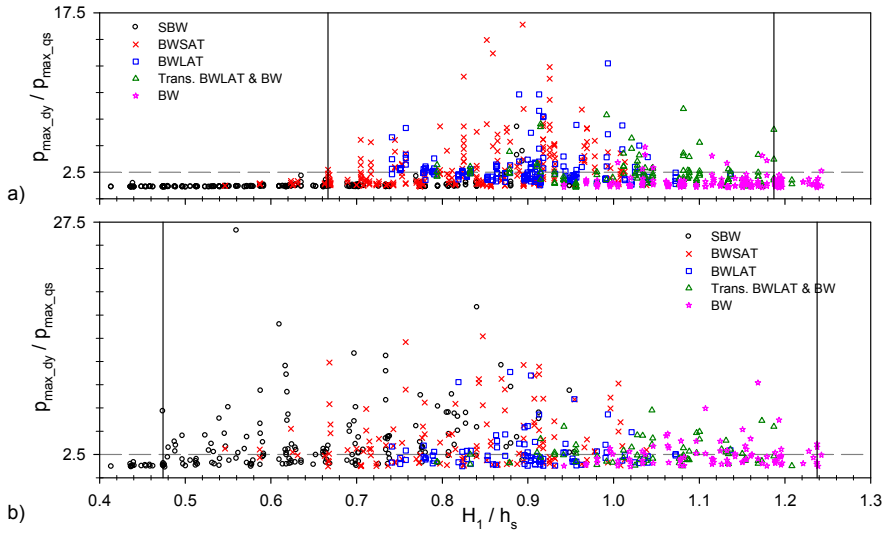

Figure 6.13 *Variation of the ratio of maximum dynamic and quasi-static peak pressures (p_{max_dy} / p_{max_qs}) with the change of H_1/h_s at $\frac{c}{h_m} = 0.55$, or $h_s = 0.135\ m$. a) Pressure ratio on the vertical part, b) Pressure ratio on the horizontal part*

Figure 6.13 represents the variation of p_{max_dy} / p_{max_qs} with the variation of $\frac{H_1}{h_s}$ for the various breaking cases. Figure 6.13a and b show the data already shown in Figure 6.11 and Figure 6.12 at $\frac{c}{h_m} = 0.55$. The scattered data of various colors represent the ratio of measured pressures in the different breaker types. A range of $\frac{H_1}{h_s}$ in which pressure ratios fall below $p_{max\_dy}/p_{max\_qs} < 2.5$ corresponds to quasi-static pressures, while the remaining area is the dynamic pressure zone.

On the vertical part, the zone of dynamic pressure, p_{max_dy} / $p_{max\_qs} \geq 2.5$, displays a high scatter between $0.67 < H_1/h_s < 1.19$. This area corresponds to the wave cases BWSAT and BWLAT (see Figure 6.13a). However, this scattering area of dynamic pressures extends to SBW and BW zones ($0.47 < H_1/h_s < 1.24$) for the pressures on the horizontal part (see Figure 6.13b). In the second case, rising water columns on the vertical part result in high impact loads on the horizontal part. Therefore, the range of H_1 which creates impact loads on horizontal part is larger than the H_1 range creating impact on the vertical part. This is compatible with the findings in Figure 6.12.

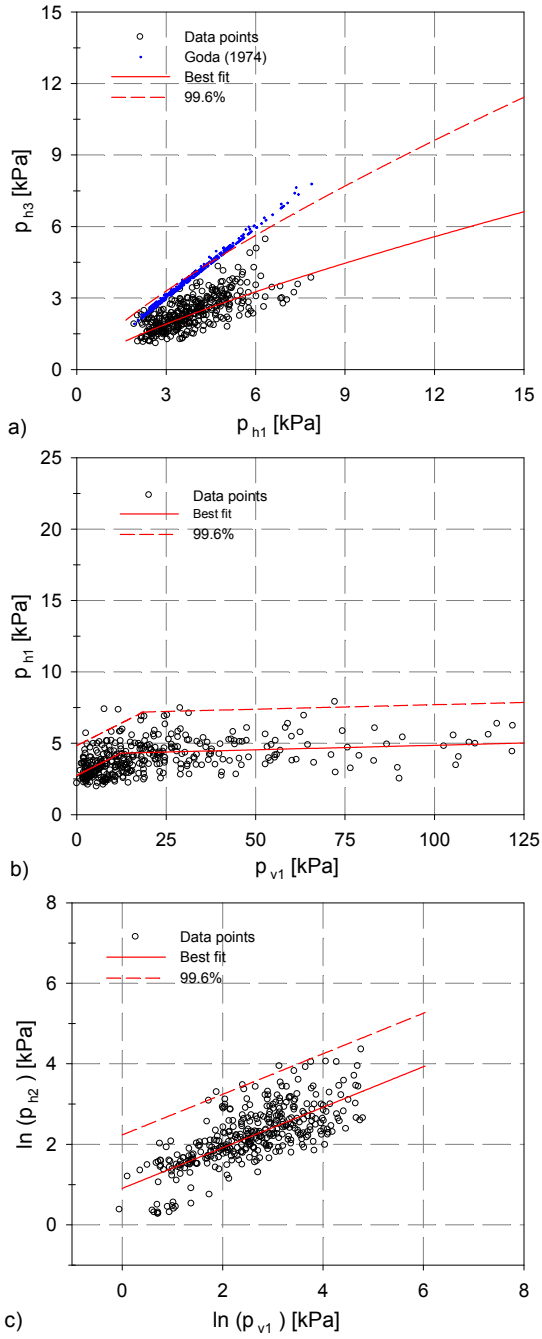

Figure 6.14 *Evaluation of maximum pressure profiles in the case of SBW. a)* p_{h3}/p_{h1}*, b)* p_{h1}/p_{v1}*, c)* p_{h2}/p_{v1}

6.4.2 Pressure profiles at SBW

In the following, the pressure profiles of four cases (SBW, BWSAT, BWLAT and BW) are discussed based on the pressure distributions shown in Figure 6.10. Pressure values represent the local maximum peak pressure at specified locations. The boundary conditions of all four cases are determined based on the classification according to the breaker type on the vertical part. The boundary region of $\frac{H_1}{h_s}$ for the first case (SBW) is the area below Equation 6.7 where $p_{max\_dy}/p_{max\_qs} \leq 2.5$ and $0.45 \leq \frac{c}{h_m} < 0.60$.

Once the maximum pressures on the vertical or horizontal part (p_{h1} or p_{v1}) are known, the relations for p_{h3}/p_{h1}, p_{h1}/p_{v1}, and p_{h2}/p_{v1} can be determined. Figure 6.14a shows the relation between maximum local peak pressures at the toe of the vertical part (p_{h3}) and maximum local peak pressures at the SWL (p_{h1}). An exponential relation between p_{h3} and p_{h1} is observed. The results are compared to the theoretical expression of Goda (1974) for pulsating waves. The Goda values are calculated under the same geometric and hydrodynamic conditions. Even Goda's method slightly underestimates the small value of p_{h3}. One should bear in mind that Goda's method is developed for pressure distributions at the time of maximum horizontal force on a simple vertical wall which will be slightly different. The proposed line merges with Goda line for most of the p_{h1} values. The Equation 6.10 represents the mean of the present data by a standard deviation s=0.2057.

Equation 6.10 $$ln(p_{h3}) = 0.77\ ln(p_{h1}) - 0.2$$

Figure 6.14b shows the relation between p_{h1} and the maximum pressure on the horizontal part (p_{v1}). p_{v1} values are calculated from sensor 8 which is the sensor closest to the vertical part (see Figure 3.1). In the case of SBW, the wave tends to break but the water level at the wall accelerates fast and results in an incomplete breaking due to the presence of the wall. Therefore, most of the energy reflects from the wall and the structure is subjected to pulsating loads. The magnitude of this pulsating pressure does not exceed 8 kPa. However, the accelerated vertical component collides on the horizontal part as an uprising water jet. This water jet results in a very high impact pressure (up to 125 kPa). For very small values of p_{h1} and p_{v1}, a linear relation is observed and this relation extends up to the maximum quasi-static pressure of p_{h1}. Hence, a constant value of p_{h1} for longer values of p_{v1} may be assumed (Equation 6.11).

Equation 6.11

$p_{v1} \leq 12$	$p_{h1} = 0.13\ p_{h1} + 2.75$	*with s=0.789*
$p_{v1} > 12$	$p_{h1} = 4.5$	*with s=1.07*

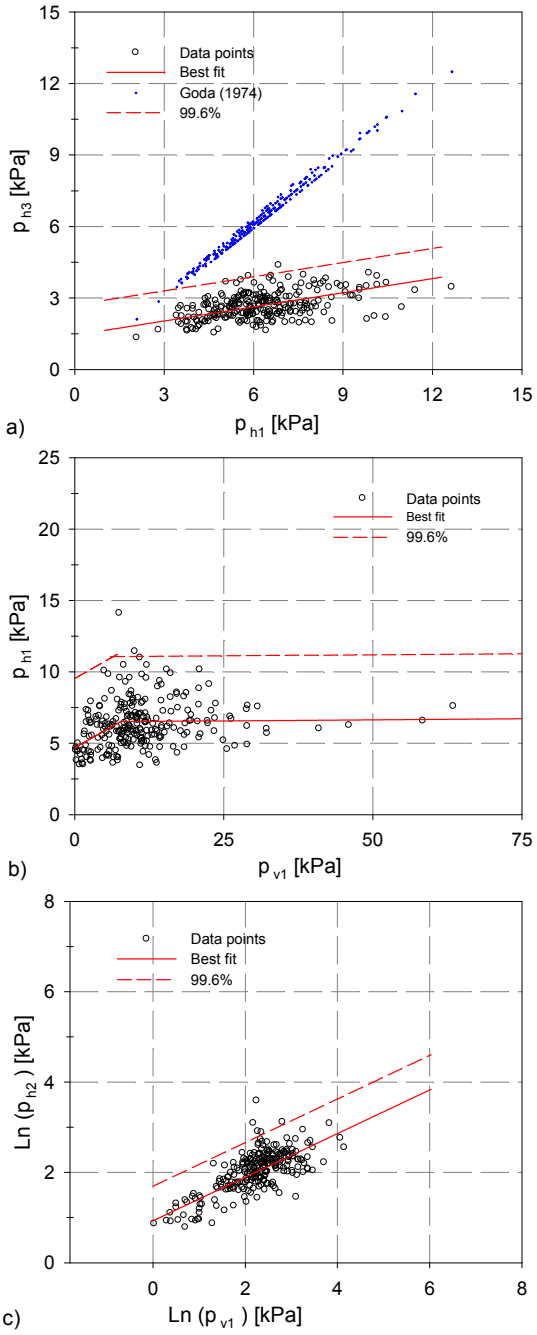

Figure 6.15 *Evaluation of maximum pressure profiles in the case of BW. a)* p_{h3}/p_{h1}*, b)* p_{h1}/p_{v1}*, c)* p_{h2}/p_{v1}

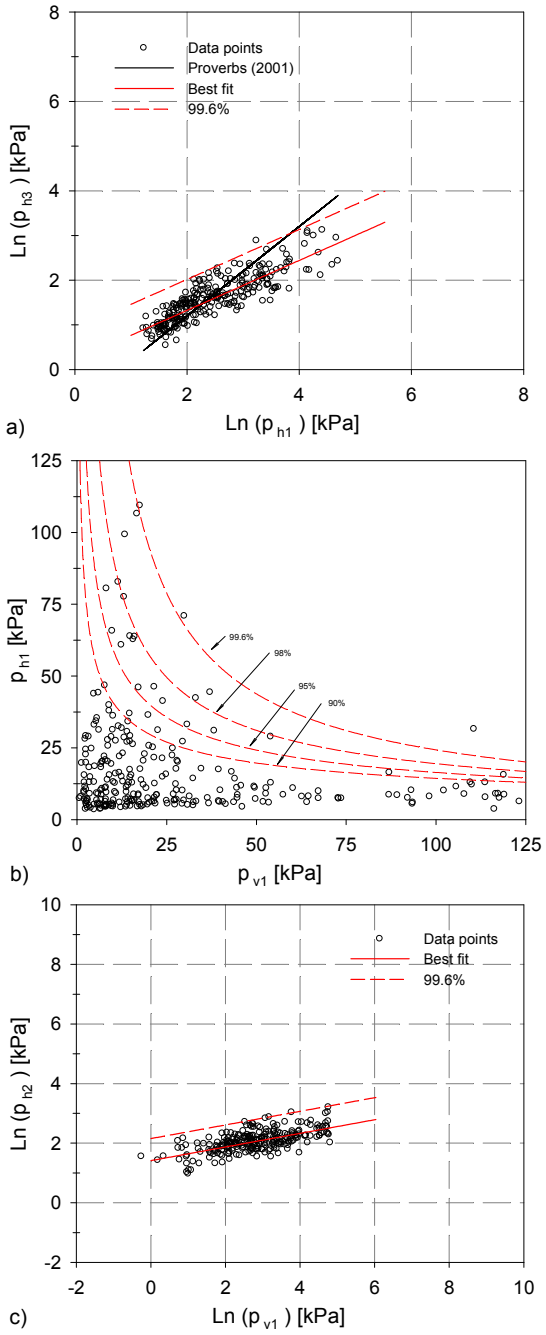

Figure 6.16 *Evaluation of maximum pressure profiles in the cases of BWSAT. a)* p_{h3}/p_{h1}*, b)* p_{h1}/p_{v1}*, c)* p_{h2}/p_{v1}

Figure 6.14c expresses the relation between the maximum pressure at the upper corner of the vertical part (p_{h2}) and p_{v1}.The values of p_{h2} are calculated from sensor 7 (see Figure 3.1). The impact force due to the water jet rising on the vertical part is the driving force for both pressures. The water jet first hits beneath the horizontal part and then influences the measurements at sensor 7. Therefore, measured p_{v1} values are significantly higher than p_{h2} values. A logarithmic relation (Equation 6.12) is considered for the mean function with s=0.4882. When the clearance is reduced, both p_{h2} and p_{v1} values increase.

Equation 6.12 $$ln(p_{h2}) = 0.51\ ln(p_{v1}) + 0.88$$

6.4.3 PRESSURE PROFILES AT BW

The boundary region of $\frac{H}{h_s}$ for BW is the area above Equation 6.6. In this region p_{max_dy}/p_{max_qs} is smaller than 2.5 and is valid between $0.45 \leq \frac{c}{h_m} < 0.75$. Figure 6.15 shows the relation between p_{h3}/p_{h1}, p_{h1}/p_{v1}, and p_{h2}/p_{v1} for the case of BW. Similar to the case of SBW, a linear relation is observed between p_{h3} and p_{h1}. The mean line is shown in Equation 6.13 (with s=0.4772) which is quite different from the line, calculated by Goda's method.

Equation 6.13 $$p_{h3} = 0.2\ p_{h1} + 1.44$$

Figure 6.15b shows the relation between p_{h1} and p_{v1}. In this case, the measured quasi-static pressure at p_{h1} is higher than the magnitude from the previous case. Here waves are breaking early and approaching the vertical part as a mixture of a water-air jet. Therefore, BW creates rather high or even dynamic pressures on the wall. However, the magnitude of p_{v1} is lower than the measurements in SBW which is due to the damping effect of air content. The following relation (Equation 6.14) is proposed between p_{h1} and p_{v1} and the logarithm in Equation 6.15 represents the relation between p_{h2} and p_{v1} with and s=0.2889.

Equation 6.14

$p_{v1} \leq 8$	$p_{h1} = 0.24\ p_{v1} + 4.7$	*with s=1.8316*
$p_{v1} > 8$	$p_{h1} = 6.5$	*with s=1.7176*

Equation 6.15 $$ln(p_{h2}) = 0.48\ ln(p_{v1}) + 0.92$$

6.4.4 PRESSURE PROFILES AT BWSAT

Figure 6.16 shows the relation of ratios p_{h3}/p_{h1}, p_{h1}/p_{v1}, and p_{h2}/p_{v1} for BWSAT. The boundary region is the area between Equation 6.6 and Equation 6.7. In this zone, $p_{max\_dy}/p_{max\_qs} \geq 2.5$ and these equations are valid for $0.45 \leq \frac{c}{h_m} < 0.60$.

In this case, waves collide on the vertical part with a more or less parallel face and only a little amount of air is enclosed (see Figure 5.2). Due to the impact effects, the wave crest breaks up into small droplets and the enclosed air compresses and bursts upwards. The breaking wave creates high dynamic impacts both on the vertical and horizontal parts. The relation between p_{h3} and p_{h1} is shown in Figure 6.16a and the results are compared with the theoretical line derived from the method in Oumeraci et al., 2001 (PROVERBS method). The theoretical line represents the best fit line in the low p_{h1} region, and it overestimates p_{h3} values in the high p_{h1} region. Equation 6.16 represents the mean of the present data with s=0.2614.

Equation 6.16 $$ln(p_{h3}) = 0.56\ ln(p_{h1}) + 0.21$$

Figure 6.16b represents the relation between p_{h1} and p_{v1} which is an inversely proportional relation. Normally, in BWSAT condition, high dynamic pressures are expected both on the vertical and horizontal part for the same wave. However, when a single wave perfectly breaks on the vertical part, it only creates a high impact pressure on the vertical part. Because it loses most of its energy on the vertical part and breaks in to small droplets, it results in relatively low pressures on the horizontal part. Equation 6.17 shows upper envelope function at 99.6% of non-exceedance level between p_{h1} and p_{v1}.

Equation 6.17 $$(p_{h1})_{99.6\%} = 1217\ (p_{h1})^{-0.88}$$

Figure 6.16c shows the relation between p_{h2} and p_{v1}. As described earlier, the pressure at the location of p_{h2} is an indirect effect of the impact occurring on the horizontal part. Hence, the latter follows a trend parallel with the increase of p_{v1}. However, it only increases up to a certain value. Beyond this value water cannot compress because one side is open and the water deflects through the open side. Equation 6.18 represents the formula of the mean line with s=0.268.

Equation 6.18 $$ln(p_{h2}) = 0.23\ ln(p_{h1}) + 1.4$$

Data related to the BWLAT case required more analyses. Therefore, in this chapter we are not suggesting any formula for this particular case.

6.5 SCALING

In general, it is said that breaking waves create impact loads while others produce quasi-static (pulsating) loads. In literature, Froude scaling is well accepted and suggested for pulsating loads. However, using the Froude similarity for scaling impact peak pressures leads to prototype pressures being overestimated (Bullock et al., 2001). This is due to the effect of aeration which strongly influences magnitudes and durations of the impact loads. Recently, Cuomo et al. (2010) suggested a practical method for adjusting the impact pressures and rise time on the vertical structures. For details of this procedure, see Section 2.5.

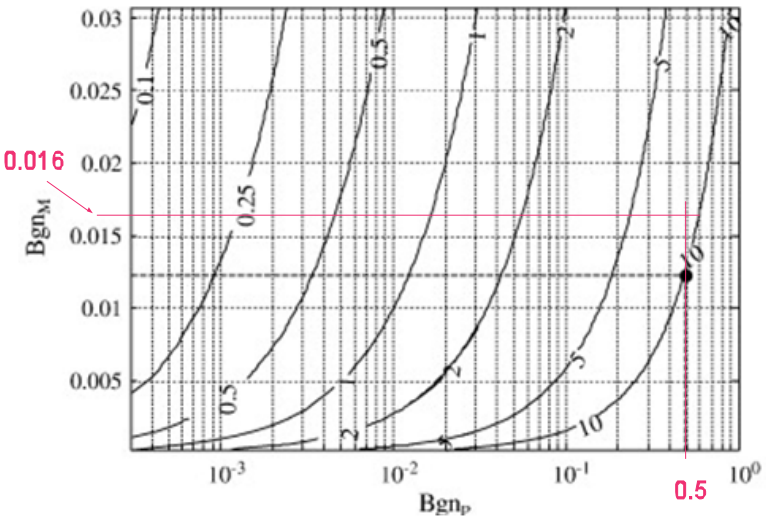

Figure 6.17 *Scale factor as a function of Bagnold numbers for no air leakage case, $\varepsilon = 0$ (after Cuomo et al., 2010)*

During the model tests, the overall highest impact pressure of 123 kPa is measured on the horizontal part at the location of sensor 8, where $x/h_s = 0.037$ in the case of BWSAT ($h_s = 0.135\,m$, $H = 0.155\,m$ and $T = 2.2\,s$). x is the horizontal distance from the vertical wall (see Figure 3.1). At prototype scale, data of the measurement on Blankenberge pier is available from 2 winter seasons ('03-'04 and'04-'05). The most extreme pressure peak that was measured: 470 kPa in a point 0.73 m away from the vertical core ($x/h_s = 0.127$), during a storm with a significant wave height of 2.93 m, a peak wave period of 8.1 s and 5.71 m water depth at the toe of the structure (Verhaeghe et al., 2006).

According to Froude scaling, a scaling factor of 20.5 is found from the scaling of the pressure relation in Table 2.1. Based on this scaling factor, the peak pressure in the prototype is calculated as 2521 kPa which is quite a bit higher than the measured values of 470 kPa in the prototype scale.

If the scaling procedure explained by Cuomo et al., (2010) is applied. Then, u_0, D and k_w are calculated as 1.7, 0.04, 0.022 and 9.2, 0.76, 0.43 for model and prototype scales respectively. Based on the above values, Bagnold numbers (Equation 2.44) will take values of $Bgn_m = 0.016$ and $Bgn_p = 0.5$. Atmospheric pressure p_0 is considered as $p_0 = 101\ kPa$. For the calculated values of the Bagnold numbers, a scaling factor (λ_s) around 8.5 can be read on Figure 6.17 for $\varepsilon = 0$ (ε is the equivalent opening ratio available for air leakage). This scaling factor leads to a 235 kPa at prototype scale. This difference might be due to a number of causes including air leakage at impact and air entrainment in the water (Cuomo et al., 2010). In addition, Cuomo's approach is developed for impact pressures on vertical structures which is not the exact case in this study. Apart from the scaling procedure, the existence of vertical piles around the prototype may be another source for the uncertainties.

In addition, the difference between the measurement locations is another critical issue. Due to the installation difficulties on the field, the closest sensor is installed at $x/h_s = 0.127$. This point may be equal to $x/h_s = 0.2$ on the model because of the circular shape of the prototype. From Figure 6.5, it can be seen that a variation of $0.11\ x/h_s$ between measurement positions results in almost 50% reduction in the value of the maximum peak pressure.

If real measured values are considered, a scaling factor of $\lambda_s = 16.7$ is found from Equation 2.49.

6.6 CONCLUSION

The pressure distribution due to the violent water wave impacts on a vertical wall with an overhanging horizontal cantilever slab is analyzed based on the results of breaking waves. Both the location and the magnitude of p_{max} on a vertical structure with an overhanging horizontal cantilever slab are determined. On the vertical part, the non-dimensional term (z_{max}/h_s) for the location of p_{max} is gradually decreasing from a point above the SWL to a point below the SWL with the increase of h_s. This relation is expressed by Equation 6.3. On the horizontal part, p_{max} is located at the attached corner of the scaled model and its magnitude decreases sharply below $10\ \rho gH$ between $x/h_s = 0.8 - 1$. The region of high local impact is bounded by the impact area of the rising jet face. The extension region is relatively small compared to the region of local peak pressures ($x/h_s = 0.3 - 0.5$).

The relation between the measured value of p_{max} on the vertical part and related t_r are plotted and compared with empirical values from literature. It is observed that the latter underestimate the measured values. Therefore, a new upper envelope function between p_{max} and t_r is proposed with for non-dimensional form. The similar inverse relation between p_{max} and t_r is also measured on the results for the horizontal part and their relation is given in Equation 6.5.

Proper determination of the boundary conditions for the region of dynamic pressures is quite important to develop a reasonable design method. The boundary expressions for the interval of normalized wave height, $\frac{H}{h_s}$, which creates a high

dynamic impact on the vertical part with the variation of the clearance, $\frac{c}{a}$, are expressed by Equation 6.6 and Equation 6.7. This corresponds to the wave range for the cases of BWSAT and BWLAT where $0.67 < H/h_s < 1.19$. In addition, boundaries for the region of dynamic pressure occurring on the horizontal part are shown by Equation 6.8 and Equation 6.9 where H/h_s lies between $0.47 < H/h_s < 1.24$. Therefore, on the horizontal part the range of wave height which creates impact loads is larger than the wave height range creating impact on the vertical part.

The spatial distribution of local p_{max} both on the vertical and horizontal part for cases SBW, BWSAT and BW are analyzed. For the pressure profiles, local p_{max} at SWL and at the top and bottom of the vertical part (p_{h1}, p_{h2} and p_{h3}) and at the attached corner of the horizontal part (p_{v1}) are considered. For each case, the relation for p_{h3}/p_{h1}, p_{h1}/p_{v1}, and p_{h2}/p_{v1} are determined.

In SBW, a linear relation is observed between p_{h3} and p_{h1} which complies with the theoretical expression of Goda (1974). In addition, the relation between p_{h1} and p_{v1} is also linear for very small values of p_{v1} and it is constant for higher values of p_{v1}. Furthermore, a logarithmic relation is fitted for the upper envelope line between for p_{v1} and p_{h2}.

In BW conditions, the relation similar to the case of SBW is observed between p_{h3}/p_{h1}, p_{h1}/p_{v1}, and p_{h2}/p_{v1}. The measured quasi-static pressure p_{h1} is higher than the measurements in the previous case. However, the pressure magnitude of p_{v1} is lower than the measurements in SBW which is due to the damping effect of air content.

The boundary region of BWSAT lies between Equation 6.6 and Equation 6.7 and dynamic pressures are measured in this case. A logarithmic relation is proposed between p_{h3} and p_{h1} and it is compared with the theoretical line derived from the method in PROVERBS. The theoretical line represents the best fit line in the low p_{h1} region, and it over estimates p_{h3} values in the high p_{h1} region. In addition, an inverse relation is observed between p_{h1} and p_{v1}. Finally, the relation between p_{h2} and p_{v1} is studied and a logarithmic relation is proposed.

Finally, the scaling issue of maximum impact pressure on the horizontal part is discussed. The scaling procedure proposed by Cuomo et al. (2010) is applied to the model results by assuming zero air leakage. The calculated scaling factor λ_s from Cuomo approach is lower compare to the λ_s based on measurements.

REFERENCES

Allsop, N.W.H.; McKenna, J.E.; Vicinanza, D.; and Whittaker, T.J.T., 1996, "*New design formulae for wave loadings on vertical breakwaters and seawalls*", Proc 25th Int. Conf. Coastal Engineering, ASCE, New York 1996, pp. 2508–2521.

Bagnold, R. A., 1939, "*Interim report on wave-pressure research"*, Proc. Inst, Civil Eng. 12, 201–226

Blackmore, P.A.; Hewson, P.J., 1984, "*Experiments on full-scale wave impact pressures*", Coastal Engineering Volume: 08 Issues: 4, pp: 331-346

Bullock, G.N.; Crawford, A.R.; Hewson, P.J.; Walkden, M.J.A.; Bird, P.A.D., 2001, "The influence of air and scale on wave impact pressures", Coastal Engng, vol 42, pp 291-312

Bullock, G.N.; Obhrai, C.; Peregrine, D.H.; Bredmose, H., 2007, "Violent breaking wave impacts Part 1: Results from large-scale regular wave tests on vertical and sloping walls" Coastal Engineering, v 54, n 8, p 602-617

Chan, E.S.; Melville, W.K., 1988, "*Deep-water plunging wave pressures on a vertical plane wall"*, Proc. Roy, Soc. London, A, 4171852, 95-131

Cuomo G.; Tirindelli M.; and William Allsop W., 2007, "*Wave-in-deck loads on exposed jetties"*, Coastal Engineering Volume 54, Issues-9, 2007, pp: 657-679

Cuomo, G.; Allsop, W.; Takahashi, S., 2010, "*Scaling wave impact pressures on vertical walls*", Coastal Engineering, Volume 57, Issue 6, June 2010, Pages 604-609

Cuomo, G.; Piscopiac, R.; and Allsop, W., 2011, "Evaluation of wave impact loads on caisson breakwaters based on joint probability of impact maxima and rise times", Coastal Engineering, Volume-58, Issues-1, 2011, pp-9-27

Goda, Y., 1974, "*New wave pressure formulae for composite breakwater*", Proc. of 14th Int. Conf. Coastal Eng., Copenhagen, Denmark, ASCE, New York (1974, pp. 1702–1720

Goda, Y., 2000, "*Random seas and design of maritime structures*" 2nd Edition, Advanced Series on Ocean Engineering vol. 15, World Scientific 2000 443 pp

Hattori, M.; Arami, A.; Yui, T., 1994, "*Wave impact pressure on vertical walls under breaking waves of various type"*, Coastal Engineering, v 22, n 1-2, p 79-114, Jan 1994

Hull, P.; Müller, G., 2002, *"An investigation of breaker heights, shapes and pressures"* Ocean Engineering, v 29, n 1, p 59-79, September 21, 2002

Kirkgoz, M.S., 1982, "*Shock pressure of breaking waves on vertical walls"* Journal of the Waterway, Port, Coastal and Ocean Division, v 108, n WW1, p 81-95, Feb 1982

Kirkgoz, M.S., 1990, "An experimental investigation of a vertical wall response to breaking wave impact", Ocean Engineering Volume-17, 1990, pp-379-391

Kisacik, D.; Troch, P.; Van Bogaert, P., 2011, "Description of loading conditions due to violent wave impacts on a vertical structure with an overhanging horizontal cantilever slab", Accepted to journal of "Coastal engineering".

Kortenhaus, A.: and Hocine Oumeraci, H., 1998, "Classification of wave loading on monolithic coastal structures", Proc. 26th. Int. Coast. Engrg. Conf.,

ASCE, pp: 867-880 p Year.1998

McConnell, K.; Kortenhaus, A., 1996, "*Analysis of pressure measurements from hydraulic model tests and prototype measurements*", Proc. Task 1 Belfast Workshop, PROVERBS Project, Leichtweiss Institut, Technical University of Braunschweig, Braunschweig, Germany, MAST III/PROVERBS

Minikin, R.R., 1963, "Wind, Waves and Maritime Structures", (2nd Ed.), Charles Griffen, London (1963)

Oumeraci, H., 1994, "Review and analysis of vertical breakwater failures lessons learned Special Issue on Vertical Breakwaters", Coastal Eng. 22 1994, pp. 3–29.

Oumeraci, H.; Bruce, T.; Klammer, P.; Easson, W.J., 1995, "*PIV measurement of breaking wave kinematics and impact loading of caisson breakwaters*" COPEDEC, no. 4, v 3, pp. 2394-2410

Oumeraci, H; Kortenhaus, A; Allsop, W; de Groot, M; Crouch, R; Vrijling, H; Voortman, H, 2001, "*Probabilistic Design Tools for Vertical Breakwaters*", Balkema Publishers, New York.

Partenscky, H., 1988, "*Dynamic forces due to waves breaking at vertical coastal structures"* Twenty First Costal Eng Conf, p 2504-2518, 1988, Twenty First Costal Eng Conf

Peregrine, D.H., 2003, "*Water-wave impact on walls",* Annual Review of Fluid Mechanics, volume 35, p: 23-43

Richert, G., 1968, "*Experimental investigation of shock pressures against breakwaters"* In: Proc. Int. Conf. Coastal Engng, ASCE, London, pp. 954–973.

Takahashi, S., 1996, "*Design of vertical breakwaters*", Port and Harbour Research Institute, Ministry of Transport, Reference documenr # 34.

Verhaeghe, H.; Cherlet, J.; Boone, C.; Troch, P.; De Rouck, J.; Awouters, M.; Ockier, M.; Devos, G., 2006, "*Prototype monitoring of wave loads on concrete structure in intertidal zone*", COASTLAB06. pp. 117-125

Walkden, M.J.A., Hewson, P.J., Bullock, G.N., 1996, "*Wave impulse prediction for caisson design*", Proc. of 25th Int. Conf. Coastal Eng., Orlando, Florida, USA, ASCE, New York, pp. 2584–2597

Weggel, J.R.; Maxwell, W.H., 1970, "*Numerical model for wave pressure distributions*", J. of the Waterways, Harbor and Coastal Eng. Division, ASCE, August, no.ww3 1970, pp. 623–642

Witte, H.H., 1990, "*Wave impact loading on a vertical wall with respect to structure response*", Report for the Federal Waterways and Research Institute - Coastal Department. 30 pp

7

COMPARISON WITH LITERATURE FINDINGS

***

7.1 INTRODUCTION

The main aspect of this chapter is to compare the results of physical experiments conducted on a vertical wall with a cantilever slab and a simple vertical wall to observe the influence of cantilever slab on the force and pressure distribution of vertical walls. Details about both models are shown in Figure 3.6. This chapter starts with a short literature review about existing prediction methods of pressure and forces (Minikin, 1963; Goda, 2000; Blackmore & Hewson, 1984; Allsop et al., 1996; Oumeraci et al., 2001; Cuomo et al., 2010). Then, the test results on the simple vertical wall are compared with methods in literature to check their reliability. The comparison is done based on the results of regular wave tests. Finally, the results of the simple vertical wall type model are compared with the results of the scaled model with cantilever slab. Based on the discussion of the test results, conclusions are formulated.

7.2 PREDICTION OF PRESSURES AND FORCES ON THE VERTICAL STRUCTURES

Waves, attacking vertical structures, are usually classified as non-breaking, breaking and broken waves. A further categorization of breaker types is discussed in Chapter 5 which includes non-breaking waves, slightly breaking waves (SBW), breaking waves with small and large air trap (BWSAT and BWLAT) and broken waves (BW). Pressures and forces due to the non-breaking waves (standing waves) are well established (Goda, 1967 and Sainflou, 1928) and not included in this study. Breaking waves create short impulsive loads on the vertical structures which introduce localized damages. Coastal structures are bulk structures and most researchers did not consider these short-duration loads in their design formulas. However, Oumeraci (1994) emphasizes the importance of impulsive loads in the design of vertical structures. Several formulas from design codes allow calculating impulsive loads on vertical structures.

Minikin (1963) suggests a parabolic pressure distribution for the breaking waves on vertical walls (see Figure 2.12). The dynamic pressure p_m (Equation 7.1) has a maximum value at the SWL and decreases to zero at $0.5H_b$ below and above the SWL. The total horizontal force (F_h) represented by the area under the dynamic and hydrostatic pressure distribution is shown in Equation 7.2 (SPM, 1984). More details are shown in section 2.4.2.1.

Equation 7.1 $$p_m = 101\rho g \frac{H_b}{L_D}\frac{h_s}{D}(D + h_s)$$

Equation 7.2 $$F_h = \frac{101}{3}\rho g \frac{H_b^2}{L_D}\frac{h_s}{D}(D + h_s) + 0.5\rho g H_b h_s \left(1 + \frac{H_b}{4}\right)$$

where D is the depth at one wavelength in front of the wall, L_D is the wavelength in water depth D and H_b is the breaker wave height.

Minikin's formula is dimensionally inconsistent. Allsop et al. (1996c) show that the horizontal impact force (F_h) predicted by Minikin's formula is incorrect due to the decrease of F_h with increasing L_D. Some incompatibilities are found between different versions of Minikin's formula which are mainly due to a unit mistake converting from British to metric units. Therefore, Minikin's formula is now out of fashion (Bullock, et al., 2004).

Goda (1974) suggests his own formula for the wave loads on the vertical walls based on theoretical and laboratory works. He assumes a trapezoidal pressure distribution on the vertical walls with maximum pressure at the SWL (Equation 7.3). His method predicts a static equivalent load instead of short impulsive loads for breaking and non breaking waves. Takahashi (1996) extends the Goda method for breaking waves by adding some new term in the maximum pressure (p_1) at SWL to take into account the effect of berm dimension.

Equation 7.3 $$p_1 = 0.5(1 + cos\,\beta)(\lambda_1\alpha_1 + \lambda_2\alpha_* cos^2\beta)\rho g H_D$$

Where β is the angle of incidence of the wave attack with respect to a line perpendicular to the structure, $\lambda_1, and\ \lambda_2$ are the multiplication factors depending on the geometry of the structure. For conventional vertical wall structures, $\lambda_1 = \lambda 2 = 1$ and HD is the highest wave out of the surf zone or is the highest of random breaking waves at a distance of $5H_s$ seaward of the structure. The total horizontal force is calculated from the area under the pressure profile shown in Figure 2.11.

Blackmore & Hewson (1984) suggest a prediction formula based on full-scale field measurements (Equation 7.4). They consider the effect of entrained air which results in a reduction in the impact pressure of field tests compared to laboratory tests.

Equation 7.4 $$p_1 = \lambda\rho C_b^2 T$$

Where C_b is the shallow water wave celerity and λ is the aeration factor with dimension [s^{-1}]. λ has a value between $0.1s^{-1}$ and $0.5s^{-1}$ at full scale and between $1s^{-1}$ and $10s^{-1}$ at model scale (Blackmore & Hewson, 1984). It is recommended to use the value of $0.3s^{-1}$ for rocky foreshore and $0.5s^{-1}$ for regular beaches (BS 6349). The total horizontal force is calculated from the area below the pressure profile shown in Figure 2.13.

According to the model tests at HR Wallingford within the PROVERBS project, Allsop & Vicinanza (1996) recommend a prediction formula for horizontal wave impact force on the vertical walls (Equation 7.5). Data were produced on a slope of 1/50 at 1/250 level for the range of $0.3 < H_{si}/h_s \leq 2$. The method is recommended in Oumeraci et al. (2001) for preliminary design.

Equation 7.5 $$F_h = 15\rho g h_s^2 (H_{si}/h_s)^{3.134}$$

where, h_s and H_{si} are the water depth and significant wave height at the model toe.

PROVERBS was an EU project to develop and implement probability based tools for an integrated design of vertical breakwaters. Within PROVERBS a prediction method has been developed based on large data sets include small and large scale physical tests and field measurements. The overall horizontal impact force on the vertical breakwater is calculated from Equation 7.6.

Equation 7.6 $$F_h = F_h^* \rho g H_b^2$$

where, H_b is the breaking wave height and F_h^* is the relative maximum wave force calculated using this generalized extreme value (GEV) distribution (Equation 7.7).

Equation 7.7 $$F_h^* = \frac{\alpha}{\gamma}\{1 - [-lnP(F_h^*)]^\gamma\} + \beta$$

where, $P(F_h^*)$ is the probability of non exceedance of the impact force (generally taken as 90%) and α, β, γ are the statistical parameters for GEV distribution and changing with bed slope. The pressure profile on the vertical walls according to PROVERBS is shown in Figure 2.15.

Cuomo et al, (2010) recently suggest a prediction formula for the horizontal impulsive load $F_{h,imp,1/250}$ on the vertical walls on level of 1/250 (Equation 7.8).

Equation 7.8 $$F_{h,imp,1/250} = C_r^{1.65} \rho g \, H_{mo} \, L_{hs} \left(1 - \frac{|h_b - d|}{d}\right)$$

where, C_r is the reflection coefficient, L_{hs} is the wavelength at the toe of the structure for $T = T_m$, h_s is the water depth at the structure toe, d is the water depth at the wall and h_b is the water depth at breaking. h_b is determined from Miche's breaking criteria (Equation 7.9) by assuming $H_b = H_{mo}$

Equation 7.9 $$h_b = \frac{1}{k} arctanh\left(\frac{H_{mo}}{0.14 \cdot L_{hs}}\right)$$

where, k is calculated from, $k = 2\pi/L_{hs}$

Eq. 8 is valid in the range of $0.2\,m < H_{mo} < 0.7\,m$, $0.5\,m < h_s < 1.3\,m$ and $2\,s < T_m < 3.7\,s$.

7.3 COMPARISION OF MEASURED HORIZONTAL FORCES ON THE SIMPLE VERTICAL WALL TYPE MODEL

Figure 7.1 to Figure 7.6 show the comparison of measured horizontal forces F_h on the simple vertical wall type model with the existing well known prediction formulas for various values of the wave height (H_7) which are measured at the toe of the model (see Figure 3.1). Horizontal force F_h and wave height H_7 are normalized by $\rho g h_s^2$ and water depth h_s respectively. Because a simple vertical wall type model has no horizontal part, all 10 pressure sensors are used for horizontal force F_h calculation by the pressure integration method described in Section 3.2.5.2. These three new sensors are located at $z = 0.045,\ 0.105$ and $0.225\ m$ to improve the vertical pressure profiles at the time of the maximum horizontal force. As it is shown in Figure 3.15, increasing pressure sensor resolution improves the measurement of horizontal forces especially for the high values. Tests on the simple vertical wall conduct at $h_s = 0.135\ m$ and $T = 2.2\ s$ for regular waves.

All these methods are developed for irregular waves and considered statistical wave height values like H_s, H_D or H_b to calculate the forces. In this particular set of data, force and wave height, measured by zero down crossing method, are correlated directly rather than showing a statistical relation. Therefore, wave heights (H_7), measure at the location of sensor 7, are considered for the force calculations in all methods except Goda. Because, Goda considers wave heights at $5H_s$ before the structure, which is equivalent to the wave heights measured at the location of sensor 5 (H_5). The data set contains results of breaking waves on the simple vertical wall type model within the range of waves $0.6<H_7/h_s<1.05$. These are breaking waves including both breaker types of BWSAT and BWLAT. A wooden plate is installed at the top of the simple vertical wall type model to block the overtopping. Because the scaled model does not allow overtopping due to its special geometry with horizontal part, both cases are able to test for non-overtopping condition. The measured data sets show a high scatter.

Both Minikin and extended Goda methods (see Figure 7.1 and Figure 7.2) are under estimating the horizontal forces on the vertical walls. In all methods, H_b is considered as the height of incident waves (H_7) at the location of structure (h_s). However, the Goda method considers incident wave heights $5H$ before the structure (H_5). The Allsop & Vicinanza formula (Figure 7.3) is under estimating some of the values but shows a good agreement with the trend of data. Results from the Blackmore & Hewson method (Figure 7.4) show an envelope line for the measurements with an aeration factor 10 which is the highest value suggested for small scale tests. Proverbs method (Figure 7.5) fairly estimates the maximum values. For these calculations, $P(F_h^*) = 0.996$ is considered which comes to the 1/250 level in the Goda's method. However, for design a value of $P(F_h^*) = 0.90$ is suggested which estimates the force except for the waves creating very high impact around H_7/h_s=0.9. The Cuomo method (Figure 7.6) shows good agreement with the general data trend and it underestimates very high values. It considers the effect of breaker type by reflection coefficient. In general, Minikin (1963), Goda

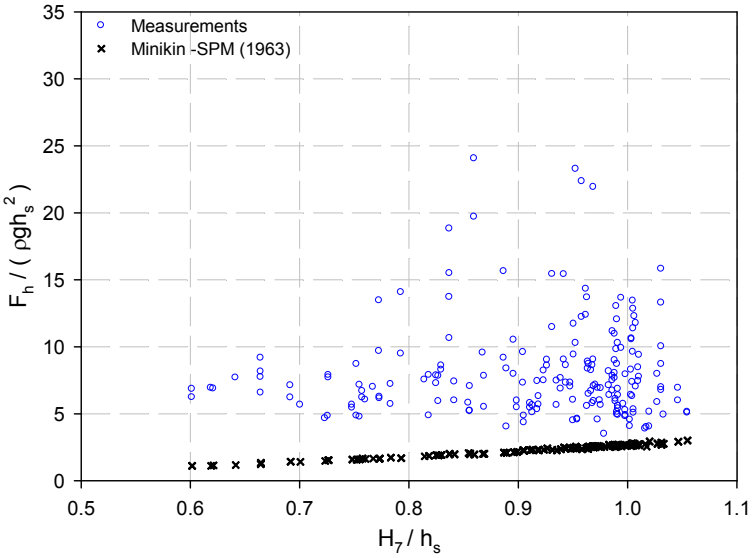

Figure 7.1 *Comparison between the measured horizontal impact force on a vertical wall type model with the predicted horizontal force by Minikin formula (SPM version) (Regular waves, T=2.2 s, h_s=0.135 m).*

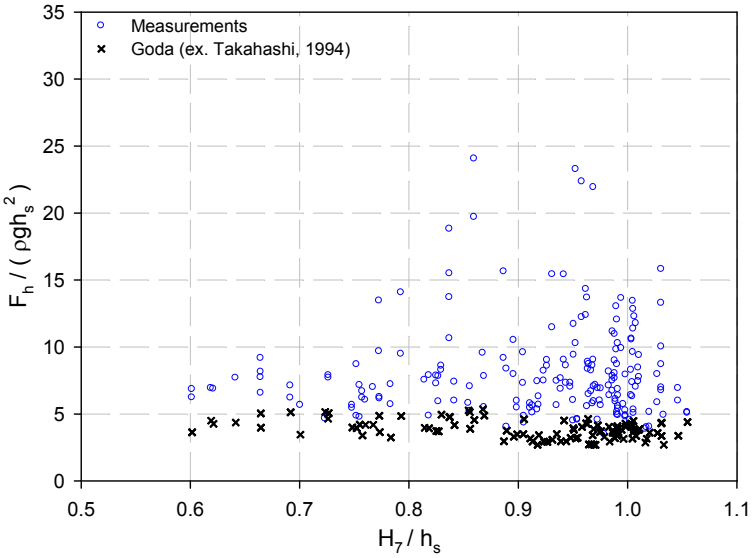

Figure 7.2 *Comparison between the measured horizontal impact force on a vertical wall type model with the predicted horizontal force by Goda formula (ex. Takahashi) (Regular waves, T=2.2 s, h_s=0.135 m).*

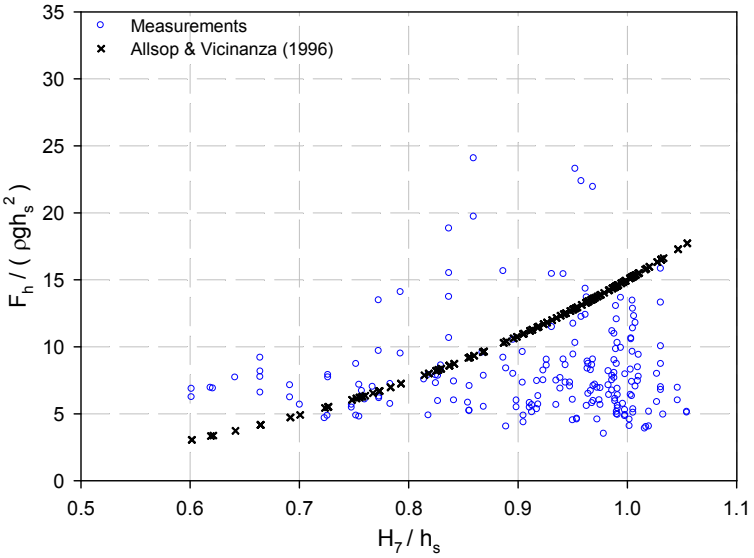

Figure 7.3 *Comparison between the measured horizontal impact forces on a vertical wall type model with the predicted horizontal force by Allsop & Vicinanza formula. (Regular waves, T=2.2 s, h_s=0.135 m)*

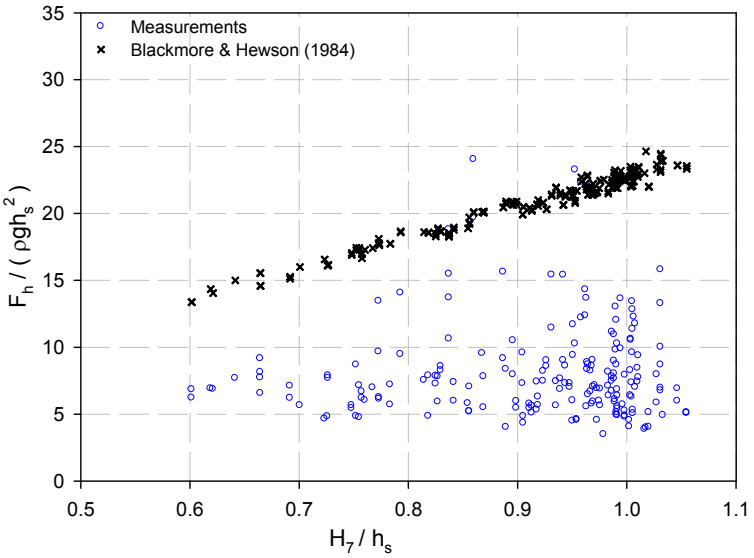

Figure 7.4 *Comparison between the measured horizontal impact forces on a vertical wall type model with the predicted horizontal force by Blackmore & Hewson formula. (Regular waves, T=2.2 s, h_s=0.135 m)*

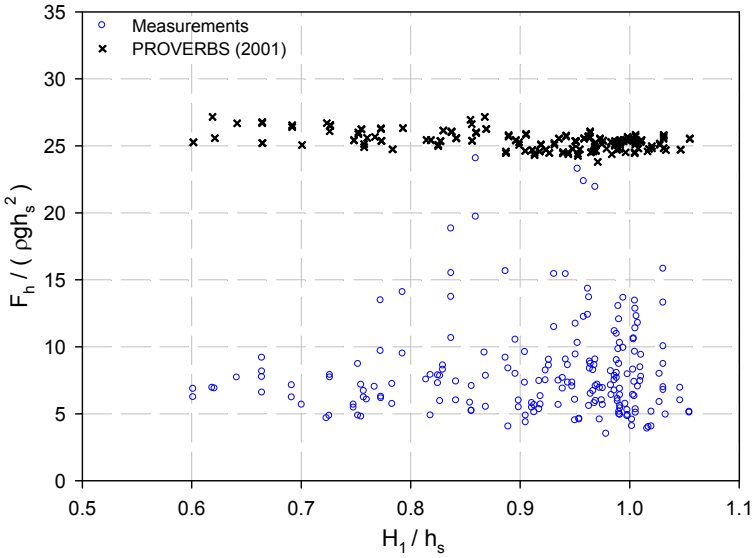

Figure 7.5 *Comparison between the measured horizontal impact forces on a vertical wall type model with the predicted horizontal force by PROVERBS formula. (Regular waves, T=2.2 s, h_s=0.135 m)*

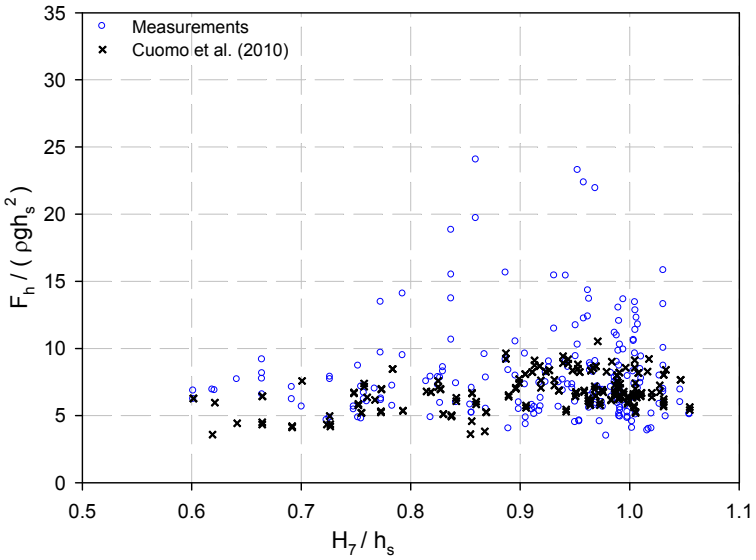

Figure 7.6 *Comparison between the measured horizontal impact forces on a vertical wall type model with the predicted horizontal force by Cuomo formula. (Regular waves, T=2.2 s, h_s=0.135 m)*

(ex. Takahashi, 1994), Allsop & Vicinanza (1996) and Cuomo et al. (2010) methods are predicting the measured impulsive force on the vertical walls. However, PROVERBS (2001) and Blackmore & Hewson (1984) prediction methods are accurate for designing according to the results from small the scale tests for regular waves.

7.4 PRESSURE DISTRIBUTION ON THE SIMPLE VERTICAL WALL TYPE MODEL

Figure 7.7 to Figure 7.10 show the comparison between the instantaneous pressure distribution for 5 impacts which create the highest value of forces on the simple vertical wall type model and the predicted pressure profile for the envelope functions. Instantaneous pressure profile is determined from the 10 pressure sensor results at the time of peak force calculated from Equation 3.6 for each individual impact. Here results are shown for the 5 highest maximum values measured at $h_s = 0.135\ m$ and $T = 2.2\ s$. There is a high scattering seen also for the location and value of peak pressures. Maximum peak pressures were observed between SWL and $0.5h_s$ above the SWL. Minikin, Blackmore & Hewson and PROVERBS methods (Figure 7.7, Figure 7.9 and Figure 7.10) are fairly good assuming the upper boundary of the pressure profile. However all methods apparently do not predict the maximum peak pressures as found in the tests. Approaching wave crest hits around SWL to produce the maximum pressure and the impact pressure quickly shifts both downwards and upwards from the initial impact point (see Section 5.5.2). This creates a phase difference between the results of sensors at the upper corner part and the results of sensors at lower parts of the simple vertical wall type model. Due to the phase difference, the instantaneous pressure at the upper corner shows negative values which appear just before impact rise. This phenomenon is described by Hattoria et al. (1994) as a result of an extremely high velocity jet shooting up the wall face (see Section 5.5.2).

7.5 COMPARISION BETWEEN THE SIMPLE VERTICAL WALL TYPE AND THE SCALED MODEL

Figure 7.11a shows the comparison between the measured horizontal force F_h both on the simple vertical wall type model and the scaled model which has the cantilever slab. Horizontal force is shown on axis of wave height H_1, measure at the toe of the foreshore. For the both cases, wave height ranges between $0.085 < H_1 < 0.145$. To have a comparison under the identical condition, horizontal forces on the simple vertical wall type model are measured from the records of 7 sensors located at the same positions on the scaled model. In this way, effect of sensor resolution is excluded from the results. It is seen from the figure that the both measurements are compatible each other and show high scatter (Figure 7.11a). However, scatter on the results of the scaled model is high. As discussed in Section 5.2, measured forces

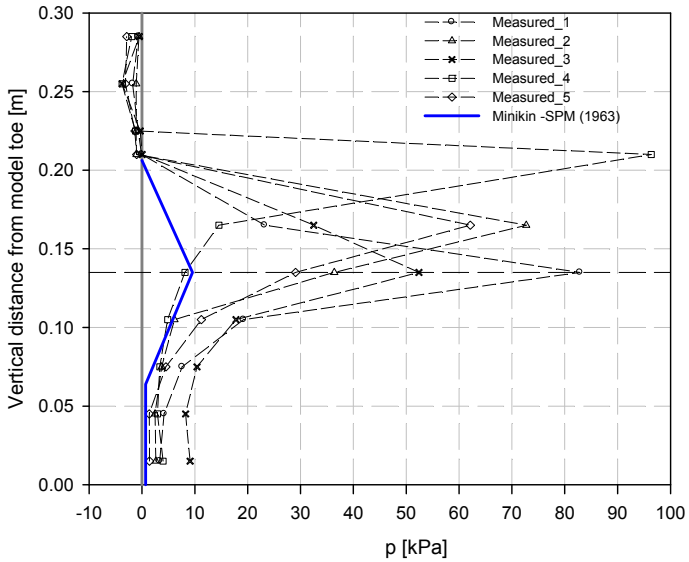

Figure 7.7 *Comparison between the measured vertical pressure profile of 5 waves creating the highest impact force with the highest predicted pressure profile using the Minikin method. (Regular waves, T=2.2 s, h_s=0.135 m)*

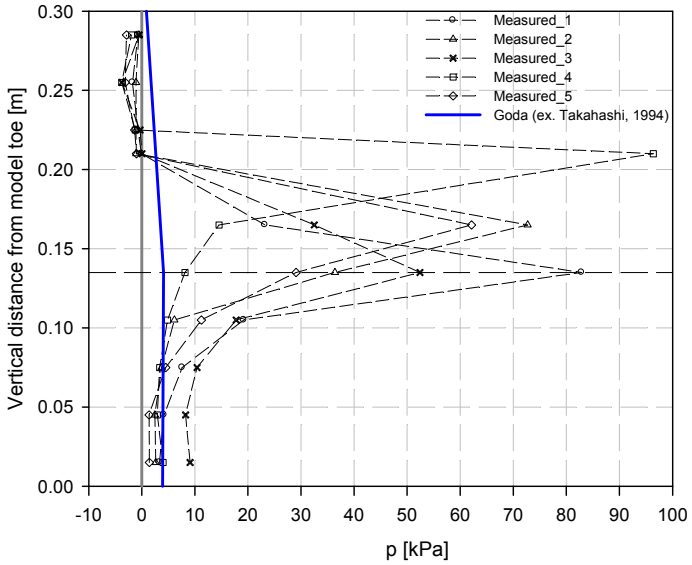

Figure 7.8 *Comparison between the measured vertical pressure profiles of 5 waves creating the highest impact force with the highest predicted pressure profile using the Goda (extended) method. (T=2.2 s, h_s=0.135 m)*

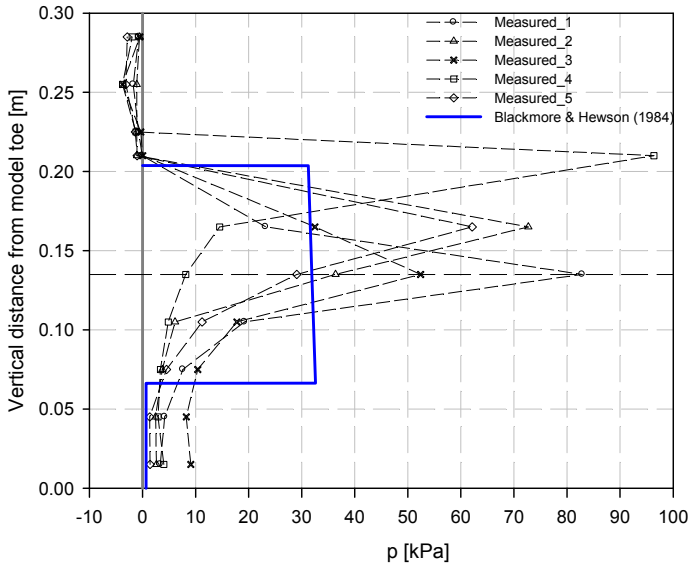

Figure 7.9 *Comparison between the measured vertical pressure profile of 5 waves creating the highest impact force with the highest predicted pressure profile using the Blackmore & Hewson method. (T=2.2 s, h_s=0.135 m)*

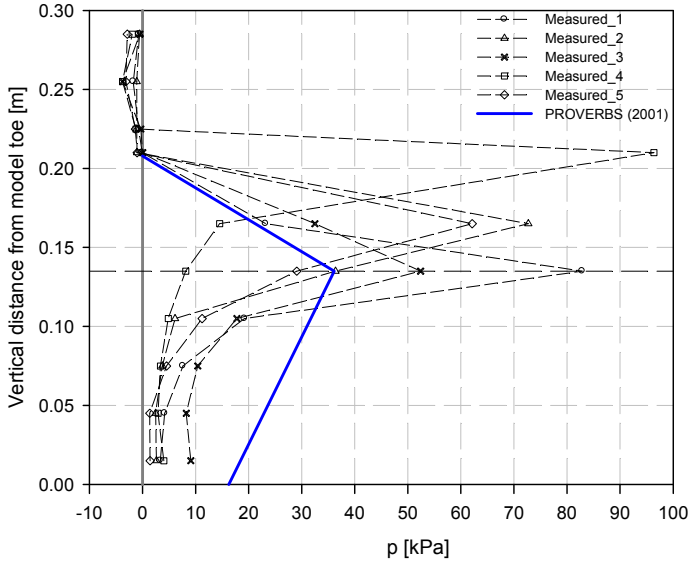

Figure 7.10 *Comparison between the measured vertical pressure profile of 5 waves creating the highest impact force with the highest predicted pressure profile using the PROVERBS method. (T=2.2 s, h_s=0.135 m)*

due to the breaking waves on the vertical structures are non-repeatable and high values are randomness. Therefore, it is obvious to measure higher values on the scaled model tests with a bigger data set. In general, breaking waves result in F_h with a sharp peak and short rise time. This peak is mainly dominated by maximum pressure p_{max} around SWL (see Figure 7.10). In addition, as it is seen from Figures 5.13 and 5.19b, show the instantaneous pressure profiles at the time of maximum horizontal forces, there is no influence of the horizontal part on the pressure distribution for the impacts with very high dynamic pressures or forces. The influence of horizontal part exists when pressures are in the range of quasi-static pressures or force.

Figure 7.11b shows the comparison of overturning moment M turning around the model toe. The overturning moment M presents on the variation of wave height H_1. Both data measured on the scaled and simple vertical wall type modes are compatible. However, in the range of small M values, results on the scaled model are higher than the results on the simple vertical wall type model. In this range of M, moment levering arm increases due to the pressure increase at the upper corner of the scaled model.

Figure 7.12 compares results for the quasi-static horizontal forces due to the slightly breaking waves (SBW). Both data sets more or less show a similar scatter. However, there is a significant effect of the cantilever slab is observed on the total horizontal force of the scaled model for especially small values of F_h. Even there is a phase difference between peak pressures around SWL and upper corner of the scaled model, calculated quasi-static forces from this pressure profiles reflect pressures at the upper corner due to its long-lasting character (see Figure 5.4 and 5.5). This small increase is more critical during overturning moment calculations (Figure 7.12b). Because the moment lever for F_h is larger compared to the moment lever on the simple vertical wall type model. Due to the high pressures at the upper corner, the centroid of the pressure profile shifts upwards this increases the moment levering arm. This issue is discussed in deep in Section 5.5.2.

In SBW, the wave tends to break but the water level at the wall accelerates fast and results in an incomplete breaking due to the presence of the wall. Therefore, it should be borne in mind that quasi-static loads referred to in this section do not correspond to the pulsating loads exerted by standing waves, for which well established prediction methods exists (Goda, 1967; Sainflou, 1928).

Cuomo et al. (2010) expressed the total quasi-static horizontal force of SBW waves on the seaward face of a wall as:

Equation 7.10 $$F_{h,qs+(1/250)} = \alpha\, \rho g\, H_{m0}^2$$

where H_{m0} is the significant wave height at the toe of the structure and α=4.76 is an empirical coefficient. The subscript (1/250) indicates that the corresponding parameter has been evaluated as the average of the highest four events in a (nominally) 1000-wave test.

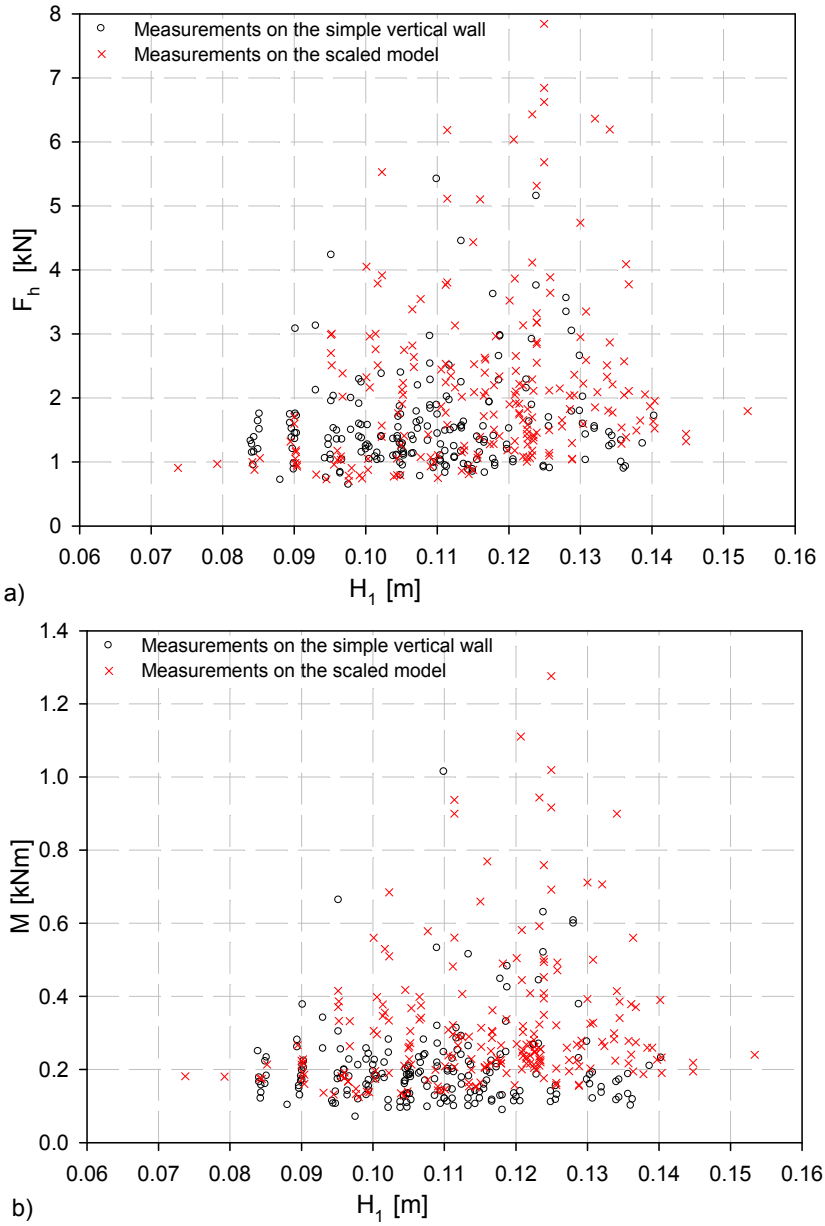

Figure 7.11 *Comparison of the results due to breaking waves (BWSAT & BWLAT) on the simple vertical wall type model and the scaled model with cantilever slab, a) Horizontal force F_h, b) Overturning moment M, (Regular waves, T=2.2 s, h_s=0.135 m)*

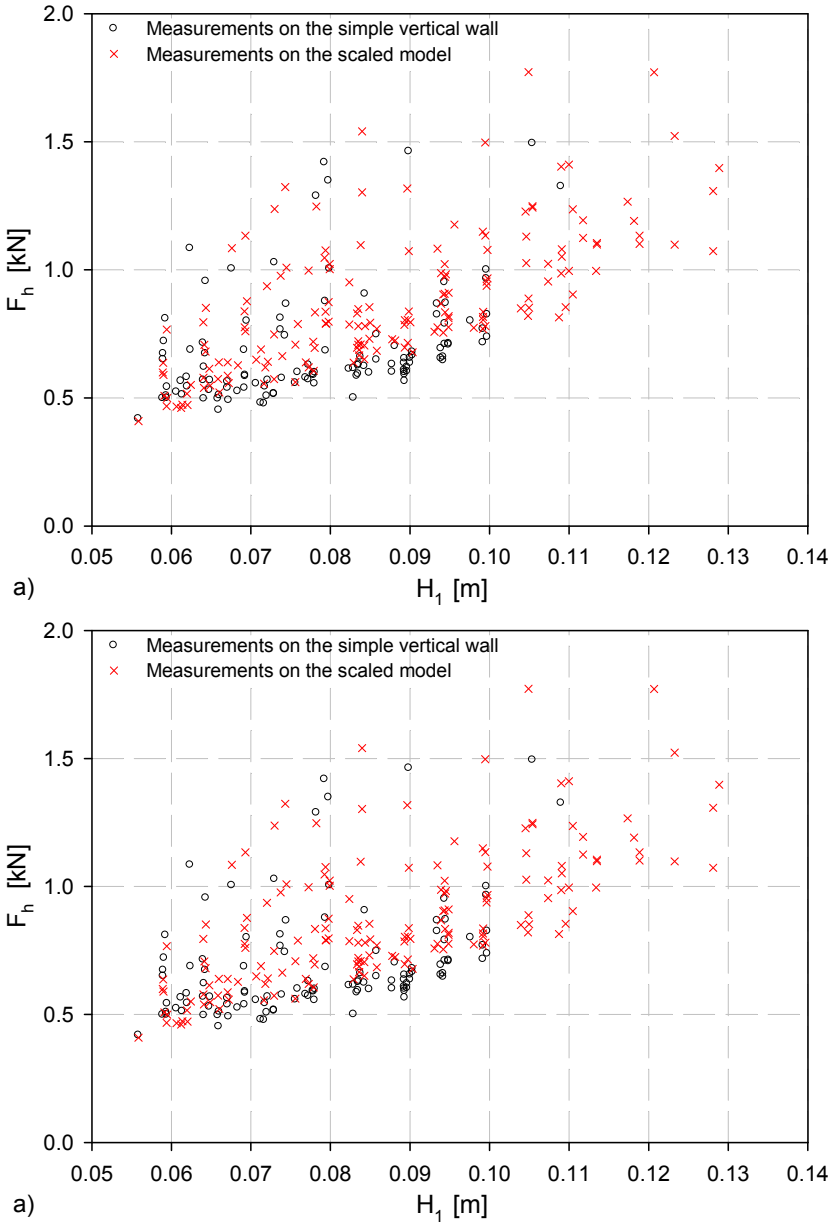

Figure 7.12 *Comparison of the results due to slightly breaking waves (SBW) on the simple vertical wall type model and the scaled model with cantilever slab, a) Horizontal force F_h, b) Overturning moment M, (Regular waves, T=2.2 s, h_s=0.135 m)*

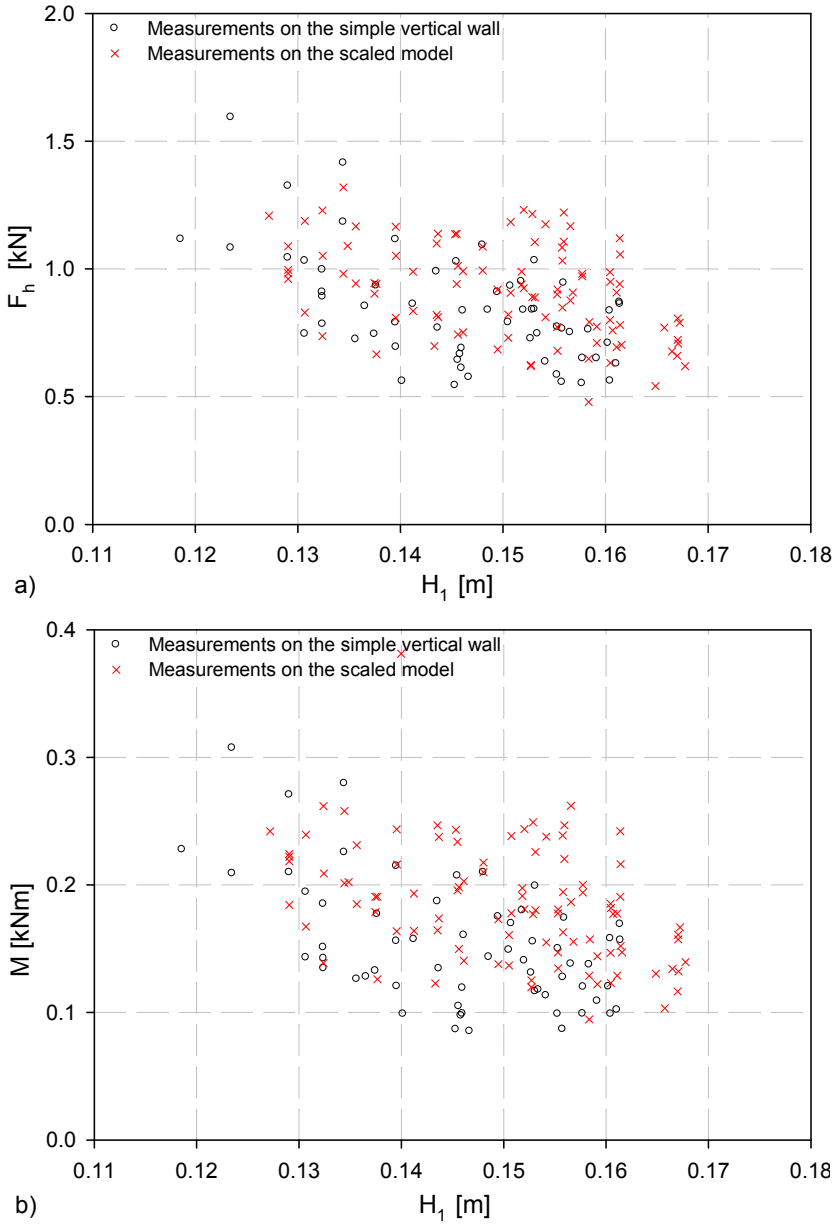

Figure 7.13 *Comparison of the results due to broken waves (BW) on the simple vertical wall type model and the scaled model with cantilever slab, a) Horizontal force F_h, b) Overturning moment M, (Regular waves, T=2.2 s, h_s=0.135 m)*

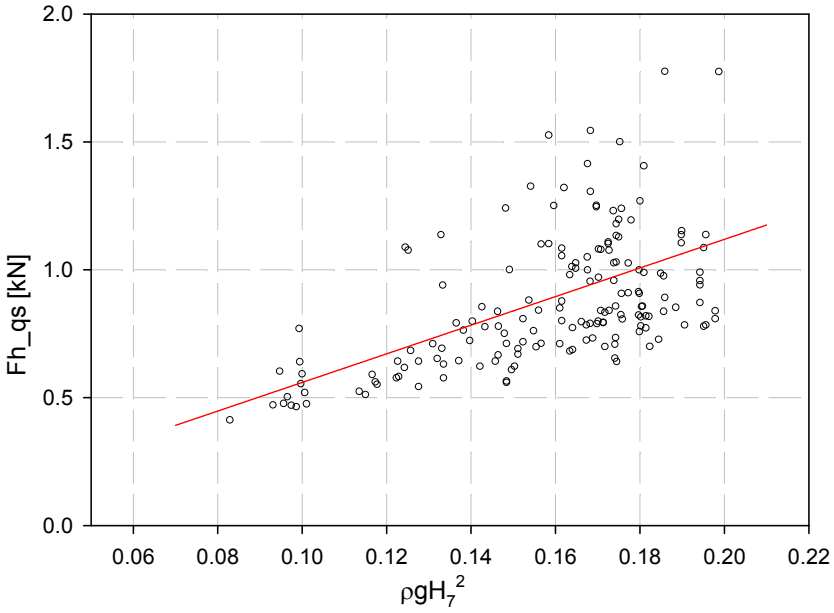

Figure 7.14 *Variation of quasi-static forces measured in the SBW with the variation of* $\rho g H_7^2$

In the same manner, a new line is adopted to the new data set of SBW measured on the scaled model (Figure 7.14) with $\alpha = 5.6$ (The foreshore slope is 1/20).

Equation 7.11 $$F_h = 5.6\, \rho g\, H_7^2$$

where H_7 is the wave height at the toe of the scaled model.

The scatter in the new data set is higher than the scatter in the Cuomo's data. Cuomo's date represent $F_h = F_{h\_qs}$, however new data set covers values between $1 < F_h \;/\; F_{h\_qs} < 2.5$ which is slightly higher than F_{h_qs}.

Figure 7.13 shows the comparison of horizontal forces F_h and overturning moment M due to broken waves (BW) measured on the simple vertical wall type model and scaled model. Similar to the case SBW, a small influence of cantilever slab is found on the measured relative low values of F_h. On the both models, F_h values are decreasing linearly with the increase of wave height H_7 measured at the foreshore toe.

7.6 CONCLUSIONS

A simple vertical wall type model and the scaled model with cantilever slab are tested in a small scale test set-up (at scale 1:20) using regular waves. Force and pressure measurements on the simple vertical wall type model are used to evaluate the existing prediction formulas. The prediction formulas of Minikin (1963), Goda (ex. Takahashi, 1994) and Allsop & Vicinanza (1996) underestimate the impulsive force on the vertical walls. The prediction formulas of PROVERBS (2001), Cuomo et al. (2010) and Blackmore & Hewson (1984) are overestimating the force. In addition, instantaneous pressure profiles are compared with the predicted values of Minikin (1963), Goda (1994) and Proverbs (2001) and Blackmore and Hewson (1984). However all methods diverge considerably to predict effectively the maximum peak pressures.

Finally, measured horizontal forces are compared between two different model tests in different breaker types to evaluate the influence of cantilever slab. In breaking waves, the both data sets show high scatter, but there is no evidence of force increase due to the cantilever slab in the horizontal direction. However, in both slightly breaking waves SBW and broken waves BW a force increase is observed especially on the small values of F_h . A new curve is adapted to the new data sets in SBW with $\alpha = 5.6$. This small increase is more critical during overturning moment calculations because of increase in the moment levering arm.

REFERENCES

Allsop, N.W.H.; McKenna, J.E.; Vicinanza, D.; and Whittaker, T.J.T. (1996), "*New design formulae for wave loadings on vertical breakwaters and seawalls*", Proc 25th Int. Conf. Coastal Engineering, ASCE, New York (1996), pp. 2508–2521

Allsop, N.W.H.; Vicinanza, D.; Calabrese, M.; Centurioni, L., (1996c), "*Breaking Wave Impact Loads on Vertical Faces*", ISOPE- International Offshore and Polar Engineering-Conference, pp-185, Los Angeles, California

Allsop, N.W.H.; Vicinanza, D.; McKenna, J.E., (1996), "*Wave forces on vertical and composite breakwaters*", Strategic Research Report SR 443, HR Wallingford, Wallingford (1996), pp. 1–94 March 1996

Blackmore, P.A.; Hewson, P.J., (1984), "*Experiments on full-scale wave impact pressures*", *Coastal Engineering* Volume:08 Issues:4, pp:331-346

Bullock, G; Obhrai, C.; Müller, G.; Wolters, G.; Peregrine, H.; Bredmose, H., (2004), "*Characteristics and design implications of breaking wave impacts*" -Coastal Engineering Conference, pp: 3966

Cuomo, G; Allsop, W; Bruce, T; Pearson, J, (2010), "*Breaking wave loads at vertical seawalls and breakwaters*", Coastal Engineering, Volume 57, Issue 4, April 2010, Pages 424–439

Cuomo G.; Tirindelli M.; and William Allsop W., 2007, '*Wave-in-deck loads on exposed jetties*', Coastal Engineering Volume 54, Issues-9, 2007, pp: 657-679

Goda, Y., (1967), "*The fourth order approximation to the pressure of standing waves*", Coastal Engineering in Japan, 10 (1967), pp. 1–11

Goda, Y., (1974), "*New wave pressure formulae for composite breakwater*, Proc. of 14th Int. Conf. Coastal Eng., Copenhagen, Denmark, ASCE, New York (1974), pp. 1702–1720.

Goda, Y., (2000), 'Random seas and design of maritime structures" (2nd Edition), Advanced Series on Ocean Engineering vol. 15, World Scientific (2000) 443 pp

Hattori, M.; Arami, A.; Yui, T., (1994), "*Wave impact pressure on vertical walls under breaking waves of various types*", Coastal-Engineering, Volume:22 Issues:1-2-1994-pp-79-114

McConnell, K.J; Allsop, N.W.H; Cuomo, G; and. Cruickshank, I.C, 2003, *'New guidance for wave forces on jetties in exposed locations*', Paper to Conf. COPEDEC VI, Colombo, Sri Lanka pp: 20

Okamura, M., (1993), '*Impulsive pressure due to wave impact on an inclined plane wall'*, Fluid Dynamics Research, volume 12, issue 4, pp. 215-228

Oumeraci, H. (1994), "Review and analysis of vertical breakwater failures lessons learned Special Issue on Vertical Breakwaters", Coastal Eng. 22 (1994), pp. 3–29.

Oumeraci, H; Kortenhaus, A; Allsop, W; de Groot, M; Crouch, R; Vrijling, H; Voortman, H, (2001). "*Probabilistic Design Tools for Vertical Breakwaters*", Balkema Publishers, New York.

Sainflou, G., 1928, "*Essai sur les digues maritimes verticals*", Ann. Ponts Chaussées Paris, 98 11 (1928), pp. 5–48 (in French).

Shore Protection Manual. 1984. 4th ed., 2 Vol U.S. Army Engineer Waterways Experiment Station, U.S. Government Printing Office, Washington, DC

Takahashi, S., (1996), "*Design of vertical breakwaters*", Port and Harbour Research Institute, Ministry of Transport, Reference documenr # 34.

Verhaeghe, H.; Cherlet, J.; Boone, C.; Troch, P.; De Rouck, J.; Awouters, M.; Ockier, M.; Devos, G., 2006, '*Prototype monitoring of wave loads on concrete structure in intertidal zone*', Proceedings of the First International Conference on the Application of Physical Modelling to Port and Coastal Protection COASTLAB06. pp. 117-125

8

PARAMETRIC ANALYSES

***

8.1 INTRODUCTION

Based on structure geometry and wave conditions, a set of basic parameters and some combination of them, responsible for the prediction of the wave loading on a vertical wall with a cantilever slab, is presented. The parametric investigation is based on data from a series of small-scale model tests discussed in Chapter 3. In addition, the results from the regular as well as the irregular waves are compared. Further developments of these parameters, investigation of the used dimensionless parameters and the definitions of wave loading types are discussed. Finally, a semi empirical model is developed to predict vertical impact forces on the horizontal part and the predicted values are compared with the measurements.

8.2 PARAMETRIC ANALYSIS OF IMPACT THE FORCES

The main parameters used in the parameter map for the determination of the wave loading on a structure are the wave height (H), water depth at the model toe (h_s), wave period (T) or wave length (L), impact velocities of the fluid mass (u and v) and the geometrical parameters of the structure. The ratios of any of these parameters, like the relative wave height H/h_s, are important for the normalization of the results. The wave height H is experimentally determined in the water depth h_s (H_7) and at the toe of the foreshore (H_1), while L is determined by linear wave theory for any depth. Geometric parameters l_m, h_m and c (model length and height and clearance between SWL and horizontal part respectively) are defined in Figure 3.1. For the comparison of parameters such as T and h_s, wave results include mainly dynamic loadings since mostly slightly breaking or breaking wave types are used.

8.2.1 VARIATION OF THE WAVE HEIGHT

Figure 8.1 shows the comparison of the maximum horizontal and vertical forces (F_h and F_v) from regular and irregular waves as a function of the wave height (H_1) measured at the toe of the foreshore. This particular example concerns $h_s = 0.135\ m$ and $T = 2.2\ s$. On the figure, the regular wave results are categorized based on their breaker types as slightly breaking, breaking (including both breaking with small and large air trap) and broken waves (see discussions about categorization of breaker types in Section 5.4). Red crosses display the irregular wave results at 1/250 significance level with the change of wave height (H_{m0}) measured at the toe of foreshore. The term 1/250 significance level indicates that the corresponding parameter has been evaluated as the average of the highest two events in a (nominally) 500-wave tests. As seen on the Figure 8.1a, horizontal force from regular waves (F_h) displays a high scatter in the breaking wave zone (0.095 m<H_1<0.16 m) and this scattering region extends to the slightly breaking and broken wave zone (0.073 m<H_1<0.16 m) for the measured vertical forces (F_v) (see Figure 8.1b). This extension on the region of the vertical force is the result of the

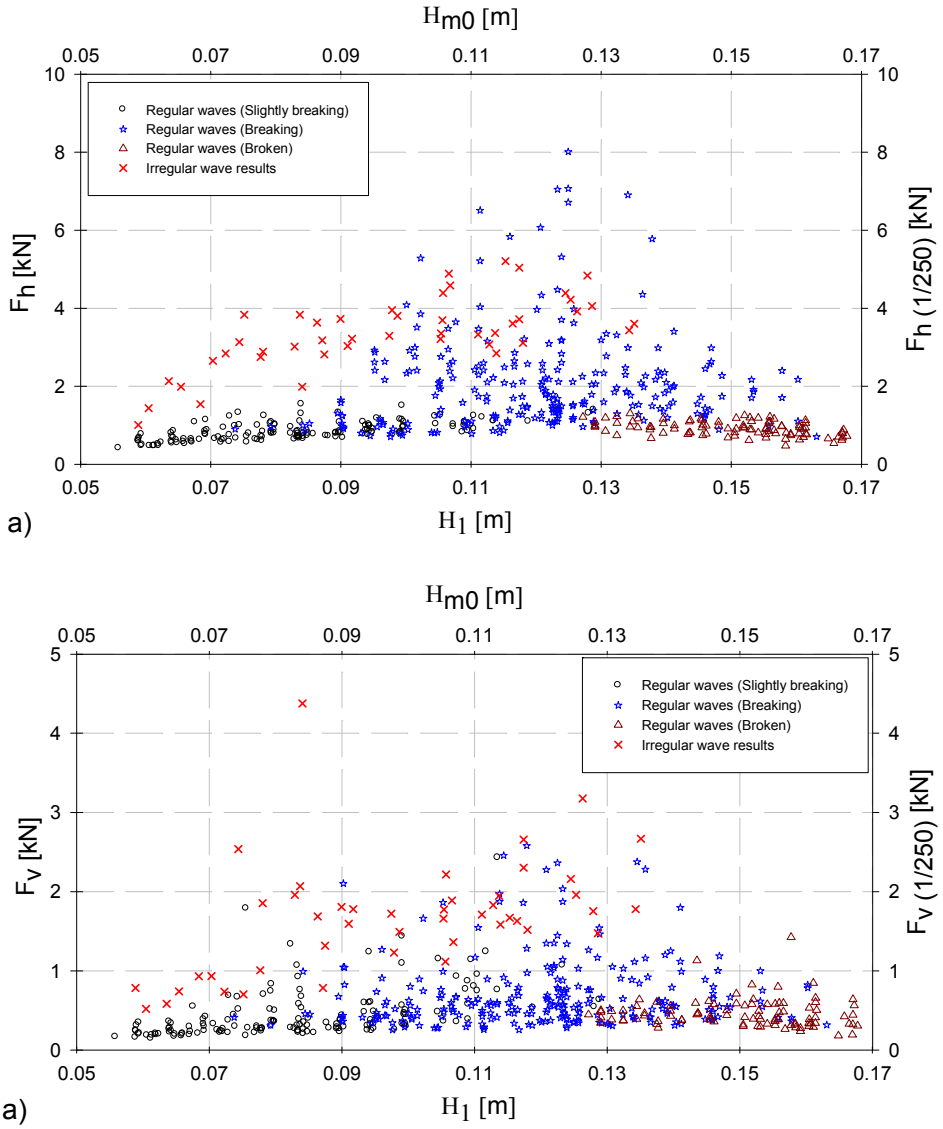

Figure 8.1 *Variation of wave impact forces (F_h and F_v) with the change of the wave height (H_1) measured at the toe of the foreshore ($h_s = 0.135$ m and T=2.2 s). For irregular waves, F and H are calculated as $F_{1/250}$ (1/250 significance level) and H_{m0} respectively. a) is the maximum horizontal force (F_h), b) is the maximum vertical force (F_v).*

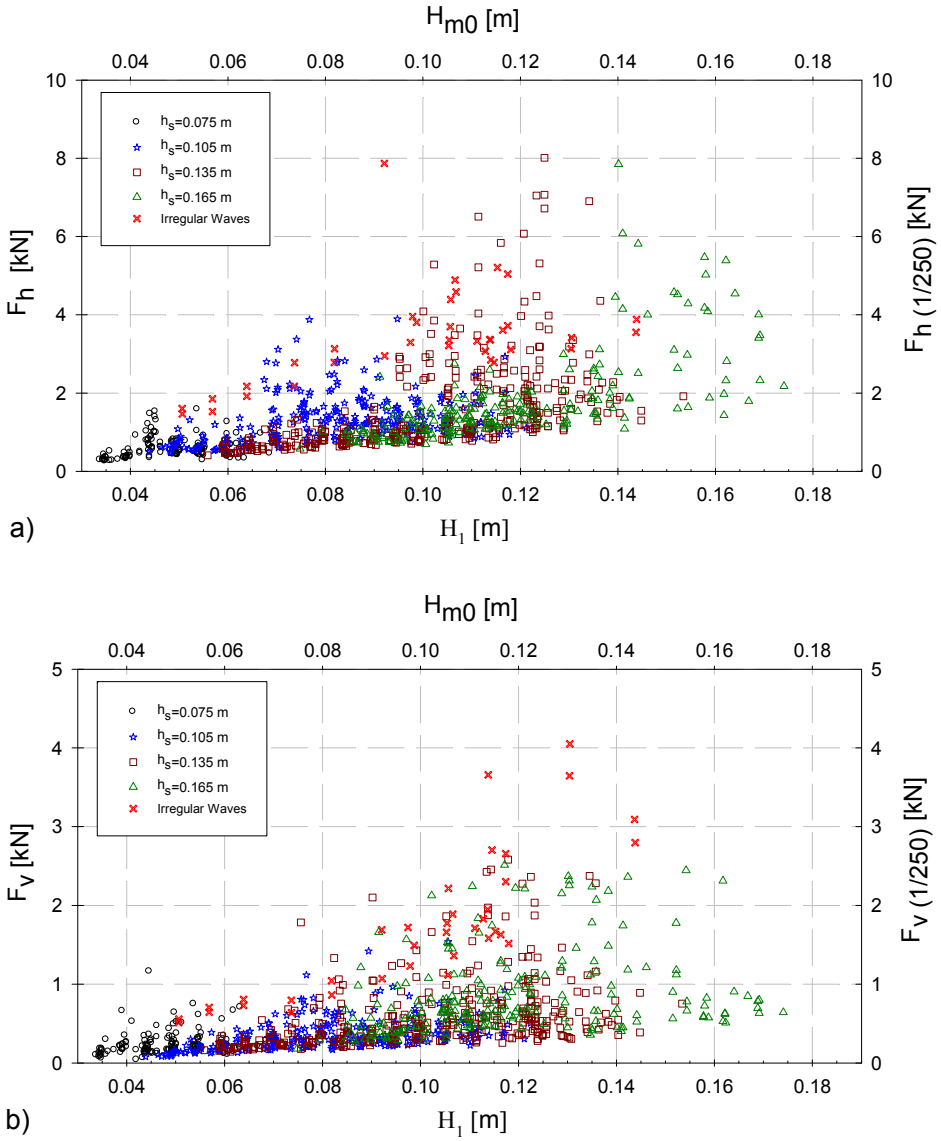

Figure 8.2 *Variation of wave impact forces (F_h and F_v) with the change of the water depth (h_s) measured at the toe of the model (T=2.2 s). For irregular waves, F and H are calculated as $F_{1/250}$ (1/250 significance level) and H_{m0} respectively. a) is the variation of maximum horizontal force (F_h), b) is the variation of maximum vertical force (F_v)*

impacts due to the accelerated water columns on the vertical part of non-breaking waves. Within these boundaries the horizontal part is exposed to dynamic forces. Outside these parameter regions, smaller waves will cause pulsating loads and larger waves will have broken by the time they reach the structure, causing wave loads which will be less severe than impact loads.

It is also surprising to observe an additional narrow band of wave height between 0.073 m<H_1<0.090 m with extraordinary high vertical forces. This is the most probable region close to the occurrence of the breaker types called "flip-trough" explained in Section 5.4. It is know that the vertical acceleration of a wave component reaches its highest value just before the flip through.

A similar behavior is also observed on the results of irregular waves. In general, regular and irregular wave results are of the same order of magnitude and show high scattering in the breaking wave zones. However, in the slightly breaking wave zone, the irregular wave results are significantly higher than the regular wave results. This is the result of some highly random waves in the irregular wave train even in gentle wave conditions.

8.2.2 VARIATION OF THE WATER DEPTH

Figure 8.2 displays the variation of both measured maximum force values (F_h and F_v) with the variation of the water depth (h_s) at the toe of the scaled model. For the comparison, the results of the wave height range between $0.7< H_1/h_s < 1.1$ are used for four different water depths which are considered at h_s= 0.075, 0.105, 0.135 and 0.165 m. Each different color represents the results of a different water depth. Both the regular and irregular wave results show that measured force values are very sensitive to the variation of h_s and the increasing h_s results in high impact forces both on the horizontal and vertical part of the scaled model. On the vertical part, relatively low values are found for the highest water level (h_s=0.165 m). For this water level, some of the waves first hit on the free end of the horizontal part when they are developing breaking. This reduces the energy of the developing wave and its ability to create high impact force.

For the vertical forces, rather than the basic water depth, the ratio of water depth to the clearance between SWL and the horizontal part (c/h_s) is more important. Due to the special shape of the scaled model (see Figure 3.1), increasing the water depth also results in a decrease in the clearance which is relevant to the magnitude of the vertical forces.

8.2.3 VARIATION OF THE WAVE PERIOD

Figure 8.3 illustrates the variation of both measured maximum force values (F_h and F_v) with the wave period (T) measured at the toe of the foreshore for the case of breaking waves. Five different wave periods are considered for the comparison

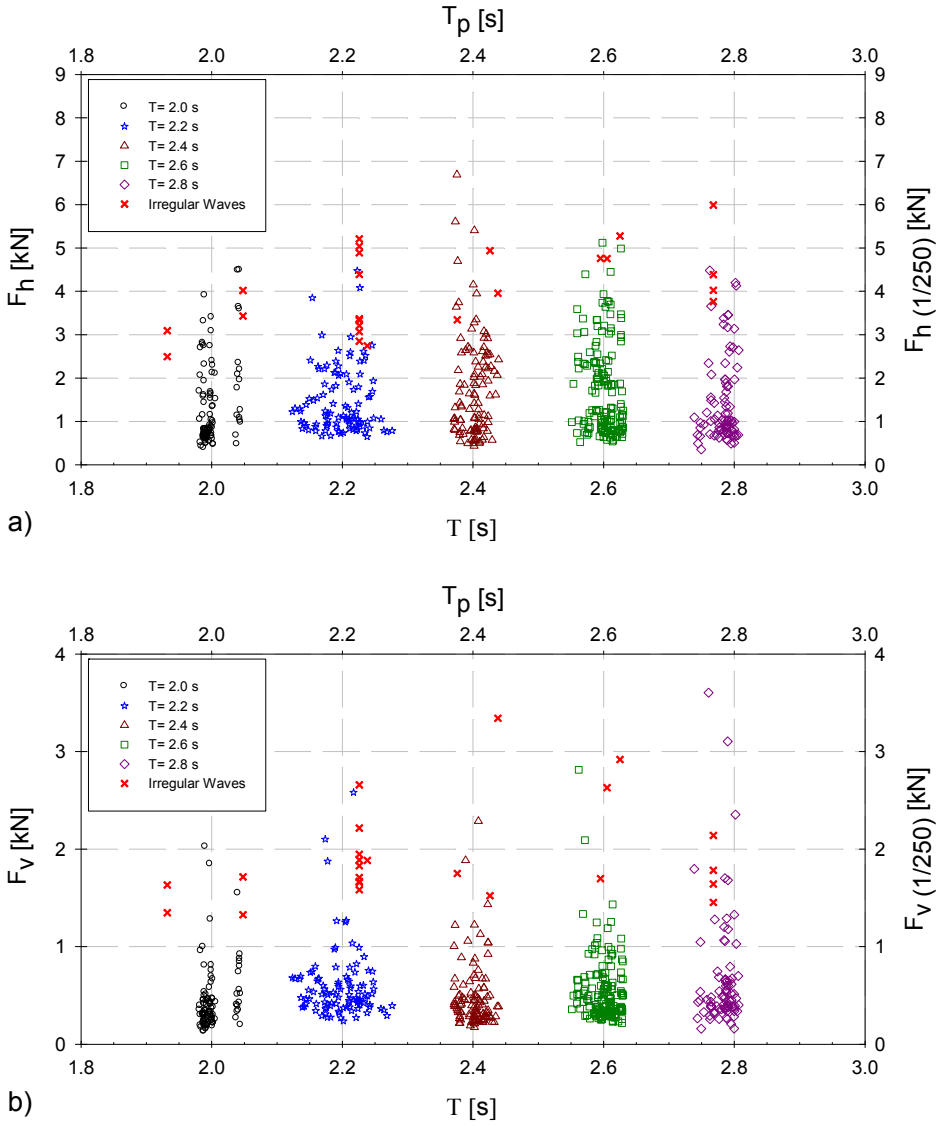

Figure 8.3 *Variation of wave impact forces (F_h and F_v) with the change of the wave period (T) measured at the toe of the foreshore ($h_s = 0.135\ m$). For irregular waves, F and H are calculated as $F_{1/250}$ (1/250 significance level) and T_p respectively. a) is the variation of maximum horizontal force (F_h), b) is the variation of maximum vertical force (F_v)*

(T=2.0, 2.2, 2.4, 2.6 and 2.8 s). For irregular waves, F and T values are calculated as $F_{1/250}$ (1/250 significance level) and T_p, respectively. As illustrated in Figure 8.3, the measured maximum force values display a dependency on the variation of the wave period (T). However, the influence of the T-variation in the considered specific range ($2.0\ s \leq T \leq 2.8\ s$) is rather low compared to the variation of H and h_s.

8.2.4 VARIATION OF THE RISING TIME

The relation between the impact pressure and the rising time is discussed in Chapter 6. Similar to the Equation 6.2, a formula can be derived for the relation between the maximum force (F_{max}) and the related rising time (t_r) (Equation 8.1). Cuomo et al. (2010) found values of a=7 and b=-0.6 in Equation 8.1 which were derived based on large scale model test at CIEM/LIM in Barcelona. However, the form of Equation 8.1 is dimensionally inconsistent. Therefore, McConnell and Kortenhaus (1996) suggested the dimensionally consistent form of F_{max} and t_r (Equation 8.2).

Equation 8.1 $$F_{max} = a[t_r]^b$$

Equation 8.2 $$\frac{F_{max}}{F_{max\ \_qs}} = a\left[\frac{t_r}{T}\right]^b$$

where $F_{\max\ \_qs}$ is the maximum quasi-static force and T is the wave period.

Figure 8.4 shows the normalized maximum horizontal and vertical forces (F_h/F_{h_qs} and F_v/F_{v_qs}) with the variation of the normalized rising times (t_r/T). Each different color represents data from a different water depth (h_s).

For determining confidence intervals, all data points are divided in to 30 different intervals along the axis t_r/T. For each interval non-exceedance levels at 90, 95, 98 and 99.6% are defined and best fit lines from these points are determined. Equation 8.3 and Equation 8.4 show the function of lines at 99.6% of non-exceedance level with $a = 0.35\ and\ 0.22$ and $b = -0.67\ and\ -0.56$ for the horizontal and vertical forces respectively. Since a wave impulse is a finite quantity, most intense wave impacts have shorter rise times. This is confirmed in Figure 8.4 with impact peak forces plotted versus their corresponding rise times.

Equation 8.3 $$\left(\frac{F_h}{F_{h\_qs}}\right)_{99.6\%} = 0.35\left[\frac{t_r}{T}\right]^{-0.67}$$

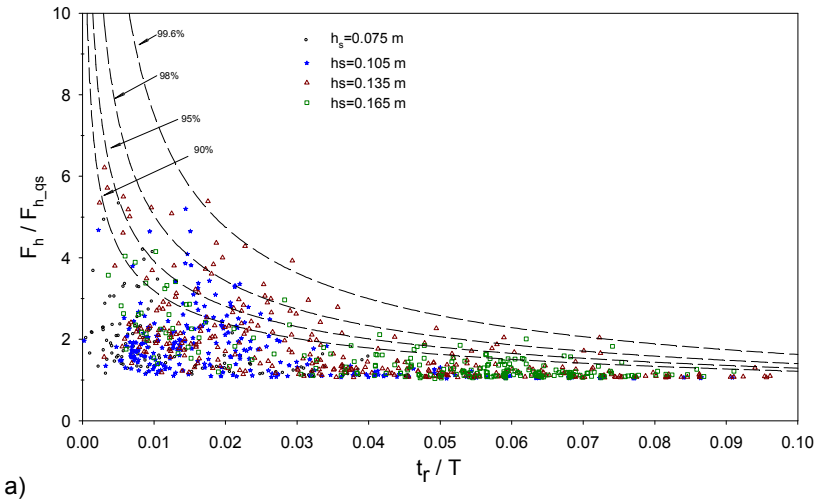

a)

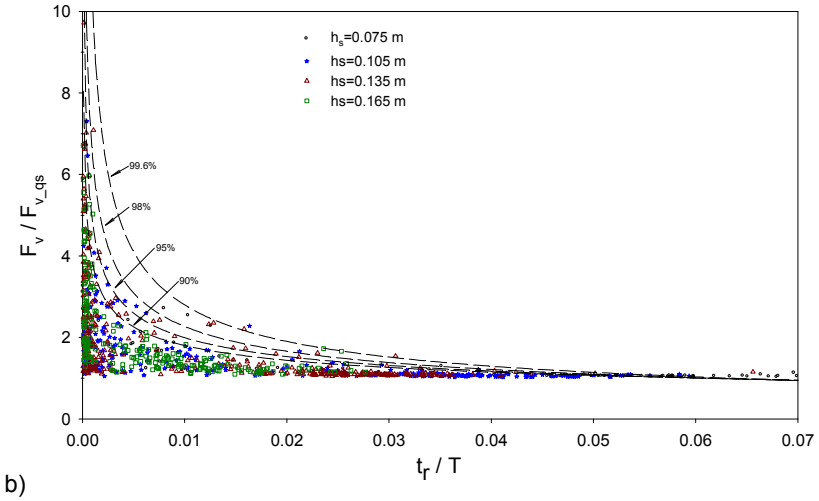

b)

Figure 8.4 *Normalized maximum impact forces and rise times recorded both on the vertical and horizontal parts. a) An envelope line at 99.6% of non-exceedance level (Equation 8.3) with coefficients a=0.35 and b=-0.67 is fitted to the horizontal forces, b) An envelope line at 99.6% of non-exceedance level (Equation 8.4) with coefficients a=0.22 and b=-0.56 is fitted to the vertical forces*

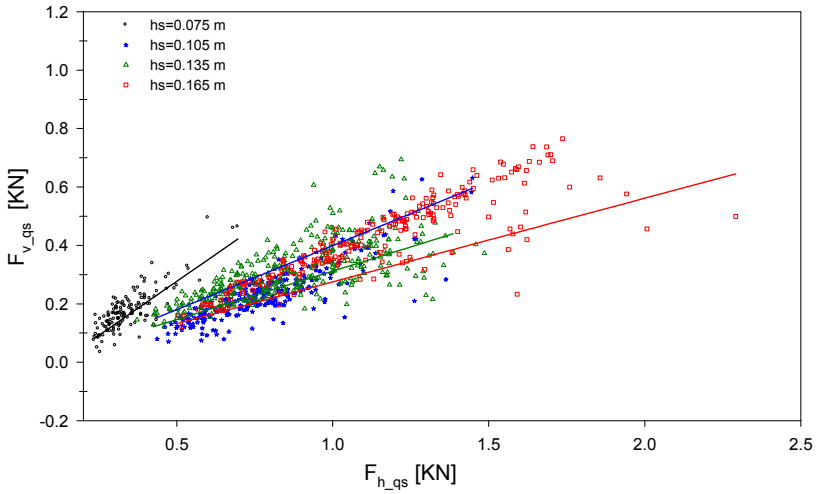

Figure 8.5 *Variation of the maximum horizontal quasi-static forces with the maximum vertical quasi-static forces*

Equation 8.4 $$\left(\frac{F_v}{F_{v\_qs}}\right)_{99.6\%} = 0.22\left[\frac{t_r}{T}\right]^{-0.56}$$

Compared to the horizontal forces, vertical forces have higher intensity with smaller rising times. During the physical model tests, it was observed that the largest impacts recorded on the vertical part had rise times of $t_r = 0.15\ ms$ but significant impacts were recorded with $t_r = 0.3\ ms$.

Figure 8.5 shows the variation of the maximum horizontal quasi-static forces (F_{h_qs}) with the variation of the maximum vertical quasi-static forces (F_{v_qs}). In general, measured quasi-static forces on the vertical part (F_{h_qs}) are higher than the measured quasi-static forces on the horizontal part (F_{v_qs}). The observed linear relation between quasi-static forces is given by Equation 8.5 with coefficients γ_1 and γ_2.

Equation 8.5 $$F_{v\_qs} = \gamma_1 F_{h\_qs} + \gamma_2$$

where, $\gamma_1 = 0.054\ (c/h_s)^2 + 0.25$ and $\gamma_2 = -0.01\ (c/h_s)^2 - 0.005$

Figure 8.6 shows the variation of γ_1 and γ_2 with the variation of $(c/h_s)^2$. For γ_1, the value at $(c/h_s)^2 = 0.67$ does not follow the proposed line. This is the incomplete case because of early hit of the wave crest at the free end of the horizontal part.

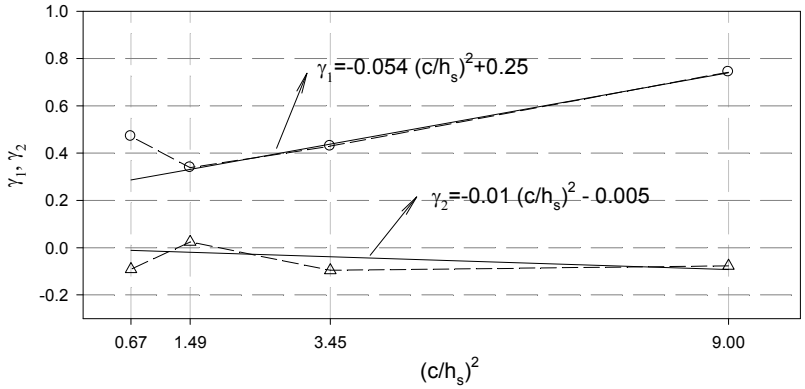

Figure 8.6 *Variation of γ_1 and γ_2 with the variation of $(c/h_s)^2$*

8.2.5 VARIATION OF THE VERTICAL VELOCITY

The vertical velocity of the water jet is an important parameter related to the impact forces in the vertical direction. The jet velocity is dependent on the approaching wave properties, the water depth at the model toe, the clearance between SWL and the horizontal part and the breaker types. However, it is difficult to measure the exact velocity which is responsible for the impact. Instead, an average velocity is proposed as:

Equation 8.6 $$V_{av} = \frac{c}{\Delta t}$$

where V_{av} and c are the average vertical velocity and clearance between SWL and the horizontal slab. Δt is the time interval between the times of peak pressures measured from sensors at SWL and at the attached corner of the horizontal slab (Sensors 3 and 8 in Figure 3.1). These two sensors are located at the impact locations on the vertical and horizontal parts and bounding the distance of clearance. Figure 8.7a shows the calculated vertical averaged velocities at different water depths ($c = 0.135, 0.165, 0.195\ and\ 0.225\ m$).

In Section 5.9, the shallow water wave celerity is shown to be:

Equation 8.7 $$u = \sqrt{g(h_s + H_1)}$$

Equation 8.7 can be rearranged in the form shown in Equation 8.8.

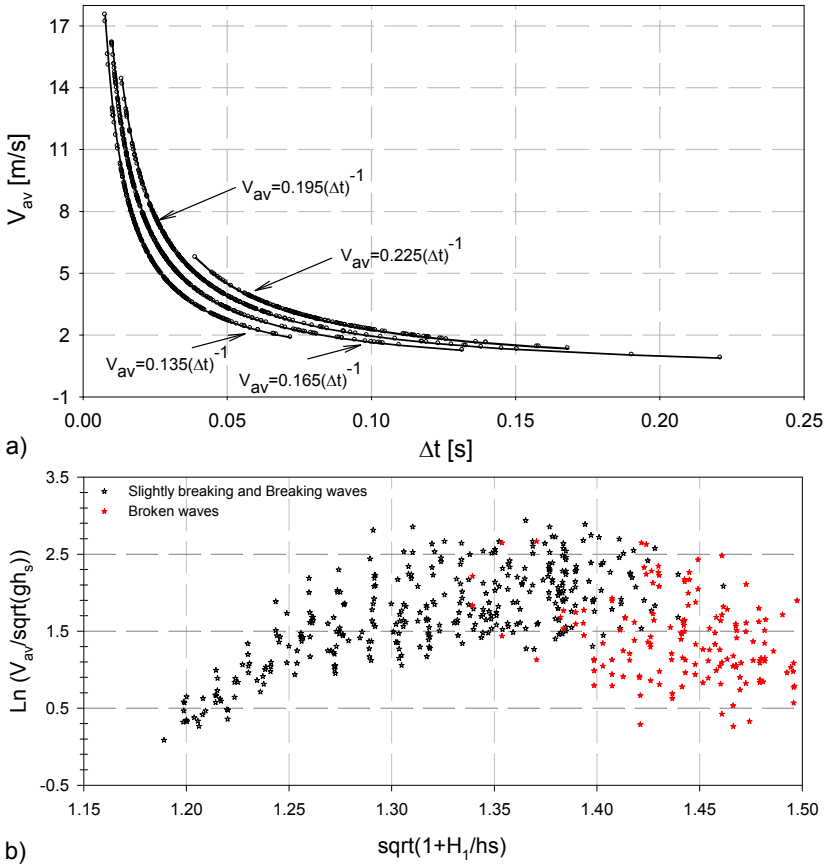

Figure 8.7 *a) Relation between V_{av} and Δt for four different clearance c, b) Variation of normalized vertical velocity with the variation of $\sqrt{1+\frac{H_1}{h_s}}$ on a semi-log scale*

Equation 8.8 $$u = \sqrt{gh_s}\sqrt{1+\frac{H_1}{h_s}}$$

The vertical averaged velocity (V_{av}) is proportional to the approaching shallow water velocity (u). The expression can be rewritten in non-dimensional form as:

Equation 8.9 $$\frac{V_{av}}{\sqrt{gh_s}} \sim \sqrt{1+\frac{H_1}{h_s}}$$

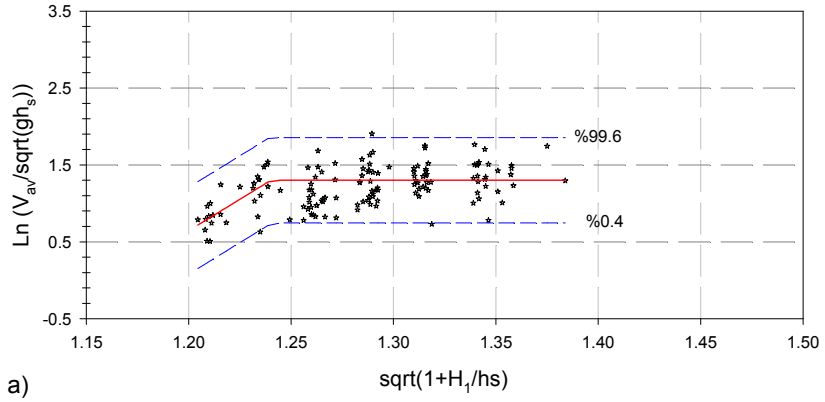

a)

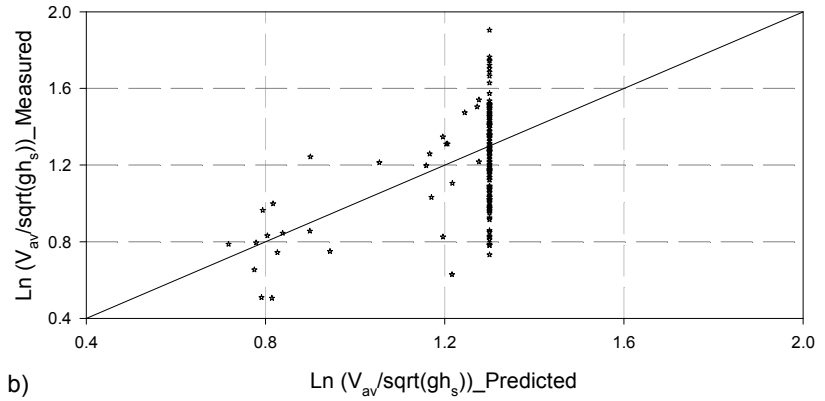

b)

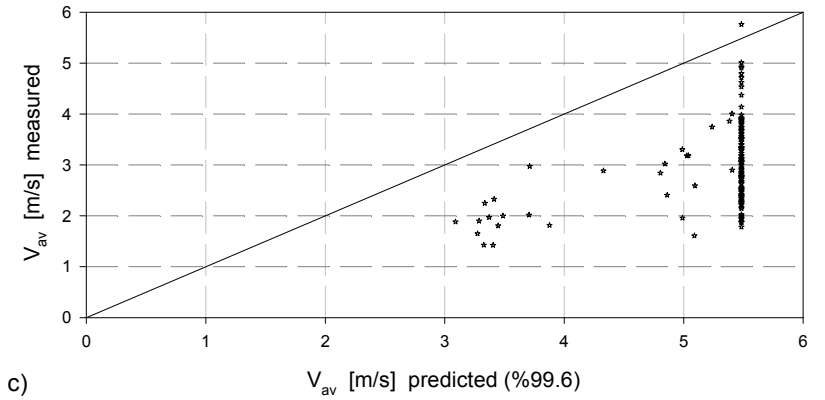

c)

Figure 8.8 *a) Variation of $V_{av}/\sqrt{gh_s}$ with $\sqrt{1+H_1/h_s}$ on the semi log scale. Lines represent Equation 8.10 with 99.6% exceedance intervals for $h_s = 0.075\ m$, b) Comparison of the predicted and the measured $V_{av}/\sqrt{gh_s}$ on the log-log scale, c) Comparison of the predicted (99.6%) and measured V_{av} on the normal scale.*

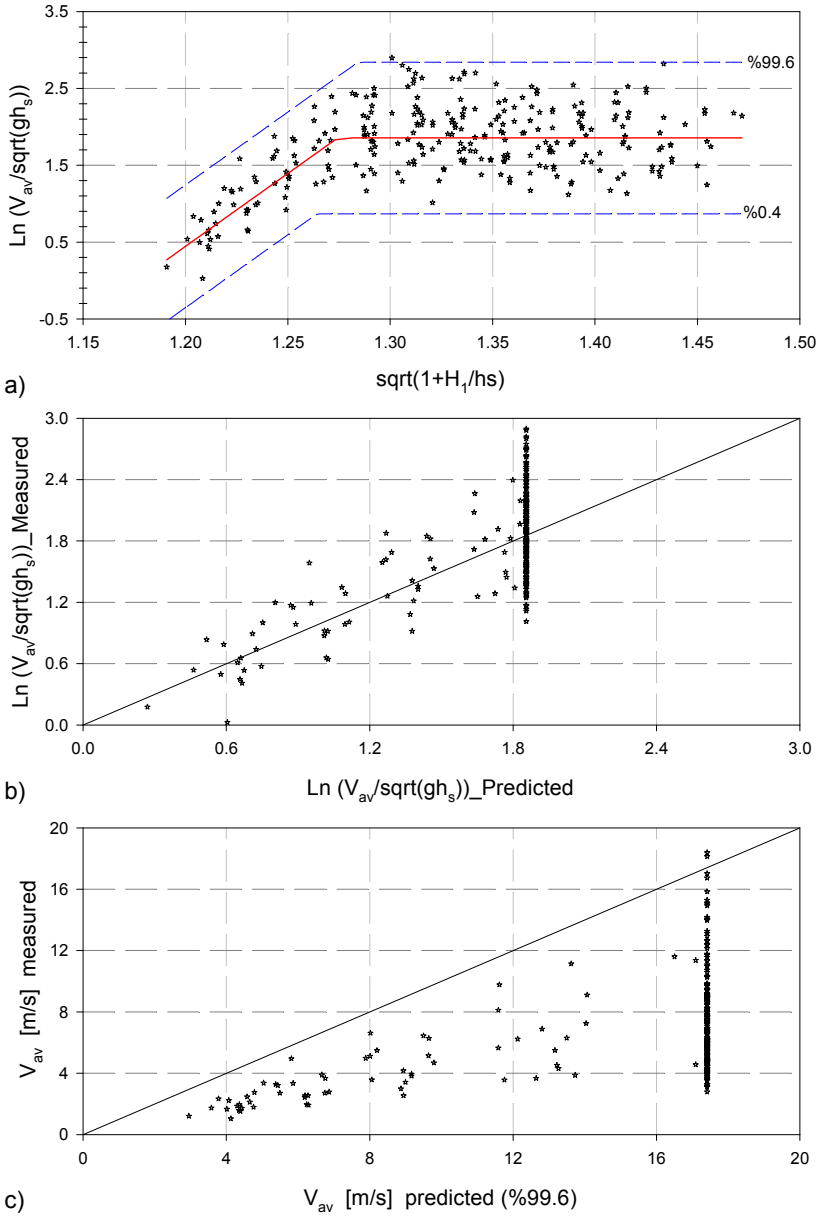

Figure 8.9 *a) Variation of $V_{av}/\sqrt{gh_s}$ with $\sqrt{1+H_1/h_s}$ on the semi log scale. Lines represent Equation 8.10 with 99.6% exceedance intervals for $h_s = 0.105$ m, b) Comparison of the predicted and the measured $V_{av}/\sqrt{gh_s}$ on the log-log scale, c) Comparison of the predicted (99.6%) and measured V_{av} on the normal scale.*

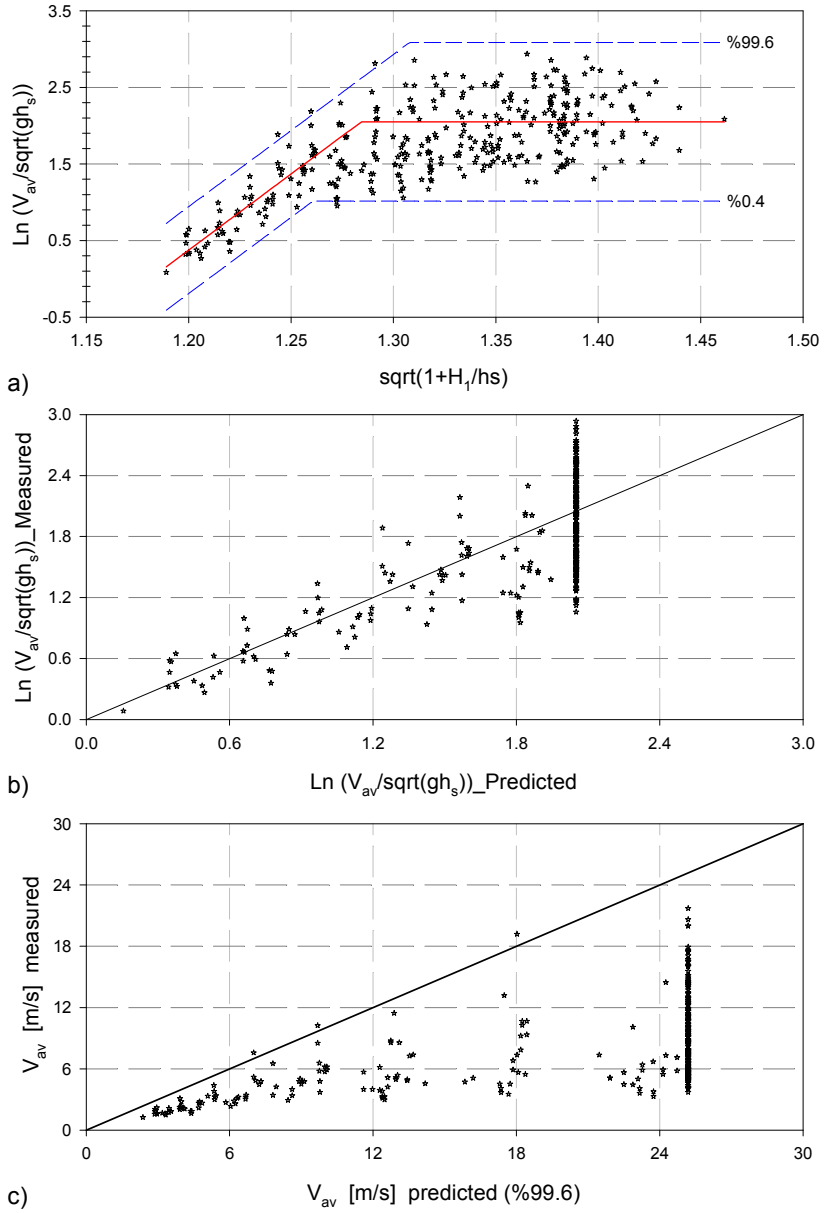

Figure 8.10 *a) Variation of $V_{av}/\sqrt{gh_s}$ with $\sqrt{1+H_1/h_s}$ on the semi log scale. Lines represent Equation 8.10 with 99.6% exceedance intervals for $h_s = 0.135\ m$, b) Comparison of the predicted and the measured $V_{av}/\sqrt{gh_s}$ on the log-log scale, c) Comparison of the predicted (99.6%) and measured V_{av} on the normal scale.*

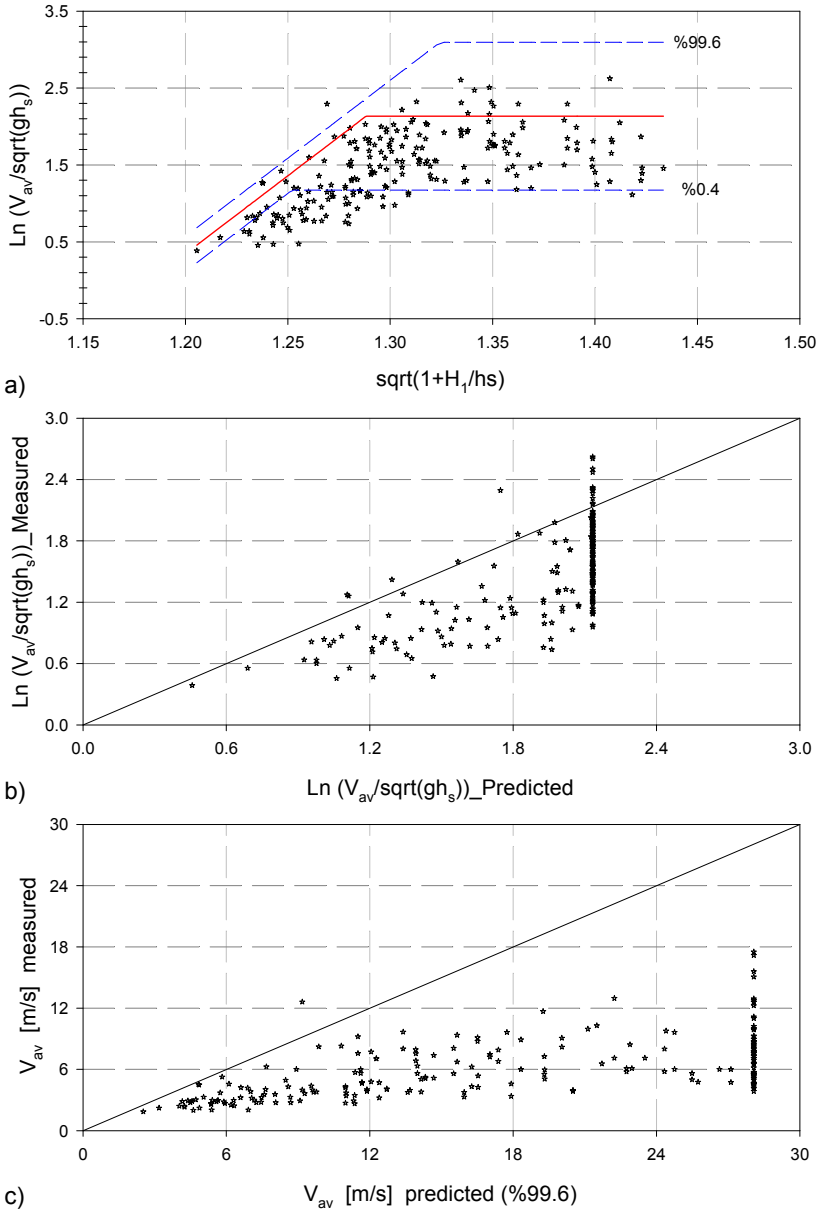

Figure 8.11 *a) Variation of $V_{av}/\sqrt{gh_s}$ with $\sqrt{1+H_1/h_s}$ on the semi log scale. Lines represent Equation 8.10 with 99.6% exceedance intervals for $h_s = 0.165\ m$, b) Comparison of the predicted and the measured $V_{av}/\sqrt{gh_s}$ on the log-log scale, c) Comparison of the predicted(99.6%) and measured V_{av} on the normal scale.*

Figure 8.7b shows the variation of the normalized vertical velocity with the variation of $\sqrt{1+\frac{H_1}{h_s}}$ on a semi-log scale. Scattered data points with a black color shows the results of SBW and BW (includes both BWSAT and BWLAT) while data points with a red color shows the results of broken waves. It is seen that the averaged velocities increase linearly with the increase of $\sqrt{1+\frac{H_1}{h_s}}$ and reach a maximum value for the results of SBW and BW. Furthermore, averaged velocities decrease in the broken wave region. In the following paragraphs, results of broken waves are excluded for the development of an exponential expression to predict the averaged vertical velocities.

Equation 8.10 represents the developed expression for the averaged vertical velocity (V_{av}) with coefficients α_1 and α_2. It is a linear relationship up to the point where $\sqrt{1+\frac{H_1}{h_s}} \leq m$. Then it is constant with a coefficient n. α_1, α_2 and n are the best fit lines of function of $(c/h_s)^2$.

Equation 8.10 $$V_{av} = \sqrt{gh_s}\,.exp\,(\alpha_1\sqrt{1+H_1/h_s}+\alpha_2) \quad \sqrt{1+H_1/h_s} \leq m$$

$$V_{av} = \sqrt{gh_s}.\exp\,(n) \qquad \sqrt{1+H_1/h_s} > m$$

$$\alpha_1 = -0.47\left(\frac{c}{h_s}\right)^2 + 20.6$$

$$\alpha_2 = 0.6\left(\frac{c}{h_s}\right)^2 - 24.4$$

$$n = -0.1\left(\frac{c}{h_s}\right)^2 + 2.2$$

$$m = \frac{\mathrm{n} - \alpha_2}{\alpha_1}$$

Figures from 8.8a to 8.11a show the variation of the natural logarithm of $V_{av}/\sqrt{gh_s}$ with the variation of $\sqrt{1+\frac{H_1}{h_s}}$. A good agreement of the Equation 8.10 and the experimental data is found for the first three water depth ($h_s = 0.075, 0.105\ and\ 0.135\ m$). In the fourth case, the proposed line overestimates the predicted velocities. This is logical because most of the waves which can produce high velocities were excluded from the analysis due to an early impact with the horizontal part. Figures from 8.8b to 8.11b compare the measured and predicted values on log-log scale while Figures from 8.8c to 8.11c compare measurements with predicted values at 99.6% confidence level on normal scales. Except few point, all data points fall below the 99.6% confidence level.

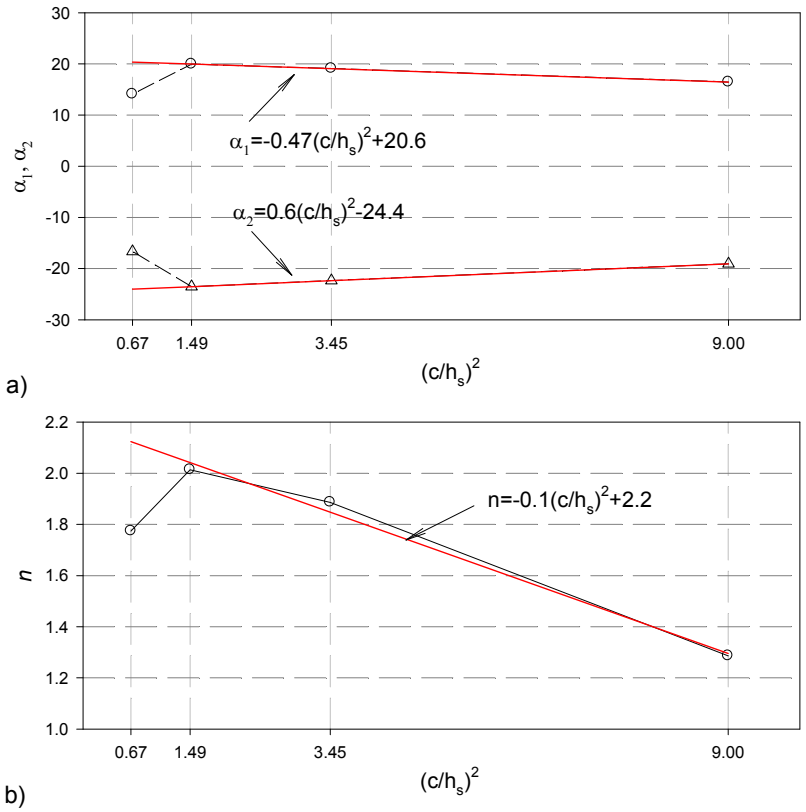

Figure 8.12 *a) Variation of α_1 and α_2 with the variation of $(c/h_s)^2$, b) Variation of n with the variation of $(c/h_s)^2$*

Figure 8.12 shows the variation of α_1, α_2 and n with the variation of $(c/h_s)^2$. The values at $(c/h_s)^2 = 0.67$ generally do not follow the proposed lines. This is the case with the highest water depth ($h_s = 0.165\,m$) in which most of the well developed wave results are excluded due to an early impact at the free end of the horizontal part.

8.3 INITIAL CALCULATION OF VERTICAL FORCES

In PROVERBS (2001), it is suggested to use Allsop and Vicinanza's (1996) method to calculate a first estimation of the impact forces on vertical walls for parameters including slightly breaking waves or impact loads. The response of F_h to wave and geometry was described by a simple empirical equation. All forces were given at a 1/250 level thus taking the mean out of the highest two wave impacts (500 waves per test were measured). The magnitude of the horizontal impact force can then be estimated from:

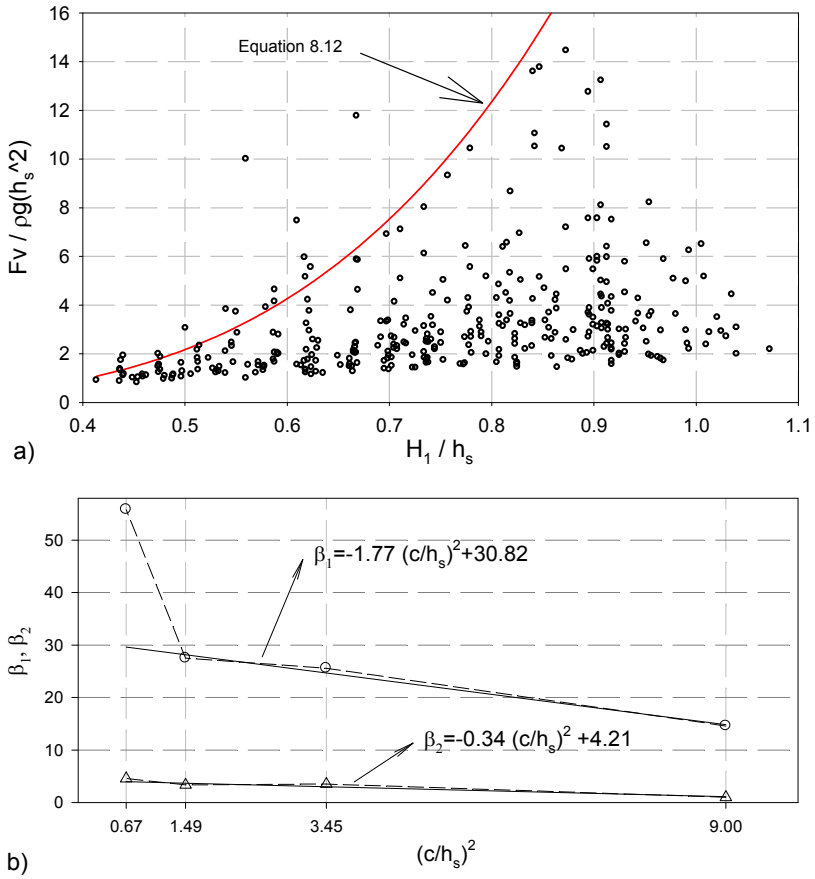

Figure 8.13 *a) Comparison of the predicted and measured dimensionless vertical forces with the variation of H_1/h_s ($h_s = 0.135\ m$ and $= 2.2\ s$), b) Variation of β_1 and β_2 with the variation of $(c/h_s)^2$*

Equation 8.11 $$F_{h\_A\&V} = 15\rho g h_s^2 (H_{si}/h_s)^{3.134}$$

where, H_{si} is the significant wave height at the structure.

Similar to the work done for the horizontal forces (F_h), a new expression is proposed in this work for the initial estimation of vertical forces (F_v) in Equation 8.12 with additional parameters (β_1 and β_2). β_1 and β_2 are functions of $(c/h_s)^2$ (see Figure 8.13b). The proposed expression represents the best fit line through the 95% of non-exceedance calculated in each intervals of 0.05 H_1/h_s. The proposed expression does not consider the several high points due to the flip-through around 0.6 H_1/h_s and other data points already show low values after $0.9H_1/h_s$.

Equation 8.12 $$F_{v\_initial} = \beta_1 \rho g h_s^2 \, (H_1/h_s)^{\beta_2}$$

where, $\beta_1 = -1.77 \, (c/h_s)^2 + 30.82$ and $\beta_2 = -0.34 \, (c/h_s)^2 + 4.21$

It is very evident that F_v should have a similar expression as F_h. Since F_{v_qs} and F_{h_qs} are strongly correlated.

Figure 8.13a shows the variation of the non-dimensionalized vertical forces ($F_v/\rho g h_s^2$) with the variation of the relative wave height (H_1/h_s). Good agreement of Equation 8.12 and the experimental data is found for all data sets from four different water depths.

The data sets include results of slightly breaking and breaking waves (impact loads). It is important to emphasize that if the structure is in relatively shallow water on a bed slope shallower then 1:50 it is quite possible that many of the larger waves can break before the structure. The sea in front of the structure will be highly aerated and wave forces will be reduced.

8.4 PREDICTION OF VERTICAL FORCES

Since Bagnold's pioneering work in 1939, impact forces on vertical walls were found to vary largely even for fixed nominal conditions whereas the force impulse I, defined in Equation 8.13, is far more repeatable.

Equation 8.13 $$I = \int F dt$$

Impulses being finite quantities, shorter rise times will correspond to more intense impact forces and vice versa. The first stochastic description of the correlation between impact forces on vertical walls and their rise time can be found in Oumeraci et al. (2001) for the prediction of horizontal impact forces on vertical walls.

In the following, a formula for the maximum vertical impact forces beneath the horizontal part is derived based on the impulse theory and solitary wave theory which is completely similar to the method applied for the horizontal forces on vertical walls.

The forward momentum of a fluid mass M hitting beneath the horizontal part with a vertical velocity v will induce a vertical force impulse.

Equation 8.14 $$\int_0^{t_r} F_v(t) \cdot dt = M \cdot v$$

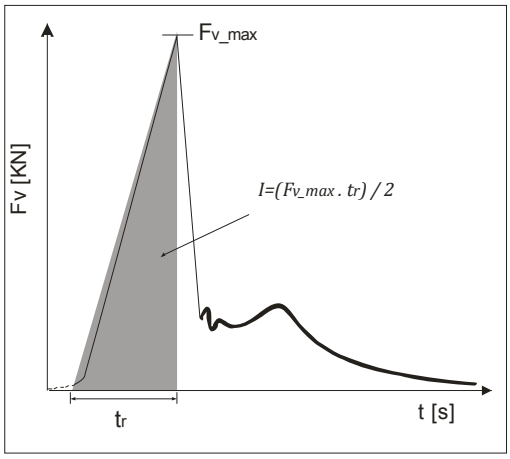

Figure 8.14 *Impact loading of horizontal part-definition sketch*

Where t_r is the rise time up to the peak forces F_{v_max} and $F_v(t)$ is the vertical force time duration (see Figure 8.14). v is the vertical velocity at the time of impact. Assuming a linear temporal increase of the force $F_v(t)$ like in Figure 8.14.

Thus leading to the peak force:

Equation 8.15 $$\frac{F_{v\_max} \cdot t_r}{2} = Mv$$

The most difficult part of the Equation 8.15 is to determine the Fluid mass (M). However, this mass might be estimated to the overtopping discharge by assuming the cantilever slab does not exist. Under this assumption, the crest freeboard, h_c, is equal to clearance, c, which is shown in Figure 3.1. Then, the structure will be a simple vertical wall and the overtopping mass is expressed by the following equation:

Equation 8.16 $$M = q.T.\rho$$

where, q is the overtopping discharge, T the wave period and ρ the water density.

It is well established that the wave overtopping discharge, q on many kinds of coastal structures generally decreases exponentially as the crest freeboard, h_c, increases, with a form:

Equation 8.17 $$\frac{q}{\sqrt{gH_{m0}^3}} = a \cdot exp\left(-b\frac{h_c}{H_{m0}}\right)$$

where H_{m0} is the spectral significant wave height, and a and b are fitting coefficients. For vertical breakwaters or seawalls, EurOtop (2007) gives a = 0.04 and b = 2.6.

However, there has long been evidence that the overtopping process at vertical and steep walls cannot be described for all conditions by equations like Equation 8.17. Therefore, a new empirical fit (Equation 8.18) of the same form with a power law decrease in overtopping discharge with freeboard rather than an exponential one was proposed for breaking waves (impact loads) based on physical model studies in the 1990s (Bruce and van der Meer, 2008).

Equation 8.18 $$\frac{q}{h_*^2\sqrt{gh_s^3}} = 15 \cdot 10^{-4}\left(h_* \frac{h_c}{H_{m0}}\right)^{-3.1} \text{ over } 0.03 < h_* \frac{h_c}{H_{m0}} < 1.0$$

where, $h_* = 1.35 \frac{h_s}{H_{m0}} \frac{2\pi h_s}{gT^2}$

Assuming that the actual vertical velocity of the fluid mass during impact may be approximated by V_{av}, which is shown in Equation 8.10, then the forward momentum of the fluid mass M involved in the impact process is obtained from Equation 8.10, Equation 8.15 and Equation 8.16 which leads to:

Equation 8.19 $$M \cdot v = (qT\rho)V_{av}$$

Thus giving a peak force of:

Equation 8.20 $$\frac{F_{v\_max} \cdot t_r}{2} = (qT\rho)V_{av}$$

A linear relation is obtained between the natural logarithm of F_{v_max} and $\frac{2(qT\rho)V_{av}}{t_r}$ in Equation 8.21.

Equation 8.21 $$F_{v\_max} = exp\left(\beta_1 ln\left(\frac{2(qT\rho)V_{av}}{t_r}\right) + \beta_2\right)$$

Where, β_1 and β_1 depend on $\left(\frac{c}{h_s}\right)^2$.

$$\beta_1 = -0.015\left(\frac{c}{h_s}\right)^2 + 0.22$$

$$\beta_2 = -0.074\left(\frac{c}{h_s}\right)^2 - 2.2$$

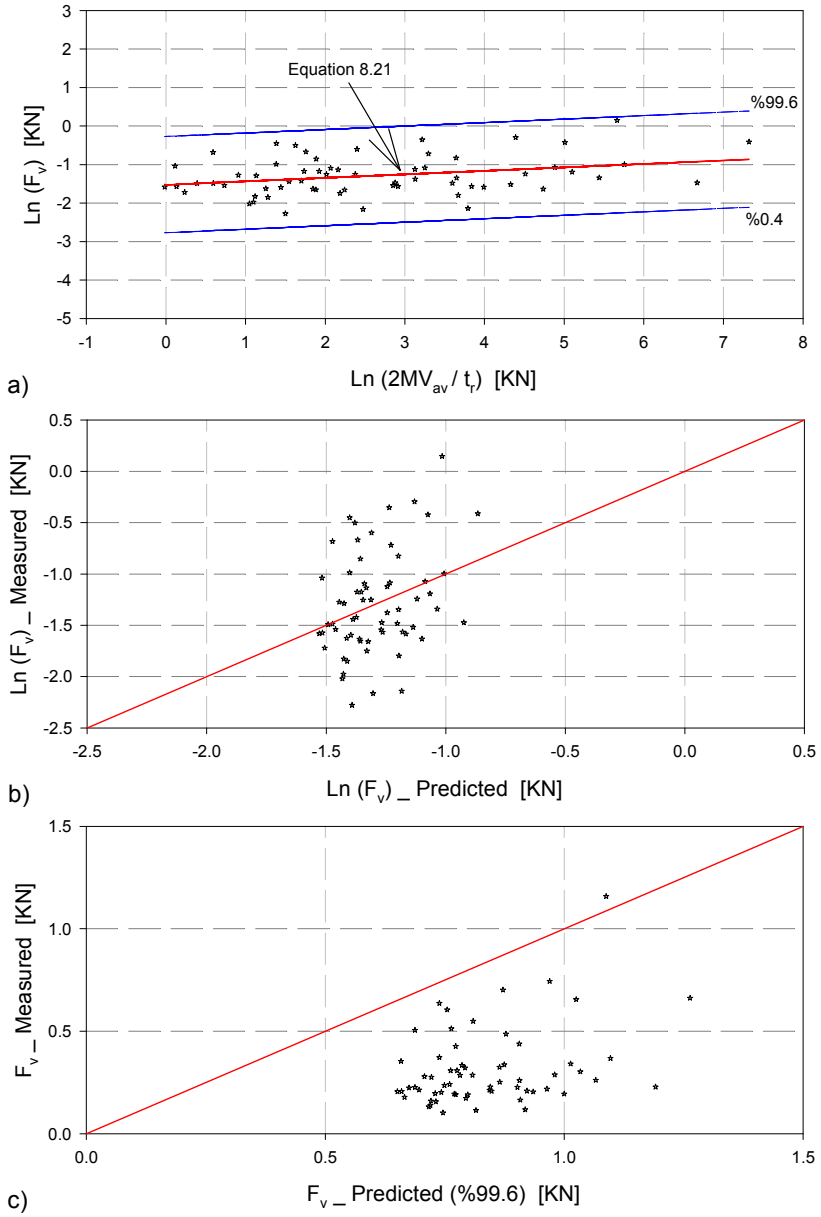

Figure 8.15 *a) Natural logarithm of maximum vertical forces (F_v) versus natural logarithm of $2MV_{av}/t_r$ and comparison of data with Equation 8.21, ($h_s = 0.075\ m$) b) Comparison of the natural logarithm of the measured and the predicted maximum vertical forces, c) Comparison of the measured and the predicted maximum vertical forces*

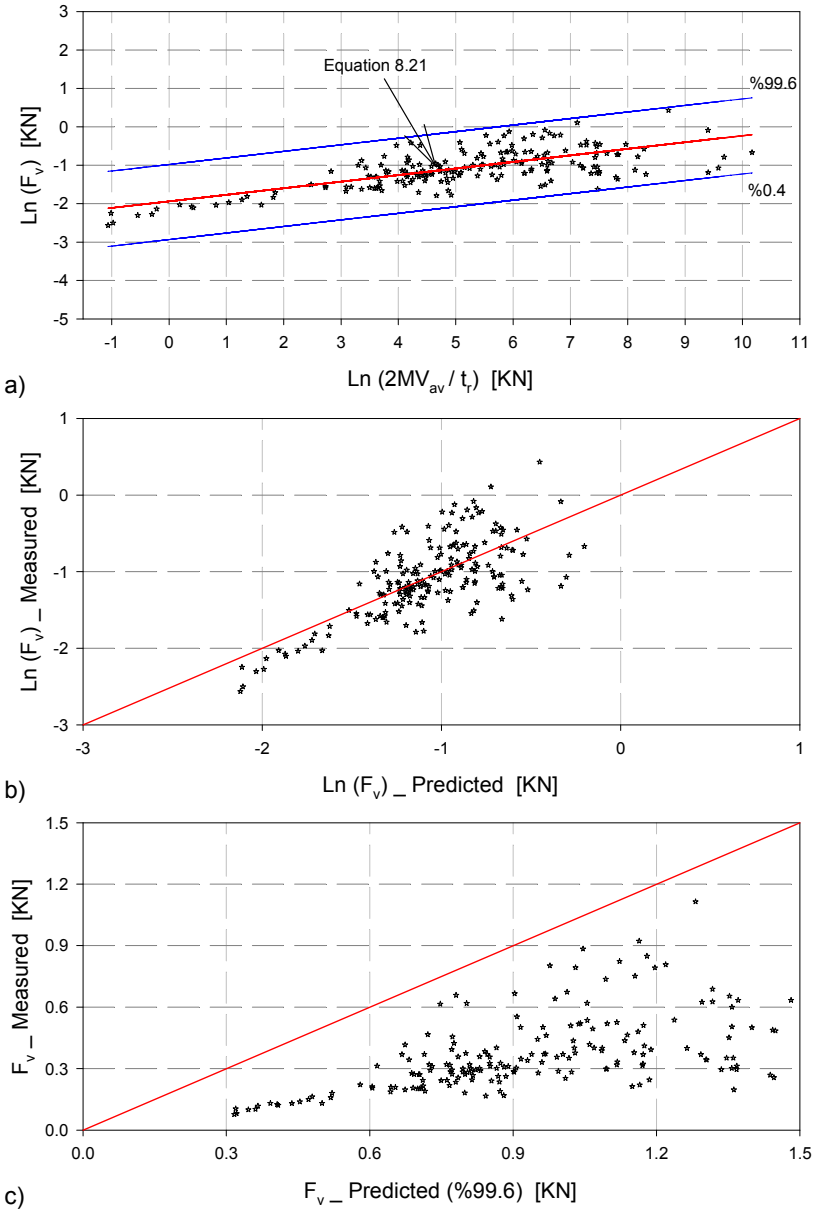

Figure 8.16 *a) Natural logarithm of maximum vertical forces (F_v) versus natural logarithm of $2MV_{av}/t_r$ and comparison of data with Equation 8.21, ($h_s = 0.105\ m$) b) Comparison of the natural logarithm of the measured and the predicted maximum vertical forces, c) Comparison of the measured and the predicted (99.6%) maximum vertical forces*

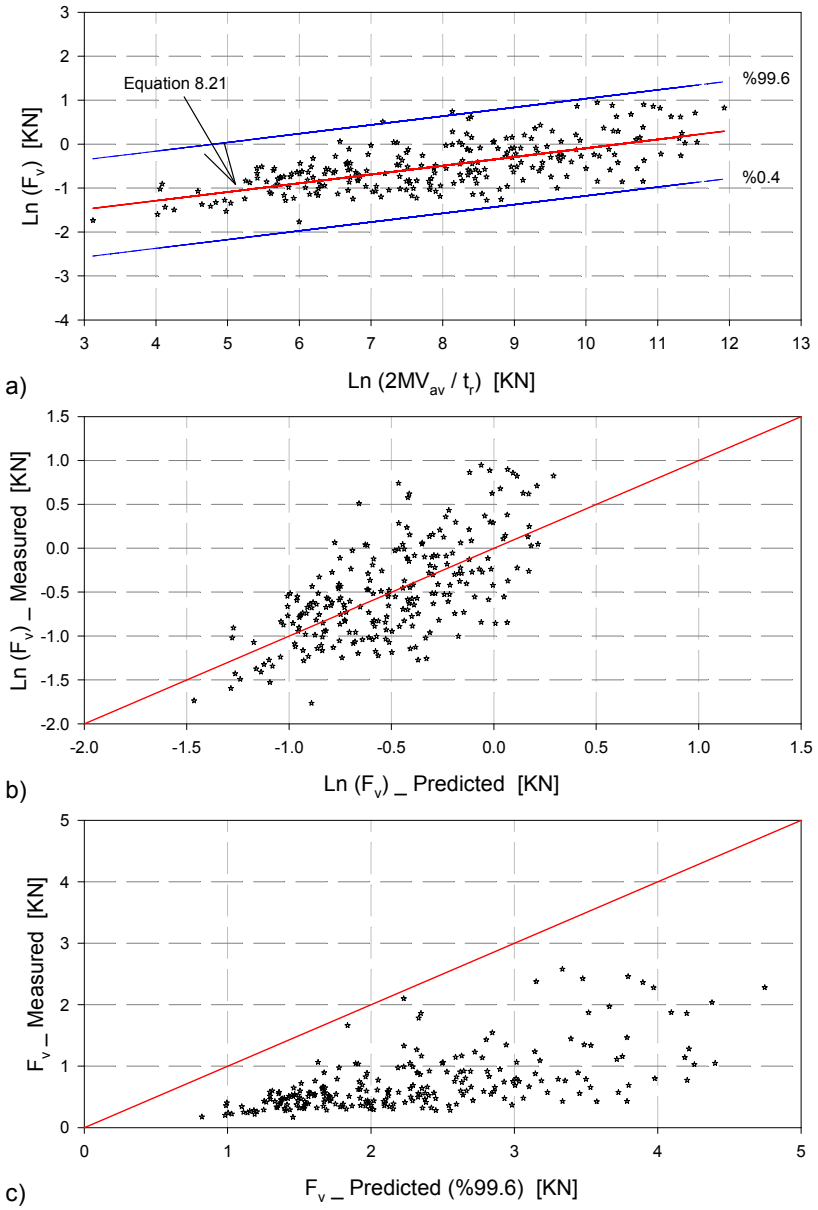

Figure 8.17 *a) Natural logarithm of maximum vertical forces (F_v) versus natural logarithm of $2MV_{av}/t_r$ and comparison of data with Equation 8.21, ($h_s = 0.135\ m$) b) Comparison of the natural logarithm of the measured and the predicted maximum vertical forces, c) Comparison of the measured and the predicted (99.6%) maximum vertical forces*

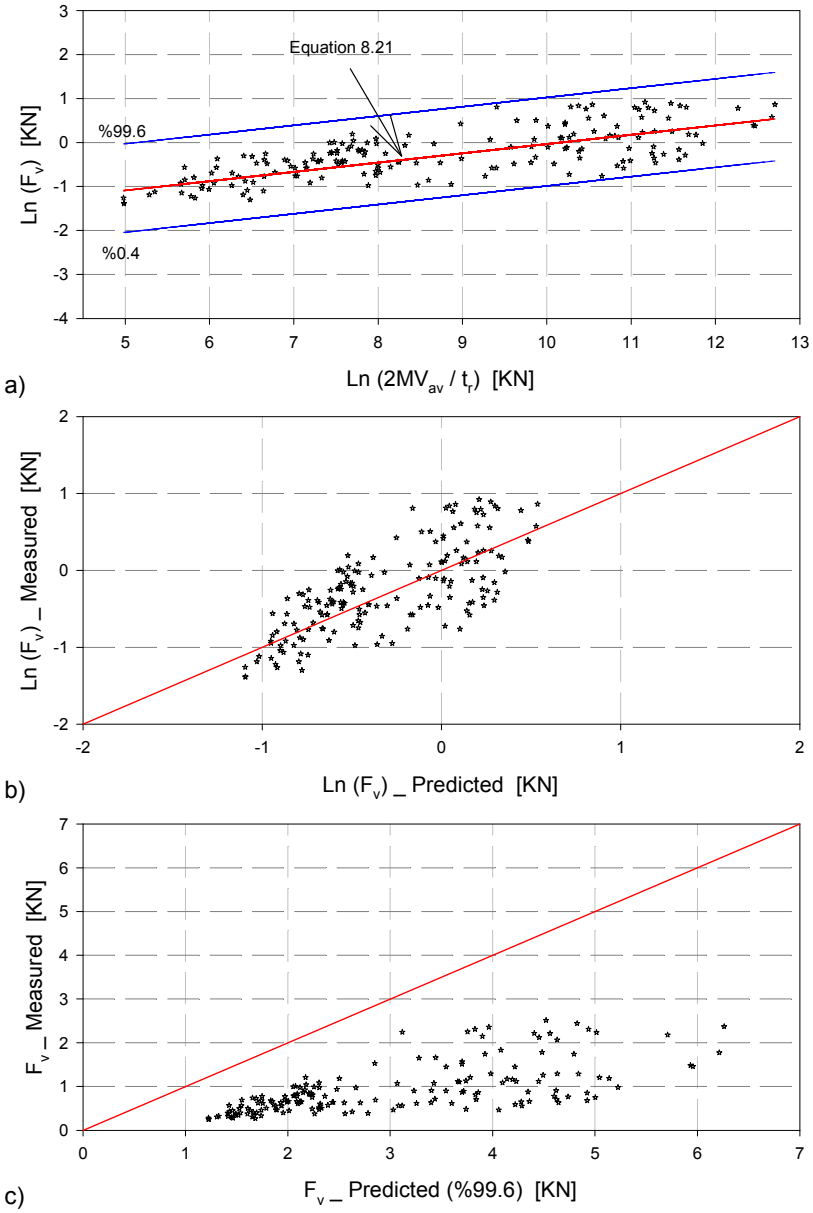

Figure 8.18 *a) Natural logarithm of maximum vertical forces (F_v) versus natural logarithm of $2MV_{av}/t_r$ and comparison of data with Equation 8.21, ($h_s = 0.165\ m$) b) Comparison of the natural logarithm of the measured and the predicted maximum vertical forces, c) Comparison of the measured and the predicted (99.6%) maximum vertical forces*

Figure 8.15a to Figure 8.18a show natural logarithm of maximum vertical forces (F_v) versus natural logarithm of $2\mathrm{MV_{av}}/\mathrm{t_r}$ for four different water depth (h_s). The linear relation between the parameters is represented by Equation 8.21. The lower and upper lines show the lines of non exceedance at level 99.6% and 0.04. All the scattered data lies in between the confidence intervals. In addition, Figure 8.15b to Figure 8.18b show the comparison of vertical forces calculated by proposed method in Equation 8.21 on log-log scale. In addition, measured values are compared with the predicted values at 99.6% confidence level on normal scales. All data points fall successfully below the 99.6% confidence level. However, designers should keep in mind that the Equation 8.21 is not written in non-dimensional form. Therefore, results from the equation should be corrected for scale effects in other scale applications.

8.5 VALIDATION OF PROPOSED METHOD FOR THE MAXIMUM VERTICAL FORCES

Figure 8.19 and Figure 8.20 show the comparison of measured and predicted vertical forces versus rising time (t_r) for four different water depths. Best fit lines (Equations 8.22 - 8.25) are adapted to the measured values by power type linear regression. Then two R^2 values are calculated for each water depth.

$$R^2 = \frac{\sum(y_1 - \overline{y})^2}{\sum(y - \overline{y})^2}$$

where, y_1 is the predicted vertical force. For the first R^2, y_1 is calculated from Equation 8.21 and from best fit lines (Equations 8.22 - 8.25) for the second R^2 values. y is the measured vertical force while $\overline{y}$ is the mean of measurements.

The aim is to make a comparison for validation of the predicted forces given by Equation 8.21. For y_1 calculated from Equation 8.21, R^2 values are found 0.096, 0.340, 0.273 and 0.429 for four different water depths in ascending order respectively. In the same manner, R^2= 0.327, 0.199, 0.167 and 0.250 are found for best fit lines. Except the first value from the smallest water depth ($h_s = 0.075\ m$), all other values show that predicted values from Equation 8.21 have better correlations compared to the correlation of measured data.

Using the procedure described in this chapter, the vertical force (F_v) can be evaluated for the impact loads of slightly breaking or breaking waves beneath the horizontal part.

1) Evaluate the initial vertical force $F_{v\_initial}$ by identifying the Equation 8.12 for the given wave height (H_1) and water depth (h_s).

2) Find the relative rising time (t_r/T) from Equation 8.4 by using $F_{v\_initial}$. The quasi-static component of the vertical force (F_{v_qs}) can be identified from Equation 8.5. For the horizontal quasi static component (F_{h_qs}), the force from the Sainflou method or Goda method is a fair estimation.

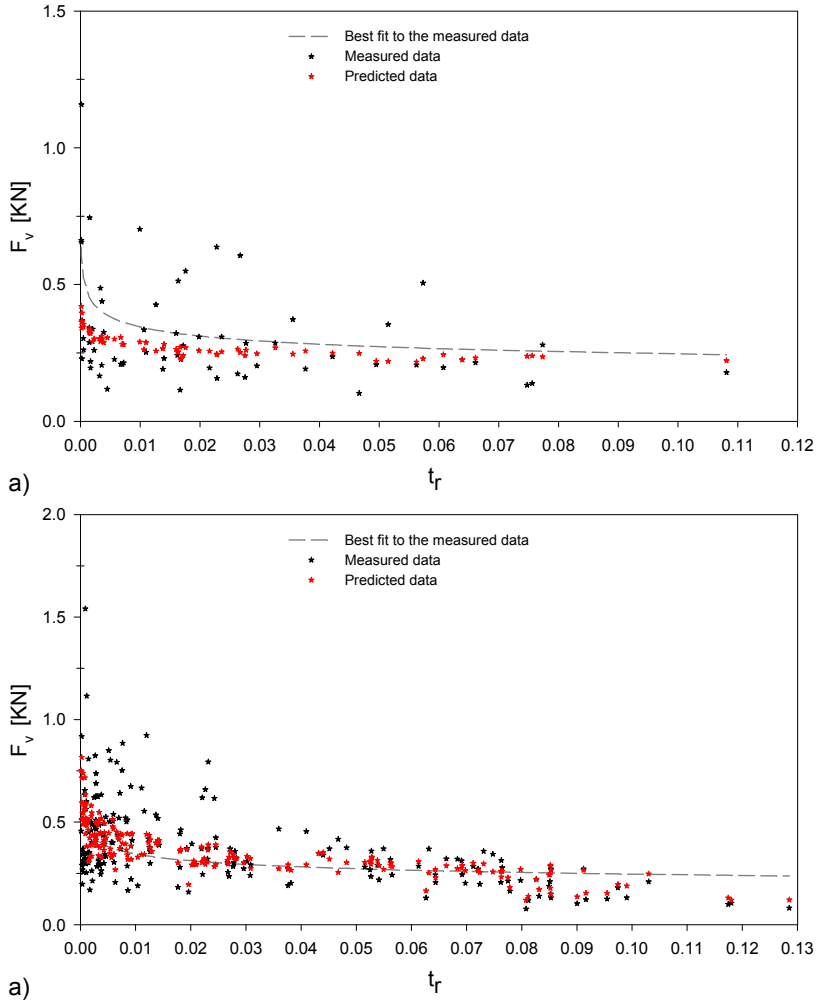

Figure 8.19 *Comparison of measured and predicted (Equation 8.21) maximum impact vertical forces versus rise times. The scatter in the logarithm of the predicted data about the mean prediction is characterized by a standard deviation (s), a)* $h_s = 0.075\ m$*, b)* $h_s = 0.105\ m$

Equation 8.22 $$F_{v\_measured} = 0.16\ t_r^{-0.117},\ h_s = 0.075\ m$$

Equation 8.23 $$F_{v\_measured} = 0.18\ t_r^{-0.146},\ h_s = 0.105\ m$$

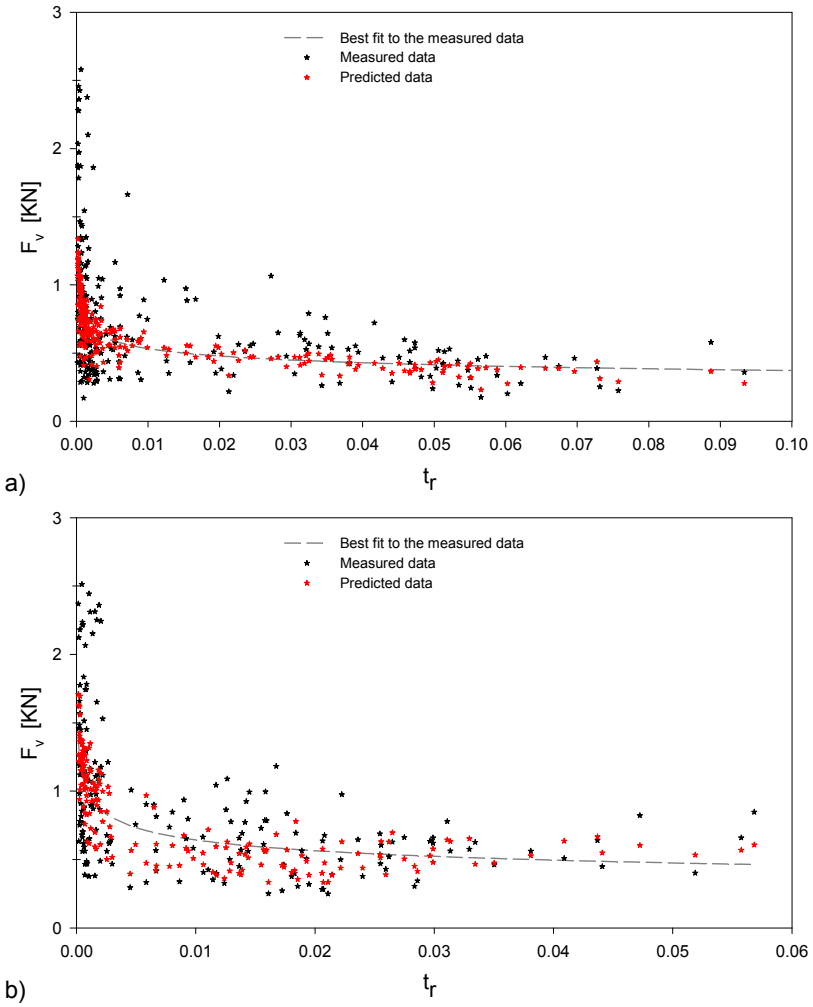

Figure 8.20 *Comparison of measured and predicted (Equation 8.21) maximum impact vertical forces versus rise times. The scatter in the logarithm of the predicted data about the mean prediction is characterized by a standard deviation (s), a)* $h_s = 0.135\ m$*, b)* $h_s = 0.165\ m$

Equation 8.24 $$F_{v\_measured} = 0.26\ t_r^{-0.156},\ h_s = 0.135\ m$$

Equation 8.25 $$F_{v\_measured} = 0.27\ t_r^{-0.188},\ h_s = 0.165\ m$$

3) Vertical averaged velocity (V_{av}) can be calculated from Equation 8.10.

4) The overtopping discharge (q) which is responsible for the impact mass (M) is calculated from Equation 8.18 for impact loadings in the EurOtop Manual (2007).

5) Then by knowing q, T, V_{av} and t_r, F_v for impact loading can be calculated from Equation 8.21 by knowing the geometric parameter $\frac{c}{h_s}$.

However, for the universal use of the method, the parameters and introduced formulas should be validated with different data sets and field measurements.

8.6 CONCLUSIONS

A set parameter responsible for the prediction of wave loading on a vertical wall with a cantilever slab is investigated. The results of regular and irregular waves are compared. Wave height (H_1), water depth at the model toe (h_s), wave period (T), overtopping discharge (q) and vertical averaged velocity (V_{av}) are found to be the main parameters influencing the vertical impact forces. In addition, a variation of the geometric properties, like (c/h_s) is also having an effect.

Based on the impulse theory and experimental investigations on breaking wave kinematics and impact loads, prediction formulas for impact forces have been derived for vertical forces below the horizontal part of a vertical wall with overhanging horizontal cantilevering slab. The design concept for breaking wave loads is developed.

Hydraulic model tests have been performed to assess the vertical averaged velocities involved in the impact process and to verify the results obtained from theory. It was found that the proposed formula represents the mean value of the measurement results.

Future research work is directed towards further improvement of the proposed prediction formulae. This will be achieved by a better definition of the fluid impact mass (M) and of the vertical impact velocity. Moreover, the parameters and introduced formulas should be validated with different data sets and field measurements.

REFERENCES

Allsop N.W.H; Vicinanza D. 1996, "*Wave impact loadings on vertical breakwaters: development of new prediction formulae* " Proc. 11th Int. Harbour Congress, pp 275-284, Royal Flemish Society of Engineers, Antwerp, Belgium.

Bruce, T.; van der Meer, J.W. 2008, "*Integrated prediction tools for wave overtopping at vertical structures*", ASCE, Proc. ICCE 2008, Hamburg, pp. 3110-3119

Oumeraci, H; Kortenhaus, A; Allsop, W; de Groot, M; Crouch, R; Vrijling, H; Voortman, H, 2001, "*Probabilistic Design Tools for Vertical Breakwaters*", Balkema Publishers, New York.

Pullen, T.; Allsop, N.W.H; Bruce, T; Kortenhaus, A; Schüttrumpf, H; and van der Meer, J.W., (2007), "*EurOtop Wave Overtopping of Sea Defenses and Related Structures: Assessment Manual*", Archive for Research and Technology on the North Sea and Baltic Coast, ISBN 978-3-8042-1064-6

Sainflou, M., 1928, "*Essai sur les Digues Maritimes Verticales*", Annales des Ponts et Chaussees, Vol. 98, Pt. 1, Tome 11

9

GENERAL CONCLUSIONS AND RECOMMMENDATIONS

***

9.1 GENERAL CONCLUSIONS

Wave loading on a vertical structure with an overhanging horizontal cantilever slab is analyzed based on the correlation between the kinematics of breaking waves and the height, distribution, duration and characteristics of the wave impacts, by using traditional physical model tests.

For this purpose, two dimensional scaled model tests are carried out in the wave flume with dimensions 30 m x 1 m x 1.2 m. The model is located 22.5 m away from the wave paddle on a uniform slope with 0.5 m depth at the location of the structure. A scale factor of 1:20 is selected to ensure correct reproduction of all wave processes. The scaled model is instrumented with 10 sets of pressure sensors, 9 sets of wave gauges and a high speed camera (HSC). A very high sampling frequency of 20 kHz is used for the pressure recordings which allow a detailed look into the problem. The scaled model is tested for the variation of parameters like the wave period (T), incident wave height (H) and water depth (h_s). Tests are carried out for regular and irregular waves. Wave heights (H) are arranged somehow that the scaled model became exposed to full impacts from non-breaking to broken waves.

Within this research, the following general outcomes are achieved.

Wave conditions given by wave height (H), wave period (T) are identified by taking account of wave shoaling, reflection, and breaking. Wave shoaling has been analyzed for regular waves with test results without taking into account the pressure of the scaled-model. It is found that along the horizontal bottom (out of the surf zone), all measured values are on the line of $H_{1/3}$. However in the surf zone, the wave heights are increasing due to shoaling and the measured values are closer to the H_{max} lines. In addition, the wave reflection is analyzed for regular and irregular waves. The reflection coefficients C_r, measured at the toe of the foreshore, are as $0.80-0.92$, $0.55-0.80$, $0.45-0.70$ and $0.33-0.50$ for SBW, BWSAT, BWLAT and BW respectively. Then, breaking wave heights from regular waves are compared with the calculated breaking wave heights using the Goda (2010) method. The Goda method is calibrated by considering a new value $A = 0.21$, instead of 0.17 and by considering a new data set. Finally, it is found that the existence of the model postpones the inception of wave breaking for some waves which would normally break without the presence of the scaled model.

The correlation between wave kinematics, impact pressures and forces are analyzed. Each approaching wave results in two individual impacts occur sequentially on the scaled model. The first one appears on the vertical part while the second one develops at the attached corner of the horizontal part. Both impact pressures and forces are non-repeatable under nominally identical conditions. Then, the breaker types are classified into four groups. For each group, the kinematic behavior of wave breaking and the related time series of pressures and forces are analyzed. Moreover, characteristics of maximum pressures and forces and the evaluation of instantaneous pressure profiles are discussed more in detail. The overall largest impact pressures are measured in the case of BWSAT: $109\ kPa$ at

the SWL on the vertical part and $123\ kPa$ at the attached corner of the horizontal part. On the vertical part, the occurrence of shock pressures is limited to the case of breaking waves (BWSAT and BWLAT). However, on the horizontal part, this critical situation will extend to SBW and BW zones by the occurrence of accelerated water jets, impacting below the horizontal part which makes the structure more vulnerable from a design view of point.

Due to the secondary impact below the horizontal part, a pressure increase is observed at the upper corner of the vertical part when compared to the case of simple vertical walls. Therefore, The total force in the horizontal direction (F_h) increases in the cases of SBW and BW. For breaker types SBW, BWSAT and BWLAT, the variation of velocity and acceleration components (V_h, V_v) and (a_h, a_v) are analyzed up to the impact time instant. In the case of SBW, V_h is slightly higher than V_v at the time of impact which does not agree with present literature. After the impact time, V_v dramatically increases due to the high vertical acceleration to a value of 20g. The highest vertical acceleration of 53g is measured in the case of BWSAT.

The pressure distribution due to the violent water wave impacts on vertical structures with cantilever slab is analyzed. Both the location and the magnitude of p_{max} on a vertical structure with an overhanging horizontal cantilever slab are determined. On the vertical part, the non-dimensional term (z_{max}/h_s) for the location of p_{max} is gradually decreasing from a point above the SWL to a point below the SWL with the increase of h_s. This relation is expressed by Equation 6.8. On the horizontal part, p_{max} is located at the attached corner of the scaled model and its magnitude decreases sharply below $10\ \rho gH$ between $x/h_s = 0.8 - 1$. The relation between the measured value of p_{max} on the vertical part and related t_r are plotted and compared with empirical values from literature. It is observed that the latter underestimate the measured values. Therefore, a new upper envelope function (Equation 6.9) between p_{max} and t_r is proposed with coefficients $a = 850$ and $b = -0.85$. The similar inverse relation between p_{max} and t_r is also measured by the results for the horizontal part and their relation is given in Equation 6.11. Then, the boundary expressions for the interval of normalized wave height, $\frac{H}{h_s}$, which creates a high dynamic impact on the vertical part with the variation of the clearance, $\frac{c}{a}$, are expressed by Equation 6.13 and Equation 6.14. Finally, for the pressure profiles, local p_{max} at SWL and at the top and bottom of the vertical part (p_{h1}, p_{h2} and p_{h3}) and at the attached corner of the horizontal part (p_{v1}) are considered. For each case, the relation for p_{h3}/p_{h1}, p_{h1}/p_{v1}, and p_{h2}/p_{v1} are determined.

The results measured with the scaled model are compared with the results measured from a simple vertical structure. The cantilever slab blocks the wave overtopping which creates an additional stress on the vertical part. Therefore, the amount of additional stress due to the cantilever slab can be tested by comparing with the results of a simple vertical structure. In both slightly breaking waves SBW and broken waves BW a force increase is observed especially on the small values of F_h. In addition, the results from the simple vertical structure are compared to the

existing prediction formulas in the literature. It is found that all methods diverge considerably to predict effectively the maximum peak pressures.

Finally, a new prediction model for the vertical forces acting on the cantilever slab is being proposed. Within this effort, a set parameter responsible for the prediction of wave loading on a vertical wall with a cantilever slab is investigated. The results of regular and irregular waves are compared. Wave height (H_1), water depth at the model toe (h_s), wave period (T), overtopping discharge (q) and vertical averaged velocity (V_{av}) are found to be the main parameters influencing the vertical impact forces. Then, based on the impulse theory and experimental investigations on breaking wave kinematics and impact loads, prediction formulas for impact forces have been derived for vertical forces below the horizontal part of a vertical wall with overhanging horizontal cantilevering slab. The design concept for breaking wave loads is developed. It is worth to mention that the proposed formula represents the mean value of the measurement results.

9.2 RECOMMENDATIONS

Some remarkable observations are made during the experiments which are performed, leading to extensive possibilities for further research:

The tests are conducted mainly on 1/20 slope. It is also known that the influence of slope is non-ignorable on the magnitude of vertical force. Therefore, the influence of slope should integrate in the final formula.

The proposed formula is considering regular wave results. It must be extended for the irregular waves as well.

The model is tested against limited range of parameters like water depth, wave period and wave height. Parameter ranges must be extended.

The geometry of the model was fixed during the all tests. Different variations of the model dimensions will play a role on the structural integrity.

For design purposes, the structural response of the monolithic overhanging structure should be known. Therefore, some additional efforts should focus on the response of the structure, the generation and proceeding of wave induced vibrations, comfort conditions for use and structural safety.

In the tests, water depth increments are considered up to a water level that still allows that most of the approaching wave crest fits into the space below the horizontal part. Results for wave crests first hitting the horizontal part are excluded from the analysis. Further research should consider those excluded parts in which waves crests first hit beneath the horizontal part.

For the applicability of the proposed outcomes, the scaling issue becomes vital. Therefore, large scale tests will be important for improving scaling problem of the present results.

Appendix I: Parameters for breaking wave formulas

Liu et al. (2011) categorized the breaking wave formulas in to four groups based on their formation types.

The functional forms of $\gamma(\theta,\lambda_0)$ (in the first type), $\alpha(s,\lambda_0)$ and $\xi(s,\lambda_0)$ (in the second type, $\alpha'(s,\lambda_0)$ and $\xi'(s,\lambda_0)$ (in the third type) and $\beta(s)$ and m (in the fourth type) obtained by the previous authors are respectively summarized in table 1 to table 4 in Liu et al. (2011).

Table 1
McCowan type formulas for inception of wave breaking.

Functional form	Sources
0.73	Boussinesq (1871) Laitone (1960)
0.78	McCowan (1894)
0.83	Gwyther (1900) Davies (1952) Yamada et al. (1968) Yamada (1957) Lenau (1966) Longuet-Higgins and Fenton (1974) Witting (1975) Longuet-Higgins and Fox (1977)
0.87	Chappelear (1959)
1.03	Packham (1952)
$[1.40-\max(s,\ 0.07)]^{-1}$	Galvin (1969)
$0.72(1+6.4s)$	Madsen (1976)
$1.062+0.137\log(s\lambda_0^{-1/2})$	Battjes (1974)
$1.1s^{1/6}\lambda_0^{-1/12}$	Sunamura (1980)
$0.937s^{0.155}\lambda_0^{-0.13}$	Singamsetti and Wind (1980)
$1.14s^{0.21}\lambda_0^{-0.105}$	Larson and Kraus (1989)
$1.12(1+e^{-60s})^{-1}-5.0(1-e^{-43s})\lambda_0$	Smith and Kraus (1990)
$0.284\lambda_0^{-1/2}\tanh[\pi\lambda_0^{1/2}]$	Camenen and Larson (2007)

Table 2
Miche type formulas for inception of wave breaking.

α	ξ	Sources
0.142	1.0	Miche (1944)
0.14	0.9	Battjes and Janssen (1978)
0.14	$0.8+5.0\min(s,0.1)$	Ostendorf and Madsen (1979)
0.14	$0.57+0.45\tanh(33\lambda_0)$	Battjes and Stive (1985)
$0.127e^{4s}$	1.0	Kamphuis (1991)
0.14	$-11.21s^2+5.01s+0.91$	Rattanapitikon and Shibayama (2000)

Table 3
Goda type formulas for inception of wave breaking.

α'	ξ'	Sources
0.17	$0.5+7.5s^{4/3}$	Goda (1970)
0.17	$0.52+2.36s-5.40s^2$	Rattanapitikon and Shibayama (2000)
0.17	$0.5+5.5s^{4/3}$	Goda (2010)

Table 4
Munk type formulas for inception of wave breaking.

m	β	Sources
−1/3	0.3	Munk (1949)
−1/4	$0.76s^{1/7}$	LeMehaute and Koh (1967)
−1/5	0.56	Komar and Gaughan (1972)
−1/4	$s^{1/5}$	Sunamura and Horikawa (1974)
−0.254	$0.575s^{0.031}$	Singamsetti and Wind (1980)
−1/4	$0.68s^{0.09}$	Ogawa and Shuto (1984)
−0.24	0.53	Larson and Kraus (1989)
$-0.30+0.88s$	$0.34+2.47s$	Smith and Kraus (1990)
−0.28	0.478	Gourlay (1992)
−1/5	$0.55+1.32s-7.46s^2+10.02s^3$	Rattanapitikon and Shibayama (2000)

Appendix II: Datasheet of the Kistler pressure sensor

Pressure

KISTLER
measure. analyze. innovate.

Quartz High-Pressure Sensor

Type 601A, 601H

Quartz pressure sensor for measuring dynamic and quasi-static pressures up to 1 000 bar at temperatures up to 200 °C. Very small dimensions.

- Very small dimensions
- Temperatures up to 200 °C
- High natural frequency

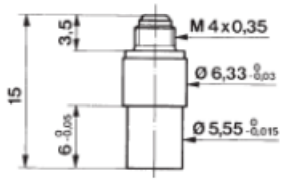

Description
The measured pressure acts through the diaphragm on the quartz crystal measuring element, which transforms the pressure p (bar) into an electrostatic charge Q (pC = pico-Coulomb).

The stainless steel diaphragm is welded flush and hermetically to the stainless steel sensor body. The quartz elements are mounted in a highly sensitive arrangement (transversal effect), which is welded hermetically to the body.

The connector is welded to the body, but its Teflon® insulator is not absolutely tight.

Application
The miniature quartz pressure sensors Type 601... are especially suited for dynamic pressure measurements on objects offering little mounting space.

If mounting space and max. measured frequency allows for, the sensor Type 701A should be selected because of its five times higher sensitivity.

Typical Applications
Pressure measurements on compressors, pneumatic and hydraulic installations (except injection pumps). Measurements of explosion and blast pressures (601H).

Technical Data

Type		601A	601H
Range	bar	0 ... 250	0 ... 1 000
Calibrated partial ranges	bar	0 ... 25	0 ... 100
	bar	0 ... 2,5	0 ... 10
Overload	bar	500	1 200
Sensitivity	pC/bar	~–16	
Natural frequency	kHz	~150	
Linearity	%FSO	≤±0,5	
Acceleration sensitivity	bar/g	<0,001	
Operation temperature range	°C	–196 ... 200	
Temperature coefficient of sensitivity	%/K	$<10^{-4}$	
Insulation resistance at 20 °C	Ω	$>10^{13}$	
Shock resistance	g	10 000	
Capacity	pF	5	
Weight	g	1,7	
Connector, Teflon® insulator		M4x0,35	

1 N (Newton) = 1 kg · m · s^{-2} = 0,1019... kp = 0,2248... lbf;
1 kgf = 9,80665 N; 1 inch = 25,4 mm; 1 kg = 2,2046...lb;
1 N-m = 0,73756...lbft

Teflon® is a registered trademark of DuPont.

KISTLER
measure. analyze. innovate.

Mounting

The sensor can be mounted directly into the measuring object or the adapter by means of a mounting nut (Fig. 1) or a connecting nipple (Fig. 2).
When mounted with a connecting nipple, the latter is preassembled with the sensor to a mounting unit. The junction between nipple and sensor can be sealed with "Loctite".

See also datasheets for:

Tools	1300_000-068
Adapter	6501_000-070
Connecting nipples	6401_000-069
Cables	1601B_000-352

Mounting Examples

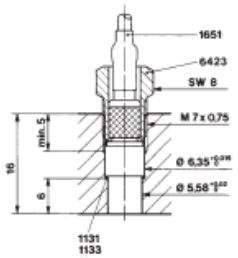

Fig. 1: Mounting with mounting nut

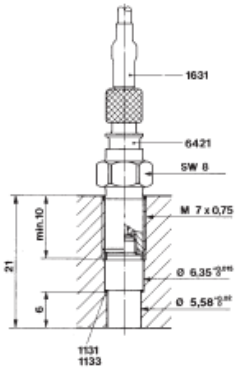

Fig. 2: Mounting with connecting nipple

Included Accessories

- None

Optional Accessories	Type/Art. No.
• Copper seal	1131
• Nickel seal	1131A
• Teflon® seal	1133
• Key WS8 for connecting nipple 6421	1301
• Step drill	1331
• Extraction tool KIAG 10-32 and M4	1311
• Mounting nut WS8	6423
• connecting nipple M4/KIAG 10-32	6421
• Connecting nipple M4/BNC	6401
• Connecting nipple M4/TNC	6411
• Connecting nipple air cooled M4/KIAG 10-32	6461
• Heat-shrink tubing for connector	1021
• Mounting adapter M10x1	6503
• Mounting adapter M14x1,25	6501
• Mounting adapter conical	6505
• Mounting adapter M3	6507
• Cooling adapter M14x1,25	6509
• Cooling adapter conical	6515sp

Ordering Key

Type 601 □

Sensor	
Type 601A	A
Type 601H	H

Appendix III: Datasheet of the Photron high speed camera

ultima APX-RS
FASTCAM

Superb light sensitivity, speed and resolution defines Photron's APX-RS high-speed system as the industry leader.

The **ultima APX-RS** provides full mega pixel resolution images at frame rates up to 3,000 frames per second (fps), 512 x 512-pixels resolution at 10,000fps and at reduced frame rates to an unrivaled frame rate of 250,000fps.

Utilizing Photron's advanced CMOS sensor technology, the **APX-RS** provides the higher light sensitivity than any other comparable high-speed imaging system. Designed as a solid one piece camera, able to withstand shock forces as high as 100G's. Both color and monochrome models are available, both with excellent anti-blooming capabilities.

A user selectable 'Region Of Interest' function enables the active image area to be defined in steps of 128 pixels wide by 16 pixels high to allow the most efficient use of frame rate, image resolution and memory capacity for any event. Up to 20 commonly used configurations can be saved to memory for future operation.

Available with Gigabit Ethernet, FireWire and fiber optic communications, this compact camera can provide exposure durations as short as 2 microseconds and is easily operated in the field with or without a computer through use of the supplied remote keypad; enabling full camera setup, operation and image replay. When a PC is used, Photron's PFV software makes setting up and operating multiple cameras easy and intuitive.

BENEFITS

- FireWire, Gigabit Ethernet and Optical interfaces available for maximum flexibility and fastest image download and reliable camera control, regardless of distance
- High-G proven for reliable operation in the harshest environments. A sealed unit is available for reliable use in hot and dusty locations
- Now available with 16GB memory option for longer recording times such as 12 seconds at 1,000 full resolution frames per second
- Full 1024 x 1024-pixels resolution up to 3,000 fps
- 10,000 fps at 512 x 512-pixels
- 250,000 fps at reduced resolution – an industry record
- Global electronic shutter to 2μs
- IRIG or GPS timing is recorded in real time on every frame – not appended later
- User selectable 'Region Of Interest' function

SLOW MOTION IMAGING SOLUTIONS

Photron®

www.photron.com
image@photron.com

SPECIFICATIONS

Frame Rate (fps)	Max. Resolution Horizontal	Max. Resolution Vertical	Record Time (seconds) 2GB	Record Time (seconds) 8GB	Record Time (seconds) 16GB	Record Time (frames) 2GB	Record Time (frames) 8GB	Record Time (frames) 16GB
60	1,024	1,024	34.1	102.4	204.8	2,048	6,144	12,288
125	1,024	1,024	16.4	49.2	98.3	2,048	6,144	12,288
250	1,024	1,024	8.2	24.6	49.2	2,048	6,144	12,288
500	1,024	1,024	4.1	12.3	24.6	2,048	6,144	12,288
1,000	1,024	1,024	2.0	6.1	12.3	2,048	6,144	12,288
2,000	1,024	1,024	1.0	3.1	6.1	2,048	6,144	12,288
3,000	1,024	1,024	0.7	2.0	4.1	2,048	6,144	12,288
5,000	768	768	0.7	2.2	4.4	3,641	10,923	21,845
9,000	640	480	0.8	2.3	4.7	6,991	20,972	41,943
10,000	512	512	0.8	2.5	4.9	8,192	24,576	49,152
10,000	512	528	0.8	2.4	4.8	7,944	23,831	47,663
15,000	384	384	1.0	2.9	5.8	14,564	43,691	87,381
30,000	256	256	1.1	3.3	6.6	32,768	98,304	196,608
50,000	256	144	1.2	3.5	7.0	58,254	174,763	349,525
70,000	128	128	1.9	5.6	11.2	131,072	393,216	786,432
100,000	384	48	1.2	3.5	7.0	116,508	349,525	699,051
150,000	128	48	2.3	7.0	14.0	349,525	1,048,576	2,097,152
210,000	256	16	2.5	7.5	15.0	524,288	1,572,864	3,145,728
250,000	128	16	4.2	12.6	25.2	1,048,576	3,145,728	6,291,456

Sensor	10-bit CMOS (Bayer system color, single sensor) with 17µm pixels, 16.7ms to 2µs global electronic shutter independent of frame rate and overexposure protection
Saved Image Formats	AVI, JPEG, PNG (10-bit), TIFF, FTIF (10-bit), BMP, and Bayer and RS-170 Video output. Images can be saved with or without image or comment data
Extended Dynamic Range	Selectable from 4 presets to prevent over exposure
Phase Lock	Enables cameras to be synchronized precisely together to a master camera or external source
Triggering	Selectable positive or negative TTL 5Vp-p, switch closure
Lens Mount	Interchangeable F-mount and C-mount supplied standard. Optional High-G block mount
Data Display	Frame Rate, Shutter Speed, Trigger Mode, Date or Time (can be switched), Status (Playback/Record), Real Time, Frame Count, Resolution System or IRIG time, and user-edited comments can be displayed beside or in the saved image area for all formats
Video Output	NTSC or PAL. Live video during recording. Ability to zoom and pan within image via keypad
Dual Speed Recording™	Enables the recording speed to be changed, up or down, by a factor of 2, 4 or 8 during a recording
Timing	Internal clock or external source such as IRIG or GPS. Indicators show current status of timing source
Event Markers	Ten user-entered event markers mark specific events within the image sequence in real time. Immediately accessible through software
Recording Modes	Start, End, Center, Manual, Random, Random Reset, Random Center, Random Manual, and Dual Speed Recording™
Partitioning	Up to 64 memory segments for multiple recordings in memory
Camera Control	Through supplied keypad and RS-422A. And either via the Photron Gigabit Optical Network, Gigabit Ethernet or FireWire
Software	Includes image rotation and ability to save images with or without time codes or comment data
Shock	100G @ 10ms any axis
Dimensions (no lens mount)	H 6.24" (158.6mm) (add 2.13" [54mm for handle and feet]) x W 5.17" (131.4mm) x L 11.39" (289.2mm)
Weight	10.8lb (4.9kg)

PHOTRON USA, INC.
9520 Padgett Street, Suite 110
San Diego, CA 92126-4446
858.684.3555
800.585.2129
f 858.684.3558
email: image@photron.com
www.photron.com

PHOTRON (EUROPE) LIMITED
Willowbank House
84 Station Road
Marlow
Bucks, SL7 1NX
United Kingdom
+44 (0) 1628 894353 f +44 (0) 1628 894354
email: image@photron.com
www.photron.com

PHOTRON LIMITED
Fujimi-Cho 1-1-8
Chiyoda-Ku, Tokyo 102-0071
Japan
+81 3-3238-2106
f +81 3-3238-2109
email:image@photron.co.jp
www.photron.co.jp

Appendix IV: List of Publications

A1 Papers

- **Kisacik**, D.; Troch, P.; Van Bogaert, P., 2011, "Description of loading conditions due to violent wave impacts on a vertical structure with an overhanging horizontal cantilever slab", Coastal Engineering, Volume 60, Issue 1, February 2012, Pages 201-226

- **Kisacik**, D.; Troch, P.; Van Bogaert, P., 2012, "Experimental study of violent wave impact on a vertical structure with an overhanging horizontal cantilever slab", Accepted to Ocean Engineering

Chapter in Books

- Müller, V.; Seibel, A.; **Kisacik**, D.; Gust, G. (2007) "Simulation of Water Column Hydrodynamics by Benthic Chambers". Chapter 3.3 in B. Westrich and U. Förstner (Eds.) Sediment Dynamics and Pollutant Mobility in Rivers: An Interdisciplinary Approach, Springer Berlin Heidelberg, pp: 90-99, 2007, ISBN 978-3-540-34782-8

Peer-reviewed conference papers (P1)

- **Kisacik**, D.; Verleysen, P.; Van Bogaert, P.; Troch, P. (2010) "Comparative study on breaking wave forces on vertical walls with cantilever surfaces", Conference proceedings, The Twentieth (2010) International Offshore and Polar Engineering Conference (ISOPE), pp:888-894, 20-26 June 2010, Beijing - China, ISBN 978-1–880653–77-7

Conferences papers (C1)

Kisacik, D.; Troch, P.; Van Bogaert, P. (2010) "Experimental results of breaking wave impact on a vertical wall with an overhanging horizontal cantilever slab", Proceedings of the International Conference on Coastal Engineering (ICCE), No 32 (2010), 30 June – 5 July 2010, Shanghai – China

- **Kisacik**, D.; Troch, P.; Van Bogaert, P. (2010) "Breaking Wave Impact on a Vertical Wall with an Overhanging Horizontal Cantilever Slab: Irregular Waves", Conference proceedings, 3rd International Conference on the Application of Physical Modelling to Port and Coastal Protection (CoastLab10), 28 September - 1 October 2010, Barcelona – Spain

- Frigaard, P.; Andersen, T. L.; Ramirez, J. R. R.; Sørensen, S. P. H.; Martinelli, L.; Lamberti, A.; Troch, P.; de Vos, L.; **Kisacik**, D.; Stratigaki, V.; Zou, Q.; Monk, K.; Vandamme, J.; Damsgaard, M. L.; Gravesen, H. (2010) "Loads on

entrance platforms for offshore wind turbines", Conference proceedings, HYDRALAB III Joint User Meeting, Hannover-Germany, February 2010

- **Kisacik**, D.; Van Bogaert, P.; Troch, P.; Van Slycken, J.; Verleysen, P. (2009) "Experimental results of loading conditions due to violent wave impacts on coastal structures with cantilever surfaces", Conference proceedings, 2nd International Conference on the Application of Physical Modelling to Port and Coastal Protection (CoastLab08), pp:587-598, 2 - 5 July 2008, Bari-Italy, ISBN 978-90-78046–07-3

- **Kisacik**, D.; Troch, P.; Van Bogaert, P. (2009) "Violent Wave Impacts on Coastal Structures with Cantilever Surfaces", 10th FirW PhD Symposium, pp: 170, 9 - December 2009, Gent-Belgium

- **Kisacik**, D.; Troch, P.; Van Bogaert, P. (2010) "Breaking Wave Impacts on Coastal Structures with Cantilever Surfaces", 11th FirW PhD Symposium, pp: XX, 1 - December 2010, Gent-Belgium

Conferences papers (C3)

- Kisacik, D.; Troch, P.; Van Bogaert, P. (2010) "Experimental results of breaking wave impact on a vertical wall with an overhanging horizontal cantilever slab", Book of Abstracts, 32nd International Conference on Coastal Engineering (ICCE), 30 June – 5 July 2010, Shanghai - China

- Kisacik, D.; Troch, P.; Van Bogaert, P. (2010) "Breaking Wave Impact on a Vertical Wall with an Overhanging Horizontal Cantilever Slab: Irregular Waves", Book of Abstracts, 3rd International Conference on the Application of Physical Modelling to Port and Coastal Protection (CoastLab10), pp:115-116, 28 September - 1 October 2010, Barcelona – Spain

- Kisacik, D.; Van Bogaert, P.; Troch, P.; Van Slycken, J.; Verleysen, P. (2009) "Experimental results of loading conditions due to violent wave impacts on coastal structures with cantilever surfaces", Book of Abstracts, 2nd International Conference on the Application of Physical Modelling to Port and Coastal Protection (CoastLab08), pp:11-14, 2-5 July 2008, Bari-Italy, ISBN 978-88-6093–046-0

- Kisacik, D.; Troch, P.; Van Bogaert, P. (2009) "Loading conditions and structural response due to violent wave impacts on coastal structures with cantilever surfaces" 10th VLIZ Young Scientists' Day Special edition at the occasion of 10 years VLIZ, pp:77, Thermae Palace, Oostende-Belgium, 27 - November 2009, ISSN 1377-0950

- Müller, V.; Seibel, A.; Kisacik, D.; Gust, G. (2006) "Simulation of Water Column Hydrodynamics by Benthic Chambers", Book of Abstracts, International Symposium on Sediment Dynamics and Pollutant Mobility in River Basins (SEDYMO International 2006), 26 - 29 March 2006, Hamburg-Germany